



Large and Small Droplet Impingement Data on Airfoils and Two Simulated Ice Shapes

*Michael Papadakis, See-Cheuk Wong, and Arief Rachman
Wichita State University, Wichita, Kansas*

*Kuohsing E. Hung and Giao T. Vu
The Boeing Company, Wichita, Kansas*

*Colin S. Bidwell
Glenn Research Center, Cleveland, Ohio*

The NASA STI Program Office . . . in Profile

Since its founding, NASA has been dedicated to the advancement of aeronautics and space science. The NASA Scientific and Technical Information (STI) Program Office plays a key part in helping NASA maintain this important role.

The NASA STI Program Office is operated by Langley Research Center, the Lead Center for NASA's scientific and technical information. The NASA STI Program Office provides access to the NASA STI Database, the largest collection of aeronautical and space science STI in the world. The Program Office is also NASA's institutional mechanism for disseminating the results of its research and development activities. These results are published by NASA in the NASA STI Report Series, which includes the following report types:

- **TECHNICAL PUBLICATION.** Reports of completed research or a major significant phase of research that present the results of NASA programs and include extensive data or theoretical analysis. Includes compilations of significant scientific and technical data and information deemed to be of continuing reference value. NASA's counterpart of peer-reviewed formal professional papers but has less stringent limitations on manuscript length and extent of graphic presentations.
- **TECHNICAL MEMORANDUM.** Scientific and technical findings that are preliminary or of specialized interest, e.g., quick release reports, working papers, and bibliographies that contain minimal annotation. Does not contain extensive analysis.
- **CONTRACTOR REPORT.** Scientific and technical findings by NASA-sponsored contractors and grantees.

- **CONFERENCE PUBLICATION.** Collected papers from scientific and technical conferences, symposia, seminars, or other meetings sponsored or cosponsored by NASA.
- **SPECIAL PUBLICATION.** Scientific, technical, or historical information from NASA programs, projects, and missions, often concerned with subjects having substantial public interest.
- **TECHNICAL TRANSLATION.** English-language translations of foreign scientific and technical material pertinent to NASA's mission.

Specialized services that complement the STI Program Office's diverse offerings include creating custom thesauri, building customized databases, organizing and publishing research results . . . even providing videos.

For more information about the NASA STI Program Office, see the following:

- Access the NASA STI Program Home Page at <http://www.sti.nasa.gov>
- E-mail your question via the Internet to help@sti.nasa.gov
- Fax your question to the NASA Access Help Desk at 301-621-0134
- Telephone the NASA Access Help Desk at 301-621-0390
- Write to:
NASA Access Help Desk
NASA Center for AeroSpace Information
7121 Standard Drive
Hanover, MD 21076

NASA/TM—2007-213959



Large and Small Droplet Impingement Data on Airfoils and Two Simulated Ice Shapes

*Michael Papadakis, See-Cheuk Wong, and Arief Rachman
Wichita State University, Wichita, Kansas*

*Kuohsing E. Hung and Giao T. Vu
The Boeing Company, Wichita, Kansas*

*Colin S. Bidwell
Glenn Research Center, Cleveland, Ohio*

National Aeronautics and
Space Administration

Glenn Research Center

October 2007

Acknowledgments

Funding for this work was provided by NASA Glenn Research Center (NASA Glenn) and the Federal Aviation Administration. The authors would like to thank the following NASA and FAA senior personnel for their encouragement and support: Tom Bond, chief, Icing Branch, NASA Glenn; and Jim Riley and Eugene Hill, Federal Aviation Administration. Thanks are also due to Robert F. Ide, Dave Sheldon, Tim Bencic, John R. Oldenburg, Charlie Andracchio, and the IRT personnel of NASA Glenn for their extensive support with the impingement tests. Finally, the support provided by The Boeing Company and the extensive contributions of Art Porter, Emily Smythe, Norma Campos, and Shu Liu, Wichita State University, to this program are acknowledged.

Available from

NASA Center for Aerospace Information
7115 Standard Drive
Hanover, MD 21076

National Technical Information Service
5285 Port Royal Road
Springfield, VA 22100

Available electronically at <http://gltrs.grc.nasa.gov>

Contents

Abstract.....	5
Executive Summary	5
List of Abbreviations and Symbols	6
1.0 Introduction	8
2.0 Background	9
3.0 Droplet Trajectory Equation and Impingement Parameters	12
3.1 Differential Equation of Particle Trajectory	12
3.2 Impingement Parameters	14
3.2.1 Liquid Water Content (<i>LWC</i>)	14
3.2.2 Cloud Droplet Distribution	14
3.2.3 Median Volumetric Diameter (<i>MVD</i>).....	14
3.2.4 Local Impingement Efficiency.....	15
3.2.5 Total Impingement Efficiency	15
3.2.6 Impingement Limits	16
3.2.7 Summary of Droplet Impingement Parameters	16
3.3 Large Droplet Impingement Issues	16
4.0 Water Droplet Splash Experiments at the Goodrich IWT.....	17
4.1 Goodrich Icing Wind Tunnel (IWT).....	17
4.2 Test Model and Installation	17
4.3 Spray System.....	18
4.4 Imaging System	18
4.5 Test Procedure and Test Matrix.....	18
4.6 Discussion of Results.....	19
5.0 Water Droplet Impingement Tests at the NASA IRT.....	20
5.1 Wind Tunnel Facility.....	20
5.2 Test Models and Instrumentation	20
5.2.1 MS(1)–0317 Airfoil.....	20
5.2.2 NACA 65 ₂ –415	21
5.2.3 GLC–305 Airfoil	21
5.2.4 Twin Otter Tail	21
5.2.5 Twin Otter Tail with 22.5- and 45-min Ice Shapes	22
5.2.6 Comparison of Test Models	22
5.3 Dye Tracer Method	22
5.4 Spray System.....	23
5.5 Spray System Data Acquisition and Control	24
5.6 Cloud Uniformity.....	25
5.7 MVD and LWC Measurements	26
5.8 Reference Collector Mechanism	26
5.9 Test Matrix	27
5.10 Surface Pressure Measurements.....	27
5.11 Impingement Test Procedure.....	28
6.0 Data Reduction Method for the Impingement Data.....	28
6.1 Reflectance Spectroscopy	29
6.2 Reflectance Calibration Curves.....	29
6.3 Data Reduction Systems.....	30
6.3.1 Laser Reflectometer	30
6.3.2 Charge-Coupled Device (CCD) Reflectometer	31
6.3.3 Colorimetric Analysis.....	32
7.0 Analysis Method.....	33

8.0 Results and Discussion.....	33
8.1 Sources of Experimental Error	34
8.1.1 Experimental Method	34
8.1.2 Data Reduction Method.....	36
8.2 Pressure Distributions	36
8.3 Impingement Results	37
8.3.1 Test Repeatability.....	37
8.3.2 Experimental and LEWICE Impingement Data	38
9.0 Summary and Conclusions	42
9.1 Large Droplet Splashing Tests at the Goodrich IWT.....	42
9.2 Large Droplet Impingement Tests at the NASA IRT	43
References.....	45
Appendix A—General Effects of Large Droplet Dynamics	169
Appendix B—Summary of Impingement Results Data	181
Appendix C—Coordinates of Airfoil Sections and Pressure Ports Locations	189
Appendix D—Run Tables	209
Appendix E—Surface Tension Measurements of Water and Blue Dye Solution	231
Appendix F—Trajectory Computations for 22.5- and 45-min Glaze Ice	233
Appendix G—Comparison of Experimental and LEWICE Maximum and Total Impingement Efficiencies.....	247
Appendix H—Colorimetric Analysis on Selected Cases	249

Large and Small Droplet Impingement Data on Airfoils and Two Simulated Ice Shapes

Michael Papadakis, See-Cheuk Wong, and Arief Rachman
Wichita State University
Wichita, Kansas 67260

Kuoshing E. Hung and Giao T. Vu
The Boeing Company
Wichita, Kansas 67277

Colin S. Bidwell
National Aeronautics and Space Administration
Glenn Research Center
Cleveland, Ohio 44135

Abstract

Typically, ice accretion results from small super-cooled droplets (droplets cooled below freezing), usually 5 to 50 μm in diameter, which can freeze upon impact with the aircraft surface. Recently, however, ice accretions resulting from super-cooled large droplets (SLD) have become a safety concern. Current ice accretion codes have been extensively tested for FAR part 25 appendix C icing conditions but have not been validated for SLD icing conditions. This report presents experimental methods for investigating large droplet impingement dynamics and for obtaining small and large water droplet impingement data. Droplet impingement visualization experiments conducted in the Goodrich Icing Wind Tunnel with a 21-in. chord NACA 0012 airfoil demonstrated considerable droplet splashing during impingement. The tests were performed for speeds in the range 50 to 175 mph and with cloud median volumetric diameters in the range of 11 to 270 μm . Extensive small and large droplet impingement tests were conducted at the NASA Glenn Icing Research Tunnel (IRT). Impingement data were obtained for four airfoil sections and two simulated ice shapes. Airfoils tested included three 36-in. chord airfoils (MS(1)–0317, GLC–305, and NACA 652–415), and a 57-in. chord Twin Otter horizontal tail section. The two simulated ice shapes were 22.5- and 45-min glaze ice shapes for the Twin Otter tail section computed with the LEWICE-2D ice accretion code. The impingement experiments were performed with spray clouds having median volumetric diameters (MVD) of 11, 21, 79, 137 and 168 μm and for a range of angles of attack. All the impingement experiments were conducted at airspeed of 175 mph corresponding to a Reynolds number of approximately 1.6 million per foot. The maximum difference in $\bar{\beta}_{\text{max}}$ of repeated impingement tests from the average ranged from 0.2 to 13 percent for 98 percent of the experimental cases presented. Computations performed with the LEWICE-2D computer code for all test configurations are presented in this report. In general, good agreement was observed between experiment and analysis for the small droplet cases. For all the large droplet cases, however, the analysis produced higher impingement efficiencies and larger impingement limits than the experiment. This discrepancy was attributed to water mass loss due to splashing experienced by the large droplets during impingement.

Executive Summary

Aircraft flying through clouds below 8000 meters (approximately 26,000 ft) at subsonic speeds can experience ice formation on critical aerodynamic surfaces. This situation can lead to

deterioration of aircraft aerodynamic performance and handling qualities. Typically, ice accretion results from small super-cooled droplets (droplets cooled below freezing), usually 5 to 50 μm in diameter, which can freeze upon impact with the aircraft surface. Recently, however, ice accretions resulting from super-cooled large droplets (SLD) have become a safety concern.

A major concern in the design and certification of ice protection systems for aircraft is the extent and amount of water impingement. The impingement characteristics of an aircraft can be used to determine size and location of ice protection systems. Computer codes are often used as a cost-effective means for the design of ice protection systems. Current ice accretion codes have been extensively tested for the FAR (Federal Aviation Regulations) part 25, appendix C icing conditions. However, these codes have not been validated for SLD icing conditions. To address this issue, the FAA Icing Plan has identified the validation of ice accretion codes as an important task (Task 11) for future research efforts.

The main objective of the research program described in this report was to develop experimental methodologies for investigating and measuring large droplet impingement, including investigation of droplet splashing. Droplet splashing was recently identified as having a significant impact on the impingement characteristics of aerodynamic surfaces (ref. 1), particularly for SLD conditions.

Experiments were conducted with a NACA 0012 airfoil section in the Goodrich Icing Wind Tunnel facility using advanced flow visualization techniques to document basic SLD impingement physics. The basic SLD physics experiments were followed by extensive impingement tests at the NASA icing research tunnel facility (IRT) with four airfoil sections and two simulated ice shapes to develop small and large droplet data for code validation and calibration.

The main accomplishments of this research program, which was completed in 2002, are summarized below:

1. The WSU 12-nozzle spray system was expanded to 16 nozzles to provide the required cloud uniformity for the SLD cases selected for the impingement tests.
2. Extensive updates were made to the hardware and software of the laser and CCD reflectometers used for the reduction of the raw impingement data.
3. New calibration curves were developed for the laser and CCD data reduction systems.
4. Experiments were conducted at the Goodrich Icing Wind Tunnel with a NACA 0012 airfoil to document large droplet splashing and to investigate the effect of the blotter paper used in the experimental method on the splashing process.
5. Experimental small and large droplet impingement data were obtained in the NASA Glenn IRT facility for four two-dimensional airfoils, and an airfoil with two simulated ice shapes. Data were obtained for median volumetric diameters of 11, 21, 79, 137 and 168 μm .
6. Correlation of the experimental impingement data with analysis data obtained with the LEWICE-2D computer code was performed.

List of Abbreviations and Symbols

AOA	Angle of Attack
CCD	Charge-Coupled Device
DAQ	Data Acquisition
DIO	Digital Input Output
FAA	Federal Aviation Administration
FS	Full-Scale

FSSP	Forward Scattering Spectrometer Probe
IRT	Icing Research Tunnel
LE	Leading Edge
LWC	Liquid Water Content
MAC	Mean Aerodynamic Chord
MVD	Median Volumetric Diameter
OAP	Optical Array Probe
PDPA	Phase Doppler Particle Analyzer
RCM	Reference Collector Mechanism
PC	Personal Computer
SLD	Super-cooled Large Droplets
SSR	Solid State Relay
TE	Trailing Edge
WRP	Wing Reference Plane
WSU	Wichita State University
A_f	Frontal area of a body projected parallel to freestream velocity direction
A_∞	Area perpendicular to freestream direction, defined by the tangent trajectories
c	Model chord length
C_D	Droplet drag coefficient
C_f	Nozzle flow coefficient
d	Droplet diameter
D	Droplet diameter
D_{max}	Maximum droplet diameter in clouds of non-uniform droplet size
D_{min}	Minimum droplet diameter in clouds of non-uniform droplet size
D_{MVD}	Droplet diameter based on MVD
\bar{E}	Total impingement efficiency in clouds of non-uniform droplet size
g	Acceleration due to gravity
Highlight	Reference point on test geometry for measuring impingement efficiency.
K	Droplet inertia parameter, $\rho_{droplet} \cdot V_\infty \cdot MVD^2 / (18 \cdot \mu \cdot c)$
K_0	Modified droplet inertia parameter, $K \cdot \lambda / \lambda_s$
L	Characteristic dimension of a body
M	Mach number of airflow relative to droplet
M_∞	Freestream Mach number of airflow
Re_c	Reynolds number based on chord length
Re_v	Reynolds number of airflow relative to droplet
Re_{MVD}	Reynolds number based on MVD and freestream speed

R_n	Normalized reflectance
S	Surface distance from highlight
$S_{\bar{\beta}_{\max}}$	Surface distance from highlight to location of maximum impingement efficiency
S_u	Surface distance from highlight to impingement limit on upper surface
S_l	Surface distance from highlight to impingement limit on lower surface
t	Time; Airfoil thickness
U_i	Initial droplet velocity
V	Potential flow velocity dimensionless with V_∞
V_i	Initial potential flow velocity
V_∞	Freestream airspeed
\dot{w}	Water flow rate from WSU spray nozzles
x, y	Cartesian coordinates
x_l	Chordwise distance corresponding to the impingement limit on the lower surface
x_u	Chordwise distance corresponding to the impingement limit on the upper surface
α	Angle of attack
$\bar{\beta}$	Local impingement efficiency
ΔP	$P_{\text{water}} - P_{\text{air}}$
δ_{ij}	Kronecker delta
ϕ	Impingement parameter, $(Re_{MVD})^2 / K$
λ	True range of droplet as projectile injected into still air
λ_s	Range of droplet as projectile following Stokes' law
μ	Absolute air viscosity
ρ	Air density
ρ_w	Density of water

1.0 Introduction

Aircraft flying at subsonic speeds through clouds below 8000 m (approximately 26,000 ft) can be subject to ice formation on critical aerodynamic surfaces. This situation can lead to deterioration of aircraft aerodynamic performance and handling qualities. Typically, ice accretion results from small super-cooled droplets (droplets cooled below freezing), usually 5 to 50 μm in diameter, which can freeze upon impact with the aircraft surface. Recently, however, ice accretions resulting from super-cooled large droplets (SLD) have become a safety concern. The impact of SLD ice accretions on aircraft safety is under evaluation by the Federal Aviation Administration (FAA) and the Joint Aviation Authorities (JAA). FAA/JAA rulemaking is under development to ensure safe flight in large super-cooled droplet (SLD) icing conditions. In support of the rulemaking, NASA has provided a "roadmap" describing the technology required for implementing the proposed SLD rulemaking, including: a) Atmospheric environment definition, b) Instrumentation, test methods, test facilities, and computer codes required to provide means-of-compliance with the proposed rule.

Aircraft icing design and certification requires evaluation of the extent and intensity of water impingement. The impingement characteristics of an aircraft can be used to determine size and location of ice protection systems. Another important aspect in aircraft icing certification is the evaluation of the effects of a range of ice accretions on aircraft aerodynamic performance and handling qualities. Airframers make use of empirical, computational and experimental methods in determining impingement characteristics and potential ice accretions for critical aerodynamic surfaces. Water droplet trajectory and ice accretion codes, such as the NASA Glenn LEWICE code, can provide cost-effective information for the design and certification of ice protection systems and for predicting ice accretions on critical aerodynamic surfaces. It is important, however, that these codes are validated with experimental impingement data and experimental ice shapes. Current ice accretion codes have been extensively tested for appendix C (FAR/JAR part 25) icing conditions but not for SLD icing conditions. Recent impingement tests (ref. 1) with large droplet clouds have demonstrated that droplet splashing can have a significant impact on the impingement characteristics of aerodynamic surfaces. Large droplet breakup prior to impingement is another phenomenon that can affect impingement characteristics. Since current ice accretion codes do not model SLD impingement effects such as splashing and droplet breakup and have not been validated for SLD icing conditions, they will need to be modified and validated so that they can be used as a means of compliance. To address this issue, the FAA Icing Plan has identified the validation of ice accretion codes for SLD conditions as an important task (Task 11) for future research efforts.

In the fall of 2000, NASA and the FAA funded Wichita State University (WSU) to conduct experiments to document large droplet splashing and to develop an experimental database of SLD impingement on two-dimensional airfoil sections. The work was conducted by WSU, the NASA Glenn Research Center, and Boeing Commercial. Droplet splashing tests were performed in the Goodrich Icing Wind Tunnel (IWT) facility using advanced imaging techniques. Large droplet impingement data were obtained at the NASA Glenn Icing Research Tunnel facility for four airfoils and for an airfoil with two simulated ice shapes. The simulated ice shapes were defined using the LEWICE ice accretion code and included 45- and 22.5-min glaze ice accretions. Small droplet impingement data were also obtained for selected cases.

In the following sections a brief summary of past and recent water impingement research efforts is provided and the experimental method and results obtained during this new research program are presented. In addition, analysis impingement data obtained with the NASA Glenn LEWICE computer code are compared with the experimental data.

2.0 Background

The first extensive water droplet impingement database was developed by NACA in the 1950's. A dye-tracer technique was developed for measuring local impingement efficiency on aircraft aerodynamic surfaces (ref. 2). In this technique, water containing a small amount of water-soluble dye was injected in the form of droplets into the air stream ahead of the body by means of spray nozzles. The surface of the body was covered with blotter material upon which the dyed water impinged and was absorbed. At the point of impact and droplet absorption, a permanent dye deposit (dye trace) was obtained. The impingement limits were obtained directly from the rearmost dye trace on the absorbent material.

Data analysis consisted of removing the dyed blotter strips from the body and punching out small segments of the blotter material for the determination of local impingement characteristics. The dye was dissolved out of each segment in a known quantity of water. The weight of dye in this solution was determined by the amount of light of a suitable wavelength transmitted through the solution by use of a calibrated colorimeter (colorimetric analysis). The weight of water that impinged at any surface location per unit time was determined from the weight of dye collected per unit area, and from knowledge of the original concentration of the dye in the water droplets.

The liquid water content in the cloud was determined using an aspirating device (refs. 2 and 3). This device consisted essentially of a tube, which sucked in the approaching air and cloud droplets at the freestream velocity (inlet velocity ratio 1) so that both the air streamlines and droplets entered the tube along straight-line paths. The dyed droplets were deposited on a filter mounted within the tube, leaving a dye trace that could be analyzed using colorimetric analysis. The droplet size distribution was determined by comparing experimental local impingement rates on cylinders of different sizes with theoretical predictions of droplet trajectories and impingement points using a differential analyzer.

Between 1955 and 1958 NACA personnel developed a water droplet impingement database for a wide range of cylinders, airfoils sections, bodies of revolution and a supersonic inlet (refs. 2 to 6). For most test configurations, the NACA method was sufficiently accurate. The error in evaluating maximum local impingement efficiency varied from 10 to 25 percent (refs. 2 and 3). The major limitations of the NACA method included reduced spatial resolution and a laborious and time-consuming process for reducing the experimental data. In addition, the uncertainty in measuring the LWC and MVD values of the spray clouds used in the impingement tests was considerable.

In 1984, a research program was initiated to further expand and update the experimental water droplet impingement database and to provide much needed impingement data for aircraft inlets and modern wing sections. This program was sponsored by the NASA Glenn Research Center in Cleveland, Ohio and the FAA Technical Center in Atlantic City, New Jersey. The work was performed by researchers at Wichita State University and Boeing. During this research program, an experimental method similar to the one used in the early 1950's by NACA researchers was developed for measuring local impingement efficiency (ref. 7). A new method for extracting the impingement data from the blotter strips was also developed. In this method, the amount of dye trace on a blotter strip obtained in a given time interval was converted into local impingement efficiency distribution using a laser reflectance spectroscopy method. Tests showed that the new data reduction method was significantly more efficient than the method of colorimetric analysis used in the 1950's by NACA personnel.

To generate the required spray clouds for the impingement tests, a twelve-nozzle spray system was fabricated. This system was designed to have a very fast on/off response because the spray duration had to be very short (approximately 2 to 4 sec) to avoid saturation of the blotter paper. For the reflectance method to be accurate, dye penetration into the blotter paper had to be kept to a minimum.

The first series of impingement tests were conducted in September of 1985 in the NASA IRT for a period of four weeks. The geometries tested included a 4-in. cylinder, a NACA 652-015, an MS(1)-0317 supercritical airfoil, three simulated ice shapes, an axisymmetric engine inlet model and a Boeing 737-300 engine inlet model. The second and final series of impingement tests were performed in the IRT facility during April of 1989 and lasted for approximately four weeks. Models tested during this phase of the research program included two simulated ice shapes, a Natural Laminar Flow airfoil section NLF(1)-0414F, an infinite span 30 degree swept MS(1)-0317 wing, a finite span 30 degree swept NACA 0012 wing, and a Boeing 737-300 engine inlet model. The experimental impingement data obtained during the 1985 and 1989 impingement tests can be found in references 7 and 8. In summary, the water droplet impingement research program conducted between 1984 and 1993 was successful and considerably expanded the impingement database.

A peer review of NASA Glenn icing research activities conducted in 1994 indicated that additional water droplet impingement data were needed. Large droplet impingement data were also requested in response to a recent commuter aircraft icing related accident which has raised the question of the effect of ice accretion due to Super-cooled Large Droplets (SLD) on aircraft performance and handling characteristics (refs. 9 and 10).

To address the needs of the icing community, the Icing Technology Branch at NASA Glenn Research Center awarded a research grant to Wichita State University (WSU) in 1995 to begin work on modernizing and expanding the water droplet impingement database. WSU and NASA conducted an industry survey in November of 1995 to identify geometries and conditions to be considered for the next series of water droplet impingement tests.

In December of 1996, NASA awarded a second grant to WSU to improve the experimental method developed during the 1984 to 1993 research program and to develop a more efficient reflectance method based on a CCD camera for extracting the impingement data from the blotter strips. In addition, extensive impingement tests were planned in the NASA Glenn Icing Research Tunnel with a range of two-dimensional airfoils, and finite wings and a turboprop S-duct engine inlet.

The first series of the IRT impingement tests was conducted during the period of July 25 to September 7, 1997. The second series of impingement tests was conducted from January 31 to March 1, 1999. A total of 11 wind tunnel models were tested during these two IRT entries. Test models included six two-dimensional airfoils, a two-dimensional high-lift system, three swept horizontal tails and an engine inlet S-duct. Tests were performed for a range of angles of attack and for median volumetric diameters of 11, 11.5, 21, 92, and 94 μm . The 92 and 94 MVD case was selected to provide preliminary SLD impingement data for assessing the performance of trajectory computer codes for large droplet conditions. Comparison of the experimental impingement data with analysis data obtained with the NASA Glenn LEWICE-2D and LEWICE-3D computer codes demonstrated good agreement for the 11, 11.5 and 21- μm cases. However, for the 92 and 94- μm cases the analysis produced considerably higher overall impingement than the experiment for nine out of the eleven models tested and for all angles of attack. Details of the 1997 and 1999 impingement research effort are provided in ref. 1. The discrepancy between analysis and experiment for the large MVD conditions was attributed to droplet splashing and droplet breakup effects, which are not currently modeled in the LEWICE code. It was determined that additional experimental work was needed to elucidate SLD impingement physics and to provide a more extensive SLD impingement database for code trajectory development and validation.

Recent developments in aviation rulemaking addressing aircraft operations in SLD conditions which are outside the current icing certification envelopes, have heightened the need for additional large droplet impingement research. Specifically, the impact of SLD ice accretions on aircraft safety is under evaluation by the Federal Aviation Administration (FAA) and the Joint Aviation Authorities (JAA). FAA/JAA rulemaking is under development to ensure safe flight in large super-cooled droplet icing conditions. In support of the rulemaking, NASA has provided a "roadmap" describing the technology required for implementing the proposed SLD rulemaking, including: a) Atmospheric environment definition, b) Instrumentation, test methods, test facilities, and computer codes required to provide means-of-compliance with the proposed rule. Since current droplet trajectory and ice accretion computer codes are not validated for SLD conditions they will need to be modified and validated so that they can be used as a means of compliance.

To address the need for validated analysis tools for simulating SLD impingement on aircraft surfaces the Federal Aviation Administration and NASA funded WSU in the fall of 2000 to:

1. Document small and large droplet impingement dynamics using advanced imaging methods
2. Apply the dye tracer method developed at Wichita State University (WSU) to obtain small and large droplet impingement data for a range of airfoils and two simulated ice shapes.
3. Improve the automated data reduction systems developed at WSU for the analysis of the raw impingement data.
4. Compare the experimental results with analysis data from the LEWICE code.

3.0 Droplet Trajectory Equation and Impingement Parameters

In this section, impingement parameters that are commonly used in the presentation of theoretical and experimental data are discussed. They constitute the governing non-dimensional form of the droplet trajectory equations. Also discussed is their relevance to conditions with icing clouds of uniform and non-uniform droplet size distributions from normal droplet to super-cooled large droplet (SLD).

3.1 Differential Equation of Particle Trajectory

The forces acting on a small spherical droplet moving in the steady flow of air include droplet drag, weight, and buoyancy (ref. 11). The predominant force exerted on a droplet is the fluid dynamic drag resulting from the relative (slip) velocity of air with respect to the droplet. The development of the droplet trajectory equations is based on a simplified approach, taken by researchers as early as the 1940's. In this approach, the quasi-steady motion of small spherical droplets moving in the steady flow of air is considered and it is assumed that the motion of droplets does not disturb the airflow. Since the physical phenomena involved in the process of ice accretion are very complex, these assumptions are necessary and are commonly used in analytical tools for modeling ice accretions. The main assumptions used in the derivation of the small particle trajectory equations are summarized below (ref. 11):

1. Single phase (air) flow about the body; flowfield is not disturbed by the presence of droplets
2. Quasi-steady-state approximation: at each instant and position, the steady state drag and other forces act on the particle
3. The drag coefficient for stationary sphere applies
4. Particles are assumed to be solid and spherical in shape
5. Particles do not rotate and have no lift and no moment
6. All drops which strike the airfoil deposit on the surface. Droplets do not splash/breakup during the impingement process
7. Droplets do not interact with other droplets
8. Compressible or incompressible potential flowfield of the gas phase about the body
9. Viscous flow effects such as thick boundary layer formation and flow separation are not considered.

Using the above assumptions and applying Newton's second law, the non-dimensional form for the particle trajectory equation is obtained:

$$\frac{dU_i}{dt} = \frac{C_D(\text{Re}_v) \cdot \text{Re}_v \cdot (V_i - U_i)}{24K} - \frac{(1 - \sigma) \cdot g \cdot L \cdot \delta_{i2}}{V_\infty^2} \quad (3.1)$$

where

- $K = \rho_p V_\infty d^2 / 18\mu L$, inertia parameter of droplet
- d = Droplet diameter
- μ = Absolute air viscosity
- V_∞ = Freestream speed
- t = Time, dimensionless with L/V_∞
- $\sigma = \rho/\rho_p$, density ratio of air to particle
- L = Characteristic dimension of body
- Re_v = Reynolds number of airflow relative to droplet
- $U_i = I^{\text{th}}$ directional component of particle velocity, dimensionless with V_∞

$V_i = i^{th}$ directional component of air velocity, dimensionless with V_∞

The above mathematical model is valid for icing conditions within the intermittent and continuous maximum icing envelopes defined in the Federal Aviation Regulation, part 25, appendix C. The maximum concentration and mean volumetric diameter (*MVD*) of droplets for these icing conditions are as follows:

	Intermittent Maximum	Continuous Maximum
<i>LWC</i>	3.0 g/m ³	0.8 g/m ³
<i>MVD</i>	50 μm	40 μm

For the concentrations and sizes of droplets that are expected to occur within icing clouds, the assumptions of undisturbed airflow and spherical shape (due to surface tension) of droplets are valid.

The droplet drag coefficient, C_D in eq. (3.1) is a function of the relative Reynolds number. It is an analytical form of the standard drag curve and the Cunningham drag correction factor for molecular slip and compressibility effects. The drag coefficient is given in the following form:

$$C_D(M, Re_v) = \frac{C_{D_{inc}}(Re_v)}{G(M/Re_v)} \quad (3.2)$$

where

$C_{D_{inc}}$ = Incompressible sphere drag coefficient

$G(M/Re_v)$ = Cunningham drag correction factor

M = Mach number of airflow relative to droplet

From Stokes' law of drag, the incompressible sphere drag coefficient can be expressed as:

$$C_{D_{inc}}(Re_v) = C_{D_{Stokes}}(Re_v) \left(1 + \frac{Re_v^{2/3}}{6} \right) \quad (3.3)$$

where

$$C_{D_{Stokes}}(Re_v) = \frac{24}{Re_v}$$

This equation agrees to within about 5 percent of the standard drag curve in the range of $0 \leq Re \leq 1000$ and for particles of diameter less than or equal 1000 μm (1 mm).

The Cunningham drag correction factor was proposed by Carlson and Hoglund (ref. 12). The following empirical fit was developed from available experimental data for the ranges of $M \leq 0.2$ and $Re_v \leq 1000$:

$$G\left(\frac{M}{Re_v}\right) = \frac{A}{B} \quad (3.4)$$

where

$$A = 1 + (M/Re_v) [3.82 + 1.28e^{(-1.25Re_v/M)}]$$

$$B = 1 + e^{(-0.427M^{-4.63} - 3Re_v^{0.88})}$$

The numerator, A in eq. (3.4), represents the drag reduction factor to account for the incompressible drag due to the molecular slip or rarefaction effects. The denominator, B in eq. (3.4), is the additional correction to account for the Mach number dependence of the particle drag (compressibility) in continuum flow.

3.2 Impingement Parameters

Spray cloud characteristics and droplet impingement parameters for clouds with a range of drop sizes are discussed below.

3.2.1 Liquid Water Content (LWC)

Generally expressed in grams of water per cubic meter of cloud, the liquid water content (LWC) of a cloud is defined as the amount of water contained in a given volume of cloud. LWC_{max} values for icing clouds according to the FAR part 25, appendix C icing envelopes are presented in section 3.1. In icing tunnels, the cloud LWC is controlled by the water and/or air pressures of the spray system used to create the spray clouds.

3.2.2 Cloud Droplet Distribution

The distribution of droplets in a cloud can be expressed in various forms (ref. 7). Briefly, the following four types of distributions are most commonly used:

1. Number density of droplets versus droplet diameter
2. Percent of liquid water content versus droplet diameter
3. Percent of liquid water content versus droplet diameter normalized to median volumetric diameter
4. Percent cumulative liquid water content versus droplet diameter normalized to median volumetric diameter.

A distribution which has been employed in various analytical studies is the Langmuir “D”. This distribution and other similar ones were established by Langmuir (ref. 13) from natural-icing cloud measurements made on Mt. Washington. The rate of deposition of ice on slowly rotating cylinders exposed to super-cooled clouds blowing over the summit was correlated with that of theoretical calculations. A dimensionless Langmuir “D” distribution is shown in figure 1.

3.2.3 Median Volumetric Diameter (MVD)

The Median Volumetric Diameter (MVD) of a droplet distribution is defined as the droplet diameter for which half the total liquid water content is contained in droplets larger than the median and half in droplets smaller than the median. Given a droplet distribution, the MVD can be calculated as follows:

1. For a continuous distribution, if $n(D)$ is the number of particles per unit sampling volume having diameters between D and $D+dD$ (volumes between V and $V+dV$) then D_{MVD} can be calculated from

$$\frac{\frac{\pi}{2} \rho_{\omega} \int_{D_{\min}}^{D_{MVD}} n(x) x^2 dx}{\frac{\pi}{2} \rho_{\omega} \int_{D_{\min}}^{D_{\max}} n(x) x^2 dx} = 0.5 \quad (3.5)$$

2. For a discrete distribution, if the particle number density is given in N discrete groups such that $n_i(D_i)$ is the number of the particles in group i having diameters between D and $D+dD$ then, eq. (3.5) can be written as

$$\frac{\frac{\pi}{6} \rho_{\omega} \sum_{i=1}^K n_i(D_i) D_i^3}{\frac{\pi}{6} \rho_{\omega} \sum_{i=1}^N n_i(D_i) D_i^3} = 0.5 \quad (3.6)$$

where

$$\begin{aligned} D_K &= \text{the diameter of group } K, \text{ is equal to the MVD } (D_{MVD}) \\ \rho_{\omega} &= \text{density of water, Kg/m}^3 \end{aligned}$$

3.2.4 Local Impingement Efficiency

Considering a body in a cloud with uniform droplet size distribution, the local impingement efficiency β for any point on the body surface is defined as the local droplet flux rate at the body surface normalized to the freestream flux rate. Referring to figure 2a, β is defined as the ratio of that infinitesimal area dA_{∞} to the corresponding impingement area on the body surface dA_s . This definition follows from the continuity of droplet mass flow.

For a continuous non-uniform cloud distribution, the impingement efficiency is given by the following expression

$$\bar{\beta} = \frac{1}{\omega_t} \int_0^{\omega_t} \beta \, d\omega \quad (3.7)$$

where β is a function of drop size and therefore can be expressed as a function of ω , the liquid content for a given drop size.

For a discrete non-uniform droplet distribution, $\bar{\beta}$ is defined as the weighted average of the local impingement efficiency values due to each droplet group in the cloud. Let ω_t be the liquid water content of the cloud, $\Delta\omega_i$ be the partial liquid water content contained in the droplets of size (d_i) in the group (i) of the distribution, and N be the total number of discrete size droplet groups available. For a body exposed to a cloud with such a droplet distribution, the local impingement efficiency due to a single droplet group of size d_i is β_i , where β is defined in figure 2a. The local impingement efficiency due to all N groups in the distribution over an infinitesimal area of the body is given by the following expression

$$\bar{\beta} = \frac{1}{\omega_t} \sum_{i=1}^N \beta_i \Delta\omega_i \quad (3.8)$$

3.2.5 Total Impingement Efficiency

The total impingement efficiency of a three-dimensional body exposed to a cloud of droplet distribution is defined as

$$\bar{E} = \frac{1}{A_f} \int \bar{\beta} \, dA_s \quad (3.9)$$

where

A_f is the projected frontal area of the body

dA_s is an infinitesimal impingement area on the surface of the body

In order to integrate eq. (3.9), $\bar{\beta}$ must be known as a function of surface location. Such a function can be defined from experimental or analytical results.

3.2.6 Impingement Limits

Droplets which start out at freestream position y_∞ (fig. 2b) with respect to a reference line that pass through the highlight (most forward point at $\alpha = 0^\circ$) of a body downstream will impinge at some location on that body. As these initial freestream droplet positions increase in distance from the reference line they will impinge farther back along the surface of the body until a maximum distance $y_{\infty, \max}$ is obtained. This limiting trajectory is defined as the tangent trajectory to the body at point P (fig. 2b). Any droplets starting at a freestream location farther from the reference line than $y_{\infty, \max}$ will miss the body entirely. The distance S_m measured along the body surface from the highlight of the body to point P is called the limit of impingement. This distance is usually expressed in dimensionless form by dividing S_m by the characteristic length (L) of the body.

For two-dimensional flow, there are two impingement limits, an upper and lower (for external flow, e.g., airfoil section) or an outer and inner (for partly internal flow, e.g., engine inlet). For three-dimensional flow, the limits of impingement may vary spanwise along the surface of a finite wing or circumferentially along the surface of an engine inlet. For a droplet distribution that varies from D_{min} to D_{max} , the impingement limits can be established for each droplet size. The maximum impingement limits are defined by the impingement limits of the largest droplet diameter in the distribution.

3.2.7 Summary of Droplet Impingement Parameters

Figure 1 provides a list of definitions and expressions for key non-dimensional parameters that affect the droplet trajectory such as droplet inertia parameter K , droplet modified inertia parameter K_0 , Reynolds number based on MVD, Re_{MVD} , true droplet range λ , and independent impingement parameter ϕ , which represents the deviation of the droplet drag force from Stoke's law and is defined in such a way that the droplet diameter, d , has been eliminated. These non-dimensional impingement parameters are also useful in linking the impingement data presented in this report with early experimental and numerical studies of airfoil water impingement characteristics (refs. 2 and 3). In some of these early studies, the impingement characteristics of bodies were in some cases presented in terms of non-dimensional impingement parameters such as K and ϕ . Note that the definitions in figure 1 are based on the reference length, typically the airfoil chord for two-dimensional sections.

3.3 Large Droplet Impingement Issues

Current droplet trajectory codes have been extensively tested for cloud conditions within the FAA, part 25, appendix C envelope and in general, have demonstrated good agreement with experimental impingement data. Application of these codes, however, to compute large droplet impingement (droplets outside the current icing certification envelope) may require additional improvements to the existing numerical models to include physical phenomena related to large droplet impingement dynamics such as droplet splashing and breakup that have been observed in recent experimental impingement studies with large droplets. The impact of these phenomena on the simulation of the impingement characteristics of aerodynamic surfaces can

be considerable, as demonstrated in section 8 of this report, where large droplet experimental and computational impingement data are compared for a range of aerodynamic surfaces. A summary of the main issues encountered in modeling SLD impingement is given in appendix A.

4.0 Water Droplet Splash Experiments at the Goodrich IWT

Experiments were conducted at the Goodrich Icing Wind Tunnel (IWT) facility to investigate small and large droplet splashing on a symmetric airfoil. Tests were performed with the clean airfoil (i.e., airfoil without blotter strip) and airfoil with a blotter strip attached to its leading edge for airspeeds in the range of 50 to 175 mph and median volumetric diameters (MVD) in the range of 11 to 270 μm . The main objectives of the investigation conducted were as follows:

- Apply an advanced imaging technique to visualize droplet splash on an airfoil surface for airspeeds representative of in-flight icing.
- Investigate if droplet splashing occurs during droplet impingement on the blotter paper used in the WSU dye tracer method for obtaining water droplet impingement data.
- Conduct preliminary parametric studies to explore the effect of MVD and airspeed on droplet splashing.

4.1 Goodrich Icing Wind Tunnel (IWT)

The Goodrich IWT, completed in 1988, is a closed-loop refrigerated tunnel measuring 40-ft by 70-ft overall, located adjacent to De-Icing Systems' engineering facility in Uniontown, Ohio. It has an external 200 hp. electric motor driving a 79-in. diameter axial fan to provide wind velocity, a 70 ton capacity refrigeration system for cooling, and two 75 hp. air compressors dedicated to it for icing cloud formation. It uses seven spray bars, heated to prevent freezeout, with NASA type spray nozzles to produce the icing cloud. A schematic of the Goodrich IWT facility is shown in figure 3a.

The test section is 22-in. wide, 44-in. high, and 60-in. long. Models are mounted horizontally between inch thick aluminum turning plates 30 in. in diameter, and can be rotated 360°, even with the tunnel in operation. There are two hinged side windows with heated glass panels measuring 13-in. by 30-in. and a 52-in. section of floor which, along with the lower fillets, hinges down to allow full-width access. The bottom door and the ceiling also have heated windows, and unheated acrylic panels can be installed in the turning plates for additional viewing if necessary. Details of the test section are depicted in figure 3b.

The IWT can run at speeds from 30 to 230 mph, though top speed is limited by temperature, spray time, and percent blockage represented by the test model. Velocity is measured with a pitot tube located at the start of the test section, and is density corrected for a "true" velocity reading. Temperature in the tunnel is microprocessor controlled from -22 to 32 °F. It can be held within ± 1 °F of setpoint through most of this range. Spray conditions can be varied from about 0.1 g/m³ to over 3.0 g/m³, with droplet sizes from 14 to over 40 μm , limited by velocity and nozzle pattern density. This allows reproduction of natural icing conditions over almost all of the intermittent maximum profile and most of the continuous maximum profile, as specified in the Federal Aviation Regulations, Part 25, appendix C.

4.2 Test Model and Installation

The test model used in the experimental investigation is shown in figure 4 and was a 21-in. chord NACA 0012 that was constructed out of aluminum. The airfoil surface was refurbished

prior to the tests by NASA personnel. The model was installed in the Goodrich IWT test section as shown in figures 5 and 6. For all tests the angle of attack was 0°.

4.3 Spray System

The Goodrich IWT spray system was not used during the splashing tests. Instead a single nozzle assembly from a spray system developed at Wichita State University for impingement testing was employed. Water under pressure from a supply tank shown in figure 7 passed through a high-pressure rubber hose to the nozzle assembly. Pressure for the supply tank was provided by a 100-psig airline, which was set to the required level using a pressure regulator. A separate 100-psig high mass flow air source (atomizing air manifold) provided air to the nozzle assembly for atomizing the water. A fast acting solenoid valve was used to turn the spray on and off. The spray nozzle was a NASA IRT MOD-1 nozzle that was capable of producing spray clouds with MVDs in the range of 11 to 270 μm . The median volumetric diameter of the spray cloud was controlled by varying the air-to-water pressure ratio.

The single WSU spray nozzle assembly was installed on the Goodrich IWT spray bars using a bracket as shown in figure 8. Figure 9 shows a close-up of the WSU nozzle during a spray test.

The main reasons for using the single nozzle WSU spray system were as follows:

- Low water loading to minimize saturation of the blotter strip and to improve visibility of the impingement region. Flexibility in controlling the placement of the spray cloud within the tunnel test section and in adjusting the location of the water impingement region on the airfoil surface. This was accomplished by moving the WSU spray nozzle to the desired location on the IWT spray bars.
- Ability to generate FAR Part 25 appendix C as well as SLD spray clouds through the use of the IRT MOD-1 nozzle and the required air and water pressures.
- Quick spray on-off response that was required during preliminary tests to explore the influence of water film on splashing intensity.

4.4 Imaging System

The system used for the visualization of droplet splashing consisted of a 512 by 512 pixel CCD PI-MAX intensified camera from Princeton Instruments, a C-mount Nikkor lens with five 27.5 mm extensions and an Infinity long distance microscope lens. Analog data from the CCD camera were routed to a Model ST-133 Controller unit where the data were converted into digital form and then they were transferred to a laptop computer for processing and display. The camera system was capable of collecting 16-bit images at a readout rate of 1 million pixels per second. The imaging system setup is shown in figures 10 and 11.

The illumination of the region of interest near the airfoil leading edge was accomplished with a 100-milliwatt red laser diode with a lens for converting the laser beam into a thin light sheet. The laser diode was attached to a tripod and was placed below the glass window on the tunnel test section floor as shown in figure 12. The plane of the laser sheet was approximately at 15° with respect to the vertical plane (i.e., the plane normal to the wing leading edge). The location of the laser sheet with respect to the wing leading edge is shown in figures 13 to 15.

4.5 Test Procedure and Test Matrix

The step sequence during a splashing visualization test was as follows:

1. The spray system air and water pressures were set to the required levels to produce the desired cloud conditions. Spray system air and water pressures and corresponding

MVDs are listed in figure 2 and were obtained from nozzle calibration tests conducted at NASA.

2. The tunnel airspeed was set to the required level and the spray system was activated for a preset duration that was controlled by the system timer. Spray times ranged from seconds to several minutes. The longer spray times were used for the clean wing tests. Shorter spray times were used for the wing with the blotter paper to avoid paper saturation. All tests were conducted under warm temperatures that ranged from 70 to 100 °F. Humidity levels in the test section ranged from 30 to 40 percent.
3. The camera system was activated and several images were recorded. Typical exposure times were of the order of 1 μ s. A total of 10 to 25 images were obtained during each test. The time period between images was 260 milliseconds. The images were transferred to the PC system where they were stored and analyzed.

The test matrix for the droplet splash experiments is provided in figure 2. During the course of the experimental investigation a number of parametric studies were conducted with the clean and the airfoil with blotter strip attached. The parametric studies included variation in airspeed for a fixed MVD size and variation in MVD size for fixed airspeed. The objective of these parametric studies was to explore the effect of droplet momentum and kinetic energy on droplet splashing behavior.

4.6 Discussion of Results

All results presented in this section are qualitative and are based on the visualization images obtained with the CCD camera. An effort was directed to develop quantitative correlations from the extensive number of images recorded using advanced image software. However, the analysis process was subject to considerable uncertainty and the results obtained are not presented.

The images presented in figures 16 to 20 are on a plane normal to the wing leading edge and correspond to a physical area of 5-mm by 5-mm. The flow in all cases is from left to right and the airfoil leading edge corresponds to the right edge of the image frame as shown in figure 16. During each test several images of a splashing event were recorded. In figures 16 to 19, only single images are presented, that is one out of the 10 to 25 images obtained during a test. In figure 20a to f, each figure is the composite of all 10 to 25 images obtained during a test. Droplet trajectories that appear faint in the figures presented were out of the plane of the laser sheet and thus were not illuminated sufficiently by the laser light source. It is also important to recognize that the results presented in the images provide only a “cross-section” of the splashing event which is a three-dimensional phenomenon. That is the droplets ejecting from the airfoil surface into the flowfield travel in all directions and the distribution in terms of droplet velocity and size may vary considerably with direction.

The main observation from the selected images presented in figures 16 to 19 is that droplet splashing is clearly evident for both the clean airfoil case and the airfoil with the blotter strip. In fact, examination of a large number of images obtained for SLD conditions with and without the blotter paper show similar results. Thus, the results prove that the blotter paper characteristics do not eliminate droplet splashing. However, it is very difficult to establish from the images presented whether the dynamics of droplet impingement on blotter paper are the same as impingement on the clean airfoil surface. In considering potential differences between droplet splashing on a clean airfoil surface versus droplet splashing on blotter paper, it is important to assess if these differences are significant for engineering applications.

Figures 16 to 19 show that as the MVD size was increased from 94 to 270 μ m for a fixed airspeed, the splashing intensity increased for both the clean and blotter cases. The composite images shown in figure 20 for the clean airfoil indicate that, for the clean airfoil droplet and MVD

of 94 μm , splashing increased as the airspeed was increased from 50 to 100 mph. However, it is not clear from figure 20 if splashing intensity increased with further increase in airspeed.

Potential effects of droplet splashing on impingement characteristics for several airfoil sections are demonstrated in figure 21, which was taken from reference 1. In this figure, large droplet impingement data obtained with the blotter and blue dye method are compared with LEWICE computations. The experimental results demonstrate considerable less overall impingement than the LEWICE computations (ref. 1) and support the results of the large droplet impingement visualization tests, which indicate droplet splashing and potential water mass loss for the clean airfoil and the airfoil with the blotter strip.

Considering the effect of large droplet splashing and breakup on the ice accretion process would require considerable more research due to the complexity of the icing phenomenon. During an icing encounter, the airfoil shape and its surface properties change considerably with every layer of ice that accumulates on the surface. As the airfoil surface properties and geometry change during the ice accretion process, the droplet impingement dynamics will clearly change. In developing simulation tools for engineering analysis, it is important to capture the fundamental effects of droplet impingement dynamics on the ice accretion process and develop methods for simulating these effects.

5.0 Water Droplet Impingement Tests at the NASA IRT

5.1 Wind Tunnel Facility

The 2001 impingement tests were conducted in the NASA Glenn Icing Research Tunnel (IRT). The IRT has a 6-ft by 9-ft test section that measures 20-ft long and can attain a maximum speed of 420 mph when it is empty. A plan view of the IRT circuit is shown in figure 22. The IRT is a closed-looped refrigerated facility with a test section static temperature range of -40 to 40 °F. The operational static pressure at the tunnel test section is near or below the atmospheric value. Test models are typically installed on the tunnel turntable using a floor mounting plate as shown in figure 23. A view of the test section is provided in figure 24. Two sets of nozzles (the standard and MOD-1 types) are utilized in the IRT spray system, which consists of 10 spray bars with 54 nozzle locations per bar. The basic IRT nozzle design is shown in figure 25. Only 129 nozzles are currently being used to generate the required icing clouds. Two mechanical vent doors located upstream of the heat exchanger can be opened and shut remotely to allow air to vent in and out of the facility. The IRT spray system is capable of simulating icing clouds with MVDs in the range of 14 to 40 μm , and Liquid Water Content (LWC) of 0.3 to 3 g/m^3 as shown in figures 26 and 27. In addition, a limited range of large droplet clouds with MVDs in the range 70 to 270 μm can be simulated in this facility. Further details regarding the IRT facility are provided in reference 14.

5.2 Test Models and Instrumentation

Details of the five test models used in the 2001 impingement experiments and their related instrumentation are given below and in appendix C.

5.2.1 MS(1)–0317 Airfoil

The MS(1)–0317 airfoil is representative of modern medium speed airfoils. It was designed in the mid 1970's for general aviation aircraft (ref. 15). This two-dimensional airfoil was constructed out of Fiberglass skin, which was epoxied to an aluminum spar and aluminum ribs. The interior of the airfoil model was filled with foam. An aluminum plate was installed at each end of the model for mounting in the IRT test section. The model had a nominal span of 72 in.

and a chord of 36 in. and it was mounted vertically in the test section. The maximum thickness for this airfoil was 6.12 in. ($t_{\max}/c = 0.17$) and was located at 37.5 percent chord. The center of rotation of the airfoil was at 42 percent chord. A total of 47 static pressure taps were available for this airfoil. These taps were distributed in the chordwise direction 35.5 in. above the tunnel floor. The MS(1)–0317 airfoil section and model installation details are given in figures 28a to c. Impingement data for this airfoil were obtained during the 1985, 1997, and 1999 IRT tests performed by WSU and Boeing. This airfoil was used during the 2001 IRT entry to verify the experimental setup and to obtain additional large droplet impingement data.

5.2.2 NACA 65₂–415

This airfoil is representative of general aviation wing sections. Airfoils suitable for low speed general aviation aircraft should have low drag and gentle stall characteristics with relatively high thickness ratio to keep structural weight low and to provide sufficient space for fuel (ref. 16). The NACA 6-series airfoils were designed to have low profile drag in a limited range of lift coefficient (drag bucket). Aerodynamic performance characteristics for the NACA 65₂–415 airfoil are provided in reference 17.

The single element NACA 65₂–415 wind tunnel model was designed and fabricated at Wichita State University. It was made out of aluminum, and had 72-in. span and 36.53-in. chord, which was truncated to 36 in. during manufacturing to allow for sufficient trailing edge thickness for installation of a pressure port at the trailing edge. The maximum thickness for this airfoil was 5.48 in. ($t_{\max}/c = 0.15$) and was located at approximately 40 percent chord. The center of rotation of the airfoil was at 50 percent chord. The airfoil was instrumented with 76 pressure taps at the mid span location, which corresponded to the IRT centerline. Twelve additional pressure taps were placed in the chordwise direction one foot above and below the centerline taps (6 taps on each side) and nine more taps were distributed spanwise at the 70 percent chord station on the upper surface of the airfoil. The 21 additional pressure taps were used to verify that two-dimensional flow was maintained for the angles of attack used in the impingement tests. The airfoil section geometry and installation in the IRT test section are shown in figure 29a to c.

5.2.3 GLC–305 Airfoil

This airfoil is representative of general aviation business jet wing sections. It was constructed at the NASA Glenn Research Center out of Fiberglass with two 2-in. thick wooden spars and seven 1-in. thick ribs as described in reference 18. It had 36-in. chord, 72-in. span and 3.12-in. maximum thickness ($t_{\max} = 8.7$ percent chord) at $x/c = 0.4$. The airfoil was instrumented with 44 static pressure taps distributed in the chordwise direction at a span location 33 in. above the tunnel floor. The center of rotation of the airfoil was at 28 percent chord. The airfoil section geometry and installation in the IRT test section are shown in figure 30a to c.

5.2.4 Twin Otter Tail

This test geometry was provided by NASA Glenn Research Center and was the horizontal tail section of DeHavilland DHC–6 Twin Otter Icing Research Aircraft. The model was a modified NACA 63_A–213 airfoil with 57-in. chord and maximum thickness to chord ratio of 12 percent at $x/c = 0.35$. It was constructed out of four span segments made of Machinable Plastic (REN) material. The four segments were supported by metal tubing spars and aluminum ribs. The model originally had a 7-ft span and was truncated to 6 ft (72 in.) to accommodate the height of the tunnel test section. It was instrumented with 59 surface pressure taps distributed chordwise at 53.63 in. above the tunnel floor. The center of rotation of the airfoil was at 16.22 percent chord. The model section and installation details are given in figure 31a to c.

5.2.5 Twin Otter Tail with 22.5- and 45-min Ice Shapes

The simulated ice shapes for the 57-in. airfoil were determined using the NASA Glenn LEWICE 2.0 computer code (ref. 19) and included a 22.5- and a 45-min glaze ice accretion. The 22.5-min glaze ice shape is typically used in aircraft certification to simulate ice build up due to an ice protection system failure. The 45-min ice shape is often used in aircraft certification to approximate ice that would accrete on an unprotected aircraft surface. The LEWICE ice shapes were obtained using the following icing conditions:

- $V=120$ Kts
- $LWC=0.5$ g/m³
- $MVD=20$ μm
- $T_{tot}=-4$ °C
- $AOA = 0^\circ$
- Pressure altitude 6000 ft
- Icing Times: 22.5 and 45 min

The two LEWICE shapes were constructed at Wichita State University out of aluminum and spanned the height of the 57-in. model as shown in figures 32 and 33. The cross sections of the 22.5- and 45-min ice shapes are given in figures 32a and 33a. The 22.5- and 45-min LEWICE shapes were instrumented with 9 and 10 pressure taps respectively. The locations of the pressure ports were selected based on Navier-Stokes computations to provide sufficient resolution of the pressure distribution over the ice shapes for a range of angles of attack. The spanwise location of the pressure ports was 48 in. above the tunnel floor. With the ice shapes installed on the airfoil leading edge 6 pressure taps on tail model were covered so the total number of pressure taps on the model (including the taps on the ice shapes) was 62 for the 22.5-min and 63 for the 45-min ice shape. The Twin Otter tail section with the 22.5- and 45-min ice shapes is depicted in figure 32a to d and figure 33a to c respectively.

5.2.6 Comparison of Test Models

Figures 34 and 37 compare the airfoil sections tested during the 2001 impingement tests. Section coordinates and pressure tap locations for all models tested can be found in appendix B.

5.3 Dye Tracer Method

The dye-tracer technique was initially developed by NACA (ref. 2) and was subsequently modified by Papadakis et al. (ref. 7). In the modified method used during the 2001 IRT impingement tests, distilled water containing a known concentration of blue dye (0.3 g of FD&C Blue No.1 dye per 1 liter of water) was injected into the air stream of the IRT in the form of a droplet spray cloud through a specially designed 16-nozzle spray system. The test model was covered with thin strips of blotter paper (James River Paper Company Verigood 100 lb Blotting Paper) in areas of interest and was exposed to the spray cloud for certain lengths of time. The amount of dye-mass per unit area of blotter strip obtained in a given time interval was measured using reflectance spectroscopy. The water impingement characteristics of a test model were obtained by converting the dye color density distribution on each strip into water impingement density using specially developed calibration curves.

5.4 Spray System

The impingement tests were conducted with an automated 16-nozzle spray system developed at Wichita State University that was capable of producing short duration repeatable sprays. The short spray duration was needed to avoid blotter saturation and dye penetration into the blotter paper as dictated by the data extraction method, which relied on surface reflectance measurements from the dye-laden blotter strips. The 16-nozzle system was based on a 12-nozzle system developed previously at WSU. Details of the development and testing of the 12-nozzle spray system can be found in references 1 and 7. The additional four nozzles constructed for the 2001 IRT entry were required to maintain or improve the area of cloud uniformity (approximately 1-ft high by 2-ft wide) that was attainable with the 12-nozzle system. From tests conducted at NASA (ref. 1), it was found that for large droplet clouds, cloud uniformity was considerably reduced and more nozzles were needed to cover the area of interest for the models selected.

The 16-nozzle spray system used in the 2001 impingement tests provided blue dye solution under pressure from a 30-gal stainless steel supply tank to 16 nozzle assemblies via high-pressure rubber hoses. Each nozzle assembly consisted of an IRT MOD-1 Spray nozzle, the nozzle housing, a fast action solenoid valve, an oil filled pressure gage, a SETRA 206 pressure transducer to monitor water pressure, an adjustable flow valve, a 0.75-in. diameter 3-ft long stainless steel pipe for the air supply, a support bracket for attaching the nozzle to the IRT spray bars and a range of fittings for connecting the nozzle to the spray system water and air supply lines.

Water pressure for the supply tank was obtained from a 125-psig airline, while a separate 100-psig high volume flow air source (atomizing air manifold) provided air to the nozzle assemblies for atomizing the water. Mechanical pressure regulators were used for setting the water and atomizing air pressures. These regulators were continually adjusted using miniature electro-pneumatic transducers to maintain the required pressures. The electro-pneumatic transducers were controlled by feedback loops incorporated into the spray system computer control unit. The activation pressure for the electro-pneumatic transducers was set to 130-psig and was obtained from a low volume, high pressure source. This source was independent of the water, and atomizing air pressure lines to ensure that fluctuations in the high volume lines did not affect the operation of the electro-pneumatic transducers.

The pressure of the atomizing air was monitored at the supply line regulator with a SETRA 204 transducer. In addition, three SETRA 206 transducers were used to monitor atomizing air pressures at selected nozzles. These transducers were added to the longest airline corresponding to each group of four nozzles. A SETRA 204 pressure transducer was installed in the water tank to monitor the water pressure. In addition, two high-precision analog pressure gauges were installed at the water tank and at the regulator of the atomizing air line to confirm the pressure readings from the electronic transducers. Pressure transducer information is provided in figure 3. Prior to the IRT test entry, the NASA Glenn flow calibration lab tested and calibrated all the pressure transducers used in the WSU spray system.

A sensitive flow meter was used to monitor water volume flow rate to make sure that the 16 nozzles injected the same amount of water into the air stream during each repeated spray test. This instrument was capable of measuring volume flow rates in the range 0.02 to 1 gal per minute with an accuracy of 0.2 percent full scale (FS). The flow meter was calibrated by the NASA Glenn flow calibration lab prior to the start of the tests.

The NASA Glenn IRT MOD-1 nozzles were selected for the 2001 impingement tests. These nozzles have a lower flow rate (approximately 1/3) for a given air pressure and delta pressure ($P_{\text{water}} - P_{\text{air}}$) than the STANDARD IRT nozzles so that longer spray times could be achieved without saturating the blotter strips. Longer spray times are desirable because they result in

more stable sprays. These nozzles were also capable of producing the large MVD sizes (79, 137, and 168 μm) that were used to generate the large droplet impingement data.

Fast acting solenoid valves were used to turn the spray on and off. During testing, the main air supply solenoid was turned on approximately 30 sec before the spray was initiated to allow the atomizing air pressure to stabilize. Next, the 16 water solenoid valves were activated by the computer system and a spray cloud was produced. The median volumetric diameter (MVD) of the spray cloud was set by varying the spray system air-to-water pressure ratio. The duration of the spray was controlled by the computer hardware.

Sixteen brackets were designed and built for mounting the 16-nozzle spray system to the IRT spray bars. The new brackets allowed for a more precise installation of the 16 nozzle assemblies. In addition to the 16 spraying nozzle assemblies, one non-spraying “dummy” nozzle assembly was installed to enhance cloud mixing.

The complete sixteen-nozzle spray system is shown in figure 38a and b. The installation of the complete spray system and the coordinates of each spray nozzle with respect to the IRT spray bars are given in figure 39. Various components of the spray system—the stainless steel pressure tank for storing the dyed solution, the main air and water pressure lines, and the air and water pressure regulators are shown in figures 40 and 41. A close-up view of one of the WSU nozzle assemblies is provided in figure 42. The schematic of the spray system shown in figure 43 provides a summary of key system components.

The WSU spray system was assembled and tested extensively at WSU before it was shipped to NASA Glenn for the water droplet impingement tests. During the impingement tests at the NASA Glenn IRT facility, several detailed analyses of recorded spray system parameters were performed. The results showed that the system was capable of maintaining air and water pressures to within ± 1 psi from the required settings as demonstrated in figure 4.

During the 2001 impingement tests, high pressure air from the IRT spray bars was used to enhance cloud mixing and to improve the uniformity of LWC in the test section. The IRT spray bars were also used periodically to produce very fine sprays in order to maintain the required relative humidity in the test section. These fine sprays were conducted prior to the start of the impingement tests. Another method used to control the humidity was water steam injection that was introduced downstream of the test section.

5.5 Spray System Data Acquisition and Control

The performance of the spray system was monitored and controlled using a personal computer. Software was developed to monitor, store and analyze the spray system performance parameters. The system consisted of a 900 MHz Pentium III personal computer with a data acquisition (DAQ) board, a digital I/O (DIO) board, seventeen (17) solid-state relay (SSR) digital signal conditioning modules installed on three backplane boards, two SETRA transducer control panels, a shielded I/O connector block (SCB) and a cable adapter board. A schematic of the main computer hardware units is given in figure 44a, while the main components of the data acquisition system are shown in figure 44b. The signals from all spray system transducers were read and processed by the DAQ board. This board had 32 input differential channels and a sampling rate capability of up to 1,200,000 samples per second. The DIO board used was a high-speed, 32 bit parallel digital I/O ISA interface. This board was used to control the SSR relay units for activation of the selected solenoid valves of the spray system. One solenoid valve was used for each nozzle assembly. A solenoid valve was also added to the main air supply, which provided high-pressure air for atomizing the water sprays.

The data acquisition and system control software was developed using LabVIEW, a graphical programming language for data acquisition and control, data analysis and data presentation. The LabVIEW software provided a Windows driven menu for controlling and monitoring the performance of the spray system. Any combination of nozzles and transducers

could be selected from the window menu. The user could also specify spray time, plot the transducer signals in real time, and store a range of test parameters as well as other information related to each test. Example windows demonstrating some of the features of the spray system LabVIEW program are provided in figure 45a and b. All test parameters and transducer readings were written out to a Microsoft® Excel file at the end of each test.

Data from the DAQ board were recorded at regular time intervals for the complete duration of spray. The sampling rates were varied based on the spray duration. For the shortest a 0.75-sec spray, the sampling time was 0.005 sec. For the longer sprays a sampling time of 0.01 sec was used. This was done to keep the size of the output files to a manageable level while providing sufficient resolution for monitoring the spray system parameters.

5.6 Cloud Uniformity

An important aspect of the experimental method is cloud uniformity. Cloud uniformity has a significant effect on test repeatability and accuracy. There are three main parameters involved in the description of a spray cloud: droplet size, droplet distribution and LWC. Of the three parameters, the LWC distribution is the most difficult to control. Extensive tests were conducted to set the location of the sixteen spray nozzles so as to obtain a 1-ft high by 2-ft wide uniform cloud region centered in the IRT test section for all cloud conditions selected for the impingement tests. Since perfect uniformity is practically not obtainable, for the purpose of the impingement tests, uniformity was accomplished when LWC variation within the 1-ft by 2-ft area was within ± 20 percent of the average. For the test models and MVD cases tested in 2001 the required uniformity region was 0.5-ft high by 1-ft wide. For this smaller region, cloud uniformity was within ± 10 percent of the average.

Cloud uniformity was measured using two methods. In one method, a 6-ft by 6-ft stainless steel grid with horizontal and vertical grid spacing of 6 in. apart was used to determine cloud uniformity as shown in figure 46. The plane of the grid was normal to the flow and passed through the center of the turntable. Blotter strips were installed on the grid to cover an area of 2-ft high by 2-ft wide as shown in figure 47. The tunnel was brought up to test speed and the blotters were sprayed. The dye distribution on each blotter was determined using the CCD reflectometer described in section 6 of this report. Next, the nozzles were adjusted to make the dye distribution and therefore the LWC more uniform. This grid/blotter method, which was laborious and time consuming, was similar to the one presented in references 7 and 8.

The second method for establishing cloud uniformity was considerably more efficient and made use of laser imaging technique. In this method a 5-W Argon-Ion laser beam was transmitted to a collimator through a fiber optic cable. Next, the beam was directed to a mirror attached to a rotating galvanometer and from there it was passed through a large (64 cm long) cylindrical lens, which produced a laser sheet that spanned the tunnel width. The laser sheet setup is shown in figure 48a to e. The location of the laser sheet plane with the respect to the IRT test section is shown in figure 49a.

A 14-bit CCD array camera attached to a boroscope and installed outside the tunnel near the second tunnel control room was used to record the cloud images. The boroscope was installed through the tunnel side wall and was placed downstream of the laser sheet as shown in figure 49a and b. Approximately 2 in. of the boroscope was extended into the tunnel and was exposed to the flow. In previous tests (ref. 1), the CCD camera was installed on the IRT spray bars inside an aerodynamic fairing and was exposed to the flow. It was found, however, that the wake from the camera had a small adverse effect on the flowfield. Thus it was decided to place the camera outside the tunnel and downstream of the plane where the uniformity measurements were conducted. The CCD camera installation and location can be found in figure 49a and b. The uniformity tests were conducted with all the lights in the test section and in the secondary control room turned off. In addition, the lights in the main control room were dimmed. It was

necessary to eliminate all light sources other than the laser light sheet to ensure that the cloud images recorded by the CCD camera were not affected by other light sources. With the tunnel set to the required airspeed (175 mph), the spray system was activated for approximately 30 to 50 sec and several CCD images were recorded. In the CCD images, the high intensity regions corresponded to high LWC region and vice versa. Using camera software, the images were analyzed to determine variations in LWC within the desired uniformity region.

Extensive tests were conducted with the laser sheet method to adjust the locations of the sixteen nozzles to provide the required cloud uniformity for all spray conditions selected for the impingement tests. The additional “dummy” nozzle assembly shown in figure 39 was installed during the uniformity tests to improve cloud mixing.

5.7 MVD and LWC Measurements

Droplet size and distribution measurements for all spray conditions were determined using the NASA Glenn Forward Scattering Spectrometer Probe (FSSP), the 1D Optical Array Cloud Probe (OAP-C) and the 1D Optical Array Precipitation Probe (OAP-P). The OAP-P is also known as the OAP-Y probe due to the geometrical arrangement of the two probe arms containing the mirrors that are used to direct the laser beam. Details of the FSSP and OAP probes can be found in reference 20. The data from these instruments were combined to obtain a single droplet distribution using algorithms customarily employed for this purpose by the IRT droplet sizing specialist. The LWC measurements were conducted using the NASA Glenn heated wire King Probe Model KLWC-5 described in reference 21. The probe operates on the theory that when a heated wire is maintained at a constant temperature, any excess power consumed by the wire impacted by the water is proportion to the mass of the water. The installation of the King Probe in the IRT test section is shown in figure 52a and b.

Two sets of droplet and LWC measurements were conducted during the six-week impingement tests. The first set was performed after the completion of the cloud uniformity tests and the second near the end of the impingement tests. Each series of droplet size, droplet distribution and LWC tests consisted of several repeated measurements of the desired spray cloud conditions. In addition, MVD and LWC measurements were conducted with the IRT spray bar air on and off, for a range of IRT spray bar air pressures, to investigate the effect of spray bar air on cloud characteristics. It was found that the IRT spray bar air had no effect on MVD and cloud droplet distribution. However, the LWC was reduced when the IRT spray bar air was turned on.

To determine the effect of cloud unsteadiness on LWC, short and long duration sprays were conducted during the LWC measurements. Traces of LWC as a function of time showed no significant impact of spray duration on the average LWC value. Measured MVD and LWC distributions obtained at the center of the IRT test section are discussed in section 8 of this report. MVD sizes and corresponding spray system air and water pressure settings are given in figure 4.

Relative humidity studies conducted during the 1997 and 1999 impingement tests (ref. 1) showed that the effect of relative humidity on LWC was considerable, particularly for the 11- μm MVD. Based on the findings of these studies, the 2001 impingement tests were conducted at a relative humidity of 75 ± 5 percent.

5.8 Reference Collector Mechanism

The Reference Collector Mechanism (RCM) designed at WSU was used to obtain local LWC measurements at all locations in the IRT test section corresponding to test model blotter strip locations. These measurements were required to correct the impingement data for local variations in LWC. By measuring the local LWC at all locations where model blotter strips were

installed, the effect of local LWC variations could be corrected, thus improving the accuracy and repeatability of the experimental impingement data. Details of the development of the collector mechanism are provided in reference 7.

The RCM had six short blades and one long blade as shown in figure 53a. Each blade was 0.2 in. wide and 1 in. in chord as shown in figure 53b. The length (span) of the collector blades was 4 in. for the short blades and 9 in. for the long blade. The collector mechanism was placed in the empty IRT test section with its 9-in. blade positioned as close as possible to the blotter strip locations on the test models. Since test model location varied depending on model installation and angle of attack, the collector mechanism had to be tested at several locations. For the collector tests, blotter strips 0.2 in. wide were placed on the collector blades so that the plane of each blotter strip was normal to the flow. The location of the blotter strip on the MS-317 airfoil with respect to the 9-in. collector blade is shown in figure 54. All collector tests were performed at the same airspeed and cloud conditions as that used for the test models. In addition, the spray duration for the collector tests was identical to that used for the airfoil tests. Several collector tests were conducted with detachable side shields installed on the 9-in. collector blade as shown in figure 55 to investigate the effect of large droplet splashing on LWC measurements. These tests are discussed in section 8.

The impingement data from the collector strips were analyzed using the data reduction methods described in section 6. The collector dye mass per unit area and its impingement efficiency were used to obtain the LWC in the freestream, which was then used to convert the raw impingement data for each test model into impingement efficiency distributions. Figure 5 provides computed impingement efficiencies obtained with the LEWICE code for the collector blades for all spray cloud conditions used in the impingement tests. The table shows that the collector blade had a high impingement collection efficiency. This is attributed to the small chord and thickness of the collector blades.

5.9 Test Matrix

Models and conditions for the 2001 impingement tests are provided in figure 6. All tests were conducted at total air temperature of 54 ± 15 °F and a relative humidity of 75 ± 5 percent. Details of test and spray conditions are given in appendix D.

5.10 Surface Pressure Measurements

The test models used in the 2001 impingement test were equipped with surface taps as discussed in section 4.2. Model surface pressure measurements were obtained with each model prior to the impingement tests. The AOA for pressure measurements ranged from a few degrees above to a few degrees below the angle of attack selected for the impingement data. This was done to ensure that there was sufficient pressure information to compare with the computed flowfields. The LEWICE computer code used for the impingement computations did not simulate the tunnel wall effects. Thus experimental and computed pressure distributions for the same geometric angle of attack did not always produce the same flowfield. In many of the computed cases presented in this report, the geometric angle of attack for the computations was adjusted by -1.85° to 0.20° with respect to the experimental angle of attack to improve the correlation with the experimental pressure data.

Surface pressure measurements were conducted using the electronically scanned pressure (ESP) system available in the IRT. The ESP system consisted of six 32-port pressure modules with a range of ± 5 psid. One data port in each module was used for pressure checks. Thus, the total number of ports available for pressure measurements was 186 ports (31 ports per module). A three-point pressure calibration system to all port transducers was used by the ESP system. The calibration pressures were measured with precision digital quartz transducers. The three-

point calibration was performed every 400 cycles (approximately 15 min) to ensure that the error in the measurements did not exceed 0.1 percent of the full-scale.

5.11 Impingement Test Procedure

To obtain water droplet impingement data for each test model, the following steps were performed:

1. The spray system air and dyed water pressures were set to generate the desired MVD. Air and water pressure settings for all MVD sizes used in the impingement tests are given in figure 4. The LWC corresponding to each MVD can be found in figure 5.
2. One or two blotter strips were attached to the model at the required spanwise locations using aluminum tape. The blotter strips were approximately 1.5 in. wide and had two different lengths (24- and 48-in.). The longer strips were used for the large MVD cases (137 and 168 μm) tested with the 57-in. chord Twin Otter tail section to capture the extent of the impingement limits.
3. The tunnel was set to the required speed and water steam was injected into the air stream to attain the required level of relative humidity. Once the speed, relative humidity, and the air stream temperature were stable, the spray system was activated for a certain period of time (0.75 to 4.5 sec, based on the MVD as shown in figure 4) and a dye trace was obtained on the blotter strips attached to the model.
4. After the spray was completed, the tunnel was then set to idle. Each blotter strip was carefully removed from the model and hung in the control room to dry before storage. The model was then wiped clean using alcohol and a new blotter strip was attached for the next test.
5. Each spray condition was tested three to four times (i.e., 3 to 4 tests per MVD and angle of attack) to establish a measure of test repeatability. In some cases the tests were performed as many as 6 to 10 times over a period of two days to evaluate the repeatability of the experimental technique.

The collector mechanism was tested several times between model tests to provide local LWC measurements for reducing the model impingement results.

During the 2001 IRT entry, a number of exploratory tests were conducted to investigate various aspects of the experimental method. One such test involved long sprays that resulted in saturation of the blotter strips. The longer sprays were conducted with all geometries and for all test conditions and were used to verify the impingement limits obtained with the short sprays. In addition, some of the saturated strips were reduced using colorimetric analysis to verify the results obtained with the laser reflectance method (see appendix H).

6.0 Data Reduction Method for the Impingement Data

Methods for reducing impingement data from the dye-laden blotter strips include a method based on colorimetric analysis (ref. 2) developed by NACA in the 1950's and a method based on diffuse reflectance spectroscopy (refs. 7, 22, and 23) developed by WSU and Boeing in the 1980's. The reflectance method was found to be significantly more efficient and was able to provide higher resolution impingement data than the colorimetric analysis method. Brief descriptions of the data reduction methods and the systems used for analyzing the 2001 raw impingement data from the blotter strips are presented below.

6.1 Reflectance Spectroscopy

The data reduction method used in this work is based on the assumption that when a dye-laden blotter strip is illuminated by a light source, the intensity of light scattered from the blotter surface is a measure of the dye mass per unit area of the blotter strip. Regions on the blotter strip corresponding to high impingement rates are darker in color and reflect less light than those corresponding to low impingement rates. Regions with no dye accumulation are white and scatter the maximum amount of light. The relation between dye concentration and reflectance is not linear and is defined from calibration tests. To enhance the sensitivity of the reflectance method, the dye must have a strong absorption at the wavelength of the light source used for illuminating the blotter strips. For improved accuracy, dye penetration normal to the blotter surface should be kept to a minimum since the data reduction method relies on surface reflectance measurements. The acceptable level of dye penetration depends on the data reduction system and is determined from experiments.

6.2 Reflectance Calibration Curves

The reflectance calibration curve relates normalized reflectance (reflectance of dye-laden blotter paper divided by reflectance of white blotter paper) from the dye-laden blotter strip to dye mass and therefore water impingement on the blotter strip. The curve is a standard against which the reflectance of each blotter strip is compared during the data reduction process.

To produce the reflectance calibration curve, blotter strips (1.5-in. by 24-in.) were laid out on a flat surface at the bottom of an enclosed 6-ft high box. Blue dye solution was sprayed at the top of the box in the form of a fine cloud mist that was allowed to dissipate over time onto the blotter strips. The concentration of the blue dye solution for spraying the blotter samples was identical to that prepared for the impingement tests. By varying the time that the strips were exposed to the spray, blotter strips with a range of uniform color densities were obtained, covering the spectrum from very light blue to dark blue color. The blotter samples were allowed to dry between sprays to minimize dye penetration into the blotter. After completion of the spray tests, all blotter samples were let dry for approximately one day. Next the blotter strips were scanned using both the laser and CCD reflectometers described below. The recorded reflectance measurements were then used to identify uniform color density regions on each sample strip. Disks with diameter of 1 in. were then punched out from these uniform color areas. The mass of the blue dye on each disc was extracted by the WSU chemistry lab using the method of colorimetric analysis described in reference 7. Subsequently, the dye mass from each blotter disc was divided by the disc area to provide the dye mass per unit area.

In addition to the calibration discs, one collector blotter strip for each MVD case tested during the 2001 IRT entry was also analyzed by the WSU chemistry lab using colorimetric analysis. Furthermore, to compensate for the effects of possible dye penetration into the blotter paper experienced during the impingement tests, a test blotter strip from a selected test condition was segmented into a number of small samples that were individually scanned by the data reduction systems. The dye mass from these samples were next extracted using the method of colorimetric analysis. The data obtained were used along with the standard calibration 1-in. blotter discs to further improve the definition of the standard reflectance calibration curves for the CCD and laser reflectometer systems. The normalized reflectance calibration curves shown in figures 56 to 57 were produced by plotting the normalized reflectance from all blotter calibration samples against the corresponding dye mass per unit area. In these curves, a normalized reflectance value of 1 corresponds to the white blotter paper and indicates zero dye mass.

6.3 Data Reduction Systems

Two systems were used to reduce the raw impingement data obtained during the 2001 impingement tests. The first system was a laser reflectometer, which was developed and tested extensively during the 1985 and 1993 research programs conducted by WSU and the Boeing Company. The second system made use of a CCD array camera for digitizing the images of the dyed blotter strips, which were then stored for later analysis. The main advantage of the CCD system was its ability of providing on-line data reduction during impingement testing. The Laser and CCD data reduction systems used in this work are described below.

6.3.1 Laser Reflectometer

The main components of the laser reflectometer, depicted in figure 58a and b, include: (a) a red He-Ne laser with a wavelength of 632.8 nm, (b) a rotating drum for mounting the blotter strips, (c) a convergent lens for focusing the reflected light from the blotter strip onto a silicon photodetector and (d) a EG&G silicon photodetector for converting the reflected light collected by the lens into a voltage (V_1) which is stored for further analysis, and (e) a splitter glass plate and another silicon photodetector for monitoring fluctuations in laser light intensity. The voltage (V_2) from the second photodetector is also stored and is used in the data analysis. Details of the laser reflectometer can be found in reference 7.

A PC based digital data acquisition system using LabView program was developed during this research program to control the operation of the reflectometer and to analyze and plot the impingement data. Note that the maximum absorption of the blue dye selected for the impingement tests occurred at 629.5 nm, which is very close to the wavelength of the laser, thus, ensuring that small changes in dye color density could be resolved by the system.

The process of converting the raw color density distribution from a dye-laden blotter strip into impingement efficiency distribution involved a number of steps. First, the raw reflectance versus surface distance data were extracted by mounting each blotter strip on the drum of the laser reflectometer and scanning the strip along its length as shown in figure 59a. The voltages V_1 and V_2 from the two photodetectors obtained during a scan were stored on disk and were used to generate the raw reflectance values. These values were then normalized by the average reflectance of a reference white blotter strip which was scanned before and after each dye-laden blotter strip. Typical normalized reflectance of a blotter strip is shown in figure 59b. Note that long blotter strips had to be scanned in segments because the reflectometer could only accommodate rectangular strips with a maximum length of 16.5 in. The raw reflectance data from each segment of the blotter were then combined using a computer program and stored for further analysis. The spatial resolution of the reflectometer was 47 data points per inch. To convert the raw reflectance values into impingement distributions a FORTRAN program developed during the course of this research was used. The steps involved in generating the final impingement distribution curves are outlined below:

1. The raw reflectance values stored in electronic format during the data extraction process were divided by the reflectivity of the bare (white) blotter paper to obtain normalized reflectance data using the equation below.

$$\begin{aligned} R_n &= \frac{\text{Raw reflectance of dyed blotter paper}}{\text{Raw reflectance of white blotter paper}} \\ &= \frac{(V_1/V_2)_{\text{Dyed blotter paper}}}{(V_1/V_2)_{\text{White blotter paper}}} \end{aligned} \quad (6.1)$$

The raw reflectance of the white blotter paper was determined by scanning several sample white strips to obtain an average value. This value was verified at the beginning and end of each data reduction session.

2. The normalized reflectance data were converted into dye mass per unit area using the standard laser normalized reflectance calibration curve shown in figure 56.
3. The impingement efficiency for each data point recorded was obtained from the following equation.

$$\beta = \frac{\text{Local Dye Mass per Unit Area}}{\text{Average Collector Dye Mass per Unit Area}} \times \beta_{collector} \quad (6.2)$$

Collector strips were reduced prior to the model strips since the collector dye mass was required to define the impingement efficiency of each test model. The value of $\beta_{collector}$ is a function of MVD and is given in figure 5.

6.3.2 Charge-Coupled Device (CCD) Reflectometer

A schematic diagram and the setup of the CCD system developed by WSU are given in figure 60a and b respectively. The system consisted of a Pentium 200 MHz PC, a CCD array camera with 14-bit resolution, a camera electronics unit, a camera PC controller, a 24 mm Nikkor lens, twelve (12) high flux red LED lights, a power supply for the LEDs, a camera stand and a portable dark room for reducing the data. The LED lighting system replaced the Quartz halogen lamps used in 1997 and 1999 impingement tests (ref. 1).

The data from each dye-laden blotter strip were extracted as follows. Each strip was placed on the table inside the dark room next to a reference scale. The highlight mark on the blotter strip was aligned with a fixed mark on the reference scale. The LED lights were set to the required intensity level by adjusting the voltage and amperage of the two power supplies. The camera shutter was activated through the PMIS software and it was kept open for a specified time period, which was determined during the system calibration. A 512 by 512 pixel array image of the blotter strip was obtained and it was stored on disk for later analysis. The camera was capable of resolving nearly 14 bits (or approximately 16000 level) of intensity values of scattered light from the blotter strip. The blue strip was removed and a white reference strip was placed on the table in exactly the same location. The process was repeated and a 512 by 512 image of the white strip was obtained and stored. The raw reflectance from the white strip was used to normalize the raw reflectance from the dyed strip.

Windows driven software, written in PV-WAVE command language and in FORTRAN, were developed for the CCD data reduction system to process the images from the dyed strips into impingement distributions. The process for generating the impingement efficiency distributions involved the following steps:

1. Each dyed strip image and the corresponding white strip image were read using the PV-WAVE software developed. Both images were corrected using the bias, dark, flat-field and reference images, which were obtained and stored during the calibration of the CCD array camera.
2. Using the computer mouse, a rectangular region was selected on the white strip image. This region was processed by the software to provide an average reflectance value for the white paper.
3. For a rectangular dye-laden blotter strip, a region that was large enough to cover the complete extent of dye impingement was selected using the computer mouse as shown

in figure 61a. The location of the highlight point on the strip (typically the point on the leading edge of the test geometry corresponding to $x/c=0$) and a length scale were defined for determining surface distance along the strip.

4. The software produced an array of dye intensity versus surface distance for the dyed strip. These values were normalized by the average white blotter paper intensity value to produce an array of normalized intensity (i.e., 0 to 1) distribution versus surface distance, as shown in figure 61b, which was then stored for further analysis.

Because impingement tests were repeated a number of times for each test condition, several blotter strips were produced for each condition tested. A FORTRAN program was developed to process the normalized intensity values from several blotter strips into a single array of averaged normalized intensity versus surface distance. This array was converted into dye mass ($\mu\text{g}/\text{cm}^2$) versus surface distance using the calibration curve shown in figure 57. Next the local impingement efficiency values were obtained from eq. (6.2), which is identical to the one used for processing the data from the laser reflectometer.

A new lighting system was developed by WSU personnel for the 2001 impingement tests replacing the Quartz halogen lighting systems. The new system consisted of twelve red high flux Light Emitting Diode (LED) illuminators as shown in the schematic provided in figure 62a. The LEDs were OptoTechnology High Flux LED Illuminators, Shark Series, OTL-630A-5-10-66-E, with 630 nm wavelength. As with the red color laser used in the Laser reflectometer, this wavelength was chosen to ensure that small changes in dye color densities could be resolved by the system. The LEDs were connected in parallel to a single power supply. A 1 K Ω potentiometer was connected in series to each LED for adjusting its light intensity so as to produce a uniform illumination region over a large area. The potentiometers were placed on a single circuit board and were mounted on to an aluminum frame designed for the 12 Light Emitting Diodes. The aluminum frame consisted of two plates with a wide rectangular slot to house the LEDs, and a T-shape bar for structural reinforcement. The rectangular slot allowed adjustment of the LED locations to achieve uniform illumination, which was determined with a sensitive light meter. The aluminum plate holding the LEDs and the potentiometers was mounted on a light steel frame attached to the CCD camera mount as shown in figure 62b. This setup allowed the light sources to move vertically with the CCD camera and eliminated the generation of shadows experienced with the old lighting system where the lamps were fixed above the camera. Extensive tests conducted at WSU showed that the new lighting system improved the reflectance measurements obtained with the CCD and resulted in better correlation between the CCD and laser reflectometer systems.

6.3.3 Colorimetric Analysis

In order to confirm the results of the reflectance method, colorimetric analyses were conducted for selected model strips obtained during the 2001 impingement tests. The principle of colorimetric analysis conforms to Beer's law which states that the light absorbance of a solute at a particular wavelength is a function of its concentration in the solution, so that absorbance measurement can be used to measure concentration. The device used in this analysis was a GENESYS 20 Spectrophotometer using a wavelength of 629 nm.

Due to the fact that the colorimetric analysis is laborious and time consuming, only a few blotter strips were analyzed with this method. The blotter strips were segmented into thin strips (2 to 5 mm wide). The location of each segment with respect to the highlight mark was carefully documented and the segment area was recorded. Next, the blotter segments were cut into several smaller pieces (typically 3 to 4) and were placed in numbered test tubes. Limiting the cutting of the thin strips to 3 to 4 pieces was done to prevent excessive disintegration of the paper which could affect the concentration reading. A precise amount of 1.5 mL of deionized

water was then added to each test tube. After sealing the tubes, the diluted strips were left in a refrigerator for 1 to 2 days to allow dye extraction to occur. The dye used in the 2001 impingement test was highly soluble so that no mechanical agitation was required to extract the dye from the blotter paper. A white thin strip was also diluted to observe if the blotter fiber in suspension affected the concentration reading and whether any correction was needed. The white strip test confirmed that the effect of the blotter fiber in water suspension on the measurements was not significant.

The dye solution concentration was then measured using the spectrophotometer. In order to obtain the concentration, a standard solution was needed. A dye sample from the 2001 impingement test was selected, diluted and used as the standard. The dilution was necessary because the spectrophotometer light was not powerful enough to penetrate the 0.3 grams of dye per liter of water solution used in the impingement tests. The concentration was multiplied by the volume of deionized water to get the dye mass, which was then divided by the area of the blotter segment to obtain dye mass per unit area. In order to obtain the local impingement efficiency, the dye mass per unit area of the segment strips was divided by the dye mass per unit area of the corresponding collector.

7.0 Analysis Method

Analysis results for all test cases presented in this report were obtained using the LEWICE-2D code version 1.6. This code is a panel-based ice accretion code that applies a time-stepping procedure to calculate an ice shape. The potential flowfield in LEWICE 1.6 (ref. 24) is calculated with the Douglas Hess-Smith 2-D panel code. This potential flowfield is then used to calculate the trajectories of the water droplets and the impingement distribution on the body.

To simulate the actual IRT cloud conditions used in the impingement tests, the measured cloud droplet distributions were converted into discrete droplet size distributions and were used in the analysis. The droplet size distributions were generated from the data obtained by the OAP-Y, OAP-C and FSSP probes for each MVD case tested. A 27-bin droplet size distribution was generated for the analysis conducted with LEWICE 1.6. The 27-bin discrete distributions for all MVD cases used in the experiments are listed in figure 7 and are presented in figure 63. A corresponding 10-bin droplet size distribution was also generated for use with the public version of LEWICE 2.0 code, which allows up to a maximum of 10 droplet sizes per distribution. The 10-bin droplet size distributions can be found in figures 8 and 64.

Prior to the impingement analysis, the computed flowfield from the LEWICE code was compared with the measured pressured distributions for each model and angle of attack tested. If the agreement between the experimental and the computed pressure was not favorable, the angle of attack in the computer code was slightly modified until a good match was obtained. This small adjustment in AOA was necessary because the LEWICE code cannot account for wind tunnel wall and potential flow angularity effects.

The LEWICE code was also used to generate droplet trajectories for the ice shapes tested to elucidate the measured impingement characteristics of these ice shapes. The computed trajectories are presented in figures 65 and 66.

8.0 Results and Discussion

In this section, small and large droplet experimental impingement data for all models tested are presented and are compared with analysis data obtained with the LEWICE computer code. All the experimental data are averaged data from repeated tests. Geometric, flow, and droplet parameters for the airfoils and ice shapes tested are summarized in figure 9.

8.1 Sources of Experimental Error

Accurate measurement of water impingement on aerodynamic surfaces provides considerable challenges for the experimentalist. The methods employed to generate the data provided in this report have been extensively tested over many years as described in references 1, 7 and 8. There are several aspects of the methodology used that could have considerable impact on the quality of the experimental results. These include the spray system performance, cloud uniformity, measurement of cloud parameters, the dye tracer method for obtaining the raw impingement data and the data reduction systems. Extensive studies have been conducted in the past to identify and quantify factors of the experimental method that could affect data quality and to develop instrumentation, test methods, and test procedures to minimize the effects of these factors on the impingement data. These efforts have led to considerable modifications to the experimental technique and have resulted in improved test repeatability and data accuracy as described in reference 1. Below, potential sources of error in the experimental methodology are briefly reviewed and the steps taken to minimize their effects on the experimental data are discussed.

8.1.1 Experimental Method

Spray system.—A repeatable spray cloud is essential in generating accurate impingement data. The main challenge in the dye tracer method is the generation of very short duration repeatable sprays. The short spray duration was needed to avoid dye penetration into the blotter paper. Dye penetration is particularly a problem with large droplet clouds due to the higher impingement rates associated with the larger droplets. The 16-nozzle spray system developed by WSU for use in a large icing facility such as the NASA IRT was designed to provide repeatable sprays with duration as short as 0.75 sec. To accomplish the required spray system performance, sophisticated computer hardware and software were developed and a large number of electronic transducers were used to monitor and control spray system air and water pressures throughout the spray system. In addition, the water flow rate from all 16-nozzles was monitored to ensure that the system delivered the same amount of water each time a spray was repeated. Figure 67 shows typical flow rates for the five MVD cases. Extensive spray tests conducted in the IRT facility prior to the start of the impingement tests showed that the WSU spray system was capable of generating clouds with MVDs in the range of 11 to 170 μm . The variation in MVD for repeated sprays was established with the NASA FSSP and OAP particle measuring probes and was ± 0.5 to 1 μm at the low end of the MVD spectrum and ± 1 to 3 μm at the high end. The repeatability of the spray system performance can also be assessed from the data presented in figure 4 which shows that the variation in spray system air and water pressures was small. Figure 68 shows typical spray system air and water pressure time histories for the five MVD cases used in the 2001 impingement tests. In all cases, the fluctuation in pressures was small throughout the spray duration.

Cloud uniformity.—Cloud uniformity and in particular LWC uniformity has a significant effect on test repeatability. Extensive cloud uniformity tests were performed using the laser sheet and the grid method to obtain spray clouds with nearly uniform LWC over a 1-ft high by 2-ft wide area at the center of the IRT test section. Figure 69a to e shows typical cloud uniformity results in terms of normalized reflectance for the five MVDs tested. The results presented were obtained using the grid/blotter method. Note that spikes are present at location where the strip back surface was against the grid, whereas the region in between is without support; this is most visible in the MVD 11 μm case in which the spray duration was the longest. Cloud uniformity images obtained with the laser sheet technique are presented in figures 69 to 71. To further minimize the effect of LWC variation within the cloud uniformity region, extensive local

LWC measurements were conducted with the collector mechanism at the same tunnel locations where the blotter strips were placed on the airfoil models during the impingement tests.

Dye recirculation.—The impingement results could be adversely affected by dye recirculation, which can artificially increase the LWC in the test section. To investigate if dye recirculation was an issue, blotter strips were attached to the turning vanes downstream of the refrigeration system, which was located just upstream of the IRT spray bars. The strips were visually inspected periodically to determine if dye deposits were present. After six weeks of testing no dye trace was found on the strips. Thus, it was concluded that the dye recirculation was not a problem.

Measurement of cloud MVD and LWC.—The level of uncertainty in these measurements is difficult to quantify. A number of studies have been conducted over the years by NASA and other scientists to evaluate the performance of particle and LWC measuring instruments. These studies have shown that for large MVD clouds some disagreement exists between various particle measuring techniques. Details of these studies can be found in reference 25. To reduce the uncertainty in the cloud droplet distribution measurements, the calibration of the NASA OAP-C and OAP-Y probes was verified prior to the tests. In addition, two sets of measurements were conducted, one prior to the start of the impingement tests and one near the end of the experiments. During each set of measurements, several test repeats were performed to assess the variation in the cloud MVD. LWC measurements were performed with the King probe which is based on the hot wire principle. For large droplet clouds, the King probe measurements are subject to droplet splashing effects and as a result the LWC values from this probe are not accurate. However, the measurements with the King probe were performed to provide additional data for assessing the freestream LWC data obtained with the reference collector mechanism. Note that only the collector measurements were used in the analysis of the impingement data. For large MVD clouds, however, the collector data are subject to the droplet splashing effects. Large droplets impinging on the collector blade could breakup into smaller droplets which then “fly” around the collector, resulting in a net water mass loss. This will result in a lower LWC measurement with respect to that in the freestream. To investigate if large droplet splashing had an effect on the collector measurements, experiments were performed with side shields attached to the collector as shown in figure 55. The purpose of these shields was to prevent the small rebound droplets from being entrained into the flow, thus preserving the total water mass. The experiments showed that the use of shields did not alter the LWC measured with the baseline collector blade. This finding is to some extent supported by icing tests conducted in the IRT with the icing blade, which is similar to the collector blade. These tests have shown that for large droplet icing clouds, the icing blade provides consistently higher LWC values compared to those obtained with the rotating cylinders. This indicates that the icing blade is less susceptible to droplet splashing effects. To further assess the effects of large droplet impingement on the collector, computations were performed with the FLUENT code (ref. 26) for all MVD cases tested. The simulations performed (not presented in this report) showed that the rebound droplets from the collector were small and had the tendency to re-impinge on the collector. The computational studies indicated that the mass loss due to droplet splashing on the collector surface was small. In summary, droplet splashing does not appear to have a significant effect on the LWC measurements conducted with the collector. However, additional tests are needed to verify the results from the preliminary studies discussed above.

Relative humidity effects.—Extensive tests conducted during the 1997 and 1999 impingement tests to quantify the effect of relative humidity on the experimental data showed that for a 21 μm MVD cloud, a 30 percent increase in relative humidity increased LWC from 0.12 to 0.21 g/m³ while for a 92 μm MVD cloud, the same increase in humidity increased LWC from 0.18 to 0.28 g/m³. In general, the results showed that changes in relative humidity of the order of ± 10 percent could result in large variations in the impingement results and that the repeatability of the data could be adversely affected by changes in relative humidity. In

particular, if the collector and the models are tested at different relative humidity levels, the experimental error can be considerable. During the 2001 impingement tests the relative humidity was maintained at 75 ± 5 percent.

Blotter paper characteristics.—Four different types of blotter paper have been tested over the years (ref. 1). From the papers tested, the 100 lb Verigood blotting paper was found to have the best overall characteristics for use in the impingement tests. The blotter paper for the impingement should be thin to conform to the body surface and to minimize changes to the body shape. The paper must be chemically inert to the dye and water and mechanically strong, capable to retain its texture and endure the aerodynamic forces during the impingement tests. The paper should also minimize water diffusion along the surface. In addition, the effect of the blotter paper surface characteristics on droplet impingement dynamics should be similar to that of the clean airfoil surface. This is particularly important for large droplet impingement where the droplet splashing behavior must be preserved. To investigate if droplet splashing occurred from the surface of the blotter paper, extensive tests were performed at the Goodrich IWT using advanced imaging techniques as discussed in section 4. The experiments showed that the blotter paper preserved large droplet splashing. However, it was very difficult to establish from the images obtained whether the dynamics of droplet impingement on the blotter paper were the same as that on the clean airfoil surface.

Blue dye characteristics.—An issue regarding the blue dye used in the impingement tests was its effect on water surface tension characteristics. Surface tension measurements of blue dye solution samples showed no change in the water surface tension properties as shown in appendix E.

8.1.2 Data Reduction Method

Blotter paper illumination methods.—Uniform light illumination of the blotter strips is very important during the data reduction process. The laser reflectometer uses a point measurement technique in which the illumination of the blotter paper is accomplished by a He-Ne laser beam 1 mm in diameter. The intensity of the incident light is assumed to be uniform over the small region of illumination. Another advantage of the laser reflectometer is that small levels of dye penetration into the blotter paper have less of an impact in the reflectance measurements because the laser can penetrate deep into the paper. The CCD data reduction system measures reflectance over large portions of the blotter strip and uniform illumination of the blotter strip is more difficult to attain. During the 2001 program, the four halogen lamps used in the earlier version of the CCD system (ref. 1) were replaced with high intensity LED lights as discussed in section 5. The use of the new LED lights improved light uniformity over the blotter strip and enhanced the accuracy of the data reduction with the CCD reflectometer.

Data reduction systems.—The laser and CCD reflectometers are complex systems and their performance can only be assessed through careful testing. To establish the repeatability of these data reduction systems, randomly selected blotter strips were scanned repeatedly over a period of several weeks. Typical results are shown in figure 72a and b for the laser reflectometer and CCD system respectively. The results indicate that the variation in the reflectance measurements obtained with the laser reflectometer and the CCD system was approximately less than 1 percent from the average reflectance of repeated scans.

8.2 Pressure Distributions

Experimental pressure distributions for the airfoils tested are compared with analysis results obtained with the LEWICE code in figures 73 to 80. Good correlation is demonstrated in all cases between the experimental and computed pressure distributions. In addition to the experimental data obtained during the 2001 IRT entry, pressure distributions obtained during

the 1997 and 1999 IRT entries (ref. 1) and experimental data from the Wichita State University 7-ft by 10-ft facility (ref. 27) are also presented in figures 73 to 80 for selected airfoils for comparison. Note that the LEWICE code uses a potential flow method to compute the flowfield about an airfoil. The code, however, does not simulate wind tunnel wall effects, tunnel flow angularity or the effects of viscosity and trailing wakes. Thus, to improve the correlation between the computed and the experimental pressures, the angles of attack used in the computations were adjusted by an increment in the range of -1.85° to 0.2° (depending on airfoil tested) with respect to the geometric angles of attack used in the experiment. It was important to have a good match between the experimental and analytical flowfields prior to the computation of the impingement characteristics.

8.3 Impingement Results

8.3.1 Test Repeatability

Repeatability is defined as the maximum percent difference of repeated test runs from the average. The maximum difference is typically observed at the point of maximum impingement efficiency. Test repeatability is an important indicator of the quality of the experimental method. Selected test repeatability data are presented in figures 81 to 86 and in figure 10 for all airfoils and ice shapes tested during the 2001 IRT entry. In most cases, each test condition was repeated two to three times (i.e., 3 to 4 test runs per condition). However, in some cases as many as nine repeats were used to evaluate the repeatability of the experimental method. The results presented indicate that the maximum difference of repeated tests from average was as follows:

- MS(1)–0317 airfoil 3.3 to 10.7 percent
- NACA 65₂–415 airfoil 2.0 to 8.5 percent
- GLC–305 airfoil 1.6 to 9.2 percent
- Twin Otter tail (clean) 1.2 to 12.9 percent
- Twin Otter tail with 22.5-min ice shape 0.2 to 21.0 percent
- Twin Otter tail with 45-min ice shape 4.1 to 11.0 percent

In summary, the data presented indicate that the maximum difference of repeated tests from the average was:

- 0.24 to 10 percent for 33 out of 38 cases presented
- 10.70 to 12.90 percent for 4 out of 38 cases presented
- 21.00 for 1 out of the 38 cases presented

All repeatability data and impingement efficiency presented were calculated with the data reduced using the laser reflectometer. Note that the laser reflectometer uses point reflectance measurements at two to three locations along the width of a blotter strip to generate the value of the local impingement efficiency as shown in figure 59a. Thus, impingement results obtained with the laser reflectometer tend to exhibit larger variation from the average than corresponding data (not shown) obtained with the CCD data reduction system. This is because at any model surface location the CCD system averages data from a large portion of the width of the blotter strip which reduces the effect of local variations in impingement characteristics between test runs. The laser illumination method used in the laser reflectometer, however, can penetrate below the surface of the blotter paper and as a result reflectance measurement errors due to dye penetration are reduced.

8.3.2 Experimental and LEWICE Impingement Data

Experimental and LEWICE impingement data presented in this section include FAR part 25, appendix C (MVDS of 11 and 21 μm) and SLD cloud conditions (MVDs of 79, 137, and 168 μm). The computations were performed with the LEWICE 1.6 computer code which does not simulate droplet splashing effects during the impingement process.

The experimental and computational results presented are for four airfoil sections and two simulated ice shapes. The freestream speed in all cases was 175 mph. A summary of geometric, aerodynamic, and impingement parameters for the airfoils tested is provided in figure 11. In this table, the symbol $S_{\bar{\beta}_{\max}}$ denotes the surface location corresponding to the maximum impingement efficiency while the symbols S_u and S_l are the upper and lower impingement limits defined as the locations on the model surface where the local impingement efficiency was 0.05 percent (i.e., $\bar{\beta} = 0.0005$). The non-dimensional chordwise locations for S_u and S_l are denoted by x_u/c and x_l/c .

All the impingement data are in the form of local impingement efficiency versus surface distance in mm. Surface distance was measured with respect to a reference point on each test model termed the highlight. Airfoil surface distance was negative along the suction side (typically the airfoil upper surface) and positive along the pressure side. For all airfoils, the highlight was located at the leading edge corresponding to a surface distance of 0 mm. For the Twin Otter tail with ice shapes, the highlight was located at the leading edge on the ice shape, corresponding to mark number 5 in figure 32d and mark number 6 in figure 33c for the 22.5- and 45-min ice shape respectively.

All experimental results are compared with LEWICE impingement data in figures 87 to 94. In addition, experimental and LEWICE maximum and total impingement efficiencies are compared in the tables provided in appendix G. All the results from LEWICE analysis presented in this section and in appendices B, G and H were computed using the droplet distributions data obtained with the FSSP and OAP probes. These distributions were discretized into 27 bins to simplify the computations. The 27-bin droplet distributions are presented in figure 7 and in figure 63. Note that public versions of the LEWICE 2.0 computer code can only handle droplet distributions with 10 droplet sizes. Thus, 10-bin versions of the droplet distributions measured are provided in figure 8 and in figure 64.

Figures 95 to 102 show experimental impingement limits plotted on the airfoil surface for all models tested. Figures 103 to 110 show the experimental impingement distributions plotted on the airfoil surfaces. These plots are for illustration purposes only and they are not to scale. The plots were constructed by plotting the local impingement efficiency value at a given surface location normal to the surface of the airfoil. All local impingement efficiency $\bar{\beta}$ values were scaled by $c/200$ where c is the chord length of the airfoil in mm. The resulting plots resemble ice accretions and are useful in demonstrating the magnitude and extent of impingement as a function of angle of attack and MVD size.

A. MS(1)–0317 Airfoil.—Small droplet impingement data for this airfoil were obtained during the 1985, 1997 and 1999 IRT entries. This airfoil is typically used as a calibration model to verify the experimental setup during each new IRT entry. In figure 87a, experimental data obtained during the 2001 impingement tests for MVD of 21 μm are compared with similar data obtained during the previous three experimental programs. Note that all the experimental data presented were reduced with the laser reflectometer. The agreement between the 2001 and the previous experimental results is good, indicating repeatability in the experimental setup. The LEWICE data provided in figure 87a are also in good agreement with the experimental results. Note that the LEWICE flowfield was computed for a geometric angle of attack of -1.85° (instead of 0° used in the experiment) to match the experimental pressure distributions as shown in figure 73.

Experimental results from 2001 impingement tests, along with the LEWICE analysis data, for MVDs 11, 21, 79, 137, and 168 μm are presented in figures 87b to f. The impingement curves obtained with the laser reflectometer and the CCD data reduction systems were in good agreement. In previous studies (ref. 1) impingement data reduced with the CCD system had lower beta values near the highlight location and higher beta values along the impingement tails compared with corresponding data from the laser reflectometer. This was attributed to problems with the illumination system used as discussed in section 6 of this report. The recent data indicate that the new LED based illumination system improved the accuracy of the CCD data reduction system considerably.

The impingement data shown in figure 87b to f indicate the following trends in impingement characteristics with MVD size:

- The maximum local impingement efficiency for all MVD cases occurred along the upper surface near the leading edge corresponding to $S_{\bar{\beta}_{\max}}$ in the range of -4 to -6 mm depending on MVD. The maximum values of $\bar{\beta}$ were 0.35 for MVD = 11 μm , 0.49 for MVD = 21 μm , 0.67 for MVD = 79 μm , 0.75 for MVD = 137 μm , and 0.87 for MVD = 168 μm .
- The total impingement efficiency increased as the MVD size was increased.
- The total extent of impingement increased as the MVD size was increased. However, the change in the extent of the lower impingement limit with MVD size was smaller than that of the upper limit.

LEWICE results are provided in figure 87b to f for comparison with the experimental data. The LEWICE impingement data shown correspond to an angle of attack of -1.85° (to match the experimental pressures) and were obtained with a 27-bin discrete droplet distribution which was defined from the experimental droplet measurements. In general, the experimental and LEWICE impingement data were in good agreement for the 11 and 21 μm cases. However, for the large MVD cases (79, 137, and 168 μm) the computed local impingement efficiencies and the impingement limits were considerably higher than the experimental results. This discrepancy is attributed to large droplet splashing effects which are not modeled in the LEWICE code. Another notable observation in the LEWICE impingement data is that the difference between the 137 and the 168 μm impingement curves is small compared to the difference observed in the experimental data.

B. NACA 65₂-415 Airfoil.—Experimental impingement data for this airfoil at angles of attack 0° and 4° and MVDs of 11, 21, 79, 137, and 168 μm are compared with LEWICE results in figure 88a to e. The LEWICE computations presented were obtained for angles of attack of -0.55° and 3.2° to match the experimental pressure distributions as shown in figures 74 and 75 respectively.

The experimental data presented in figure 88a to e show that for the 0° angle of attack case, the maximum impingement was located very close to the leading edge ($S_{\bar{\beta}_{\max}} = 0$ to 2 mm depending on MVD size). The maximum local impingement efficiency for MVDs of 11, 21, 79, 137, and 168 μm was 0.46, 0.61, 0.75, 0.90, and 0.91 respectively. As the angle of attack was increased to 4° (fig. 89a to e), the location of the maximum impingement moved toward the lower surface (i.e., between 3 to 5 mm for all MVDs). The maximum $\bar{\beta}$ for MVDs of 11, 21, 79, 137, and 168 μm was 0.39, 0.59, 0.72, 0.89, and 0.90 respectively. The impingement limits moved toward the leading edge on the upper surface and toward the trailing edge on the lower surface with respect to the 0° case. The total impingement efficiency for a given MVD size did not change significantly with angle of attack as shown in figure 11. However, in most cases the

total extent of impingement was higher for the 4° case compared to that obtained for the 0° angle of attack.

The LEWICE impingement data exhibited similar trends with that observed in the experimental results for both angles of attack. Local impingement efficiencies and impingement limits for the small MVD cases (i.e., 11 and 21 μm) computed with LEWICE were in agreement with the experimental results (fig. 88a and b, and 89a and b). However, the computed local impingement efficiencies for the large droplet cases were considerably higher than the experimental values particularly in the tail regions of the impingement curves as shown in figure 88c to e, and 89c to e.

C. GLC-305 Airfoil.—Experimental and LEWICE impingement data for this airfoil for an angle of attack of 1.5° and MVDs of 11, 21, 79, 137, and 168 μm are given in figure 90a to e. The LEWICE computations presented were obtained for $\alpha = 1.6^\circ$ to match the experimental pressure distribution shown in figure 76. The experimental data indicate that the maximum impingement efficiency for MVDs of 11, 21, 79, 137, and 168 μm was 0.48, 0.59, 0.75, 0.89, and 0.89 respectively and was located on the lower surface of the airfoil in the proximity of the leading edge. For all MVD cases the extent of impingement was greater on the lower surface than on the upper surface. The total impingement efficiency and the total impingement extent increased with MVD size as for the other two airfoil geometries tested.

Comparison of the experimental and LEWICE results for the smaller MVD cases (i.e., 11 and 21 μm) showed good agreement. For the large MVDs (i.e., 79, 137, and 168 μm), the maximum experimental $\bar{\beta}$ value in the case of the 79 μm case was considerably lower than that obtained with LEWICE; for the 137 and 168 μm MVD cases the experimental peak efficiencies were very similar to those obtained with the LEWICE code. The main discrepancy between the LEWICE and the experimental impingement data for the large MVD cases was in the region of the impingement tails. In general, for the GLC 305 airfoil, the difference between LEWICE and experiment was less than that observed for the MS(1)-0317 and NACA 652-415 airfoils.

This airfoil had the least maximum thickness of all airfoils tested and had the highest total impingement efficiency for a given MVD size than the other airfoils tested.

D. Twin Otter Tail.—The Twin Otter tail section had the largest chord, 57 in., and the largest maximum thickness, 6.84 in., compared with the other models tested. It was selected because it is representative of the tail section of commuter type aircraft. In addition, 22.5- and 45-min glaze ice shapes were available for this airfoil for impingement testing. Small and large droplet impingement data on these ice shapes were obtained to explore the application of the dye tracer method on complex aerodynamic surfaces. Furthermore, the impingement database for ice shapes is very limited and data is needed for code validation.

Experimental and LEWICE impingement data for the Twin Otter tail section are presented in figure 91a to c for $\alpha = 0^\circ$ and in figure 92a to c for $\alpha = 4^\circ$. The LEWICE analysis was performed for $\alpha = 0.2^\circ$ and 3.9° to match the experimental pressure distribution given in figures 77 and 78 respectively.

For the 0° angle of attack, the point of maximum impingement efficiency for this airfoil was near the leading edge in the range of -2 to 2 mm with respect to the highlight depending on MVD size. The maximum local impingement efficiency was 0.33, 0.52, 0.73, 0.81, and 0.82 for MVDs of 11, 21, 79, 137 and 168 μm respectively. As expected, the maximum $\bar{\beta}$, the total impingement efficiency, and the impingement limits increased as the cloud MVD was increased.

At $\alpha = 4^\circ$, the impingement curve shifted toward the lower surface and the maximum local impingement efficiency values decreased compared to the 0° case. However, the total impingement efficiency and the extent of impingement were greater for the 4° case compared to the 0° data. The maximum local impingement efficiency for the 11, 21, 79, 137 and 168 μm MVDs was 0.28, 0.46, 0.62, 0.78, and 0.81 respectively.

The LEWICE impingement data for the small MVDs of 11 and 21 μm were in good agreement with the experimental results for both angles of attack tested. For the large droplet cases (79, 137, and 168 μm), however, the agreement was not good and the magnitude and impingement limits of the experimental data were considerably lower than those obtained with the LEWICE code. For the large droplets, the difference between experiment and analysis was greater for the 4° angle of attack than that observed for the 0° case.

E. Twin Otter Tail with 22.5- and 45-min Ice Shapes.—Both ice shapes had an upper and a lower horn with a cavity region between the horns. The horns for the 22.5-min ice shape were considerably smaller than the horns of the 45-min ice shape.

Impingement characteristics for the Twin-Otter tail with the simulated LEWICE ice shapes were obtained for an angle of attack of 0° and MVDs of 11, 21, 79, and 168 μm . The experiment and LEWICE analysis results for this case are presented in figures 93a to 94d. The LEWICE results were obtained for an angle of attack of 0.2° to improve correlation with the experimental pressure distributions. The flowfield about large glaze ice shapes includes regions with considerable flow separation even at low angles of attack. Panel codes such as the one used in LEWICE are not able to simulate regions with extensive flow separation. Thus, the predicted flowfield is subject to error.

Impingement characteristics for the Twin Otter tail with the simulated LEWICE ice shapes were obtained for an angle of attack of 0° and MVDs of 11, 21, 79, and 168 μm . Experimental and LEWICE impingement results for these two ice shapes are presented in figures 93a to 94d. To help explain some of the experimental and computational impingement trends, droplet trajectories for all the MVDs tested are presented in figures 65 and 66 for the 22.5- and 45-min ice shapes respectively. These figures show that for the 11 and 21 μm MVD cases the droplet trajectories experienced considerable deflection in the proximity of the ice shapes due to the flowfield. For the large MVD cases, however, the trajectories were nearly straight due to the large droplet inertia. In addition, for the large MVDs there were regions downstream of the horns where droplet impingement is evident. Additional trajectory computations are presented in appendix F.

22.5-min Ice Shape

The experimental results indicate the following impingement trends:

- This ice shape had higher impingement on the horns than in the cavity region for the 11 and 21 μm MVD cases. For the larger MVDs, namely the 79 and 168 μm , the difference in the impingement intensity on the horns and the cavity was less notable.
- For all MVDs tested, the upper horn had higher impingement efficiency than the lower horn.
- Droplet impingement was observed along the lower surface downstream of the lower horn for the 79, 137, and 168 μm cases. In addition, droplet impingement was also observed along the upper surface downstream of the upper horn. However, the impingement on the upper surface was considerably less than that on the lower surface.

45-min Ice Shape

The experimental results indicate the following impingement trends:

- This ice shape had considerably higher impingement on the horns than in the cavity region for all MVD tested.
- For the 11 and 21 μm MVDs the upper horn experienced higher impingement rates than that observed on the lower horn. However, for the large MVDs of 79 and 168 μm the impingement on both horns was similar.

- Droplet impingement was observed along the lower surface downstream of the lower horn for the 79 and 168 μm cases. However, the impingement was less than that observed with the 22.5-min ice shape.
- Impingement in the cavity region was nearly zero for the 11 μm MVD but it increased gradually as the MVD was increased to 21, 79, and 168 μm . For the last two MVD cases, the impingement in the ice shape cavity ranged from 50 to 75 percent.

Comparison of the experimental with the LEWICE computations showed good agreement for both ice shapes for MVDs of 11 and 21 μm . For the large MVD cases, the LEWICE and the experimental results exhibited similar trends. However, the LEWICE predictions were in general higher than the experimental impingement data, particularly in the regions downstream of the horns.

9.0 Summary and Conclusions

Small and large water droplet impingement experiments were conducted in the Goodrich icing wind tunnel facility using an advanced imaging technique to investigate droplet splashing on an 18-in. NACA 0012 airfoil. Tests were performed with the clean airfoil and with a blotter strip attached to the airfoil leading edge for airspeeds in the range of 50 to 175 mph, freestream temperature in the range of 70 to 100 °F and median volumetric diameters (MVD) in the range of 11 to 270 μm . Extensive wind tunnel tests were also conducted at the NASA Glenn Icing Research Tunnel with four single element airfoils and an airfoil with 22.5- and 45-min LEWICE glaze ice shapes to expand the large droplet impingement database. The single element airfoils had maximum thickness to chord ratios in the range of 8.7 to 17 percent and were representative of sections used in general aviation and in small commuter transport aircraft. Test conditions included freestream speed of 175 mph, freestream total temperature of approximately 39 to 69 °F, relative humidity of 75 ± 5 percent, a range of angles of attack, and cloud median volumetric diameters of 11, 21, 79, 137 and 168 μm . Each experimental condition for each test model was repeated 2 to 3 times and in some cases as many as 6 to 9 times to establish a measure of test repeatability. Additional tests were also performed to investigate the repeatability of spray system performance and its effect on LWC and droplet distribution. Comparisons of experimental and analysis impingement data obtained with the NASA Glenn LEWICE-2D code were performed. Below is a summary of key findings based on the work performed.

9.1 Large Droplet Splashing Tests at the Goodrich IWT

1. The imaging technique used was able to capture the phenomenon of droplet splashing. To the author's knowledge this is the first publicly available data that document this phenomenon for cases representative of aircraft icing conditions.
2. Splashing was observed to occur for a range of airspeeds and droplet sizes for both the clean airfoil and the airfoil with blotter paper attached to the leading edge. However, the visual images could not be used to establish if droplet impingement dynamics was the same for the blotter and clean airfoil surfaces.
3. In general, the intensity of droplet splashing increased as the spray cloud MVD was increased for fixed airspeed. Also, droplet splashing intensity increased as the airspeed was increased for fixed spray cloud MVD.

9.2 Large Droplet Impingement Tests at the NASA IRT

1. The 12-nozzle WSU spray system was expanded to 16 nozzles to enhance cloud uniformity for the large droplet conditions selected for the impingement tests. The automated air and water pressure feedback control units were able to maintain system pressures at the spray nozzles to within 0.2 to 1 psi from the required settings. The system was capable of producing repeatable sprays of durations as short as 0.75 sec.
2. Repeated droplet distribution measurements with the NASA FSSP and OPA probes showed that the variation in cloud MVD was ± 0.5 to $1 \mu\text{m}$ from the average for the 11 and $21\text{-}\mu\text{m}$ clouds, and ± 1 to $3 \mu\text{m}$ from the average for the 79, 137 and $168\text{-}\mu\text{m}$ clouds.
3. Significant improvements were made to the blotter illumination system of the CCD reflectometer. The fixed halogen lights used in the earlier version of the system were replaced with an array of red LED sources whose location was adjustable to improve light uniformity over the dye-laden blotter strip for reflectance measurements. Software modifications were also made to allow the instrument to extract data from the small reference collector strips. The improvements made increased the accuracy and repeatability of the data extraction process. The results obtained with the CCD system were found to be in very good agreement with that obtained with the laser reflectometer.
4. The laser reflectometer remains the preferred system for data reduction because it is able to provide more uniform illumination of the blotter strip over the region of interest and is less sensitive to dye penetration into the blotter paper. The system software was converted from the PC DOS operating system to WINDOWS and was written using the LabVIEW graphical interface language. Considerable software improvements were made to enhance the signal to noise ratio.
5. The experimental setup was verified prior to the start of the impingement tests with the MS 317 airfoil model that has been tested in the NASA IRT facility several times during previous impingement experiments. The experimental results obtained were found to be in very good agreement with the data from the previous studies.
6. The maximum difference of repeated impingement tests from the average was in the range of 0.24 to 10 percent for approximately 87 percent of the 38 test cases presented, 11 to 13 percent for 11 percent of the test cases, and 21 percent for the remaining 2 percent of the test cases. The number of repeats performed per test condition is not sufficient to establish a statistical average. However, the small variation in test repeatability for the large number of impingement tests conducted to generate the data presented in this report indicates that the experimental methodology was repeatable.

General impingement trends for the four single element airfoils and the two glaze ice shapes tested were as follows:

7. For a fixed angle of attack, the total and maximum impingement efficiencies and the total extent of impingement increased with MVD as expected.
8. In general, for a fixed MVD the maximum impingement efficiency decreased with angle of attack. However, the reduction in maximum impingement efficiency diminished as the MVD approached $168 \mu\text{m}$. In most cases, the total impingement efficiency, increased as the angle of attack was increased. In all cases the total extent of impingement increased with angle of attack.
9. Small and large droplet impingement data were obtained for the first time for an airfoil section with simulated large glaze ice accretions. The results for the 11 and $21 \mu\text{m}$ cases showed considerable more impingement on the horns than in the cavity region between the horns. Furthermore, a sharp drop in impingement was observed downstream of the horns, caused by the horn shielding effect. For the large droplet tests with the 79 and

168 μm MVDs, significant impingement was observed on the horns and in the leading edge cavity region. In addition, droplet impingement was observed downstream of the upper and lower horns due to the higher droplet inertia effects. Total impingement was higher for the 45-min ice shape than for the 22.5-min glaze ice.

10. In general, good agreement between the experimental results and analysis data obtained with the NASA Glenn LEWICE computer code was demonstrated for the 11, and 21- μm cases presented in this report. Tests with the small droplets were used to verify the experimental setup and to provide limited small droplet impingement data for large glaze ice shapes. For the large droplet conditions, however, which included 79, 137 and 168- μm MVDs the analysis produced considerably higher overall impingement than the experiment. The observed differences between the experiment and analysis were attributed to droplet splashing effects.
11. Droplet breakup prior to impingement is another phenomenon that could impact large droplet impingement dynamics as discussed in appendix A. Additional work is needed to quantify the effects of large droplet breakup on water impingement and ice accretion processes.

References

1. Papadakis, M., Hung, K.E., Vu, G.T., Yeong, H.W., Bidwell, C., Breer, M.D., Bencic, T., "Experimental Investigation of Water Droplet Impingement on Airfoils, Finite Wings, and an S-Duct Engine Inlet," NASA/TM—2002-211700, September 2001.
2. Von Glahn, U., Gelder, T.F., and Smyers, W.H. Jr, "A Dye Tracer Technique for Experimentally Obtaining Impingement Characteristics of Arbitrary Bodies and a Method for Determining Droplet Size Distribution," NACA TN-3338, March 1955.
3. Gelder, T.F., Smyers, W.H. Jr, and Von Glahn, U., "Experimental Droplet Impingement on Several Two-Dimensional Airfoils with Thickness Ratios of 6 to 16 percent," NACA TN-3839, December 1956.
4. Lewis, J.O. and Ruggeri, R.S., "Experimental Droplet Impingement on Four Bodies of Revolution," NACA TN-3587, 1957.
5. Lewis, James O. and Ruggeri, Robert S., "Experimental Droplet Impingement on four bodies of revolution," NACA TN-4092, December 1955.
6. Gelder, T.F., "Droplet Impingement and Ingestion by Supersonic Nose Inlet in Subsonic Tunnel Conditions," NACA TN-4268, May 1958.
7. Papadakis, M., Elangovan, R., Freund, G.A., Jr., Breer, M., Zumwalt, G.W. and Whitmer, L., "An Experimental Method for Measuring Water Droplet Impingement Efficiency on Two- and Three-Dimensional Bodies," NASA CR-4257, DOT/FAA/CT-87/22, November 1989.
8. Papadakis, M., Breer, M.D., Craig, N., and Liu, X., "Experimental Water Droplet Impingement Data on Airfoils, Simulated Ice Shapes, an Engine Inlet and a Finite Wing," NASA CR-4636, DOT/FAA/CT-TN93/18, December 1994.
9. Phillips, E.H. "ATR42/72 Review Focuses on Icing," Aviation Week and Space Technology, November 14, 1994.
10. Phillips, E.H. "FAA Lifts Icing Ban on ATR Flights," Aviation Week and Space Technology, June 5, 1995.
11. Kim, John, "Particle Trajectory Computation on a 3-Dimensional Engine Inlet," NASA CR-175023, DOT-FAA-CT-86-1, January 1986.
12. Carlson, D.J. and Høglund, R.F., "Particle Drag and Heat Transfer in Rocket Nozzles," AIAA Journal, vol. 2, no. 11, pp. 1980-1984, November 1964.
13. Langmuir, I. And Blodgett, K.B., "A mathematical Investigation of Water Droplet Trajectories," Army Air Forces Technical Report No. 5418, 1946.
14. Soeder, R.H. and Andracchio, C.R., "NASA Lewis Icing Research Tunnel User Manual," NASA TM-102319, June 1990.
15. McGhee, R.J. and Beasley, W.D., "Low-Speed Aerodynamic Characteristics of a 17-Percent-Thick Medium-Speed Airfoil Designed for General Application," NASA TP-1786, 1980.
16. Torenbeek, E., "Synthesis of Subsonic Airplane Design," Delft University Press, 1982.
17. Abbott, I.H. and Von Doenhoff, A.E., "Theory of Wing Sections," Dover Publications, Inc., 1959.
18. Addy, H.E., Jr., Potapczuk, M.G., and Sheldon, D.W., "Modern Airfoil Ice Accretions," NASA TM-107423, January 1997.
19. Wright, W.B., "Users Manual for the Improved NASA Lewice Ice Accretion Code LEWICE Version 2.0," NASA/CR-1999-209409, NASA Glenn Research Center, September 1999.
20. Oldenburg, J.R. and Ide, R.F., "Comparison of Drop Size Distributions From Two Droplet Sizing Systems," NASA TM-102520, March 1990.
21. "CSIRO-KING Liquid Water Content Probe PMS Model KLWC-5—Operating and Servicing Manual," Particle Measuring Systems, Inc., Boulder, CO.
22. Frei, R.W. and MacNeil, J.D., "Diffuse reflectance Spectroscopy in Environmental Problem Solving," CRC Press, Cleveland, OH, 1973.

23. Kubelka, P., "New Contributions to the Optics of Intensely Light-Scattering Materials. Part I.," *Journal of the Optical Society of America*, vol. 38, 1955.
24. Wright, W.B., "Users Manual for the Improved NASA Lewice Ice Accretion Code LEWICE 1.6," NASA CR-198355, June 1995.
25. Ide, R.F., "Comparison of Liquid Water Content Measurement Techniques in an Icing Wind Tunnel," NASA/TM-1999-209643, 1999.
26. "Fluent User's Guide," Fluent Inc., Lebanon, NH, 2001.
27. Papadakis, M., Gile Laflin, B.E., Youssef, G.M., Ratvasky, T.P., "Aerodynamic Scaling Experiments with Simulated Ice Accretions," AIAA Paper 2001-0833, 39th Aerospace Sciences Meeting and Exhibit, Reno, NV, January 8-11, 2001.

TABLE 1.—LIST OF DROPLET TRAJECTORY PARAMETERS

Parameter	Definition	Expression
Re_{MVD}	Reynolds number based on droplet diameter	$MVD \cdot V_{\infty} \cdot \frac{\rho_{air}}{\mu}$ where MVD represents Median Volumetric Diameter, ρ_{air} is the air density and μ is the absolute air viscosity
K	Droplet inertia parameter	$\rho_{droplet} \cdot V_{\infty} \cdot \frac{MVD^2}{18 \cdot \mu \cdot c}$ where $\rho_{droplet}$ is the droplet (water) density and c is the chord length of the airfoil model
$\frac{\lambda}{\lambda_s}$	Ratio of the true range of droplet as projectile injected into still air to the range of droplet as projectile following Stokes' law	$-0.022466 \cdot x^4 + 0.20109 \cdot x^3 - 0.59067 \cdot x^2 + 0.36072 \cdot x + 0.74544$ where $x = \log(Re_{MVD})$ and $6 < Re_{MVD} < 1000$
K_0	Droplet modified inertia parameter	$K \cdot \frac{\lambda}{\lambda_s}$
ϕ	Deviation of the droplet drag force from Stokes' law	$\frac{(Re_{MVD})^2}{K}$

TABLE 2.—TEST MATRIX FOR DROPLET SPLASHING TESTS; AOA=0°

Test no.	Configuration	Vfs (mph)	MVD (μm)	Air (psi)	Water (psi)	File name
1	Clean Airfoil	150	175	5	55	V150A5W55
2	Clean Airfoil	150	270	2	24	V150A2W24
3	Clean Airfoil	150	94	6	37	V150A6W37
4	Clean Airfoil	150	70	8	40	V150A8W40
5	Clean Airfoil	150	11	43	67	V150A43W67A
6	Clean Airfoil	150	21	22	77	V150A22W77
7	Clean Airfoil	150	40	18	90	V150A18W90
8	Airfoil with Blotter	100	175	5	55	B100A5W55
9	Airfoil with Blotter	150	175	5	55	BB150A5W55
10	Airfoil with Blotter	150	11	43	67	BB150A43W67
11	Airfoil with Blotter	150	21	22	77	BB150A22W77
12	Airfoil with Blotter	150	40	18	90	BB150A18W90
13	Airfoil with Blotter	150	270	2	24	B2B150A2W24
14	Airfoil with Blotter	150	120	5	33	B2B150A5W33
15	Airfoil with Blotter	150	94	6	37	B2B150A6W37
16	Airfoil with Blotter	150	70	8	40	B2B150A8W40
17	Airfoil with Blotter	150	175	5	55	B2B150A5W55
18	Airfoil with Blotter	150	11	43	67	B2B150A43W67
19	Airfoil with Blotter	150	21	22	77	B2B150A22W77
20	Airfoil with Blotter	150	40	18	90	B2B150A18W90
21	Airfoil with Blotter	50	94	6	37	B3B50A6W37
22	Airfoil with Blotter	75	94	6	37	B3B75A6W37
23	Airfoil with Blotter	100	94	6	37	B3B100A6W37
24	Airfoil with Blotter	125	94	6	37	B3B125A6W37
25	Airfoil with Blotter	150	94	6	37	B3B150A6W37
26	Airfoil with Blotter	175	94	6	37	B3B175A6W37
27	Clean Airfoil	50	94	6	37	C50M94
28	Clean Airfoil	75	94	6	37	C75M94
29	Clean Airfoil	100	94	6	37	C100M94
30	Clean Airfoil	125	94	6	37	C125M94, C125M94A
31	Clean Airfoil	150	94	6	37	C150M94
32	Clean Airfoil	175	94	6	37	C175M94
33	Airfoil with Blotter	175	94	6	37	B4B175M94
34	Airfoil with Blotter	150	94	6	37	B4B150M94
35	Airfoil with Blotter	125	94	6	37	B4B125M94
36	Clean Airfoil	175	270	2	24	C2_175M270
37	Clean Airfoil	150	270	2	24	C2_150M270
38	Clean Airfoil	125	270	2	24	C2_125M270
39	Clean Airfoil	100	270	2	24	C2_100M270
40	Clean Airfoil	75	270	2	24	C2_75M270
41	Clean Airfoil	50	270	2	24	C2_50M270
42	Clean Airfoil	30	270	2	24	C2_30M270
43	Clean Airfoil	175	21	22	77	C2_175M21
44	Clean Airfoil	150	21	22	77	C2_150M21
45	Clean Airfoil	125	21	22	77	C2_125M21
46	Clean Airfoil	100	21	22	77	C2_100M21
47	Clean Airfoil	75	21	22	77	C2_75M21
48	Clean Airfoil	50	21	22	77	C2_50M21
49	Clean Airfoil	30	21	22	77	C2_30M21

TABLE 3.—SUMMARY OF PRESSURE TRANSDUCER CHARACTERISTICS

Transducer	Usage	Range (psig)	Error	Thermal zero shift Error	Thermal span shift error
16 SETRA 206	Water lines	0-125	±0.13% FS	±1.0% FS/100 °F	±1.5% FS/100 °F
1 SETRA 204	Main air line	0-100	±0.11% FS	±0.4% FS/100 °F	±0.3% FS/100 °F
1 SETRA 204	Water tank	0-100	±0.11% FS	±0.4% FS/100 °F	±0.3% FS/100 °F
4 SETRA 206	Nozzle air lines	0-100	±0.13% FS	±1.0% FS/100 °F	±1.5% FS/100 °F

Note: All transducers were calibrated at temperature of 50 °F.

TABLE 4.—CLOUD MVD AND CORRESPONDING SPRAY SYSTEM PARAMETERS FROM TEST MEASUREMENTS (2001 IRT TESTS)

MVD range (µm)	Average air supply pressure at regulator (psig ± psi)	Average tank water pressure (psig ± psi)	Average water pressure at nozzle (psig ± psi)	Average air pressure at nozzle (psig ± psi)	ΔP = P _{water} -P _{air} at nozzle (psi)	Average volume flow rate 16 nozzles (gpm)	Spray Time (sec)
11	43.0 ± 0.2	66.8 ± 0.5	62.5 ± 0.6	40.0 ± 0.3	22.5	0.273	4.5
21 ± 0.5	22.1 ± 0.4	77.0 ± 0.7	72.2 ± 0.7	20.0 ± 0.5	52.2	0.377	2
79	5.8 ± 0.6	36.6 ± 0.4	32.2 ± 0.5	4.8 ± 0.7	27.4	0.202	2
137 ± 2	4.8 ± 0.7	54.7 ± 0.5	50.1 ± 0.7	3.9 ± 0.7	46.2	0.152	1
168 ± 3	4.8 ± 0.3	70.0 ± 0.8	65.1 ± 0.7	4.0 ± 0.4	61.1	0.138	0.75

Pressures, flow rates and errors have been calculated from 45 randomly selected tests for each MVD case.

TABLE 5.—COLLECTOR THEORETICAL EFFICIENCY AND KING PROBE LWC MEASUREMENTS FOR 2001 TEST MVDS

MVD (µm)	Average LWC (g/m3)	Collector Efficiency (%)
11	0.188	0.82
21 ± 0.5	0.521	0.89
79	0.496	0.95
137 ± 2	0.680	0.97
168 ± 3	0.747	1.00

TABLE 6.—TEST MODELS AND CONDITIONS FOR 2001 IMPINGEMENT TESTS

Test Model	Total number of surface pressure taps	Number of active surface pressure taps	Angle of attack (α) (degree)	MVD (μm)	Avg. air-speed (mph)	Number of runs per MVD	Total number of runs
MS(1)-0317 (c = 36 in) Strip Location: Midspan	47	41	$\alpha = 0$	11, 21, 79, 137,168	175	6 to 12	44
NACA 652-415 (c = 36 in) Strip Location: Midspan	76	71	$\alpha = 0, 4$	11, 21, 79, 137,168	175	7 to 15	61
GLC-305 (c = 36 in) Strip Location: Midspan	44	42	$\alpha = 1.5$	11, 21, 79, 137,168	175	4 to 15	37
Twin Otter (c = 57 in) Strip Location: Midspan	59	54	$\alpha = 0, 4$	11, 21, 79, 137,168	175	8 to 9	41
Twin Otter with 22.5-min ice shape Strip Location: Midspan	62 <i>6 taps in the leading edge are covered; 9 additional taps on ice shape</i>	57	$\alpha = 0$	11, 21, 79,168	175	4 to 6	18
Twin Otter with 45-min ice shape Strip Location: Midspan	63 <i>6 taps in the leading edge are covered; 10 additional taps on ice shape</i>	58	$\alpha = 0$	11, 21, 79,168	175	4 to 6	18
Collector Mechanism	N/A	N/A	$\alpha = 0, 4$	11, 21, 79, 137,168	175	17 to 37	141
Uniformity 6ft x 6ft Grid	N/A	N/A	N/A	11, 21, 79, 137,168	175	1 to 4	11
MVD, LWC measurements	N/A	N/A	N/A	11, 21, 79, 137,168	175	6 to 13	53

N/A: Not Applicable

TABLE 7.—27-BIN DROPLET DISTRIBUTIONS

Bin Number	%	Analytical Droplet Size (μm)				
		MVD = 11 μm	MVD = 21 μm	MVD = 79 μm	MVD = 137 μm	MVD = 168 μm
1	4.75	2.707705	4.00077	8.988605	13.11524	14.76249
2	4.75	5.908311	8.759436	20.35465	30.90709	39.6635
3	4.75	6.894112	10.27464	24.37485	44.90622	61.07254
4	4.75	7.775586	11.76303	27.6	62.12087	79.91931
5	4.75	8.381197	13.22518	31.1886	76.16357	94.06406
6	4.75	8.815271	14.65941	35.81544	87.4384	106.8399
7	4.75	9.249346	16.06485	43.48959	97.51823	119.1028
8	4.75	9.68342	17.3624	53.69431	107.2863	131.1719
9	4.75	10.11749	18.53165	63.19995	116.9069	143.3188
10	4.75	10.55157	19.68089	71.1769	126.6328	155.5633
11	4.75	11.02683	20.8358	78.42189	136.6346	167.5805
12	4.75	11.59031	21.99513	85.57934	147.1282	179.6738
13	4.75	12.20082	23.18513	92.64336	157.8825	193.8536
14	4.75	12.81132	24.42356	100.1921	168.5923	211.1211
15	4.75	13.42183	25.71301	108.3451	180.0425	229.5783
16	4.75	14.13913	27.13809	117.3896	194.5275	248.4009
17	4.75	15.04958	28.7678	127.905	213.3668	270.472
18	4.75	16.04637	30.76125	140.4024	234.648	300.4495
19	4.75	17.21855	34.40258	155.9513	260.0141	348.0638
20	4.75	18.71356	47.86874	176.116	300.9388	427.563
21	1.00	19.70768	61.85915	192.1838	339.2	491.5684
22	1.00	20.26472	68.70525	202.3394	375.2953	522.7271
23	1.00	21.1445	76.91782	216.6304	418.7063	562.0573
24	0.50	21.88794	84.84912	232.2908	452.2953	601.5455
25	0.50	22.38356	92.38594	248.5025	485.8828	641.2162
26	0.50	23.13103	103.4067	270.4386	534.0977	705.3595
27	0.50	27.81535	163.963	310.3141	694.0631	1110.785

TABLE 8.—10-BIN DROPLET DISTRIBUTIONS

Bin No.	%	Analytical Droplet Size (μm)				
		MVD = 11 μm	MVD = 21 μm	MVD = 79 μm	MVD = 137 μm	MVD = 168 μm
1	5.00	2.733647	4.040659	9.136017	13.32621	15.0874
2	10.00	6.50498	9.67207	22.39215	41.75555	52.53882
3	20.00	8.584485	14.24772	39.92843	81.43927	102.2525
4	30.00	11.27504	20.9438	77.47293	138.2274	172.0927
5	20.00	14.68181	28.15316	123.5943	206.7984	264.3778
6	10.00	17.98731	45.23621	166.6061	285.2506	395.5832
7	3.00	20.58746	70.07175	206.4749	382.6111	530.8987
8	1.00	22.13576	88.85927	241.5367	471.4704	624.4741
9	0.50	23.13105	103.4068	270.4389	534.0984	705.3605
10	0.50	27.81619	163.9674	310.3147	693.9445	1110.787

TABLE 9.—SUMMARY OF MODEL GEOMETRY AND IMPINGEMENT PARAMETERS. ALL DIMENSIONS ARE IN ENGLISH UNITS (inch, mph); VALUES INSIDE PARENTHESIS ARE IN SI UNITS (meter, m/s).

Geometry	Chord (in)	t_{max} (in)	x/c at t_{max}	V_{∞} mph	AOA (deg.)	MVD (μm)	Re_c Million	Re_{MVD}	K	K_0	ϕ						
MS(1)-0317	36 (0.914)	6.12 (0.155)	0.376	175 (78.25)	0.0	11	4.75	57	0.032	0.014	100,336						
						21	4.77	109	0.118	0.040	101,082						
						79	4.76	411	1.676	0.327	100,778						
						137	4.78	715	5.042	0.745	101,522						
						168	4.80	882	7.592	0.995	102,461						
NACA 65 ₂ -415	36.53 (0.928)	5.49 (0.139)	0.402	175 (78.25)	0.0	11	4.82	57	0.032	0.014	101,813						
						21	4.84	109	0.117	0.040	102,570						
						79	4.83	411	1.651	0.322	102,261						
						137	4.85	715	4.969	0.734	103,016						
					4.0	168	4.87	882	7.482	0.981	103,969						
						11	4.83	57	0.032	0.014	102,361						
						21	4.85	110	0.117	0.040	102,950						
						79	4.82	411	1.651	0.322	102,129						
137	4.83	713	4.968	7.35	102,433	168	4.83	875	7.470	0.984	102,409						
												11	4.61	55	0.032	0.014	95,167
												21	4.61	106	0.118	0.041	95,179
												79	4.60	397	1.663	0.330	94,761
GLC-305	36 (0.914)	3.12 (0.079)	0.398	175 (78.25)	1.5	137	4.64	694	4.997	0.751	96,492						
						168	4.60	845	7.521	1.012	94,848						
						11	7.47	57	0.020	0.009	157,437						
						21	7.51	109	0.075	0.026	158,827						
Twin Otter	57 (1.448)	6.84 (0.174)	0.315	175 (78.25)	0.0	79	7.64	417	1.059	0.205	164,262						
						137	7.71	730	3.192	0.467	166,739						
						168	7.65	887	4.790	0.626	164,367						
						11	7.52	57	0.020	0.009	159,220						
					4.0	21	7.53	109	0.075	0.026	159,744						
						79	7.51	410	1.056	0.206	158,820						
						137	7.49	709	3.175	0.471	158,381						
						168	7.51	872	4.777	0.631	159,063						
Twin Otter with 22.5-min ice shape	57 (1.448)	6.84 (0.174)	0.315	175 (78.25)	0.0	11	7.36	56	0.020	0.009	153,423						
						21	7.38	107	0.074	0.026	153,956						
						79	7.37	402	1.052	0.207	153,772						
						168	7.41	859	4.758	0.634	155,163						
Twin Otter with 45-min ice shape	57 (1.448)	6.84 (0.174)	0.315	175 (78.25)	0.0	11	7.28	55	0.020	0.009	150,183						
						21	7.29	106	0.074	0.026	150,607						
						79	7.29	398	1.051	0.208	150,511						
						168	7.35	853	4.754	0.636	153,147						

TABLE 10.—SUMMARY OF TEST REPEATABILITY RESULTS

Test Case	AOA deg	MVD = 11 μm	MVD = 21 μm	MVD = 79 μm	MVD = 137 μm	MVD = 168 μm
MS(1)-0317	0	5.5	3.3	3.6	10.7	5.6
NACA 65 ₂ -415	0	4.5	9.9	6.5	8.5	5.5
NACA 65 ₂ -415	4	2.0	9.1	3.5	4.4	6.3
GLC-305	1.5	3.1	3.5	9.2	8.2	1.6
Twin Otter	0	12.9	4.6	1.6	3.7	9.5
Twin Otter	4	10.1	4.1	1.2	6.0	1.4
Twin Otter with 22.5-min ice shape	0	21.0	0.2	4.0	N/A	4.9
Twin Otter with 45-min ice shape	0	11.0	7.9	4.1	N/A	5.7

N/A: data not available

TABLE 11.—SUMMARY OF IMPINGEMENT EFFICIENCY DATA FOR 2001 IRT TESTS

Model	Test Conditions		$\bar{\beta}_{\max}$	$S_{\bar{\beta}_{\max}}$ (mm)	S_u (mm)	S_l (mm)	x_u/c	x_l/c	$A_{\bar{\beta}}$ (mm)	A_f (mm)	\bar{E}
	α	MVD									
MS(1)–0317	0	11	0.35	–4	–90	+45	0.0680	0.0314	10.496	155.493	0.0675
		21	0.49	–6	–95	+60	0.0732	0.0467	28.907	155.493	0.1859
		79	0.67	–5	–160	+112	0.1425	0.1019	52.371	155.493	0.3368
		137	0.75	–6	–195	+120	0.1804	0.1105	68.403	155.493	0.4399
		168	0.87	–4	–230	+150	0.2185	0.1430	81.618	155.493	0.5249
NACA 65 ₂ –415	0	11	0.46	1	–30	+23	0.0184	0.0174	9.674	137.323	0.0704
		21	0.61	0	–110	+60	0.0983	0.0558	23.697	137.323	0.1726
		79	0.75	1	–200	+160	0.1930	0.1623	45.623	137.323	0.3322
		137	0.90	2	–260	+200	0.2569	0.2053	66.666	137.323	0.4855
		168	0.91	1	–270	+220	0.2676	0.2267	59.888	137.323	0.4361
	4.0	11	0.39	5	–15	+55	0.0055	0.0505	9.760	141.329	0.0691
		21	0.59	5	–30	+187	0.0184	0.1913	28.159	141.329	0.1992
		79	0.72	3	–90	+320	0.0777	0.3344	50.861	141.329	0.3599
GLC–305	1.5	11	0.48	3	–15	+20	0.0078	0.0151	11.704	79.321	0.1476
		21	0.59	2	–27	+50	0.0199	0.0473	16.776	79.321	0.2115
		79	0.75	2	–118	+200	0.1174	0.2111	30.609	79.321	0.3859
		137	0.89	2	–150	+265	0.1521	0.2821	40.059	79.321	0.5050
		168	0.89	4	–150	+275	0.1521	0.2931	43.444	79.321	0.5477
Twin Otter	0	11	0.33	2	–60	+30	0.0294	0.0059	9.469	173.796	0.0545
		21	0.52	1	–110	+60	0.0618	0.0250	26.689	173.796	0.1536
		79	0.73	2	–190	+130	0.1154	0.0727	49.374	173.796	0.2841
		137	0.81	–2	–265	+200	0.1664	0.1206	60.554	173.796	0.3484
		168	0.82	2	–270	+220	0.1698	0.1343	63.134	173.796	0.3633
	4	11	0.28	13	–38	+63	0.0158	0.0270	9.996	189.139	0.0529
		21	0.46	8	–45	+210	0.0200	0.1275	27.963	189.139	0.1478
		79	0.62	6	–85	+410	0.0454	0.2651	53.762	189.139	0.2842
		137	0.78	10	–140	+680	0.0817	0.4512	85.883	189.139	0.4541
		168	0.81	9	–155	+690	0.0918	0.4581	88.264	189.139	0.4667
Twin Otter with 22.5-min Ice shape	0	11	0.24	–20	–30	+33	–0.0027	–0.0106	8.590	171.446	0.0501
		21	0.53	–21	–160	+35	0.0811	–0.0099	31.516	171.446	0.1838
		79	0.63	–24	–220	+120	0.1215	0.0457	44.031	171.446	0.2568
		168	0.95	–22	–300‡	+240	0.1760	0.1278	86.561	171.446	0.5049
Twin Otter with 45-min Ice shape	0	11	0.31	–33	–45	+60	–0.0147	–0.0195	12.367	173.766	0.0712
		21	0.55	–36	–270	+250	0.1307	0.1083	33.837	173.766	0.1947
		79	0.78	–36	–280	+280	0.1375	0.1288	52.849	173.766	0.3041
		168	0.95	–37	–300‡	+270‡	0.1511	0.1220	95.268	173.766	0.5483

Nomenclature for figure 11

1. $S_{\bar{\beta}_{\max}}$ represents the surface distance from the reference point (the highlight) to the location of the maximum impingement efficiency. S_u and S_l represent the surface distances of impingement limits on the upper and lower surfaces. x_u/c and x_l/c represent the stations of the impingement limits on upper and lower surfaces with respect to the chord.
2. $A_{\bar{\beta}}$ represents the total area under the local impingement efficiency curve, which is defined as $\int \bar{\beta} ds$; where ds is the infinitesimal surface distance.
3. A_f represents the projected frontal area of the airfoil.
4. \bar{E} represents the total impingement efficiency, which is defined as $\bar{E} = \frac{A_{\bar{\beta}}}{A_f}$
5. ‡ end of blotter strip

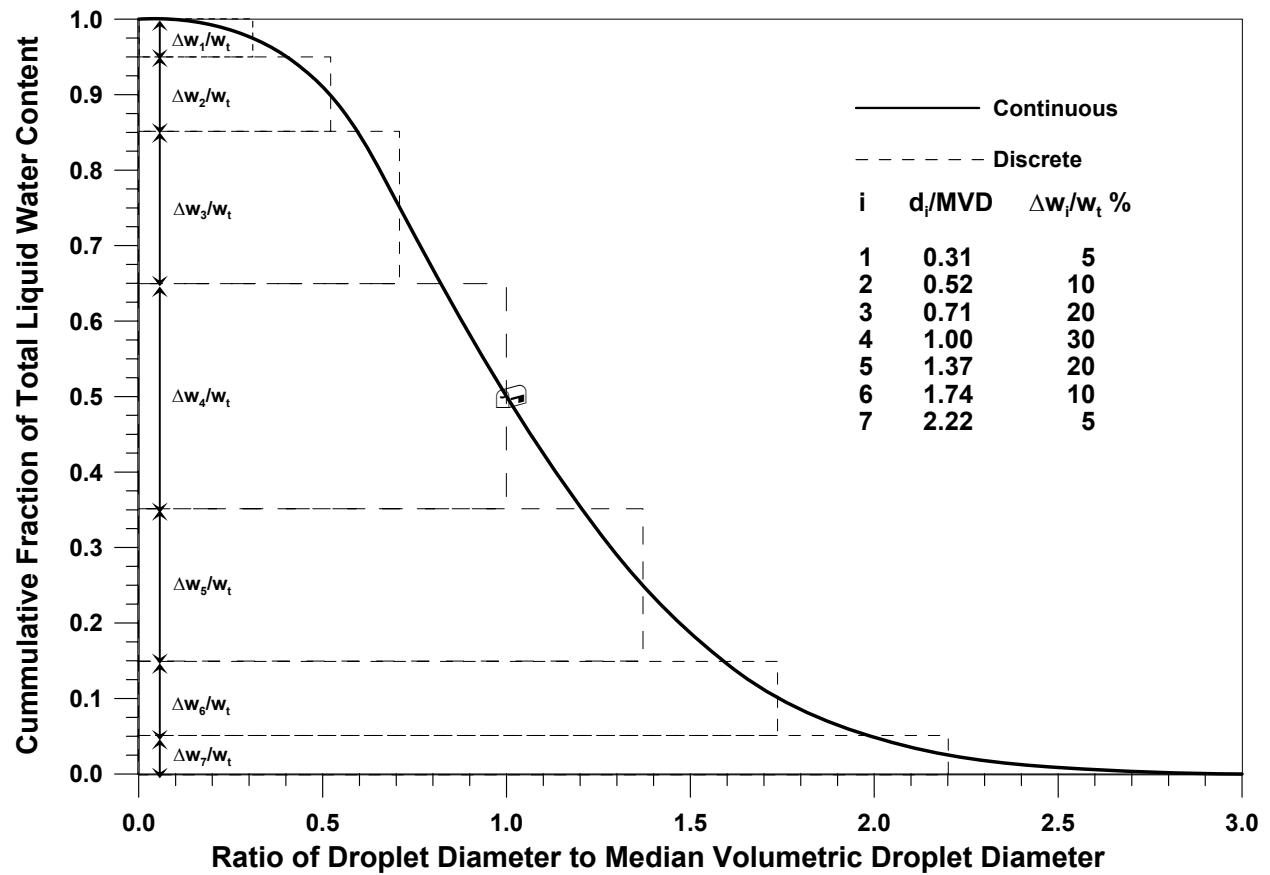


Figure 1.—Langmuir “D” dimensionless distribution of droplet sizes.

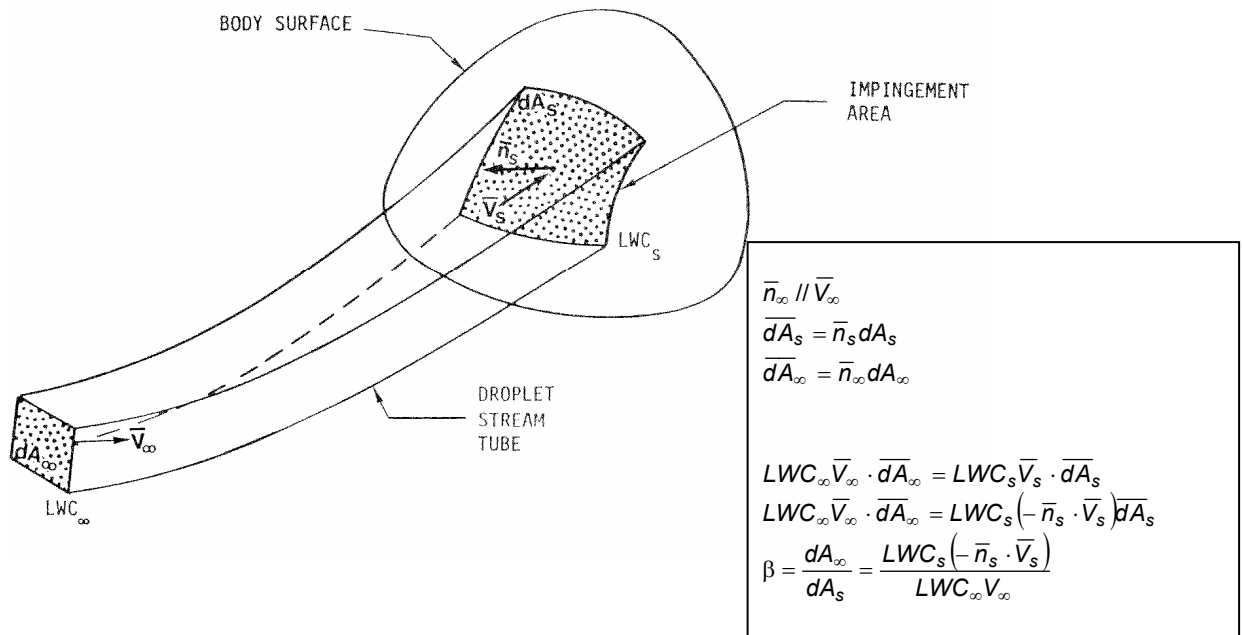


Figure 2a.—Definition of local impingement efficiency for a body in a cloud of uniform droplet size.

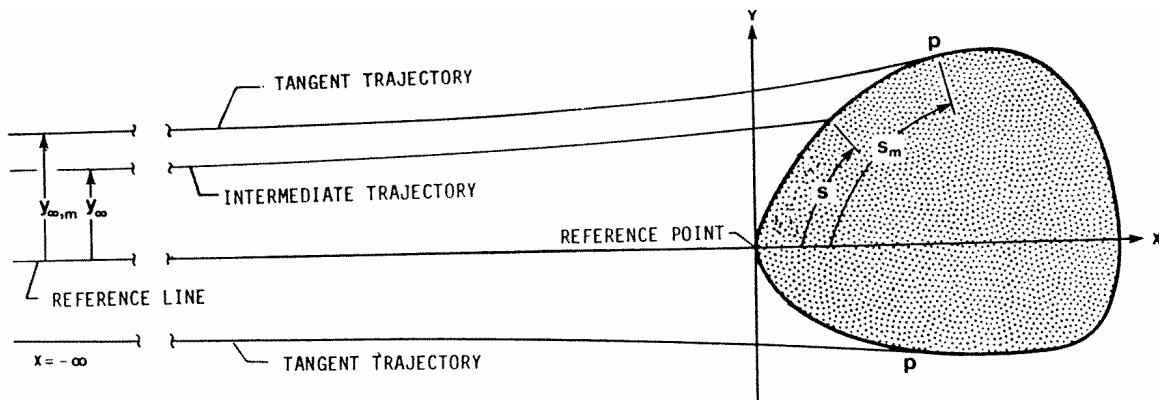


Figure 2b.—Two-dimensional droplet trajectories for a body in a cloud of uniform droplet size.

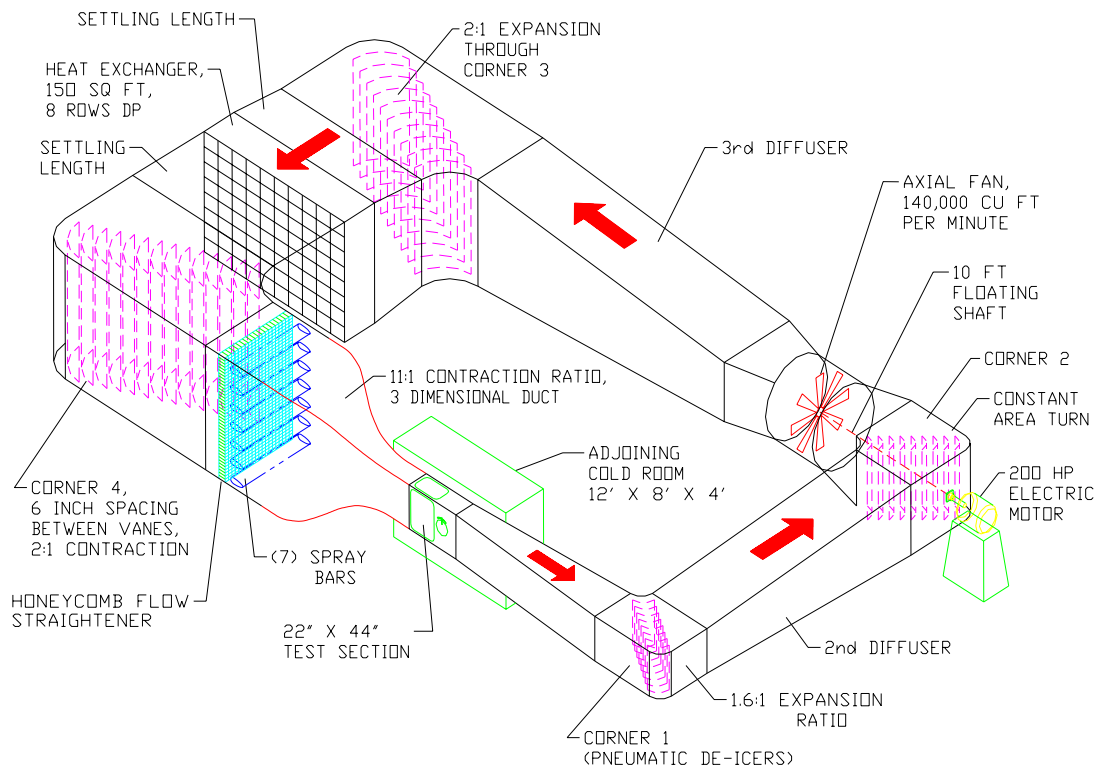


Figure 3a.—Goodrich Icing Wind Tunnel Schematic.

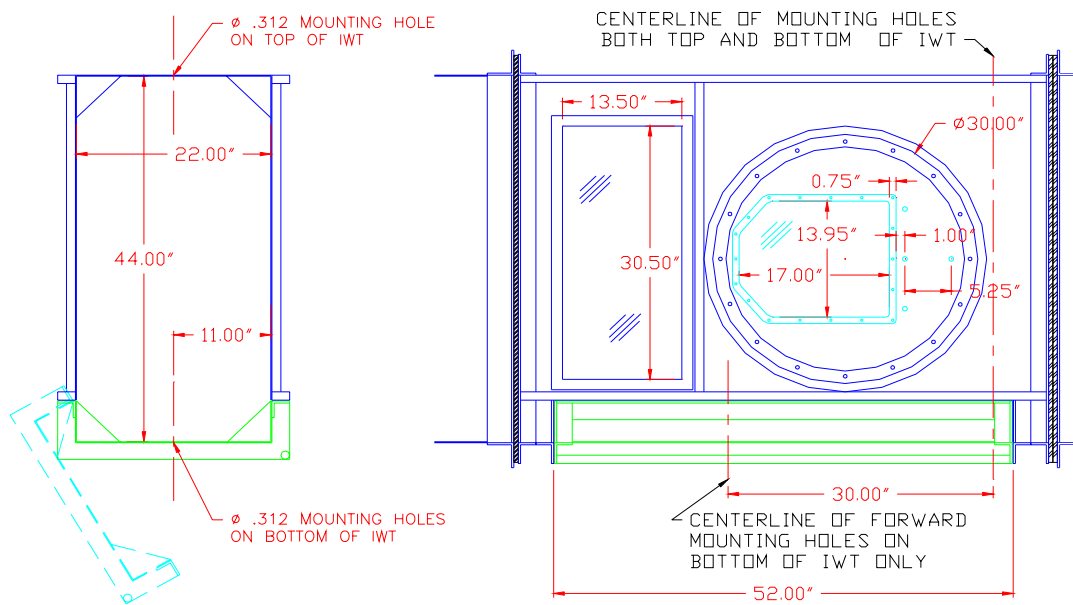


Figure 3b.—Goodrich IWT Test Section Details.



Figure 4.—NACA 0012 Airfoil (c=21 in.).



Figure 5.—NACA 0012 installed in Goodrich IWT.



Figure 6.—Goodrich IWT test section with NACA 0012 airfoil (looking downstream).



Figure 7.—WSU spray system.

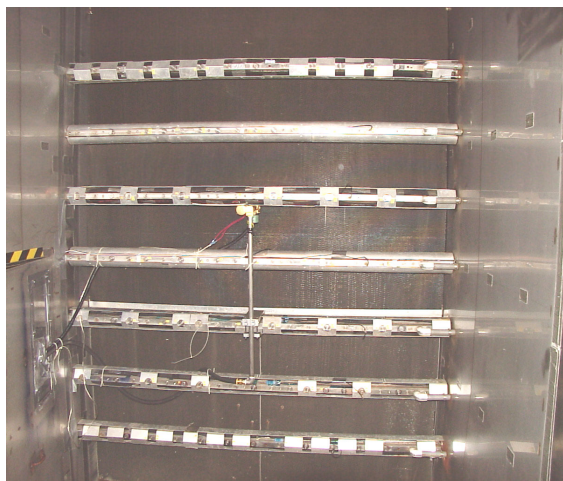


Figure 8.—WSU Nozzle assembly installed on Goodrich tunnel spray bars.

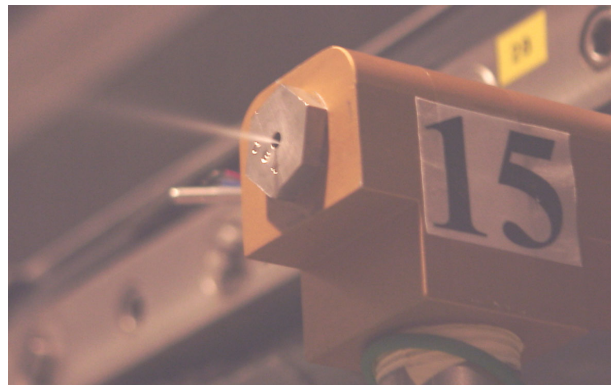


Figure 9.—Close-up of WSU nozzle housing with NASA MOD1 spray nozzle.



Figure 10.—CCD Camera, lens and laser setup.

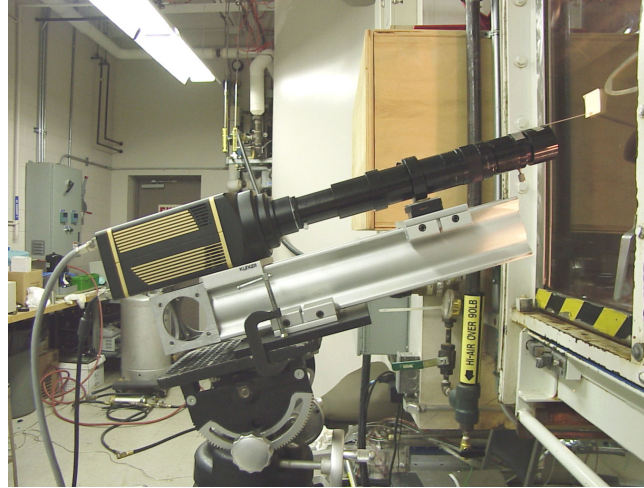


Figure 11.—Close-up of CCD and lens setup.



Figure 12.—Close-up of laser setup.

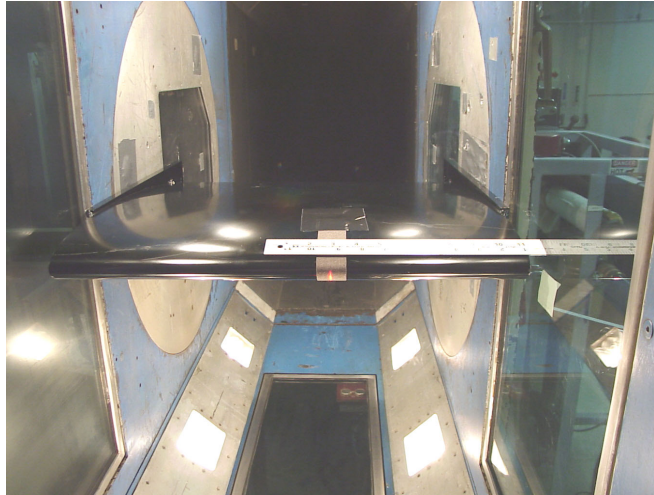


Figure 13.—Laser sheet location with respect to airfoil leading edge.

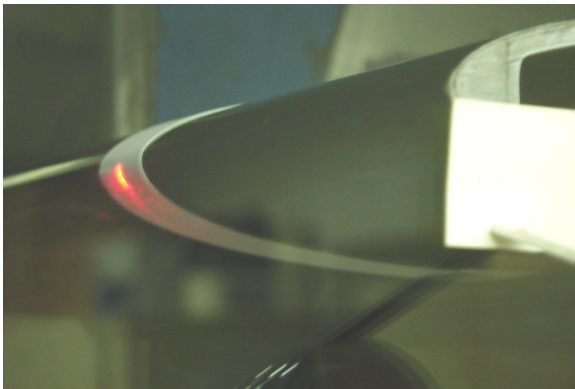


Figure 14.—Close-up of blotter strip installed NACA 0012 airfoil.

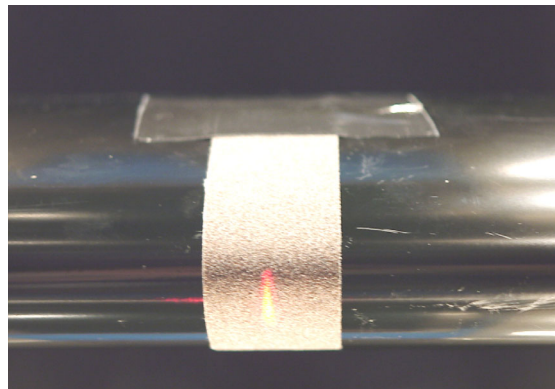


Figure 15.—Close-up of laser sheet on location with respect to airfoil leading edge.

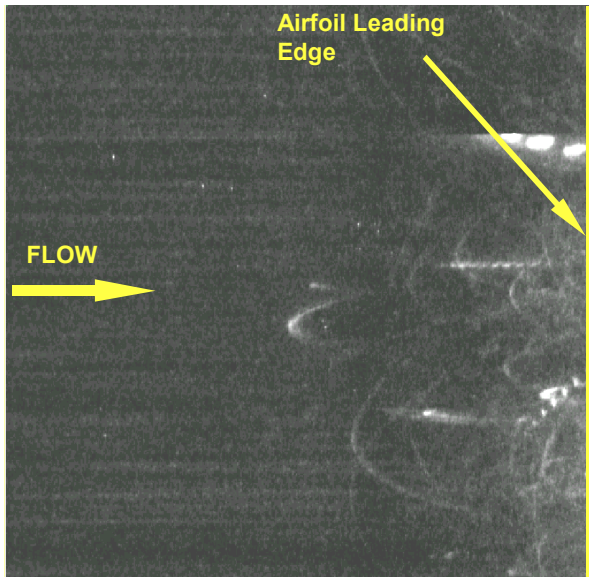


Figure 16.—NACA 0012 21-in chord Airfoil; Clean, Vfs = 175 mph, AOA = 0°, MVD = 94 μm (FN: C2_175m94 frame 3).

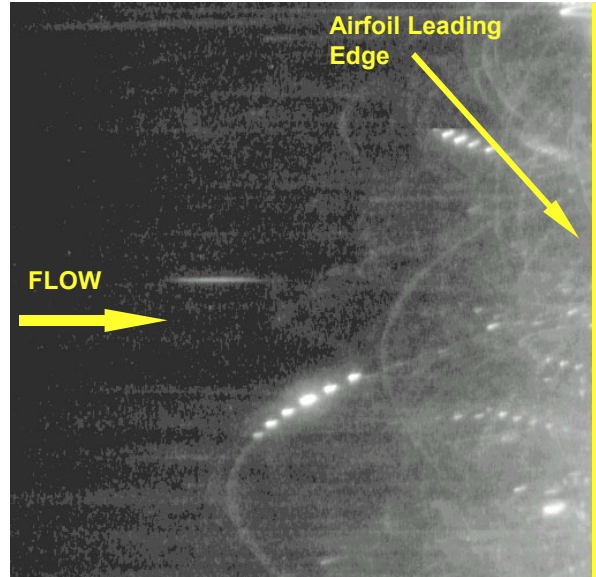


Figure 17.—NACA 0012 21-in chord Airfoil; Clean, Vfs = 175 mph, AOA = 0°, MVD = 270 μm (FN: C175M270 frame 10).

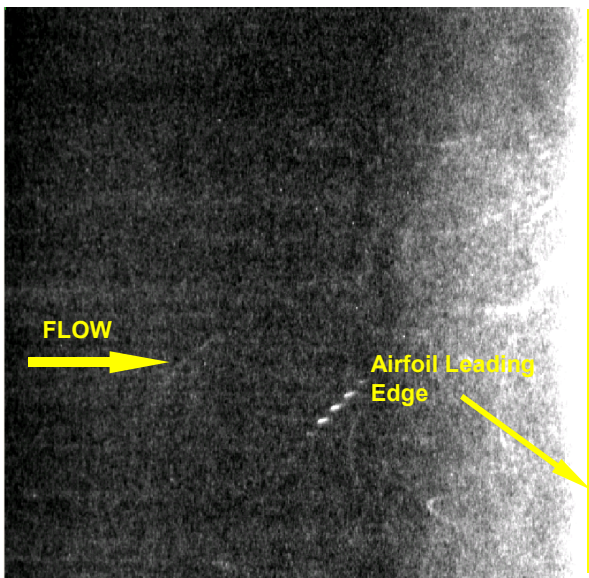


Figure 18.—NACA 0012 21-in chord Airfoil; Airfoil with blotter paper, Vfs = 150 mph, AOA = 0°, MVD = 94 μm (FN: b4b150m94 frame 11).

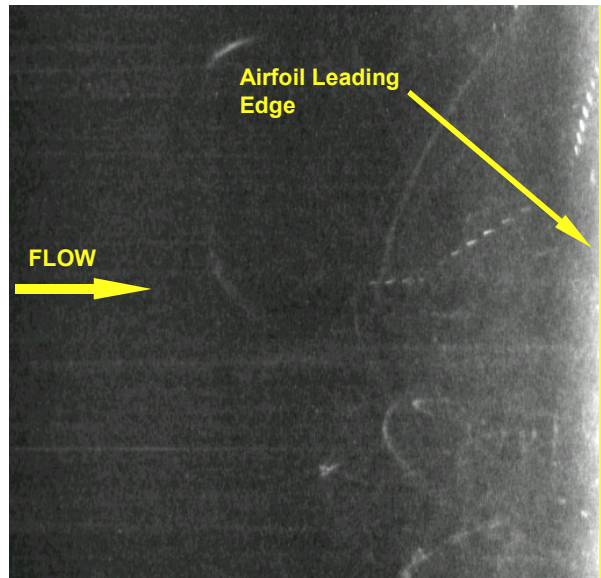


Figure 19.—NACA 0012 21-in chord Airfoil; Airfoil with blotter paper, Vfs = 150 mph, AOA = 0°, MVD = 270 μm (FN: b2b150a2w24b frame 9).

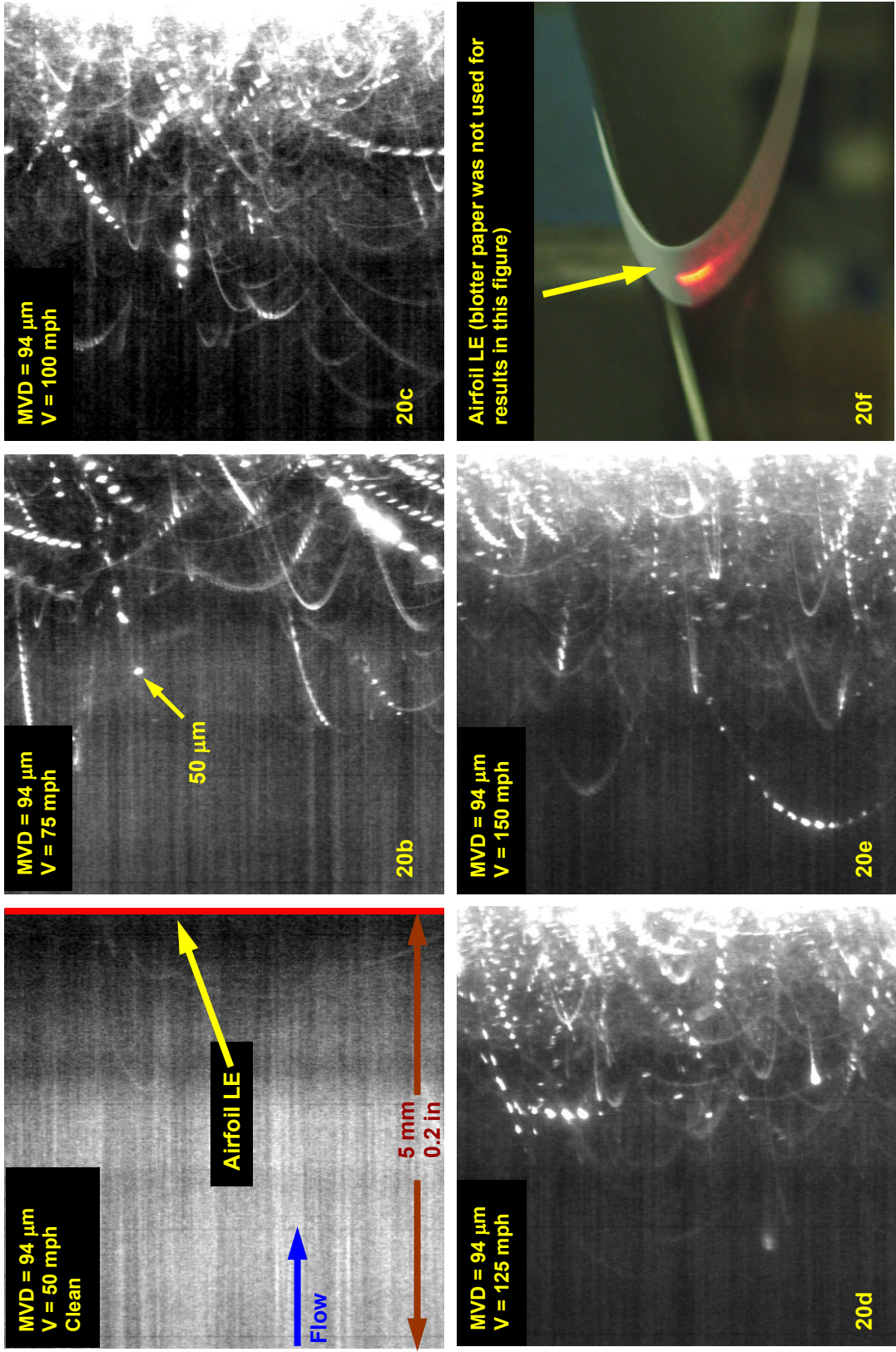


Figure 20.—NACA 0012 21-in chord Airfoil; Clean, AOA = 0°, MVD = 94 μm, composite of multiple images.

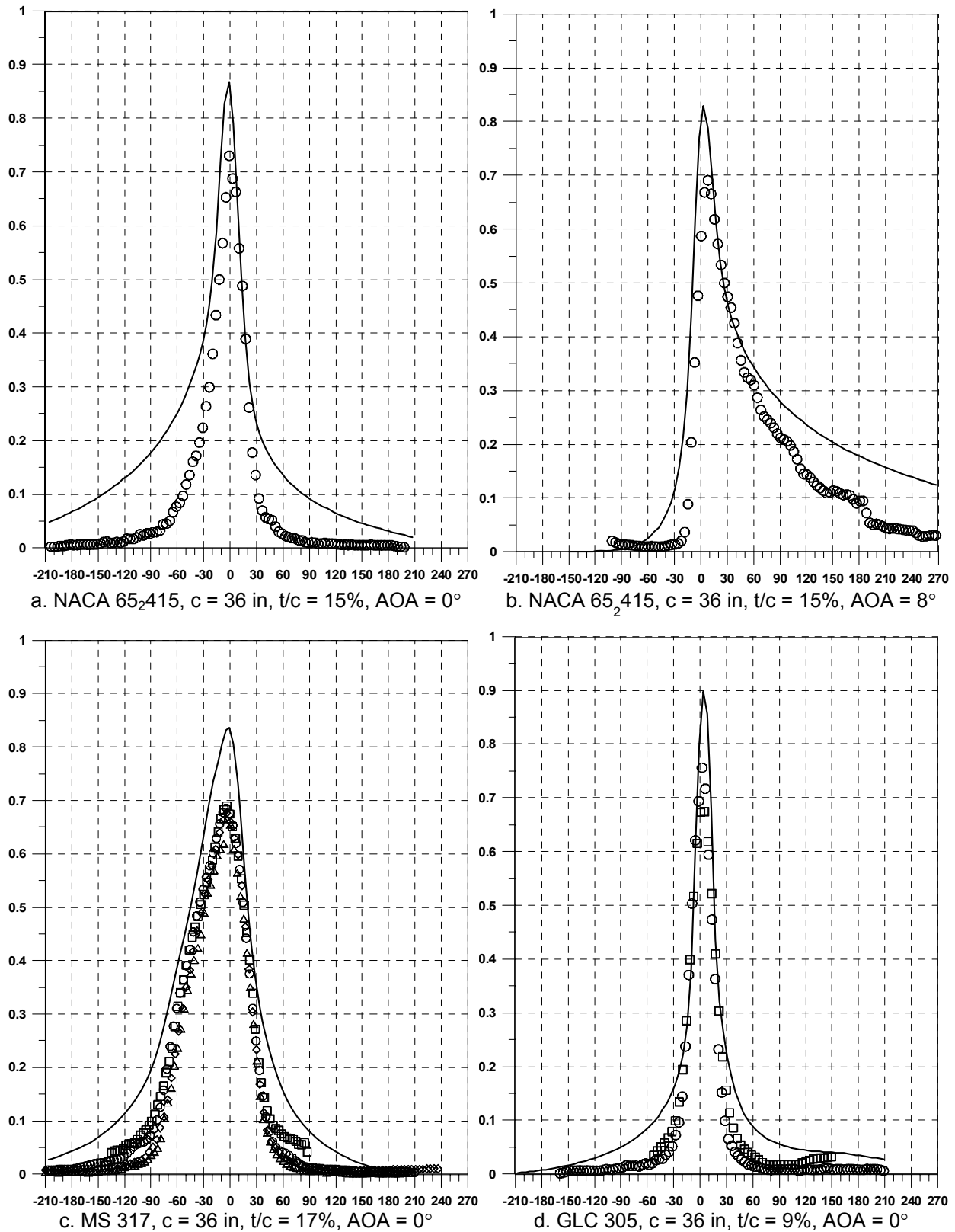


Figure 21.—Comparison of experimental and LEWICE impingement efficiency data; horizontal axis is surface distance in mm, MVD = 94 μ m, V = 175 mph; symbols: experimental; solid: LEWICE (from ref. 1).

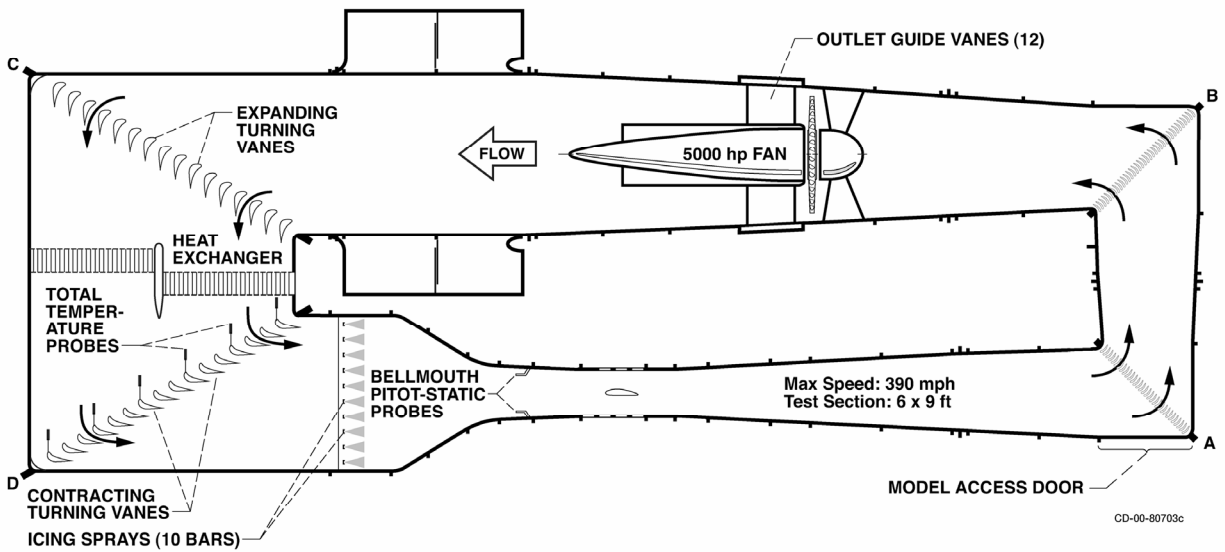


Figure 22.—Plan view of NASA Glenn Icing Research Tunnel (IRT).

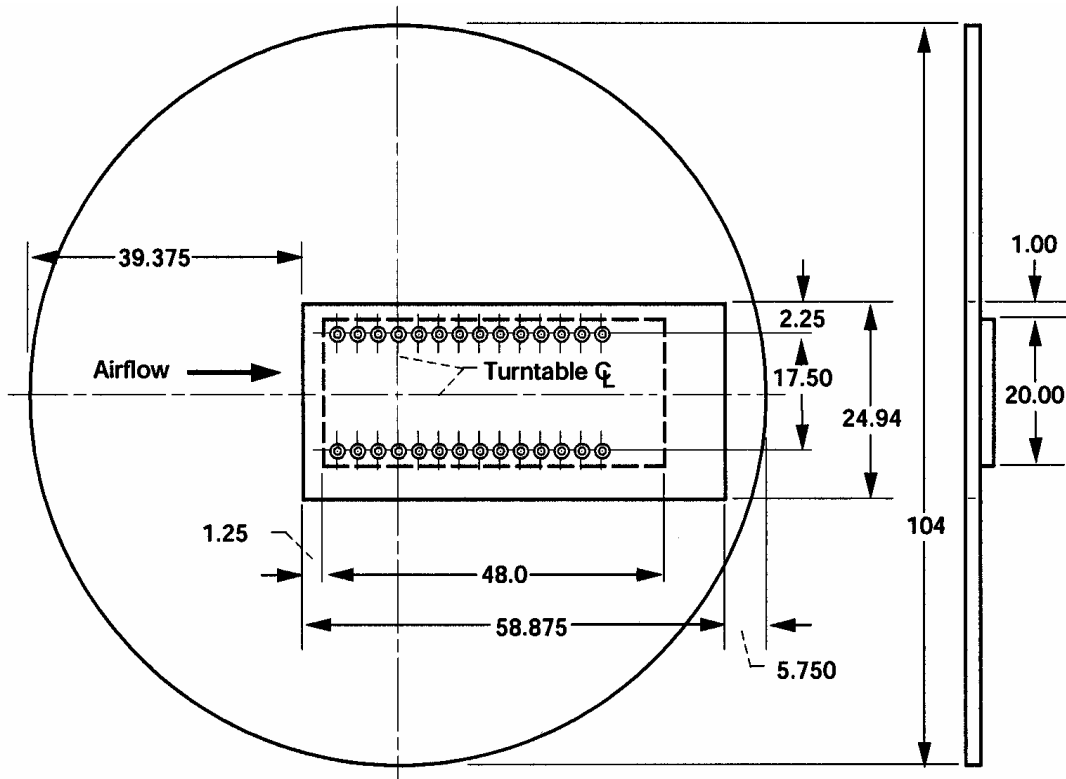


Figure 23.—Icing Research Tunnel turntable and model mounting plate (all dimensions are given in inches).

Water tube diameter of an IRT nozzle:
 Standard Nozzle – 0.025 in.
 Mod-1 Nozzle – 0.015 in.

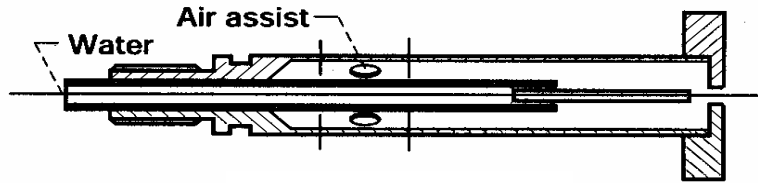


Figure 25.—Schematic of an IRT spray nozzle.

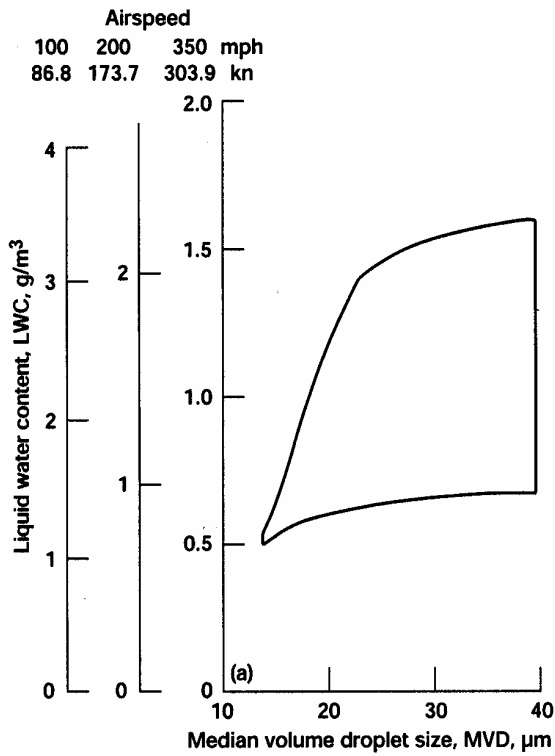


Figure 26.—IRT icing cloud operating envelopes for standard nozzles.

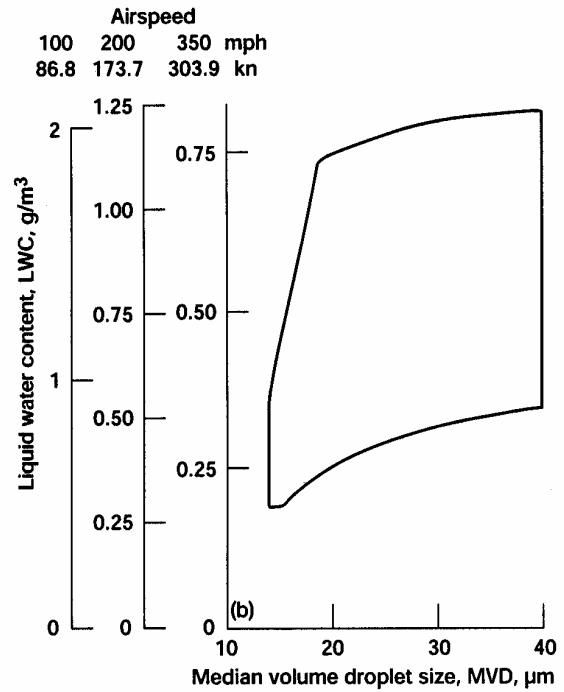


Figure 27.—IRT icing cloud operating envelopes for MOD-1 type nozzles.

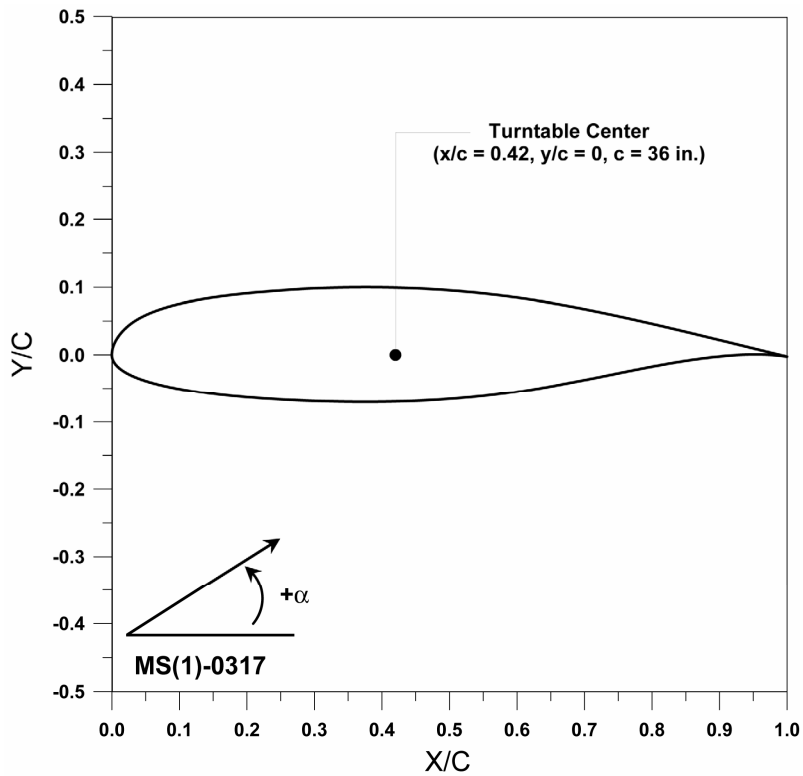


Figure 28a.—MS(1)-0317 airfoil section.

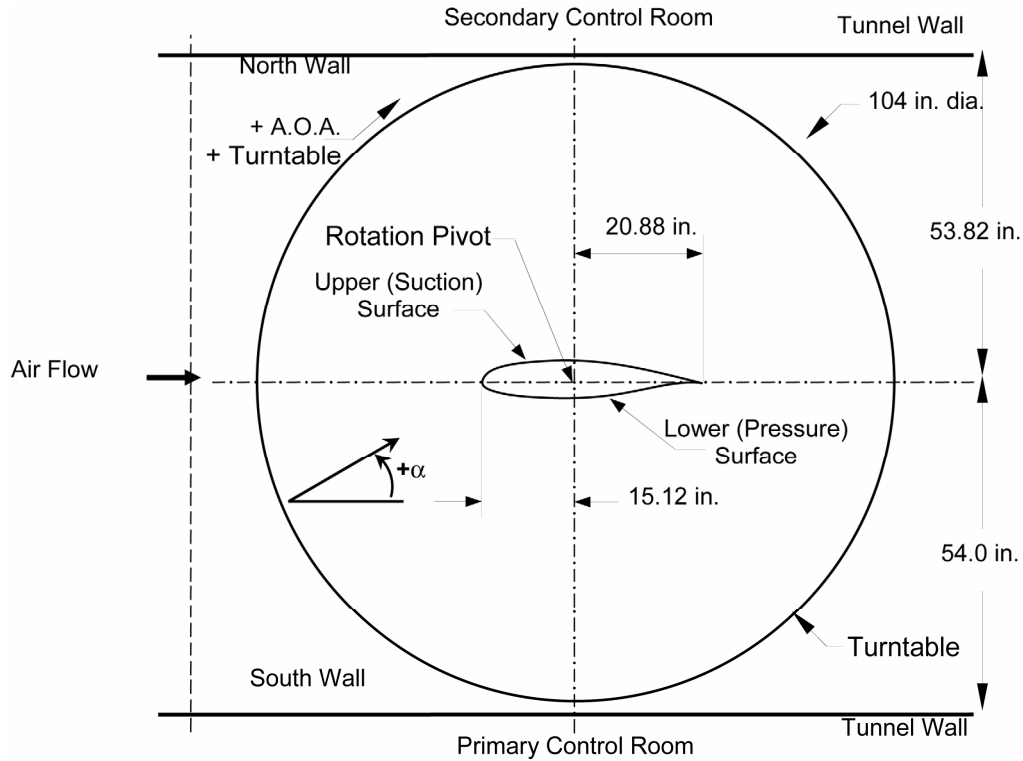


Figure 28b.—MS(1)-0317 airfoil installation in IRT test section (top view).



Figure 28c.—MS(1)–0317 airfoil installed in IRT test section.

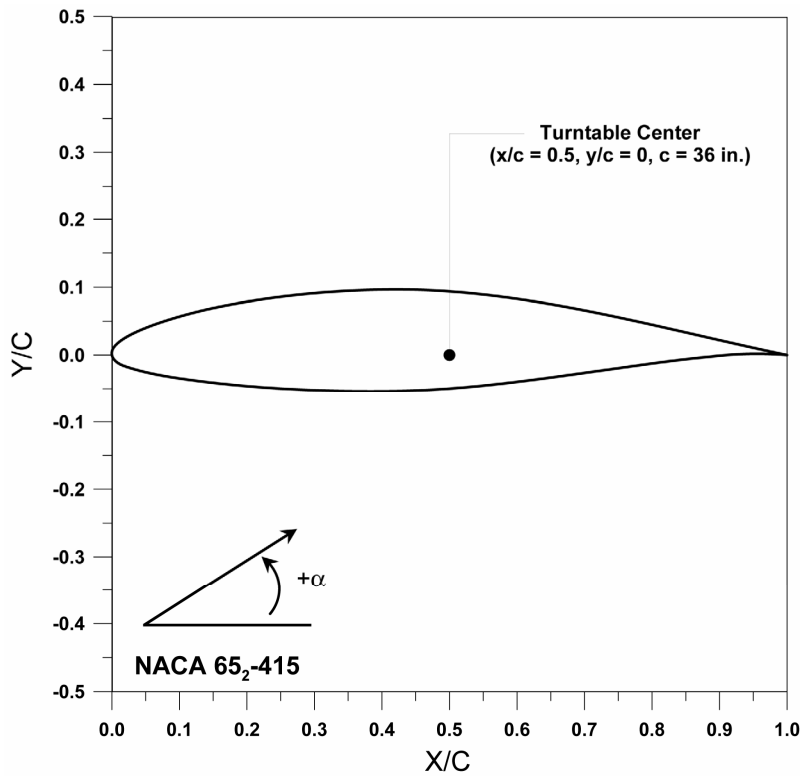


Figure 29a.—NACA 65₂-415 airfoil section.

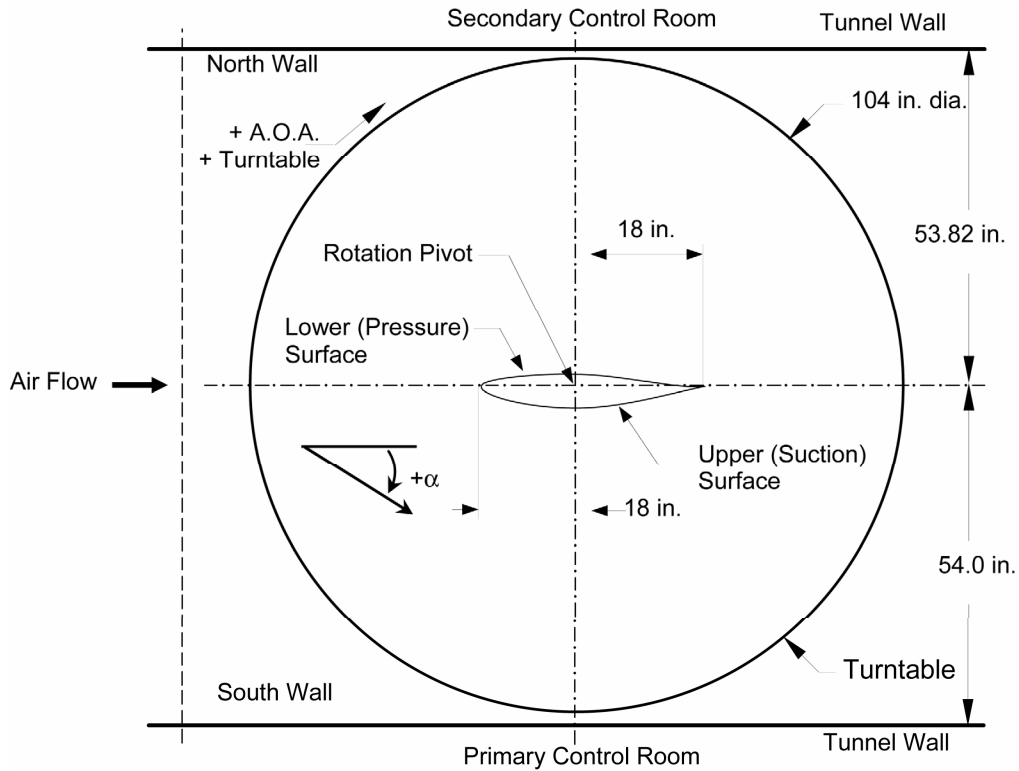


Figure 29b.—NACA 65₂-415 airfoil installation in IRT test section (top view).



Figure 29c.—NACA 65₂-415 airfoil installed in IRT test section.

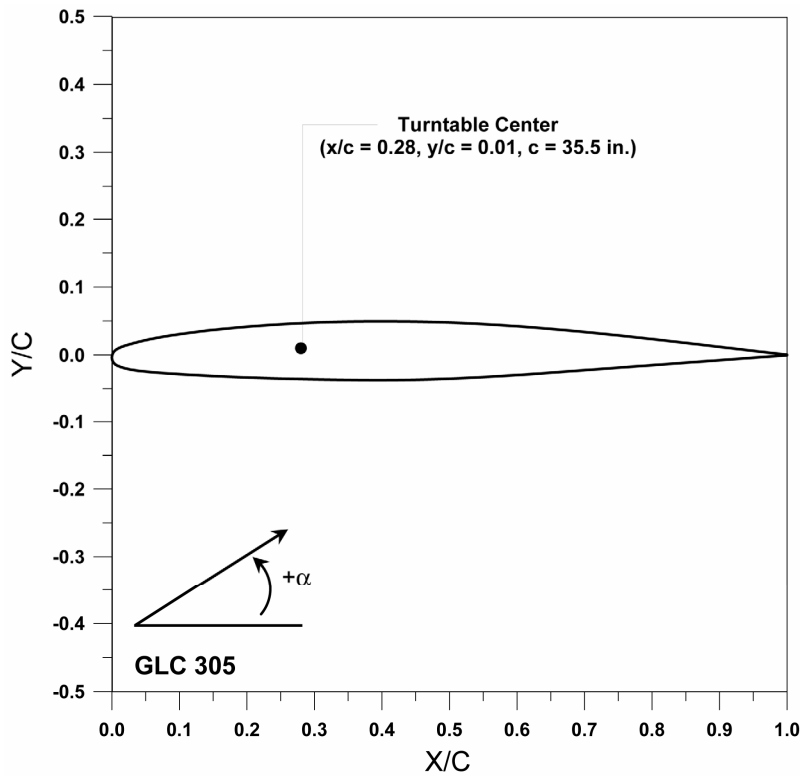


Figure 30a.—GLC-305 airfoil section.

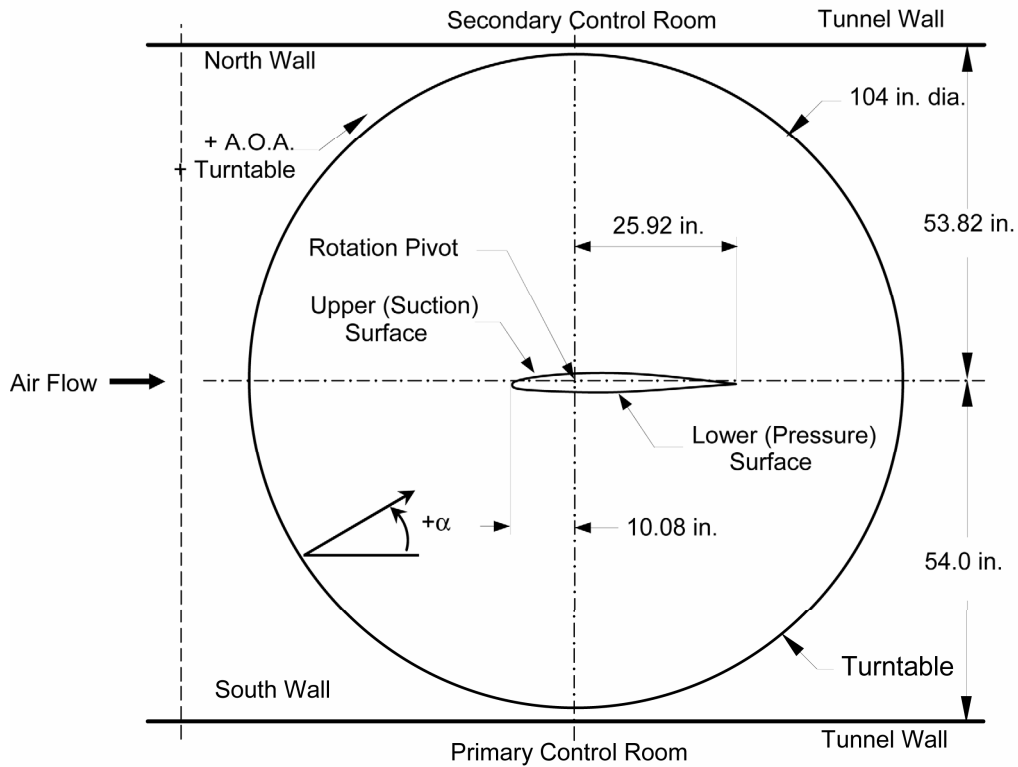


Figure 30b.—GLC-305 airfoil installation in IRT test section (top view).

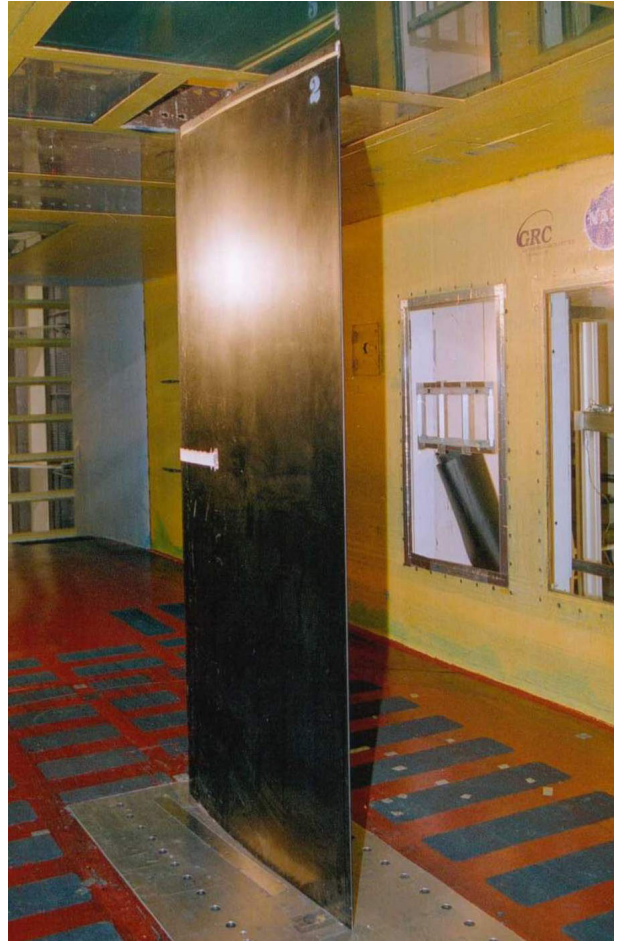


Figure 30c.—GLC 305 airfoil installed in IRT test section.

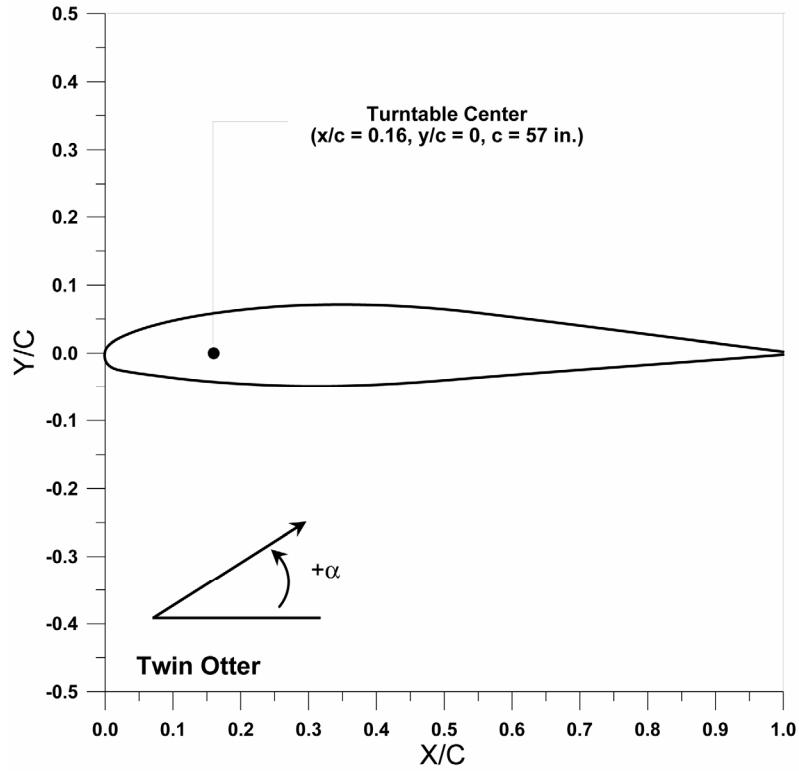


Figure 31a.—Twin Otter tail airfoil section.

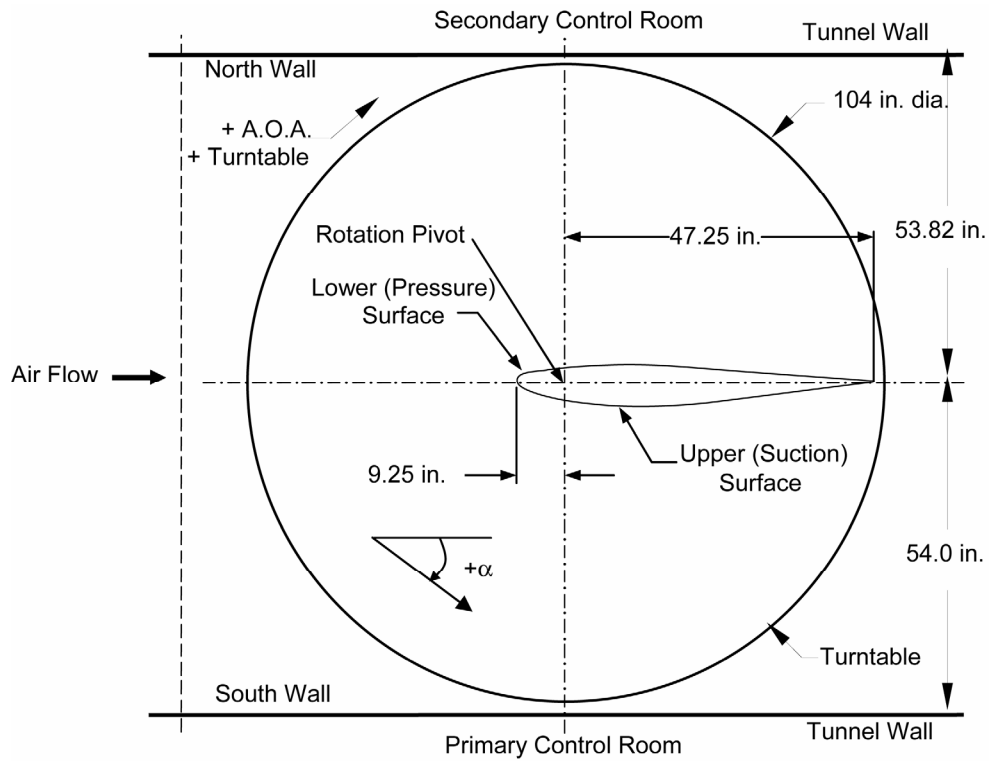


Figure 31b.—Installation of Twin Otter tail section in IRT test section (top view).



Figure 31c.—Twin Otter tail installed in IRT test section.

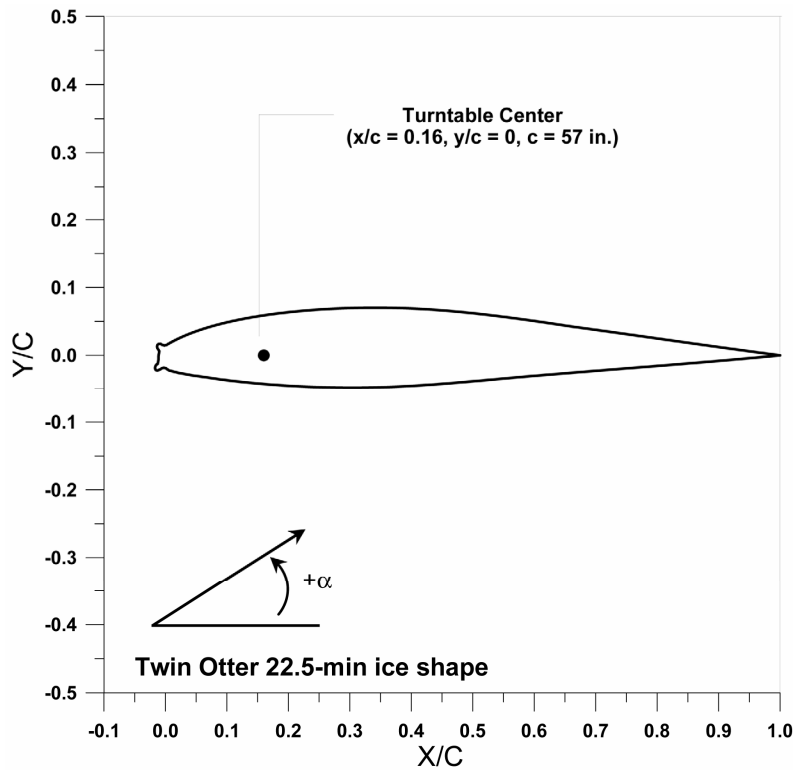


Figure 32a.—Twin Otter tail with 22.5-min ice shape.

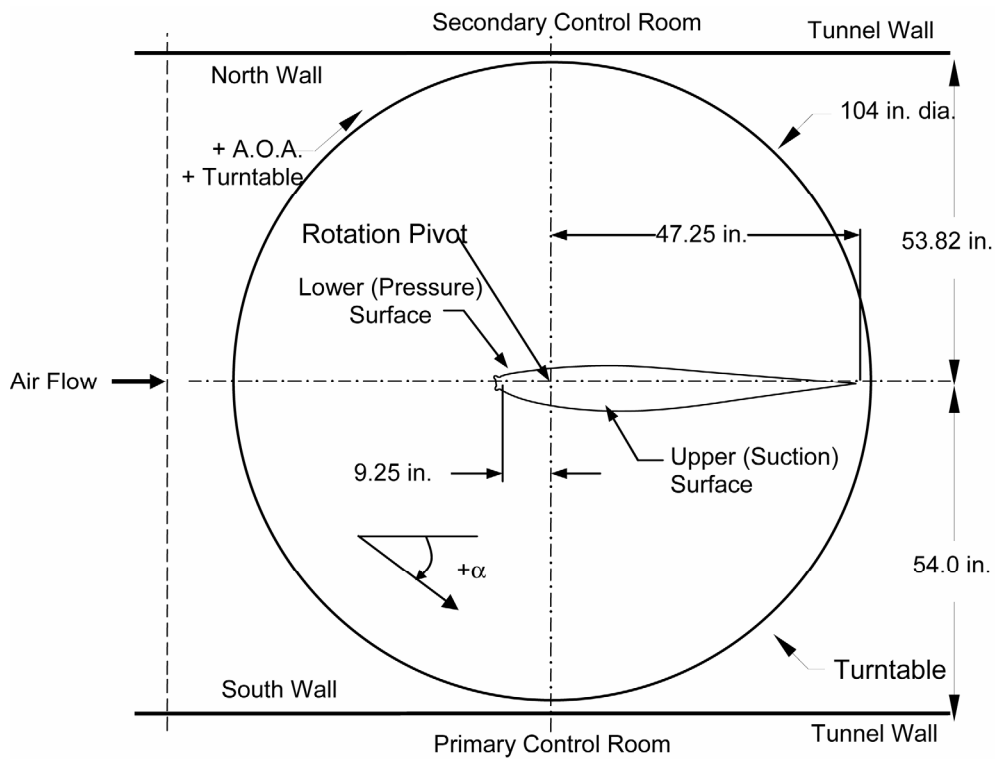


Figure 32b.—Twin Otter tail with 22.5-min ice shape installation in IRT test section (top view).



Figure 32c.—Twin Otter tail with 22.5-min ice shape installed in IRT test section.

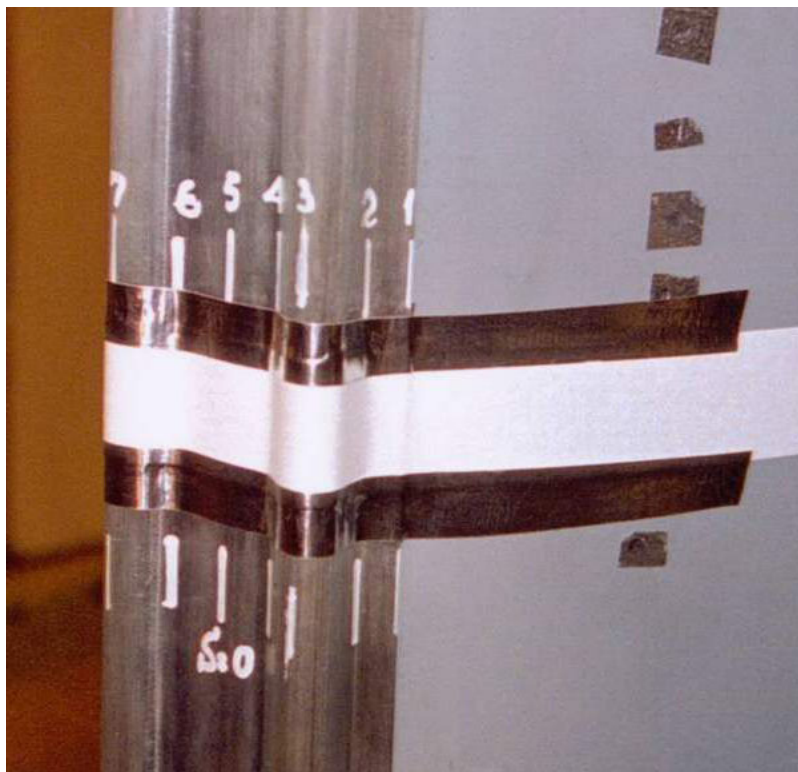
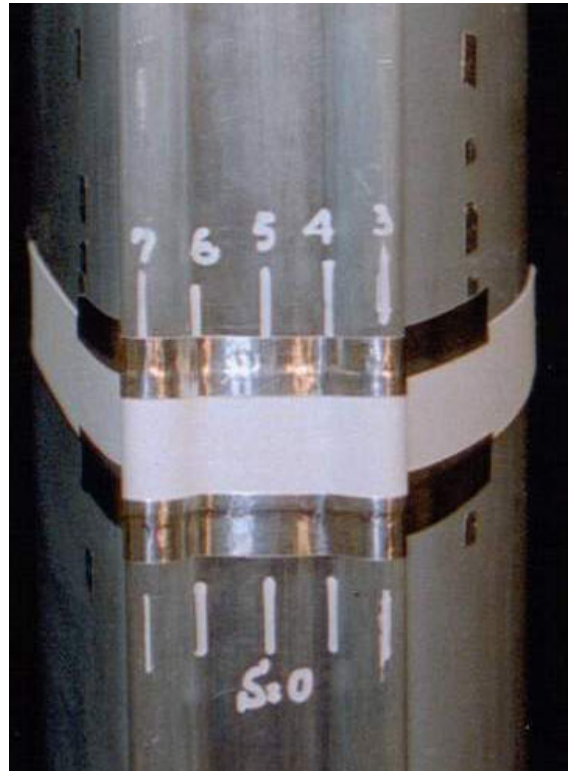


Figure 32d.—Different views of Twin Otter tail and 22.5-min ice shape in IRT test section.

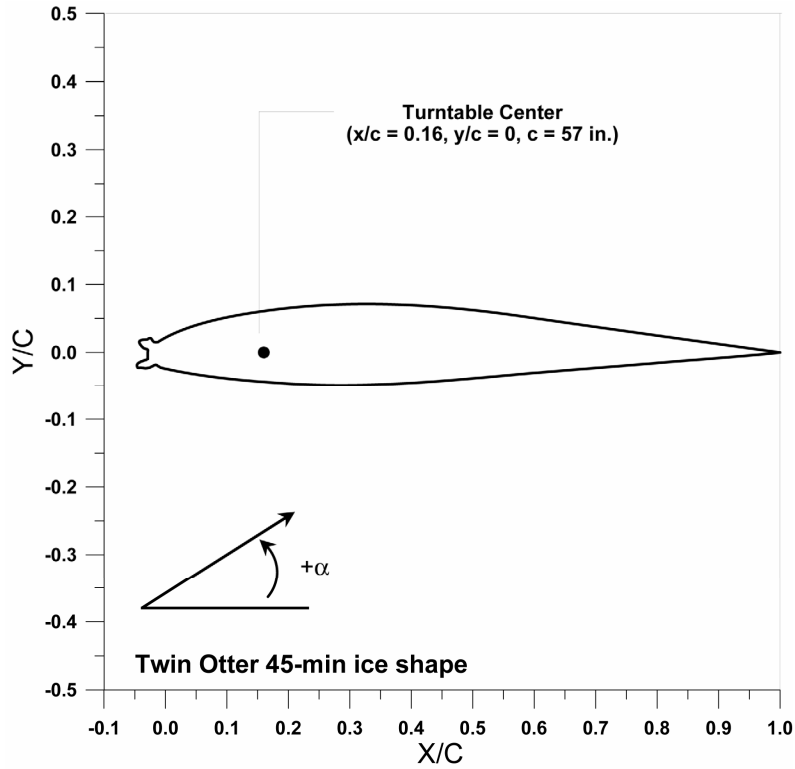


Figure 33a.—Twin Otter tail with 45-min ice shape.

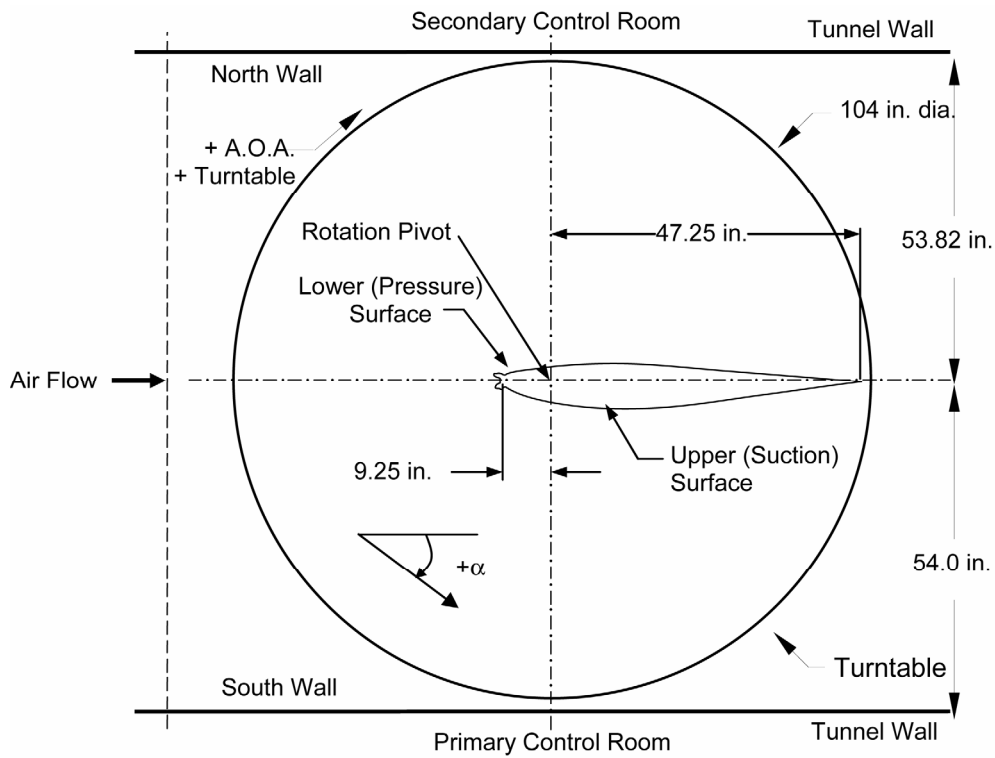


Figure 33b.—Twin Otter tail with 45-min ice shape installation in IRT test section (top view).

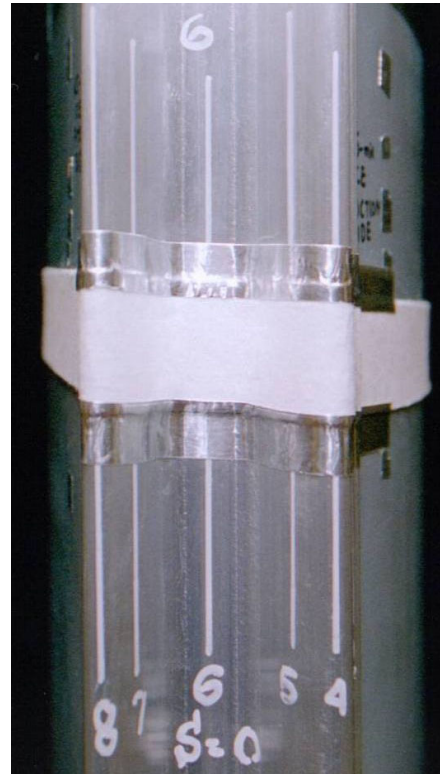


Figure 33c.—Different views of Twin Otter tail and 45-min ice shape in IRT test section.

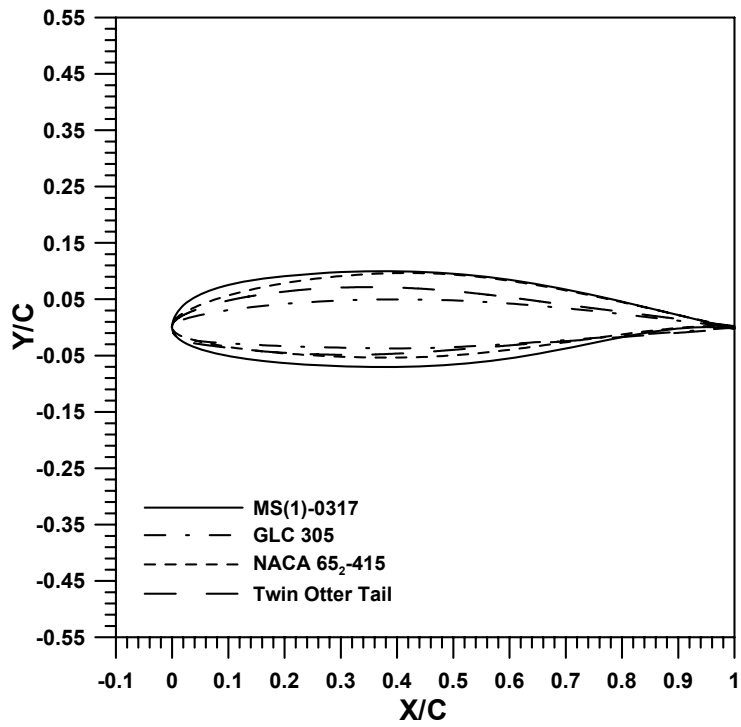


Figure 34.—Comparison of airfoil sections.

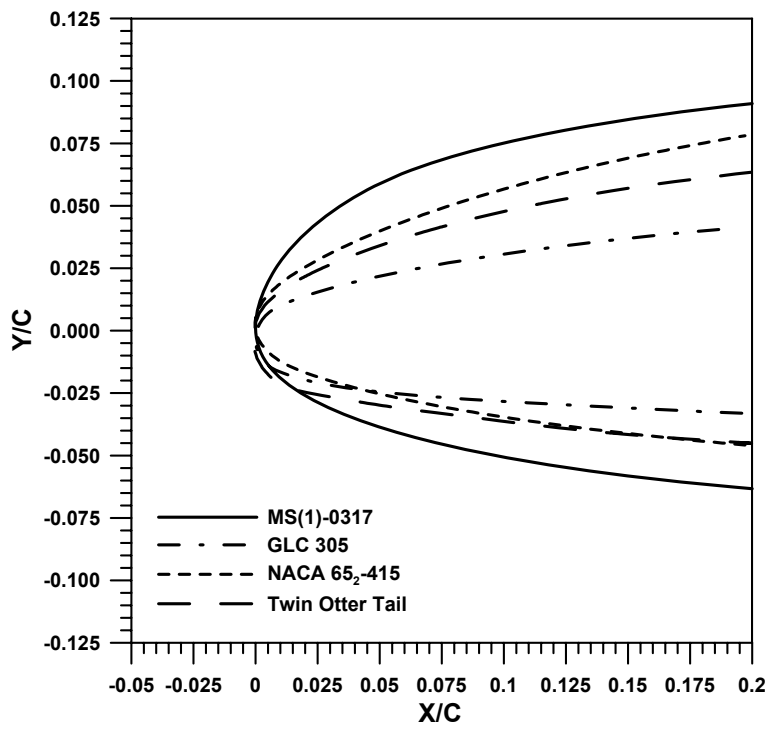


Figure 35.—Leading edge close-up of airfoil sections.

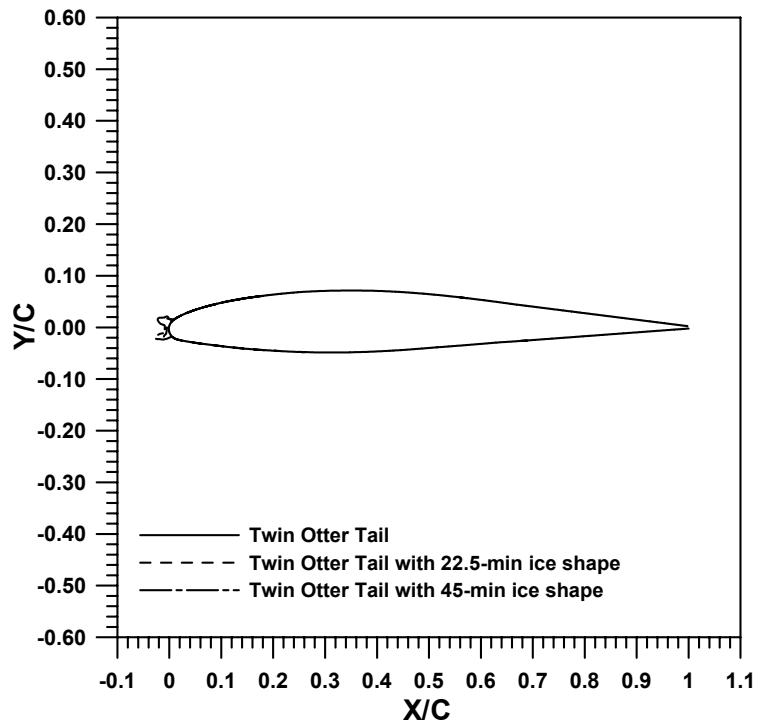


Figure 36.—Twin Otter airfoil section with 22.5- and 45-min ice shapes.

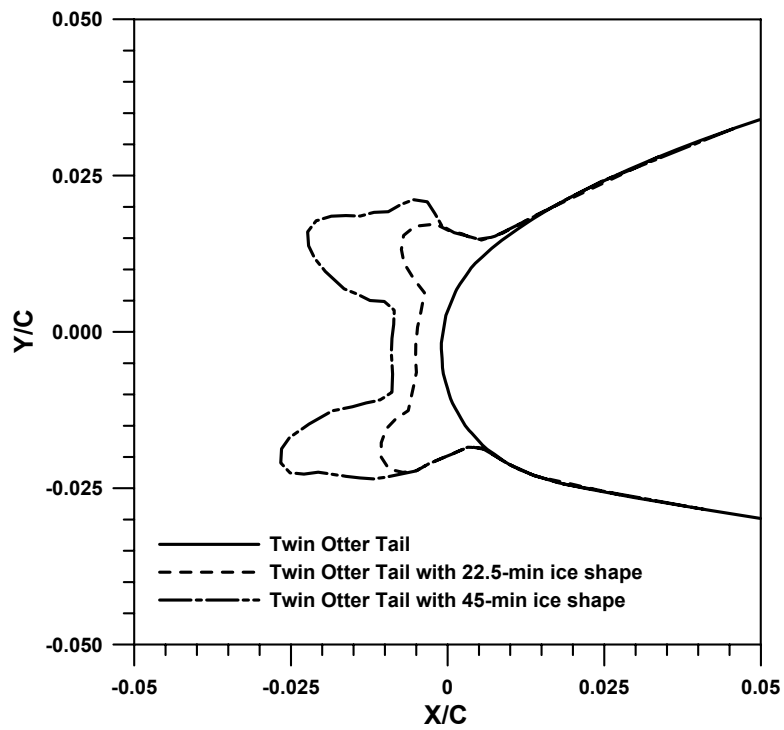


Figure 37.—Close-up of Twin Otter section leading edge and ice shape geometries.



Figure 38a.—WSU spray system installed in IRT plenum chamber.

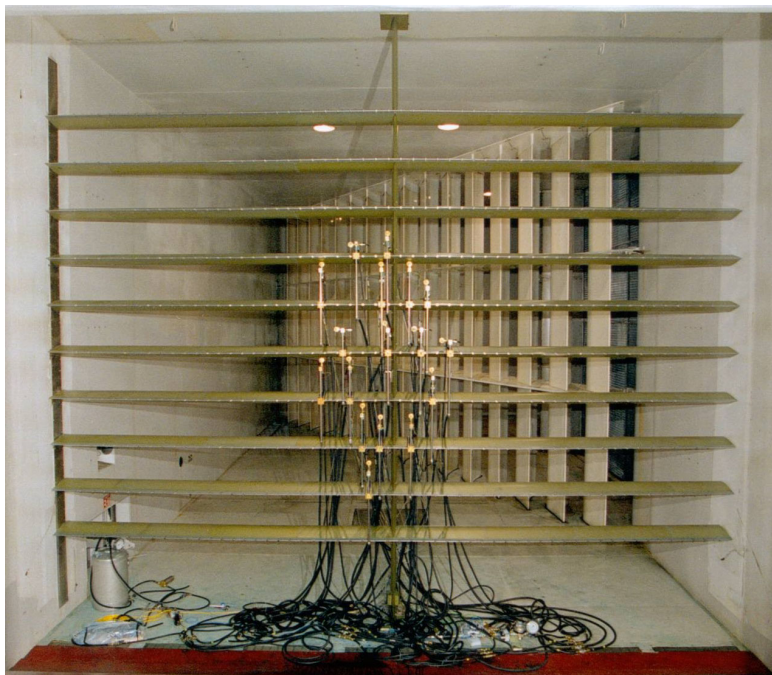
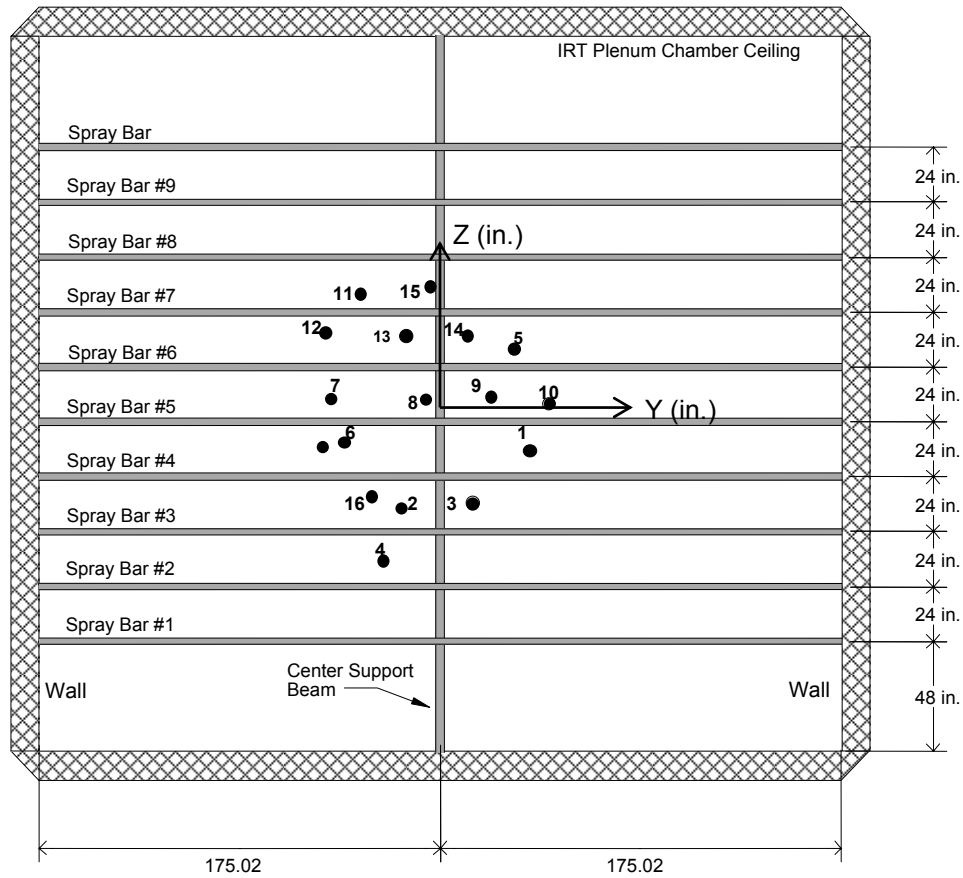


Figure 38b.—Downstream view of WSU spray system installed in IRT plenum chamber.



(2001 WSU spray system; all dimensions in inches)

WSU Nozzle Assembly no.	NASA MOD-1 Nozzle no.	C_f	Y-Coordinate (in.)	Z-Coordinates (in.)
1	277	0.00400	+19.000	+12.000/SP4
2	271	NA	-7.000	+11.500/SP3
3	234	0.00399	+8.500	+12.000/SP3
4	217	0.00398	-12.000	+12.000/SP2
5	308	0.00401	+16.125	+8.500/SP6
6	243	0.00401	-21.250	+17.250/SP4
7	300	NA	-24.250	+11.750/SP5
8	233	0.00400	-3.500	+11.500/SP5
9	242	0.00401	+12.750	+12.000/SP5
10	311	0.00406	+27.000	+6.000/SP5
11	249	0.00401	-18.000	+6.000/SP7
12	252	0.00403	-34.750	+17.500/SP6
13	269	NA	-6.500	+17.500/SP6
14	227	NA	+7.250	+17.750/SP6
15	268	NA	-3.000	+9.000/SP7
16	203	NA	-15.125	+17.250/SP3
17		NA	-34.75	+16.500/SP4

Figure 39.—WSU spray system nozzle locations with respect to the IRT spray bars (2001 IRT Entry).

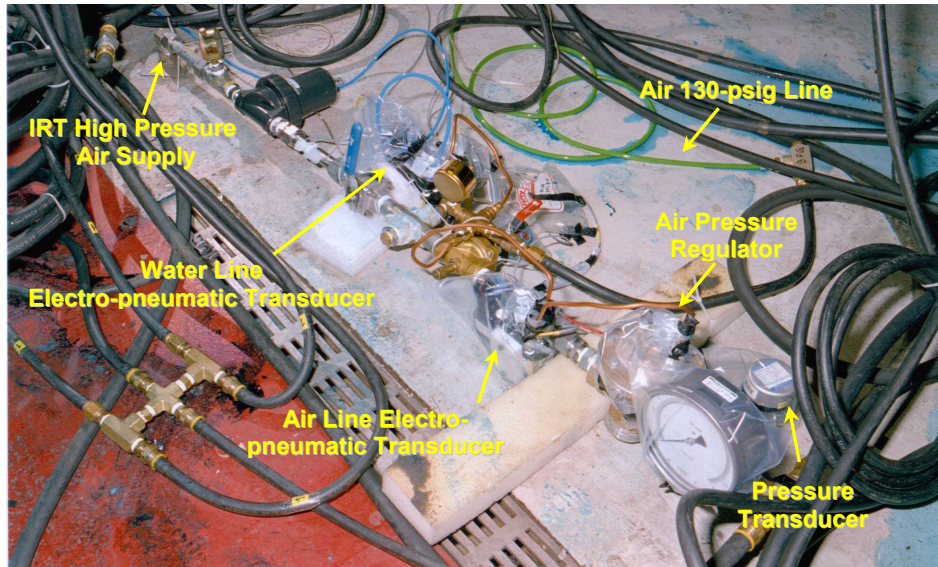


Figure 40.—Main air supply control system for WSU spray nozzles.

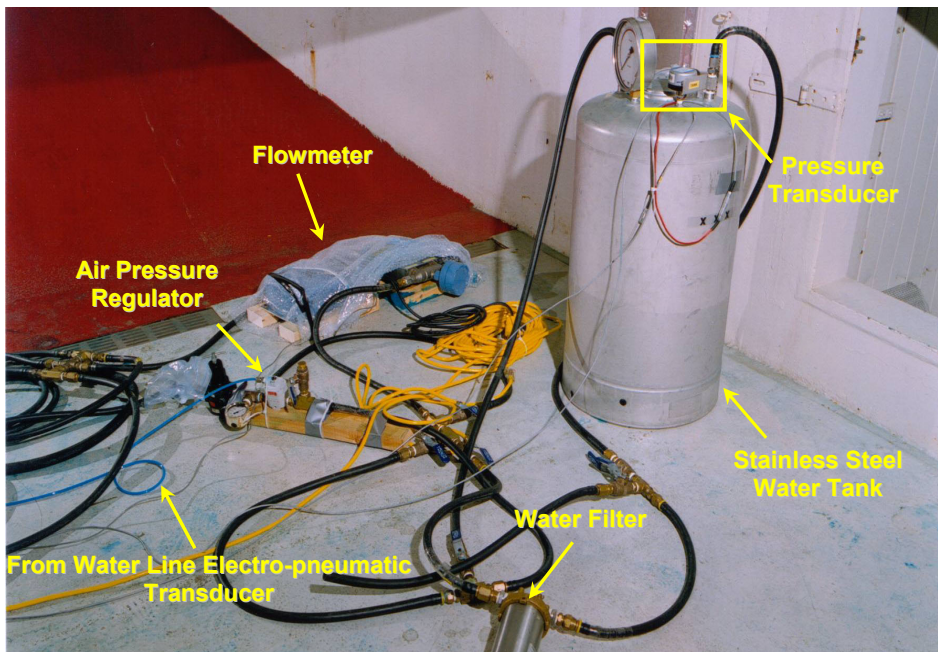


Figure 41.—Water supply tank and the water line system.

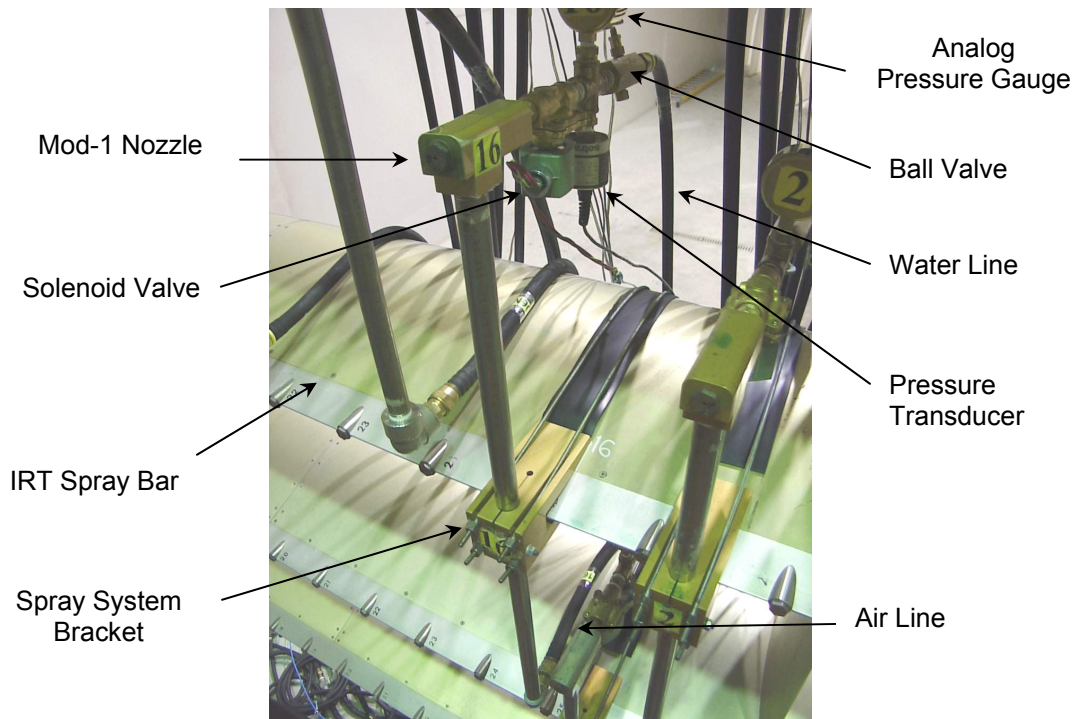


Figure 42.—Components of Nozzle Assembly.

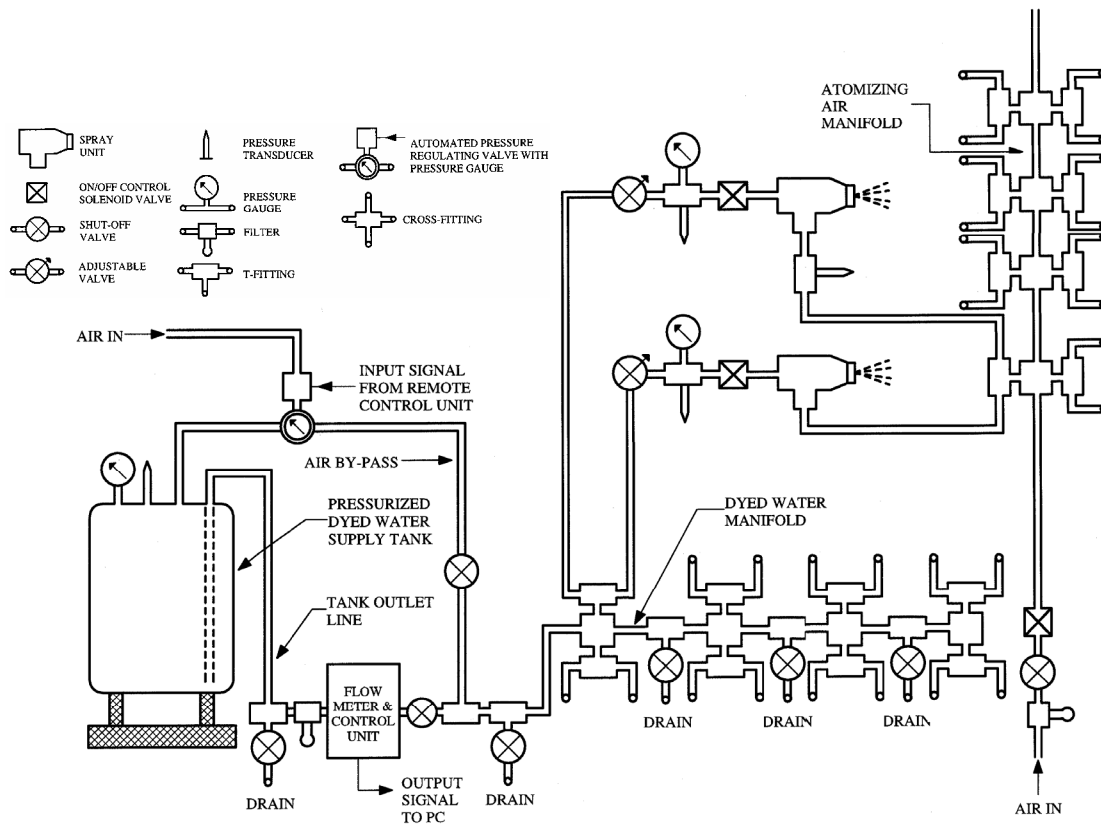


Figure 43.—Schematic of the new WSU 16-nozzle spray system.

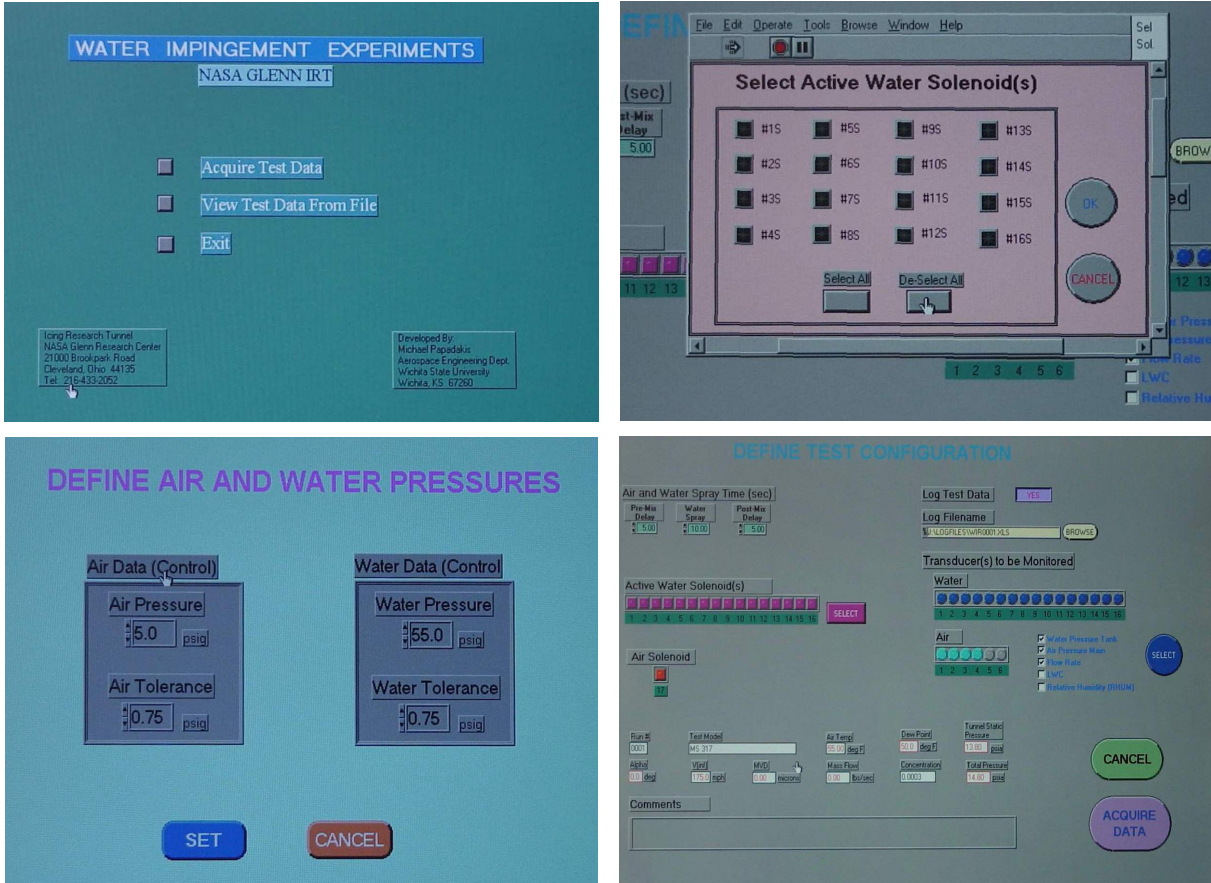


Figure 45a.—LabVIEW windows developed to control the spray system.

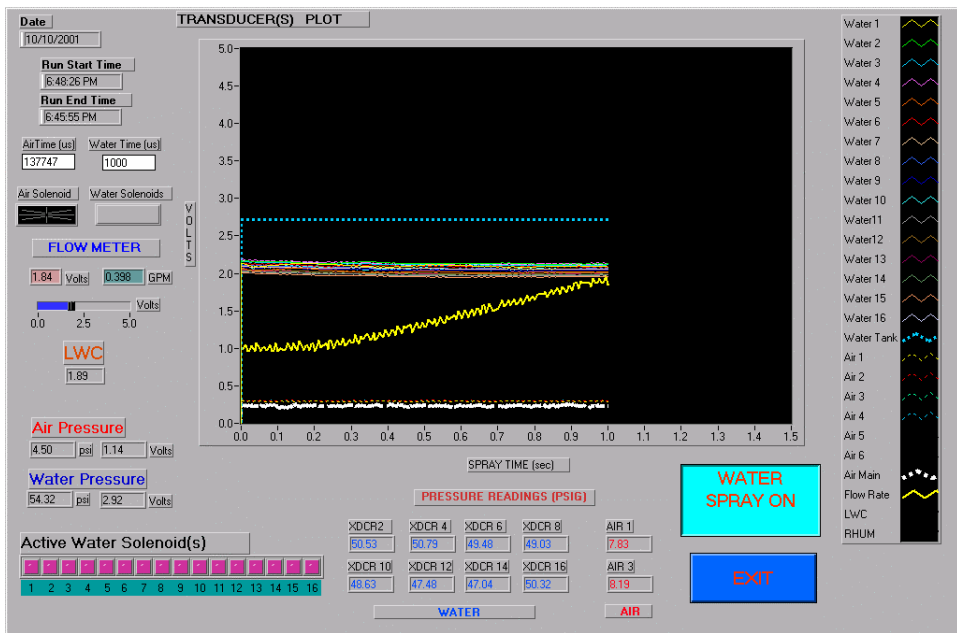


Figure 45b.—Typical spray system performance monitored in LabVIEW.



Figure 46.—6-ft by 6-ft grid installed in the IRT test section.

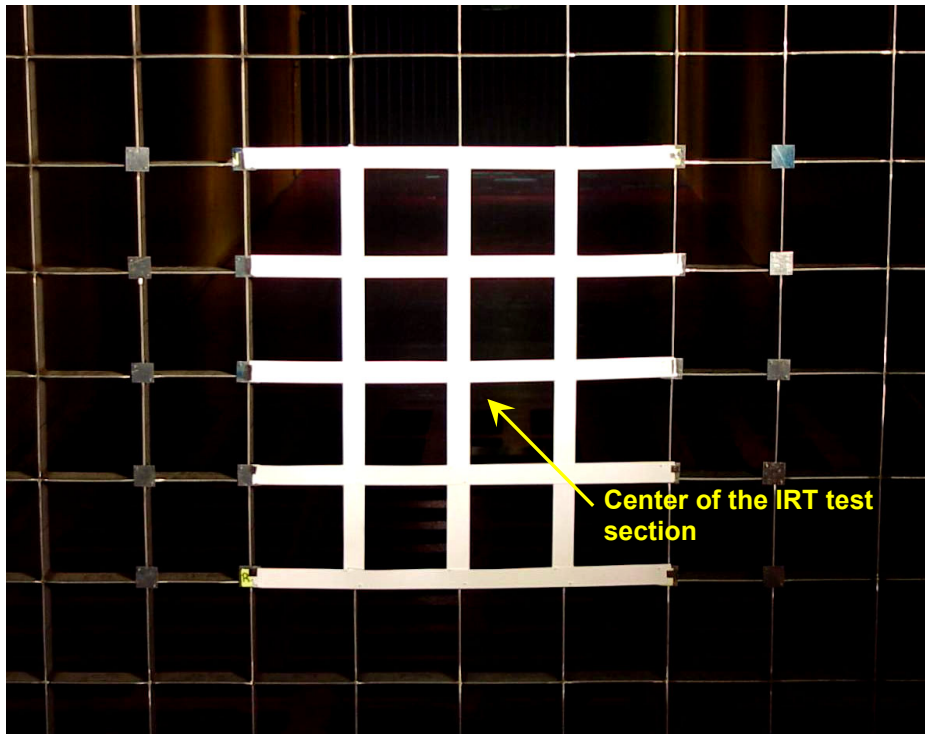


Figure 47.—Blotter strips attachment on the 6-ft by 6-ft grid.



Figure 48a.—Argon-Ion laser emission.

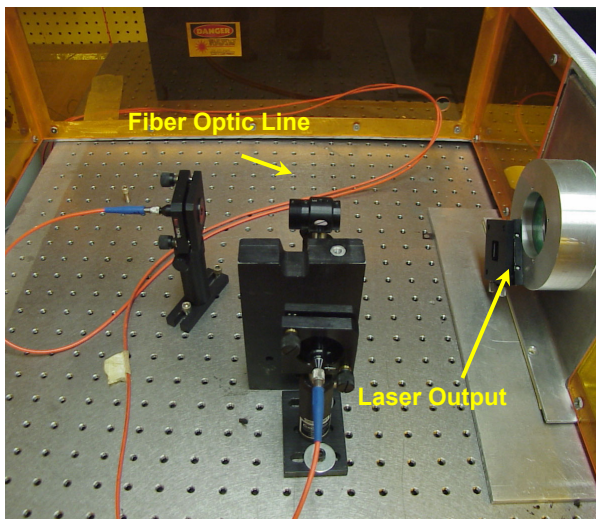


Figure 48b.—Close-up of the laser head setup.

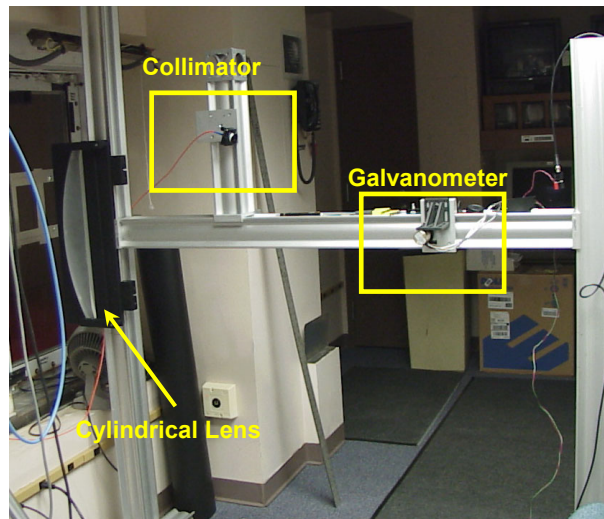


Fig 48c.—Laser Sheet generator setup.



Figure 48d.—Close-up of the Collimator.

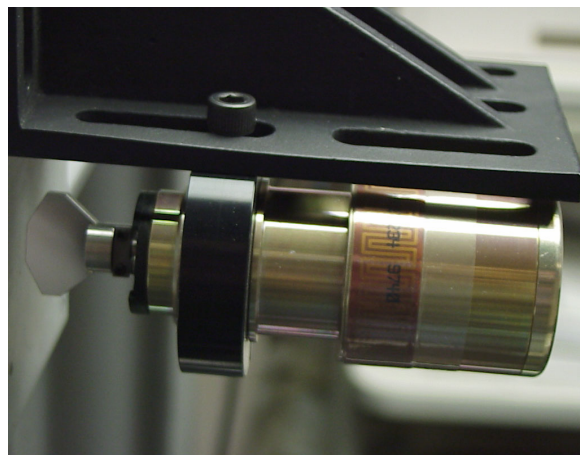


Fig 48e.—Close-up of the Galvanometer.

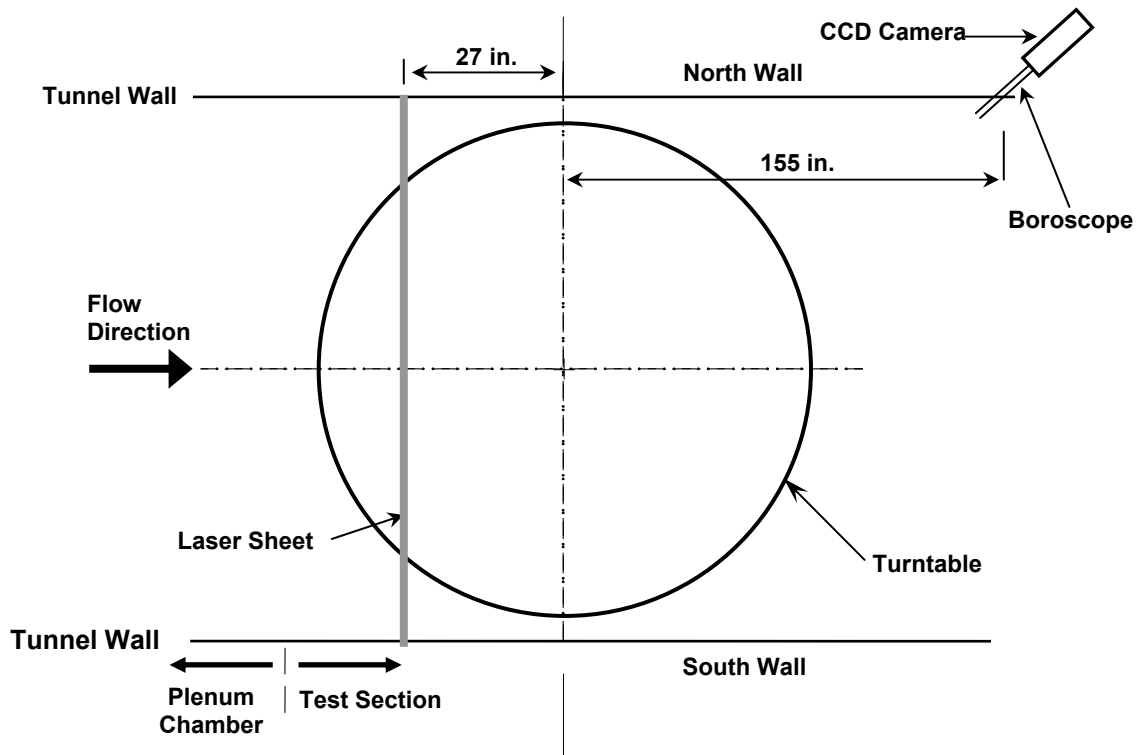


Figure 49a.—Laser sheet and CCD camera axial locations in IRT test section.

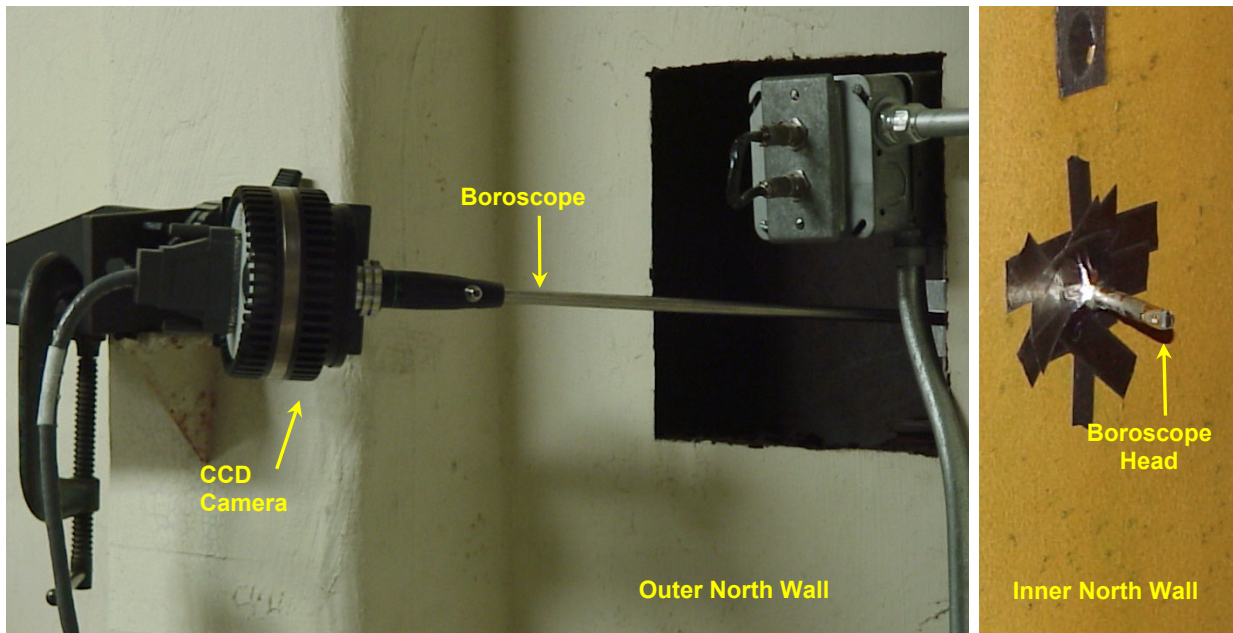


Figure 49b.—CCD camera installation in the IRT.

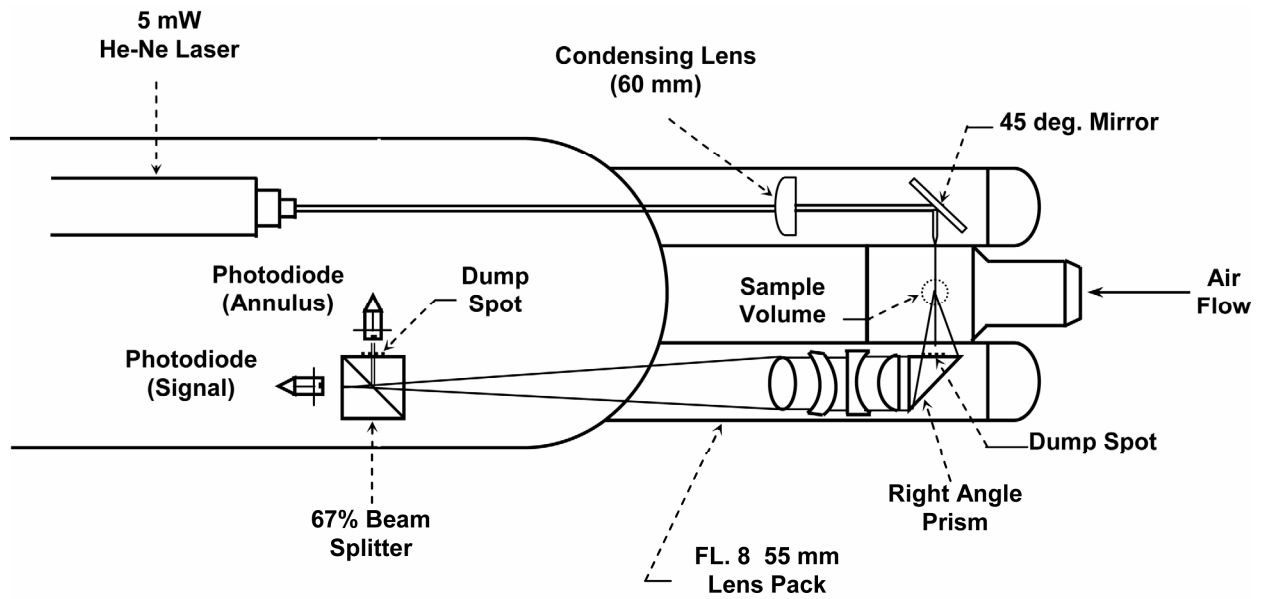


Figure 50a.—Forward Scattering Spectroscopy Probe (FSSP) optical configuration.



Figure 50b.—FSSP installed in the IRT test section.

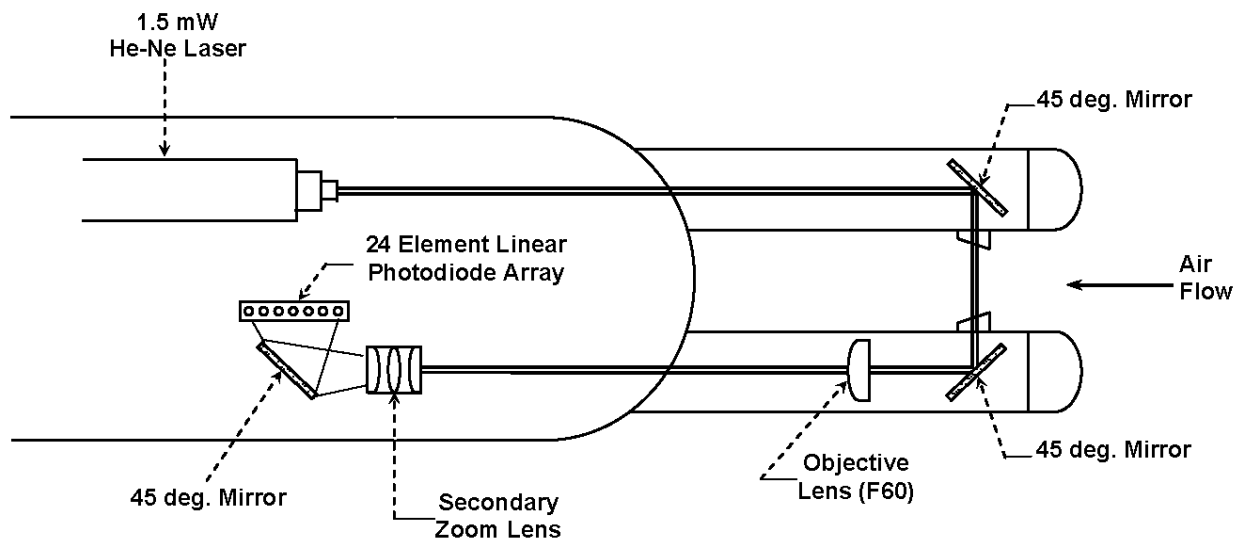


Figure 51a.—Optical Array Probe (OAP) configuration.

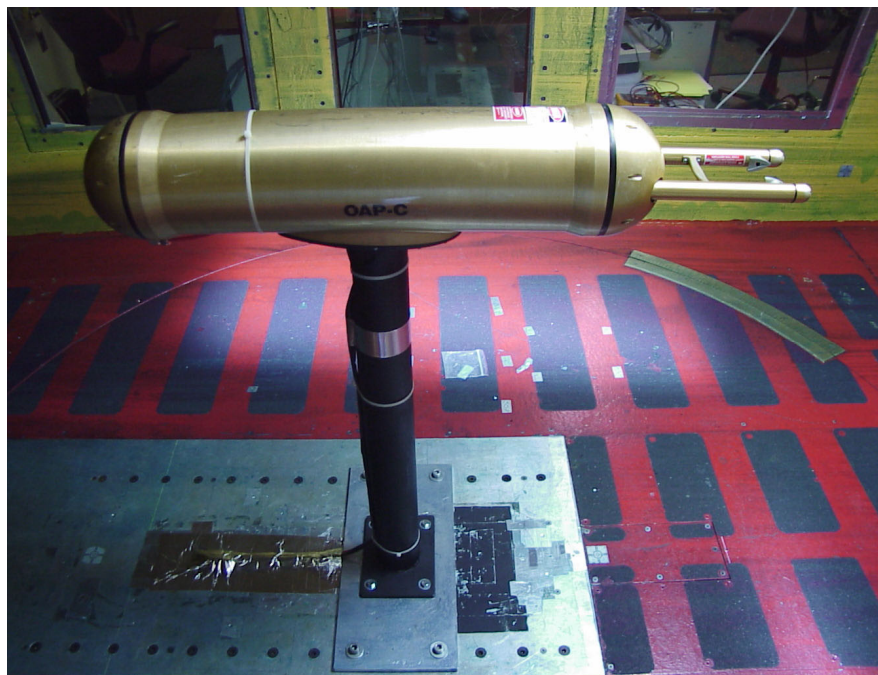


Figure 51b.—OAP-C installed in IRT test section.



Figure 51c.—OAP-Y installed in the IRT test section.



Figure 51d.—OAP-Y (looking upstream).



Figure 52a.—King Probe installed in the IRT test section.

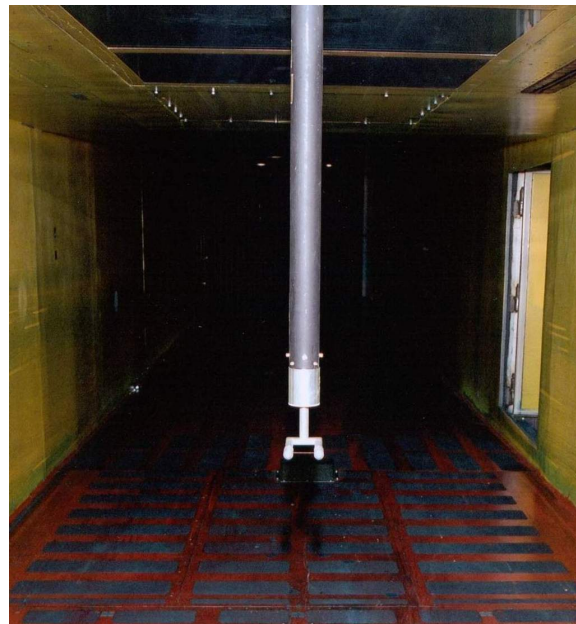


Figure 52b.—King Probe (looking downstream).

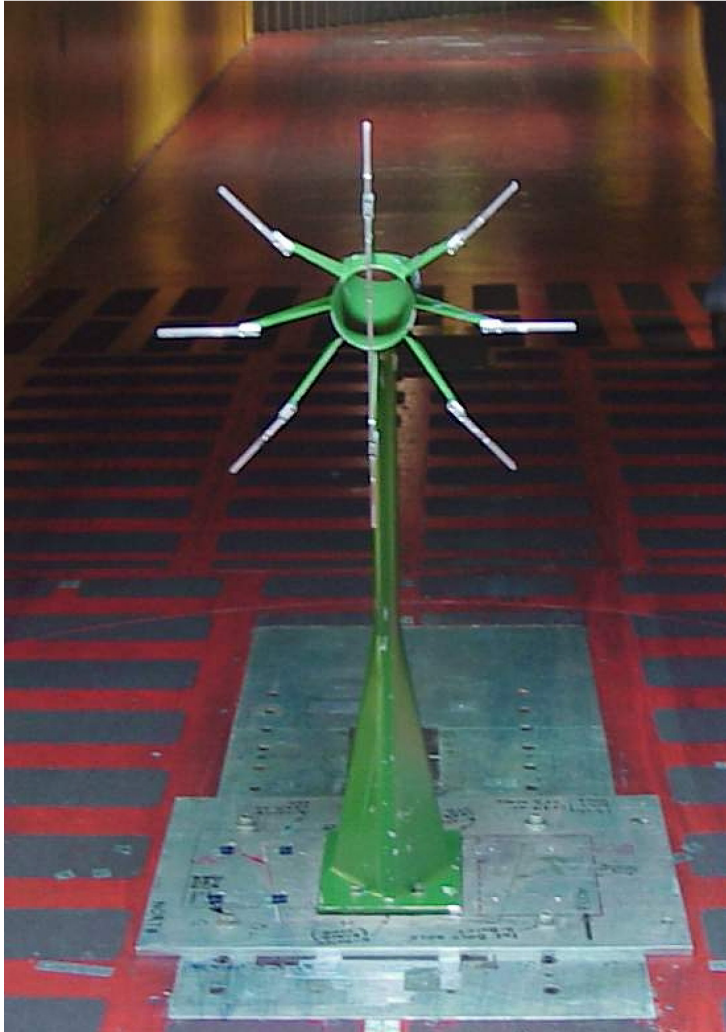


Figure 53a.—Collector mechanism installed in IRT test section.

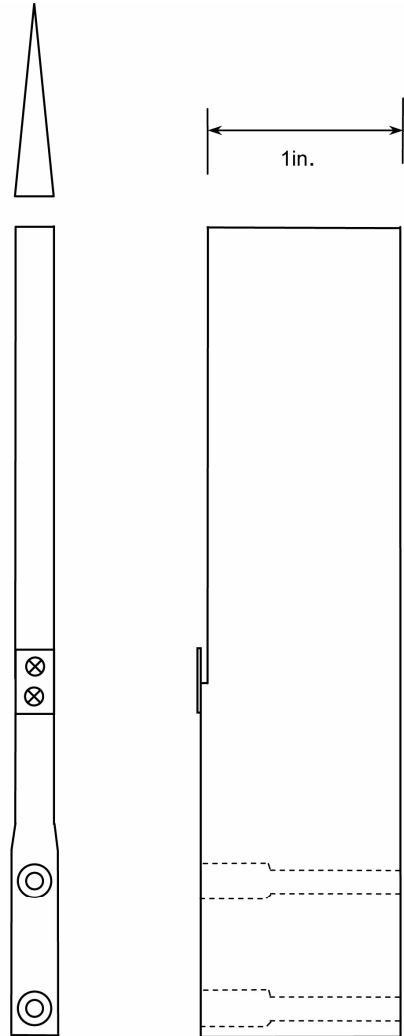


Figure 53b.—Collector blade geometry (not to scale).



Figure 54.—Location of blotter strip on airfoil and collector blade.

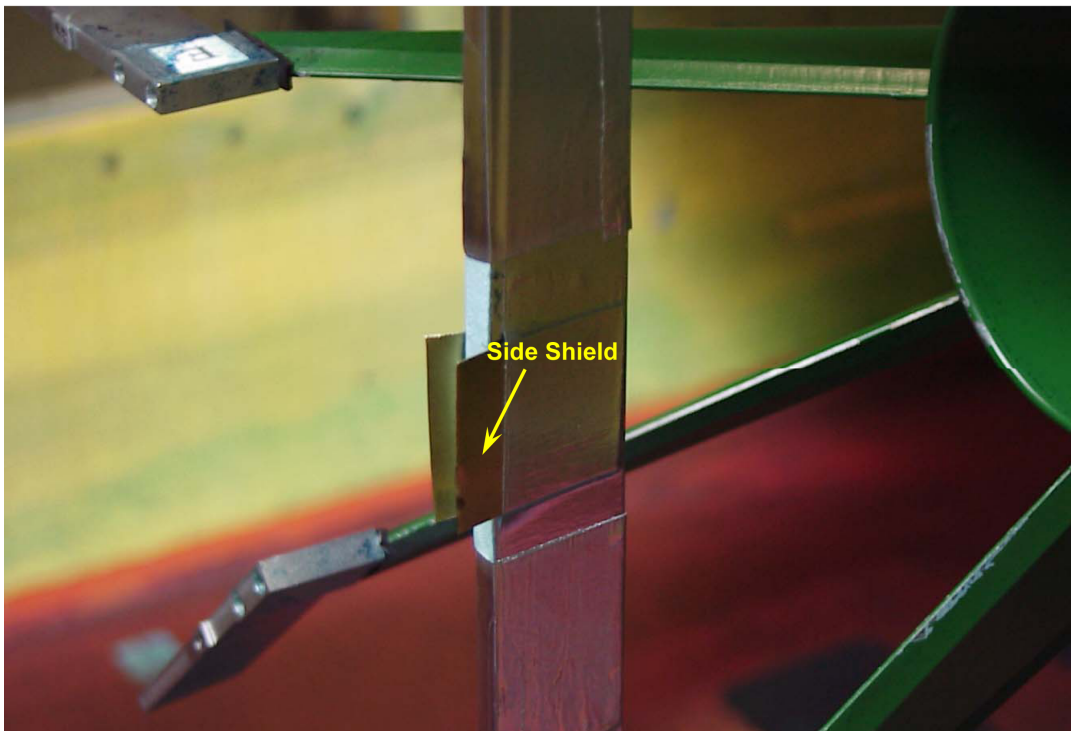


Figure 55.—Side shield attached to the collector blade.

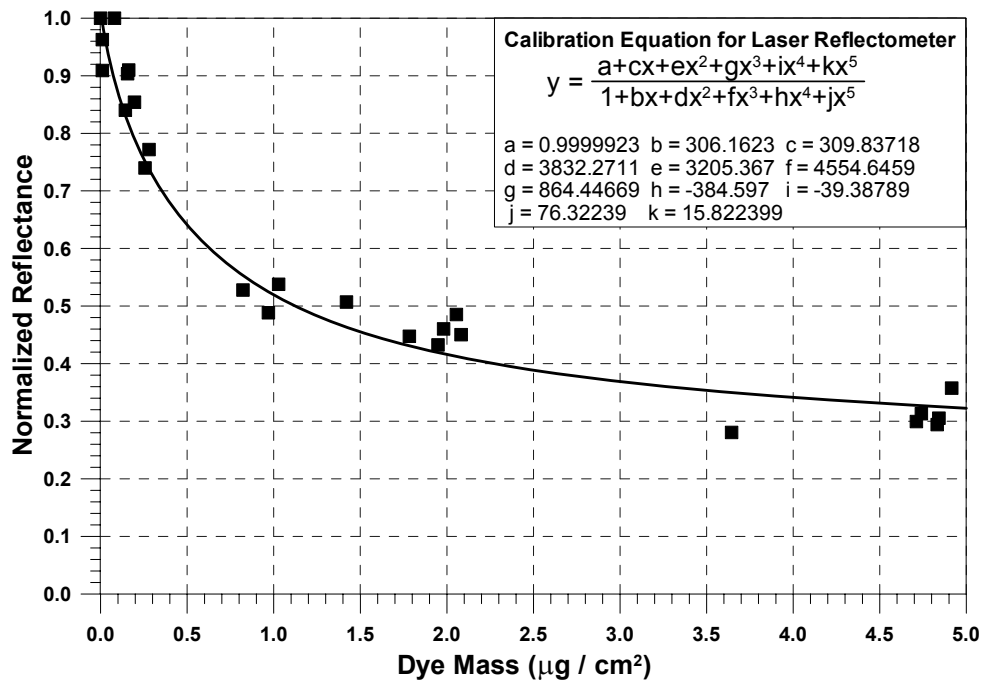


Figure 56.—Laser Reflectometer calibration curve
(Verigood 100 lb paper, 2001 IRT tests).

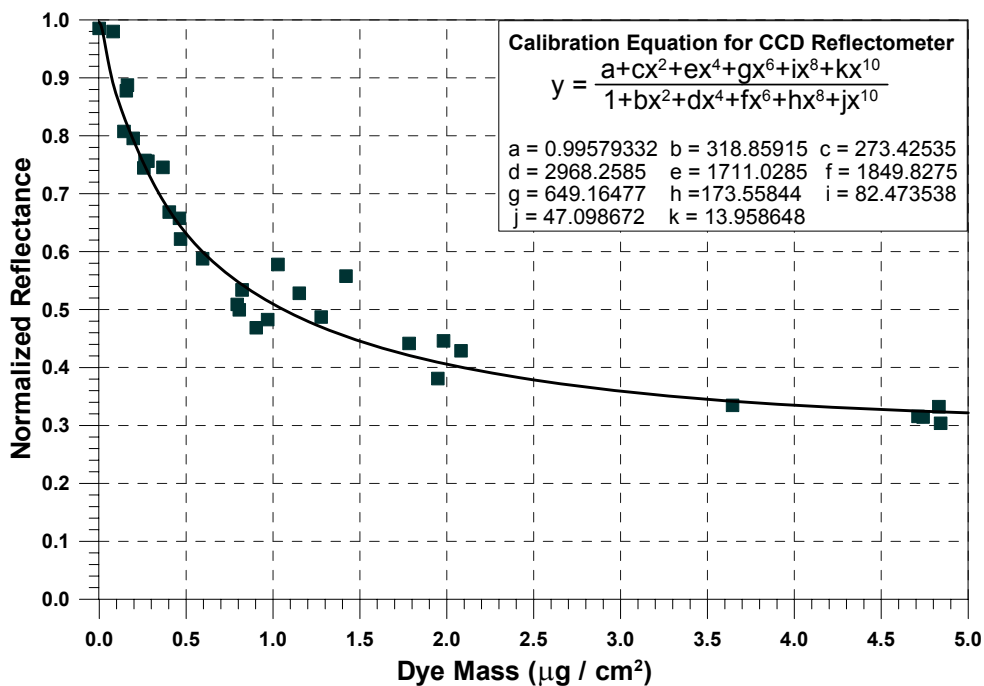


Figure 57.—CCD Reflectometer calibration curve
(Verigood 100 lb blotter paper, 2001 IRT tests).

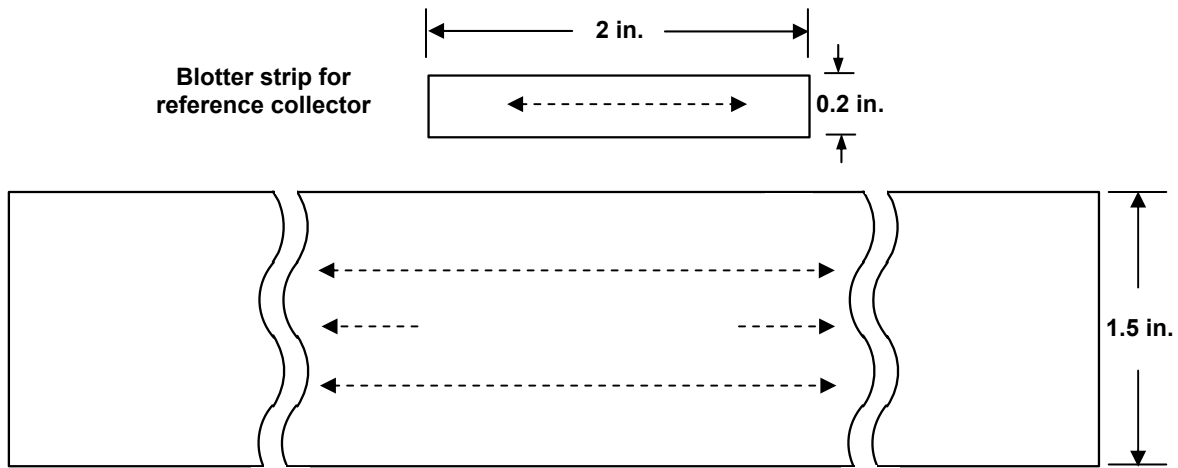


Figure 59a.—Scan locations for test model and reference collector strips.

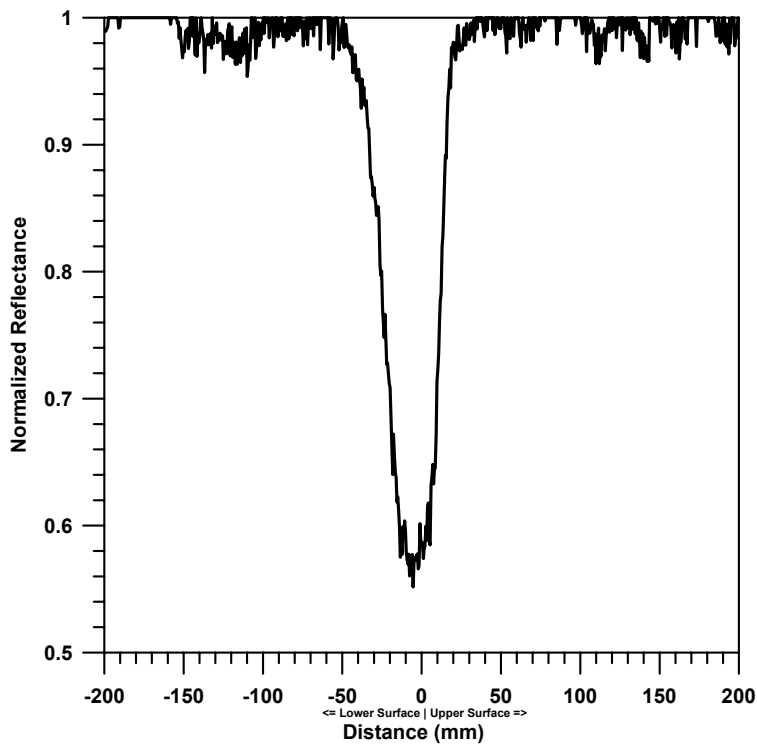


Figure 59b.—Typical normalized surface reflectance distribution for a dyed blotter strip using the laser data reduction system.

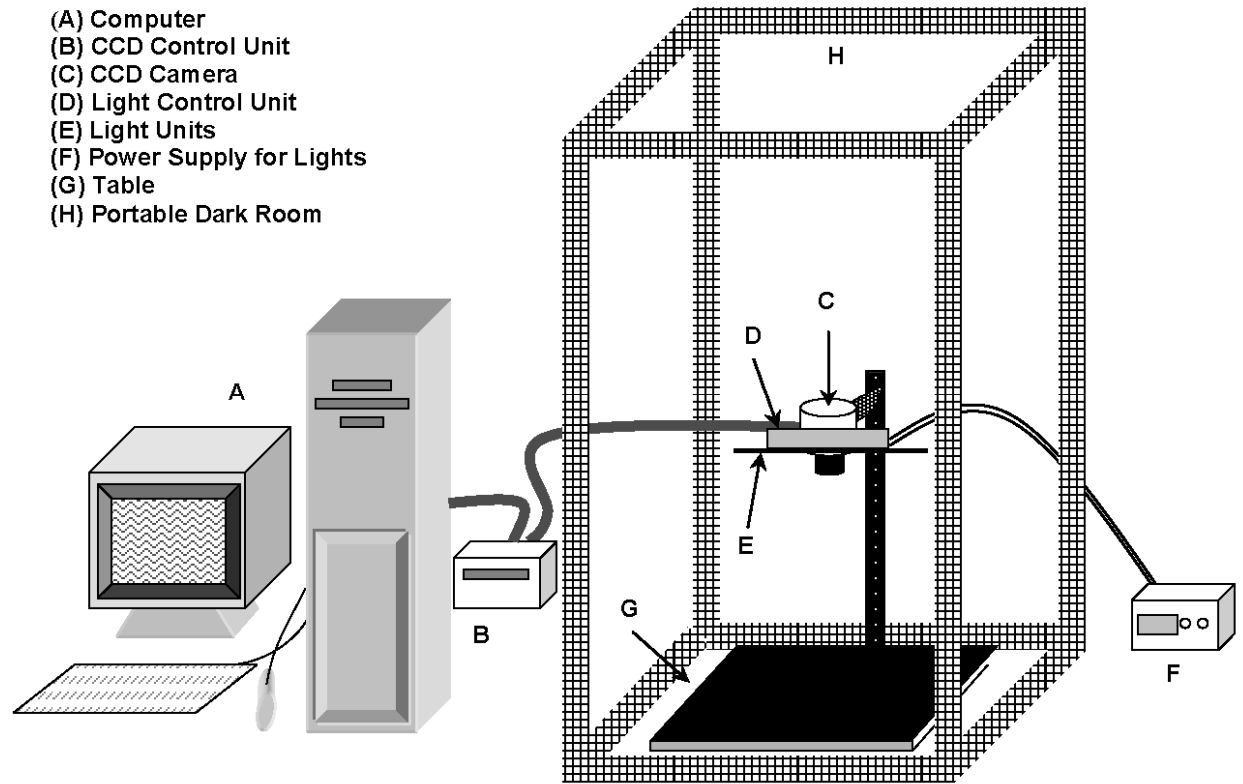


Figure 60a.—Schematic diagram of the CCD reflectometer.



Figure 60b.—CCD data reduction system setup.

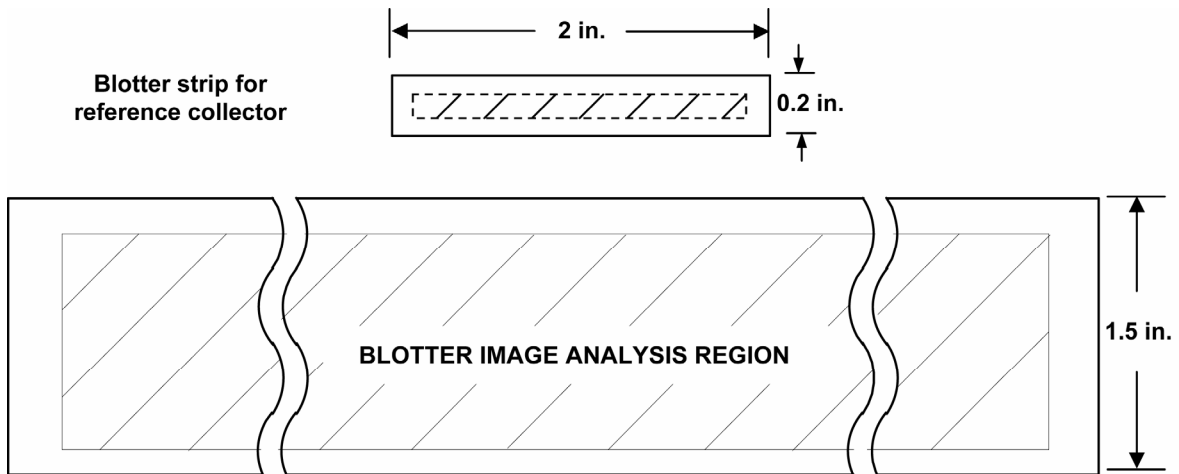


Figure 61a.—Blotter strip image analysis region for CCD data reduction system.

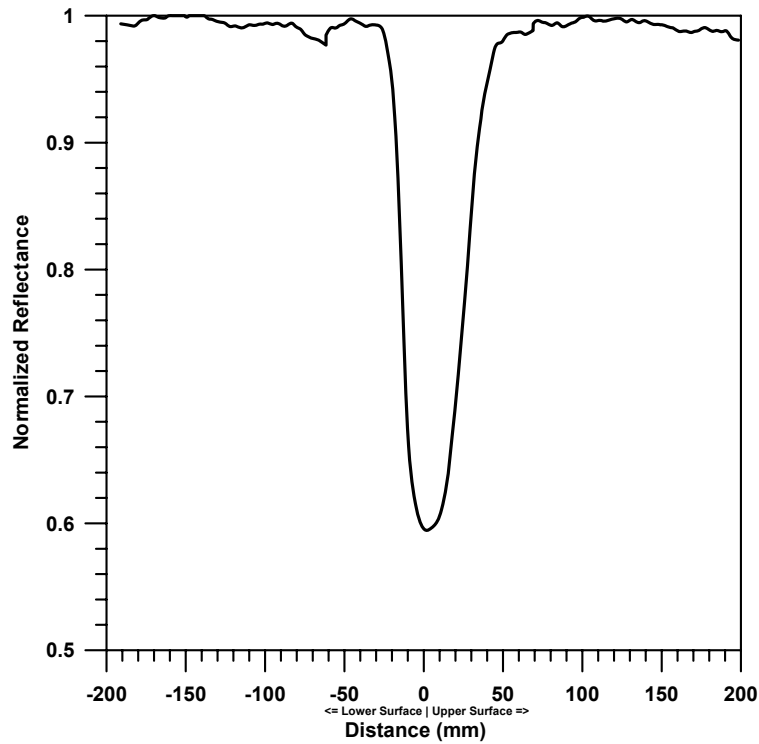


Figure 61b.—Typical normalized surface reflectance distribution for a dyed blotter strip using CCD data reduction system.

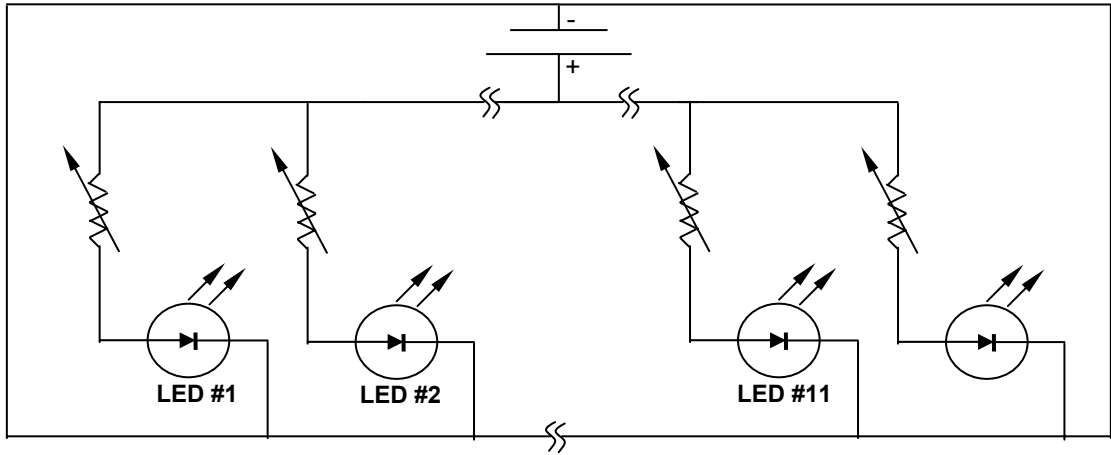


Figure 62a.—Schematic diagram of the CCD reflectometer lighting system.

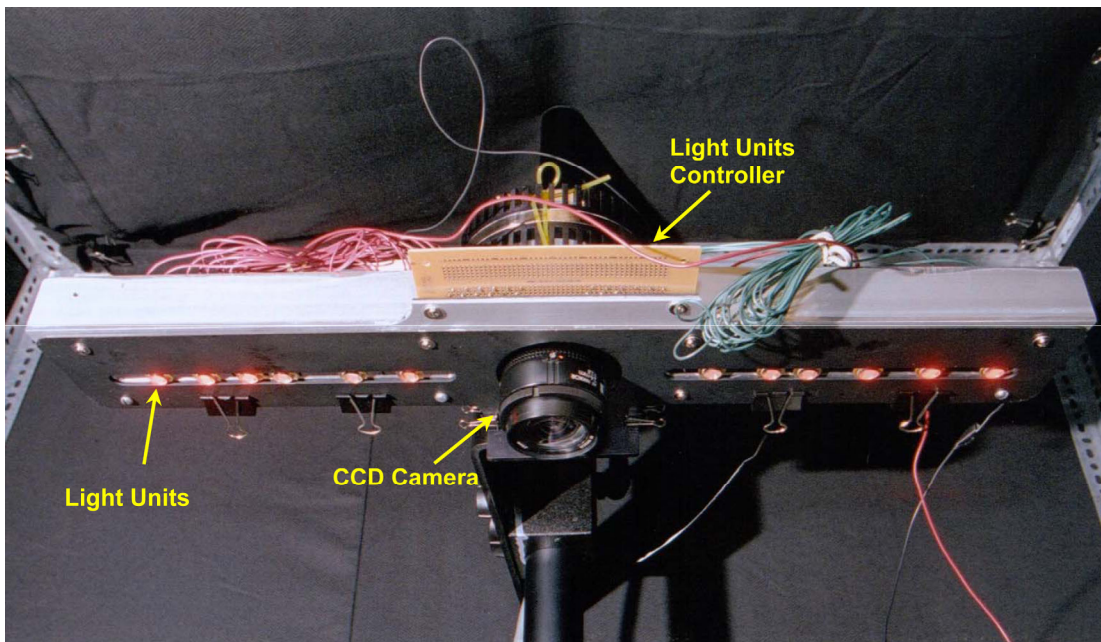


Figure 62b.—CCD reflectometer lighting setup.

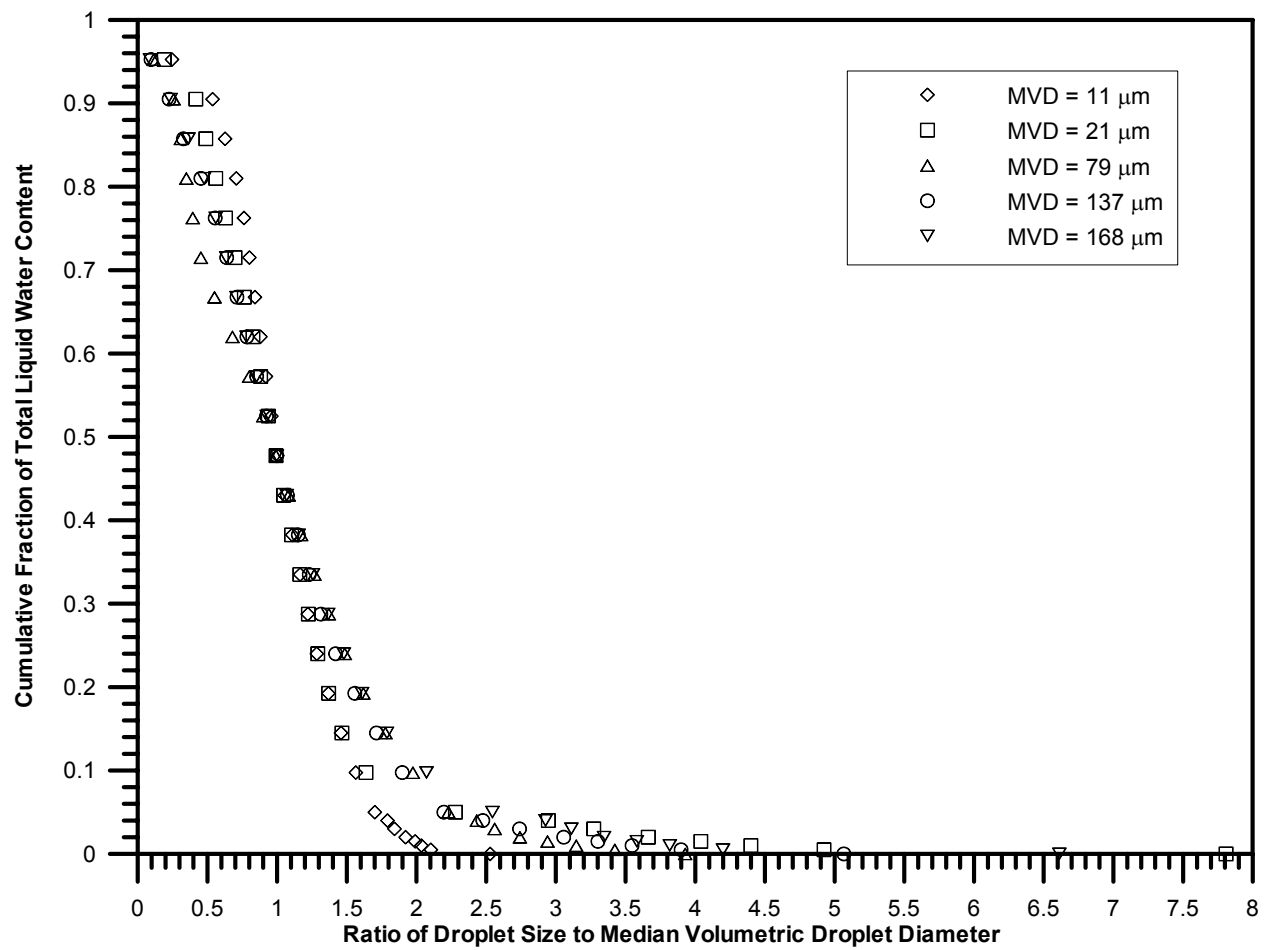


Figure 63.—27-bin droplet distributions.

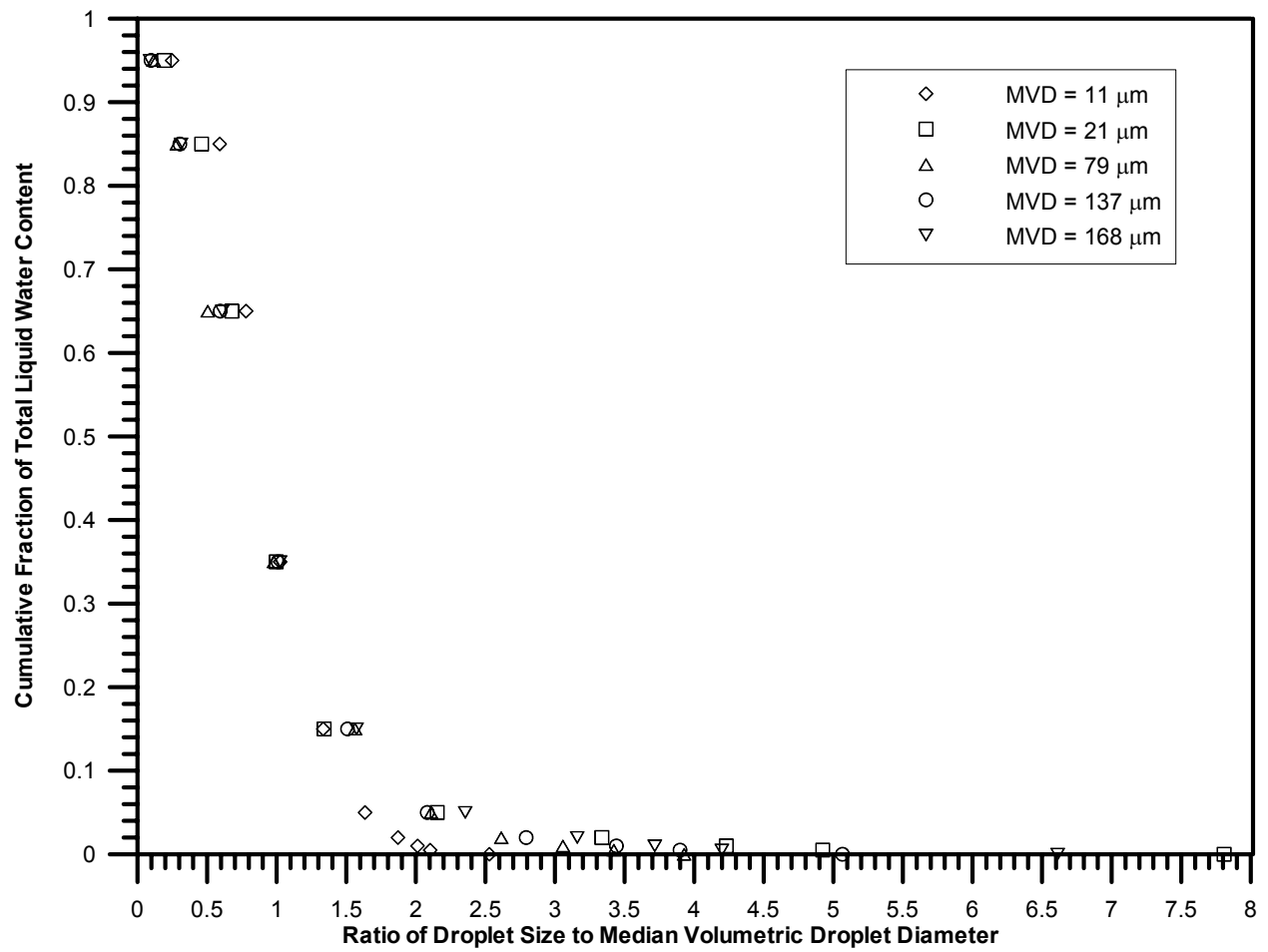


Figure 64.—10-bin droplet distributions.

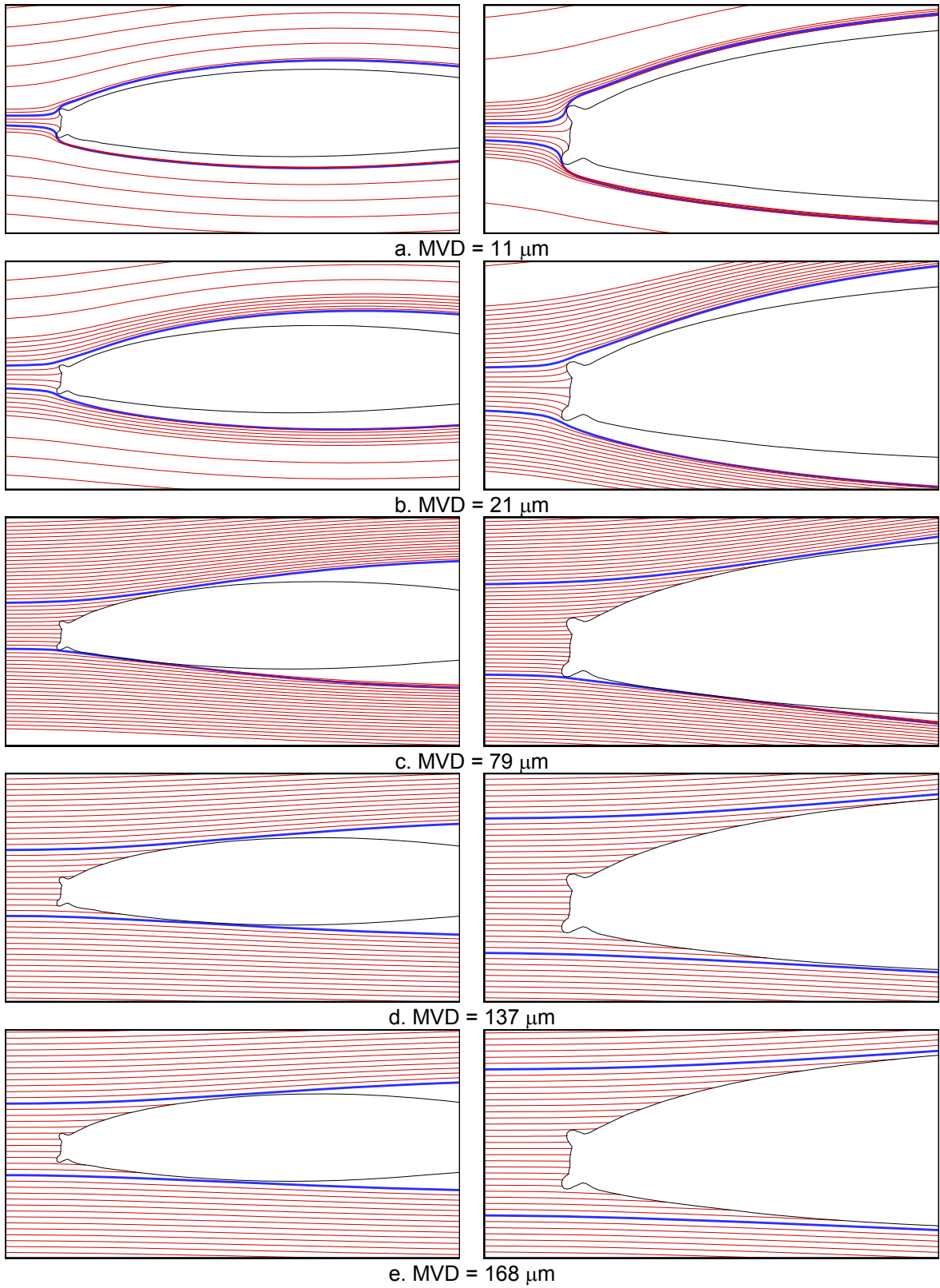


Figure 65.—Particles trajectories; Twin Otter tail with 22.5-min ice shape.

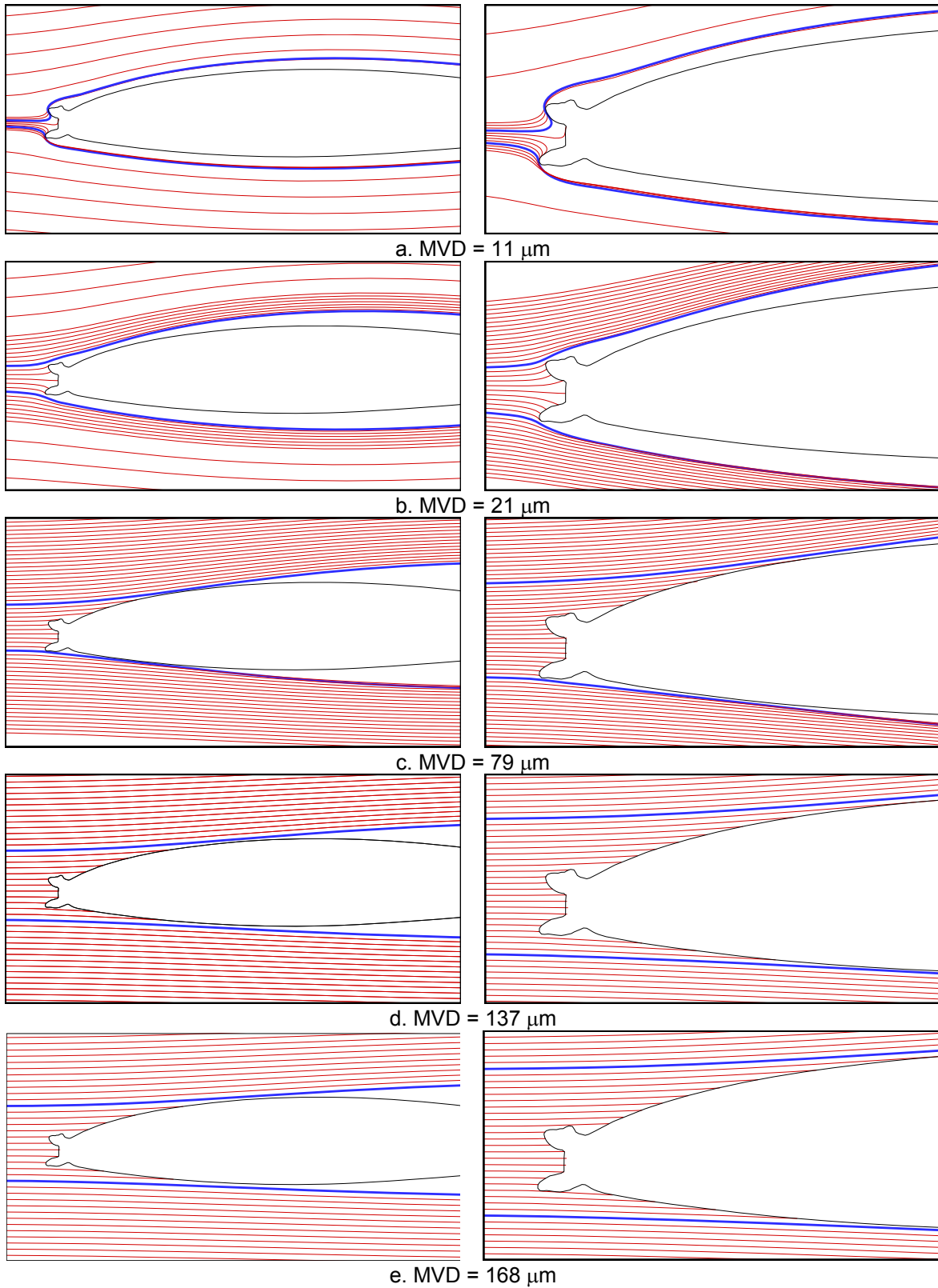
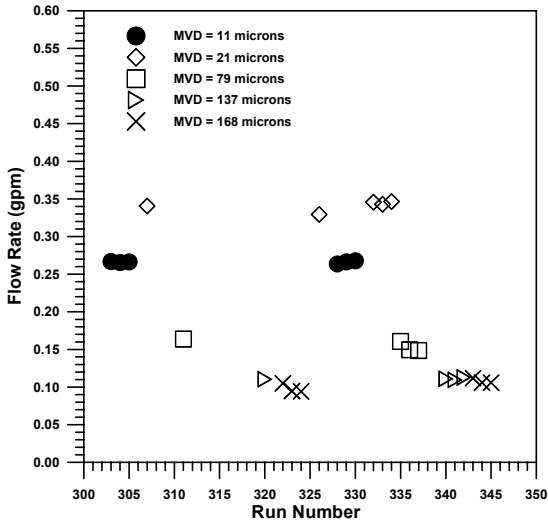
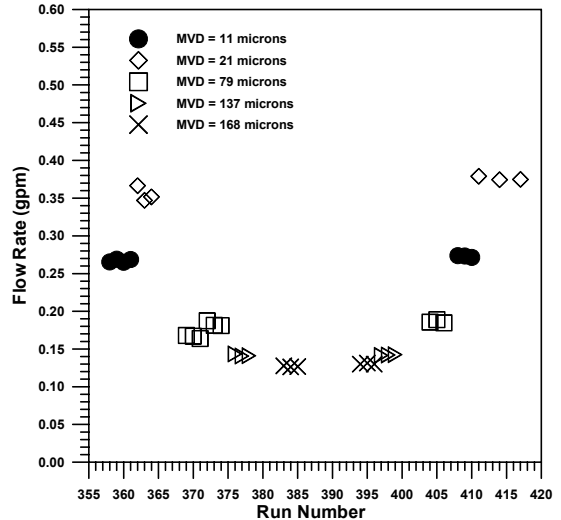


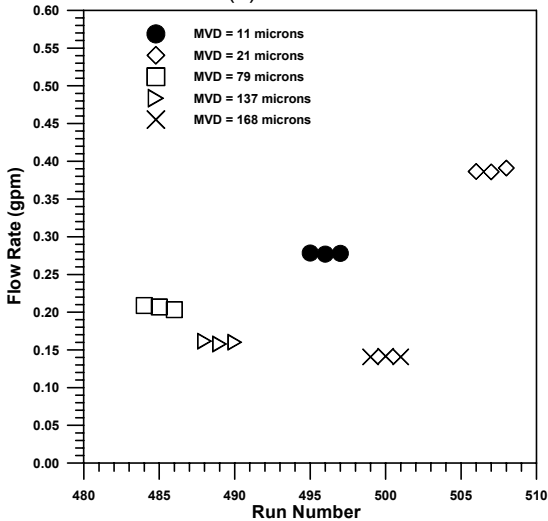
Figure 66.—Particles trajectories; Twin Otter tail with 45-min ice shape.



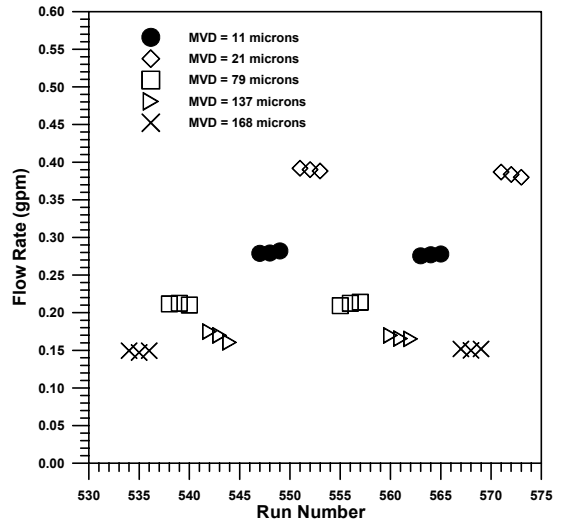
a. MS(1)-0317 airfoil



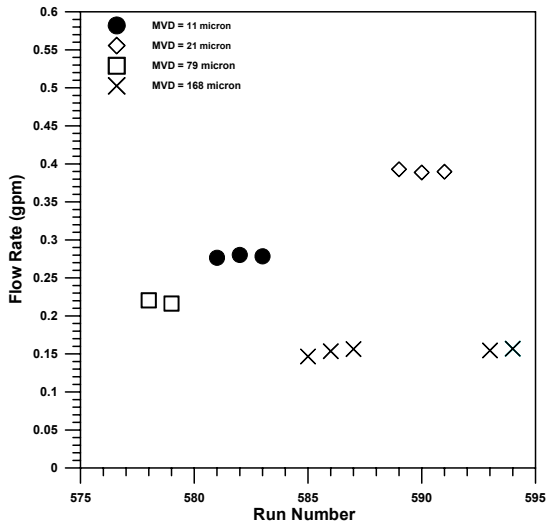
b. NACA 65₂-415 airfoil



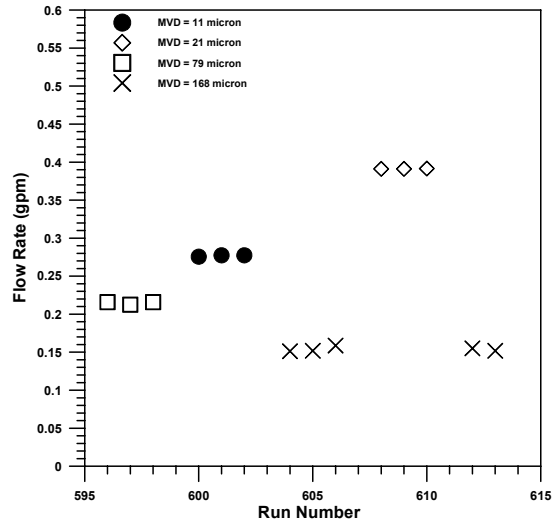
c. GLC-305 airfoil



d. Twin Otter tail



e. Twin Otter with 22.5-min ice shape



f. Twin Otter with 45-min ice shape

Figure 67.—Variation in WSU 16-nozzle spray system water flow rate (2001 tests).

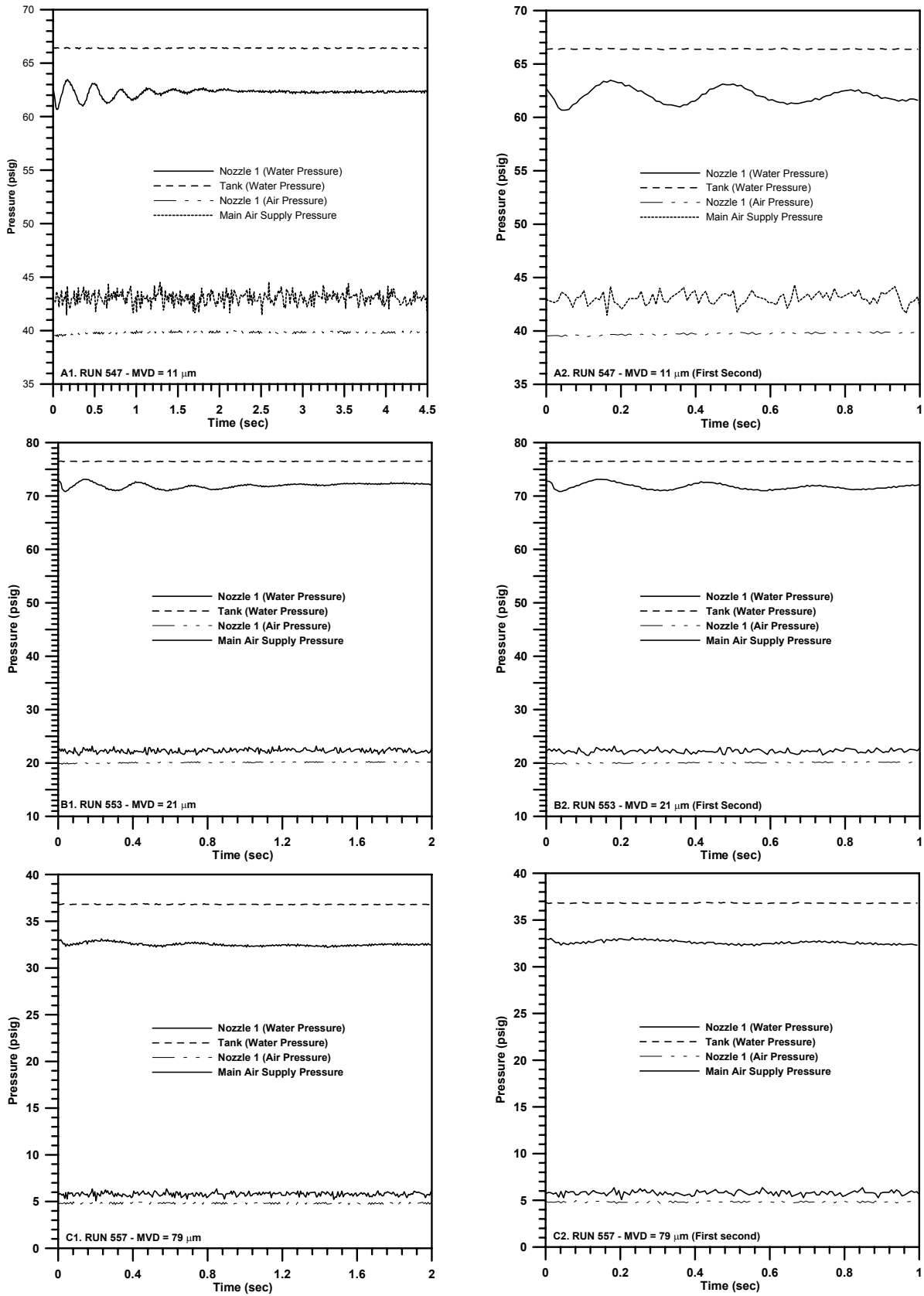


Figure 68.—Spray system pressures versus spray time for all MVD cases.

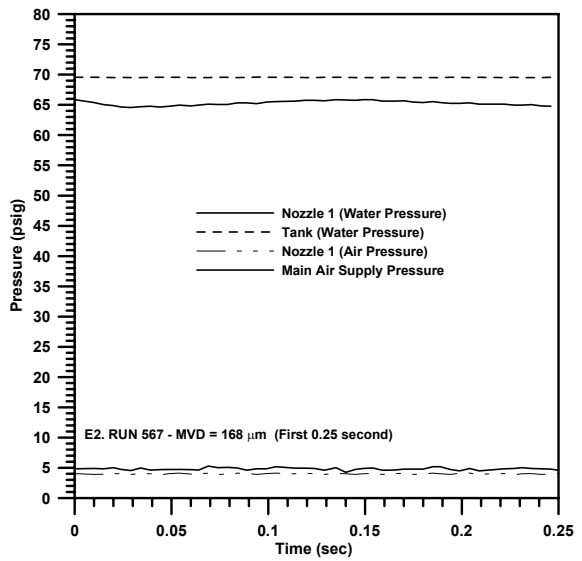
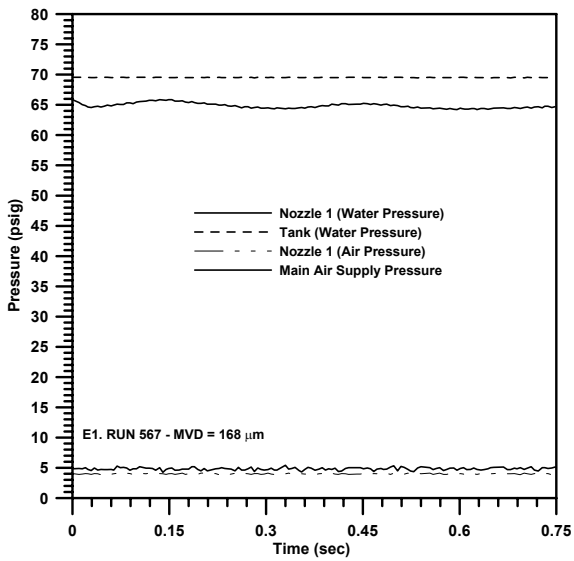
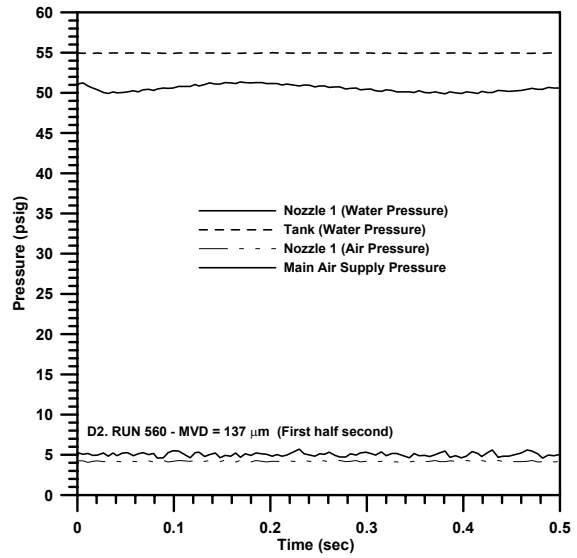
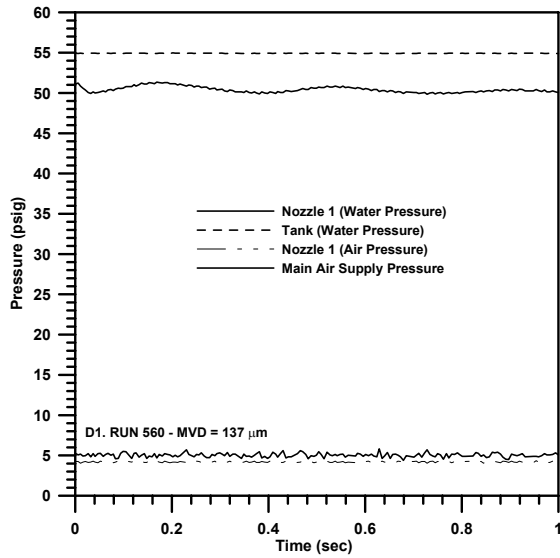


Figure 68.—Spray system pressures versus spray time for all MVD cases. (Cont.)

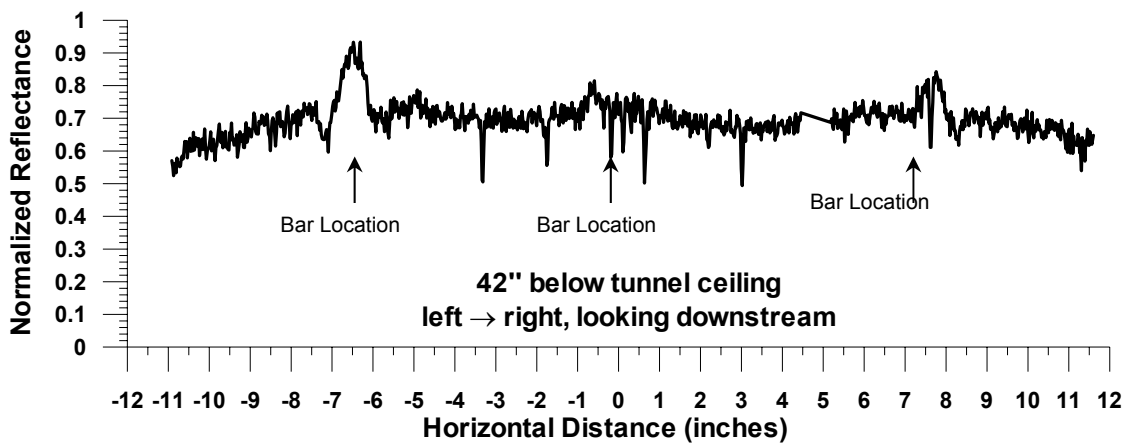
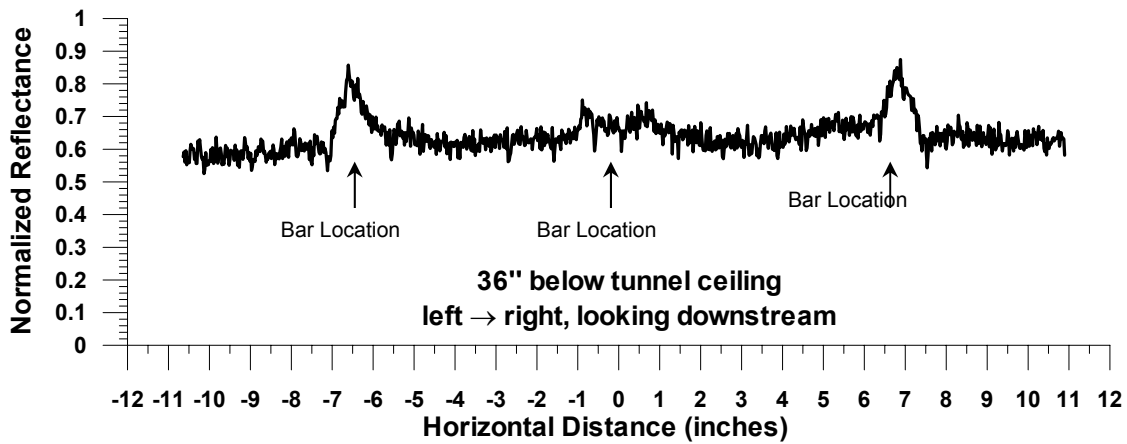
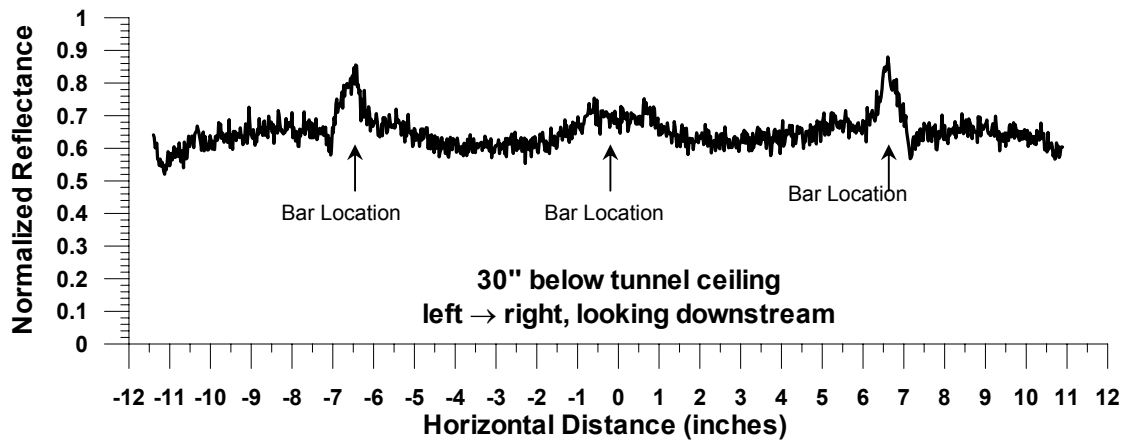


Figure 69a.—Cloud uniformity tests using IRT uniformity grid. MVD = 11 μm .

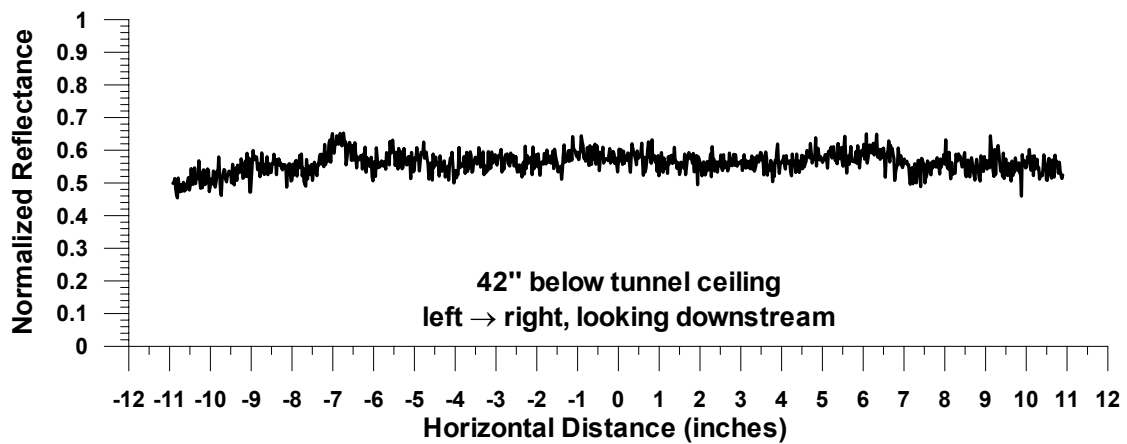
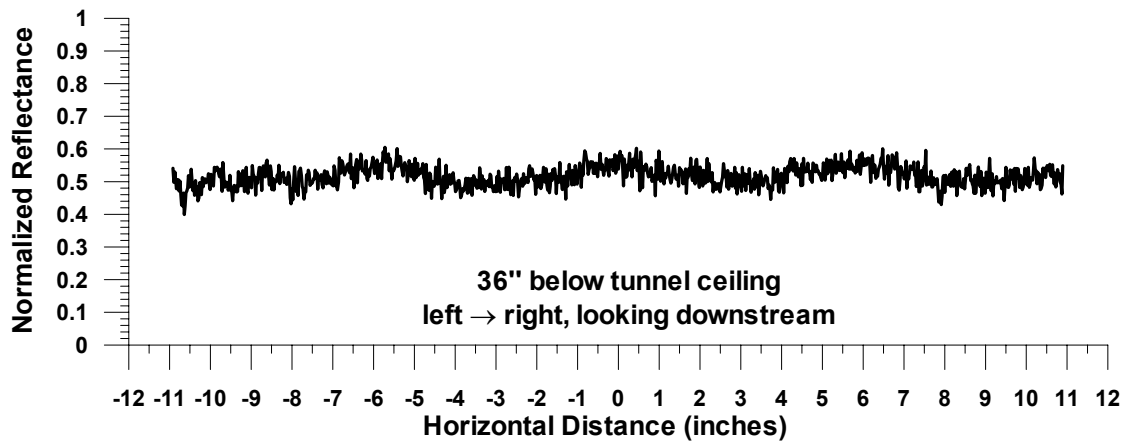
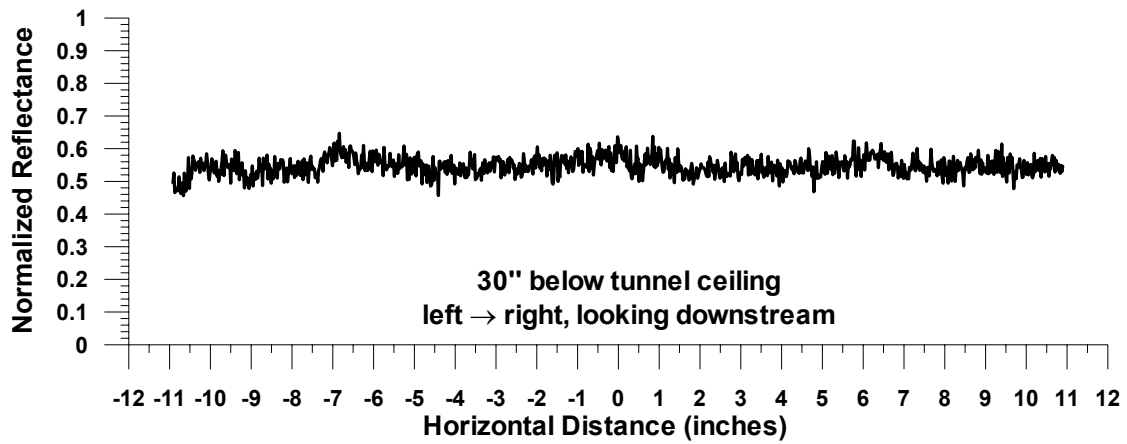


Figure 69b.—Cloud uniformity tests using IRT uniformity grid. MVD = 21 μm .

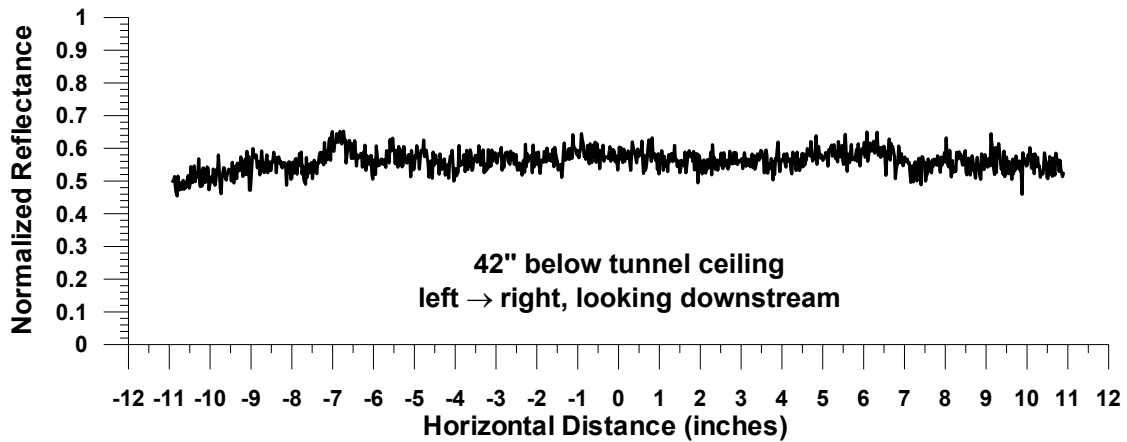
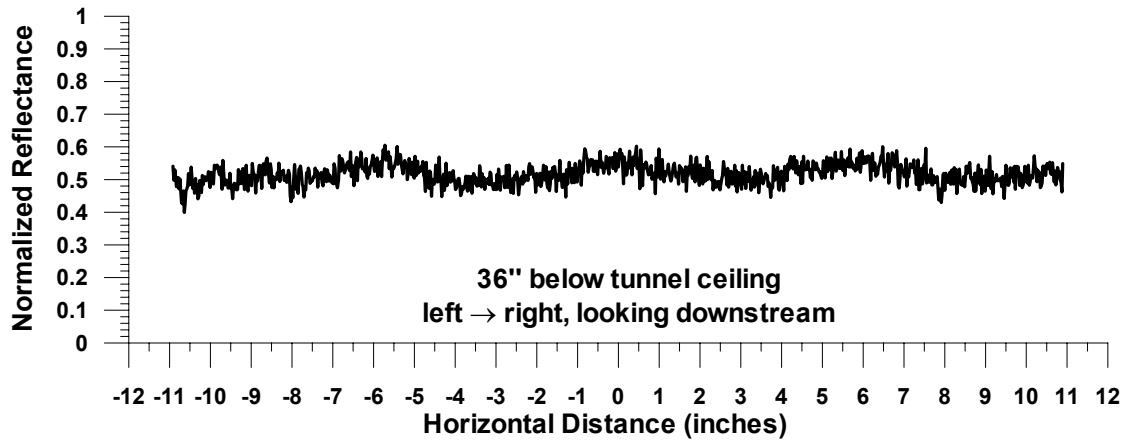
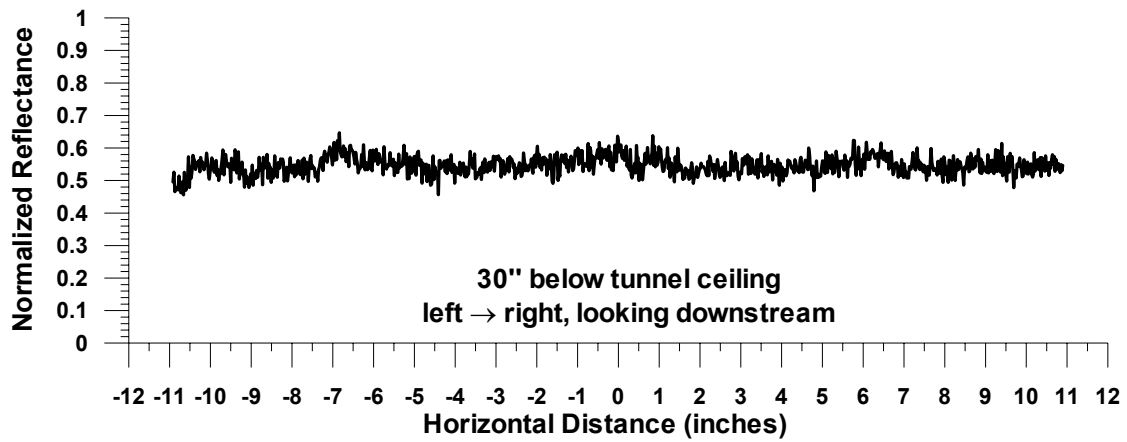


Figure 69c.—Cloud uniformity tests using IRT uniformity grid. MVD = 79 μm .

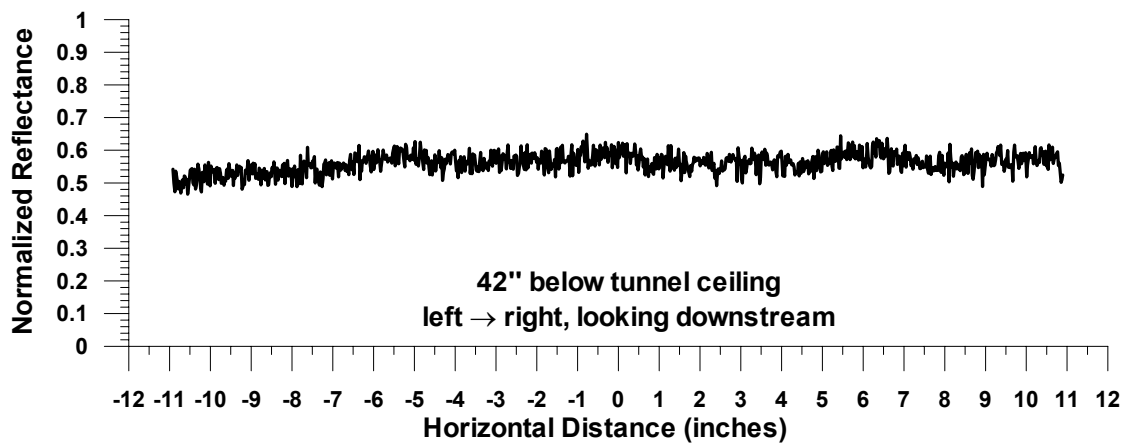
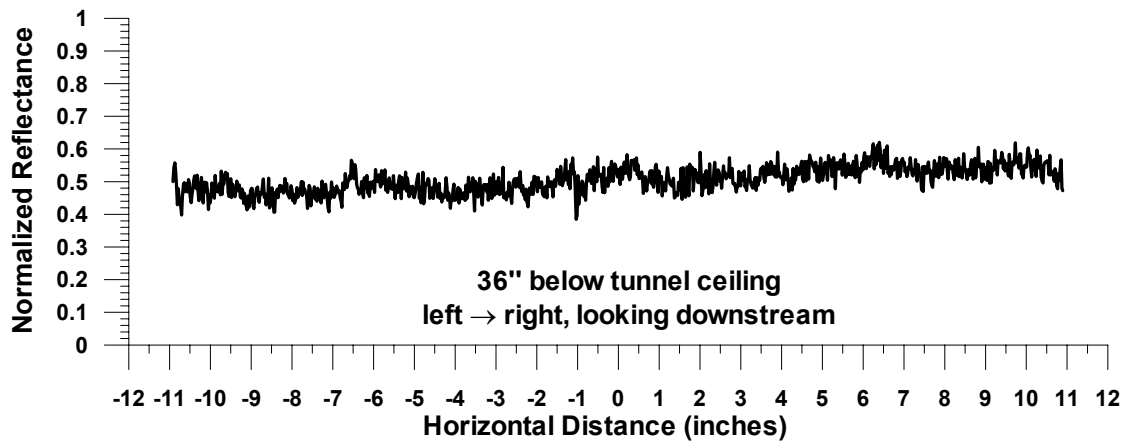
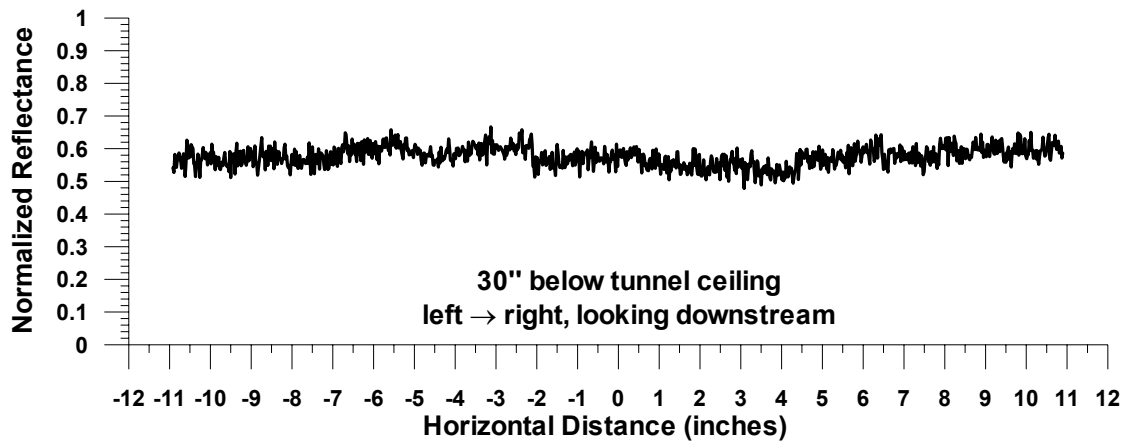


Figure 69d.—Cloud uniformity tests using IRT uniformity grid. MVD = 137 μm .

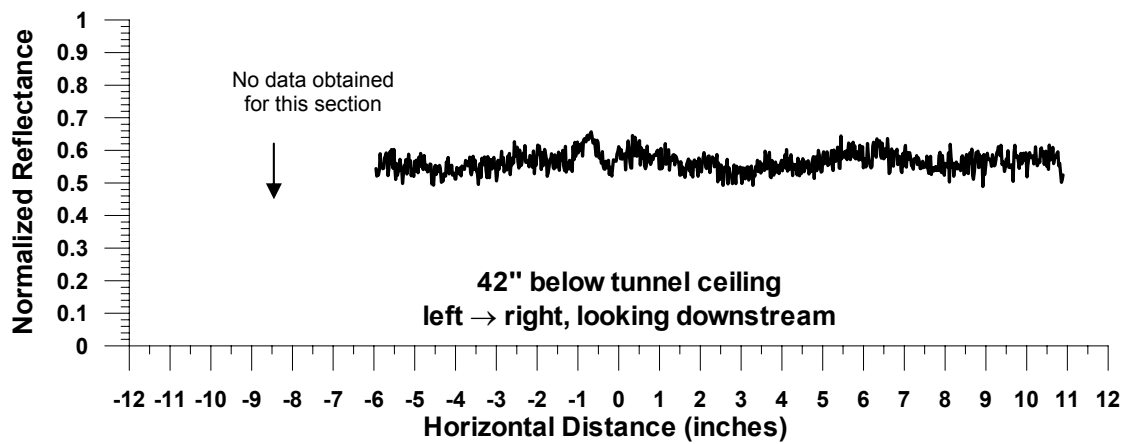
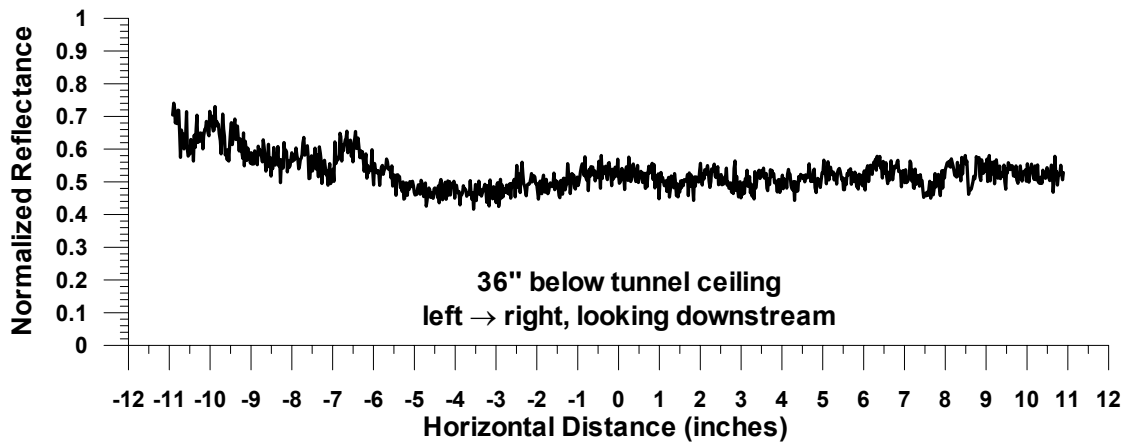
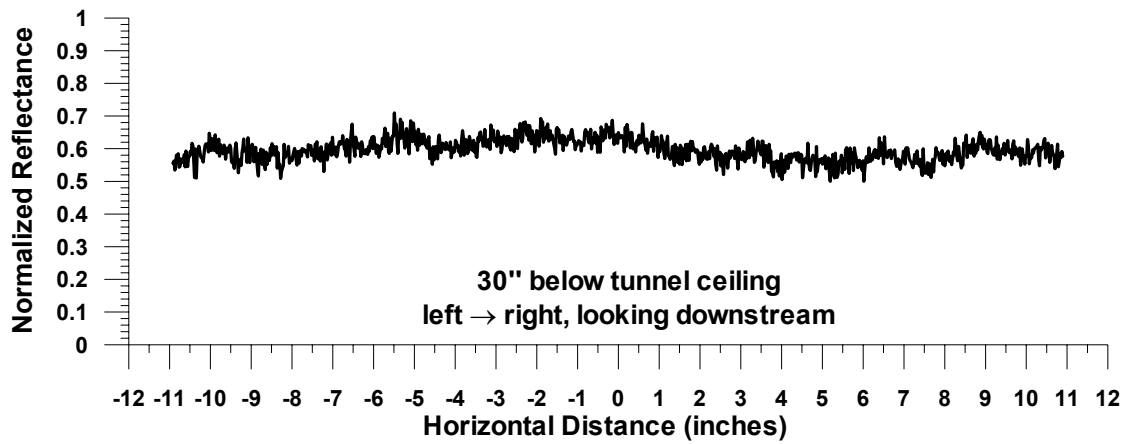


Figure 69e.—Cloud uniformity tests using IRT uniformity grid. MVD = 168 μm .

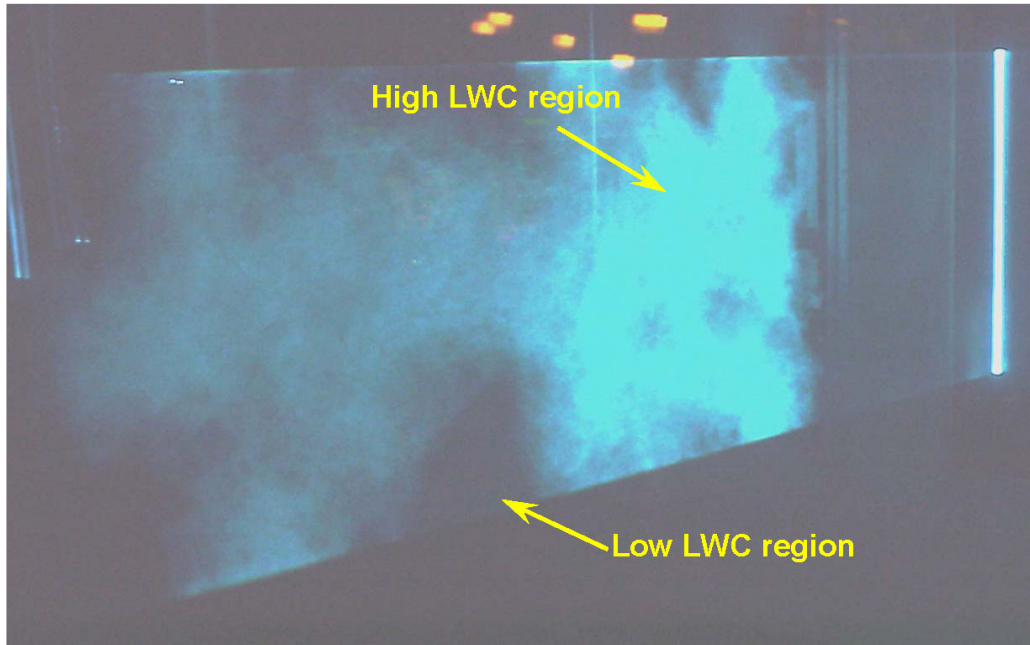


Figure 70a.—Laser sheet produced in the IRT test section prior to nozzle locations adjustment for uniformity.

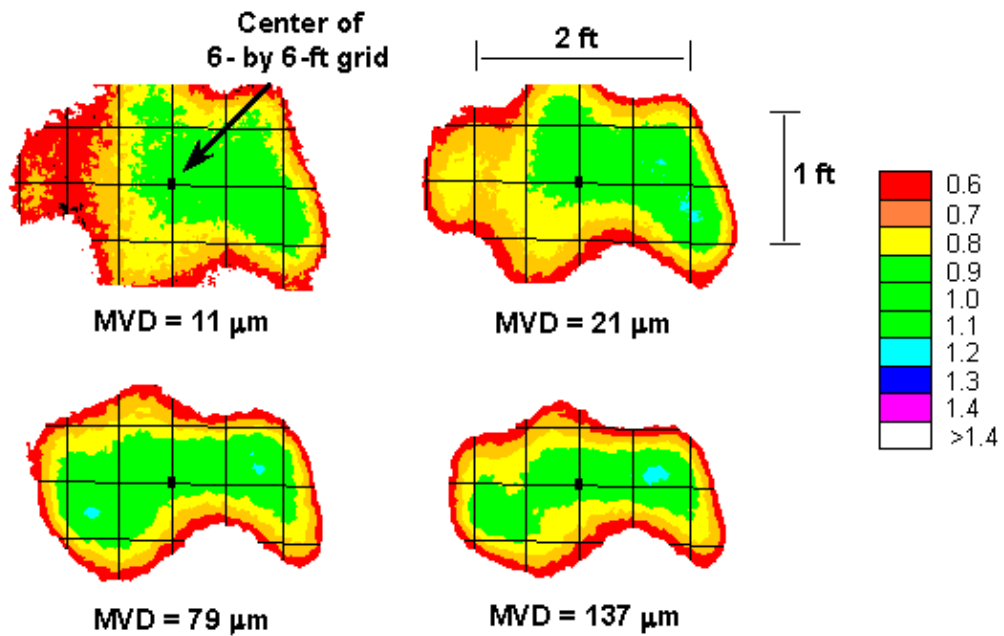


Figure 70b.—Sample of cloud uniformity images prior to nozzle locations adjustment for uniformity.



Figure 71a.—Laser sheet produced in the IRT test section subsequent to nozzle locations adjustment for uniformity.

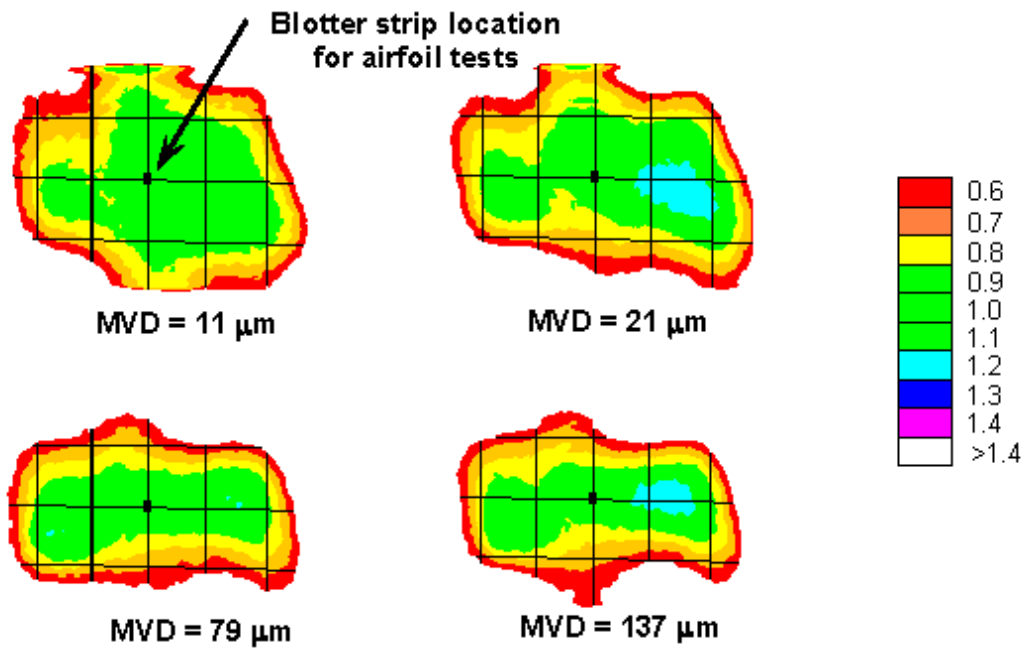


Figure 71b.—Sample of cloud uniformity images subsequent to nozzle locations adjustment for uniformity.

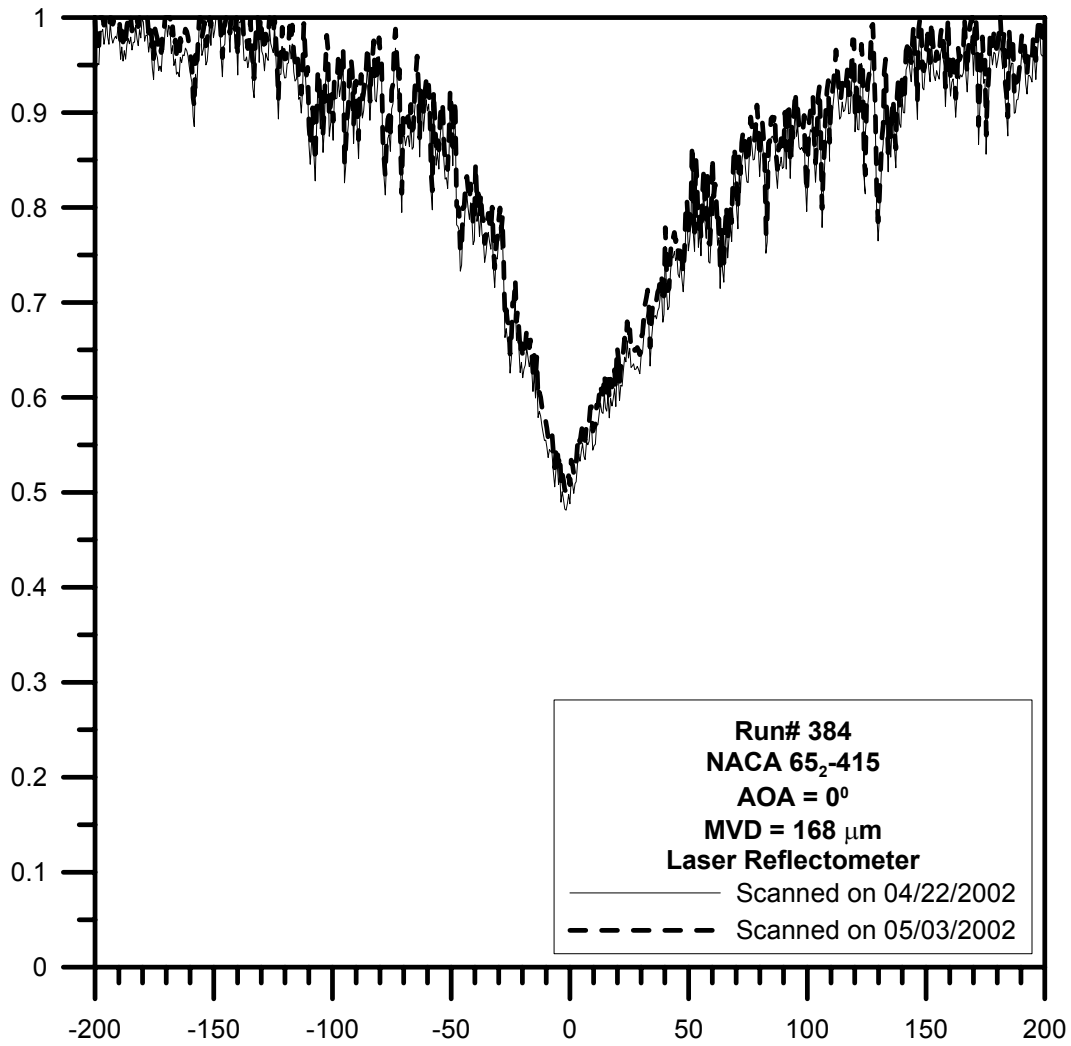


Figure 72a.—Scanning repeatability over a period of time for laser reflectometer.

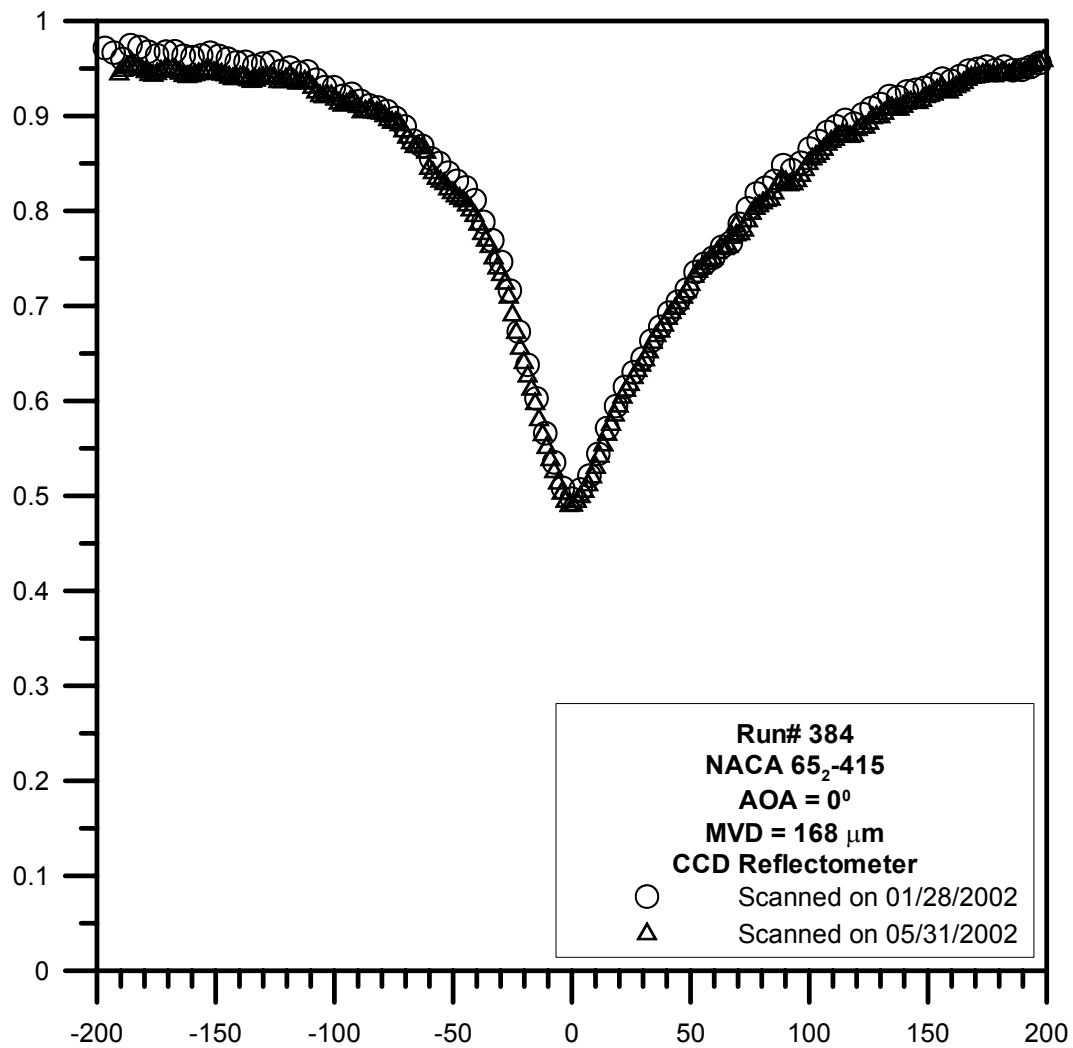


Figure 72b.—Scanning repeatability over a period of time for CCD reflectometer.

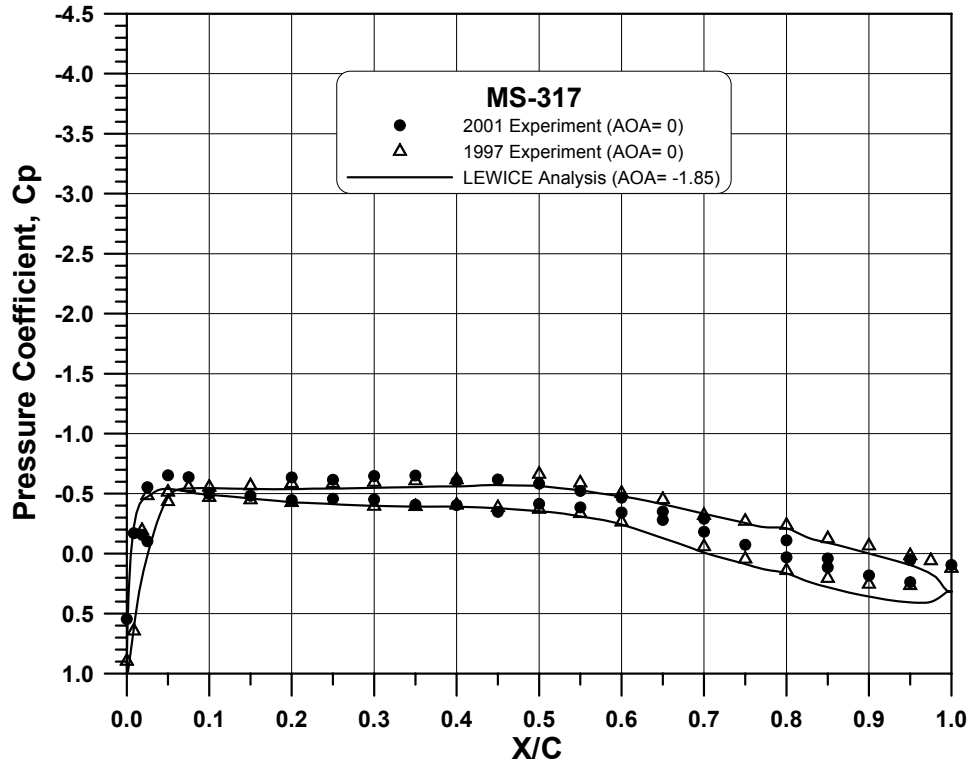


Figure 73.—Comparison of pressure distribution for MS-317 airfoil with $\alpha = 0^\circ$.

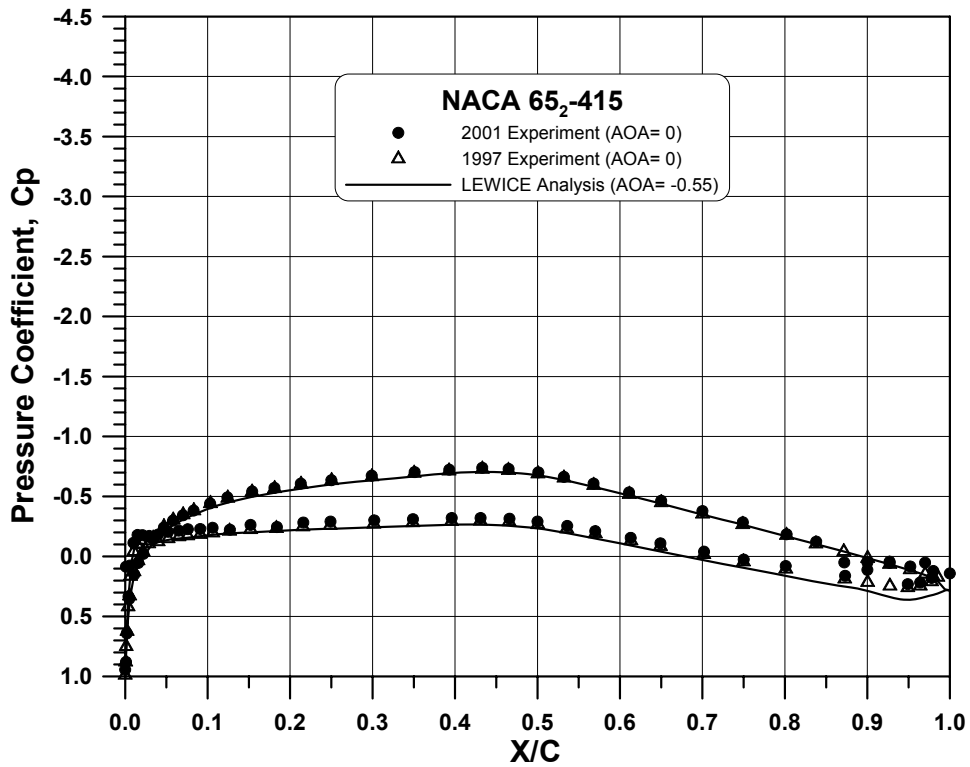


Figure 74.—Comparison of pressure distribution for NACA 65₂-415 airfoil with $\alpha = 0^\circ$.

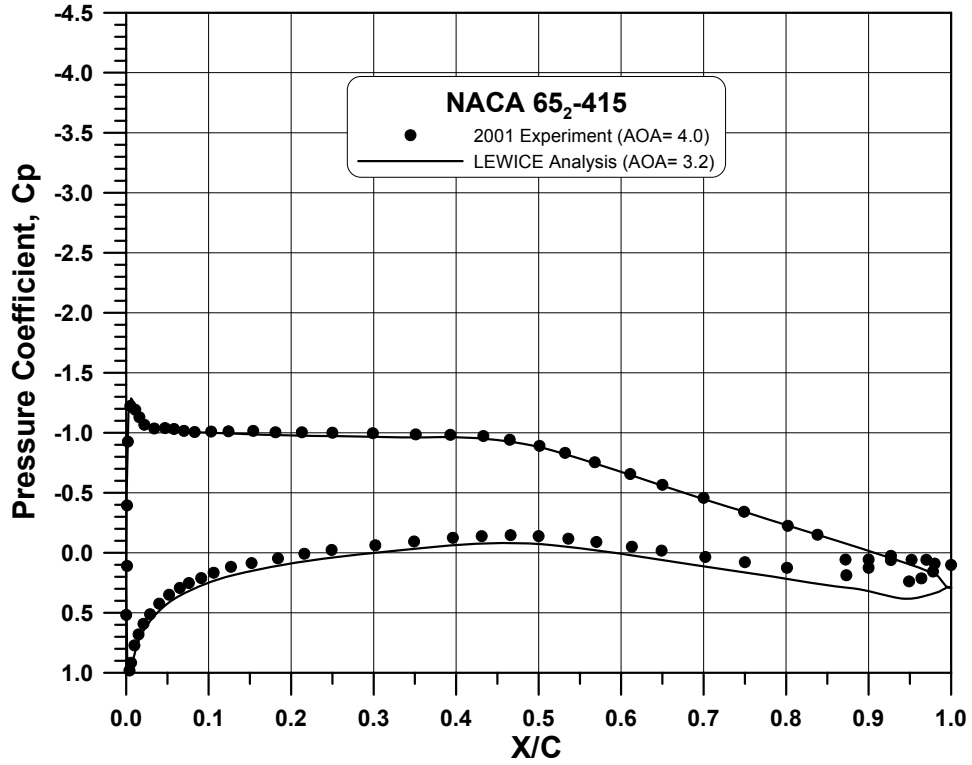


Figure 75.—Comparison of pressure distribution for NACA 65₂-415 airfoil with $\alpha = 4^\circ$.

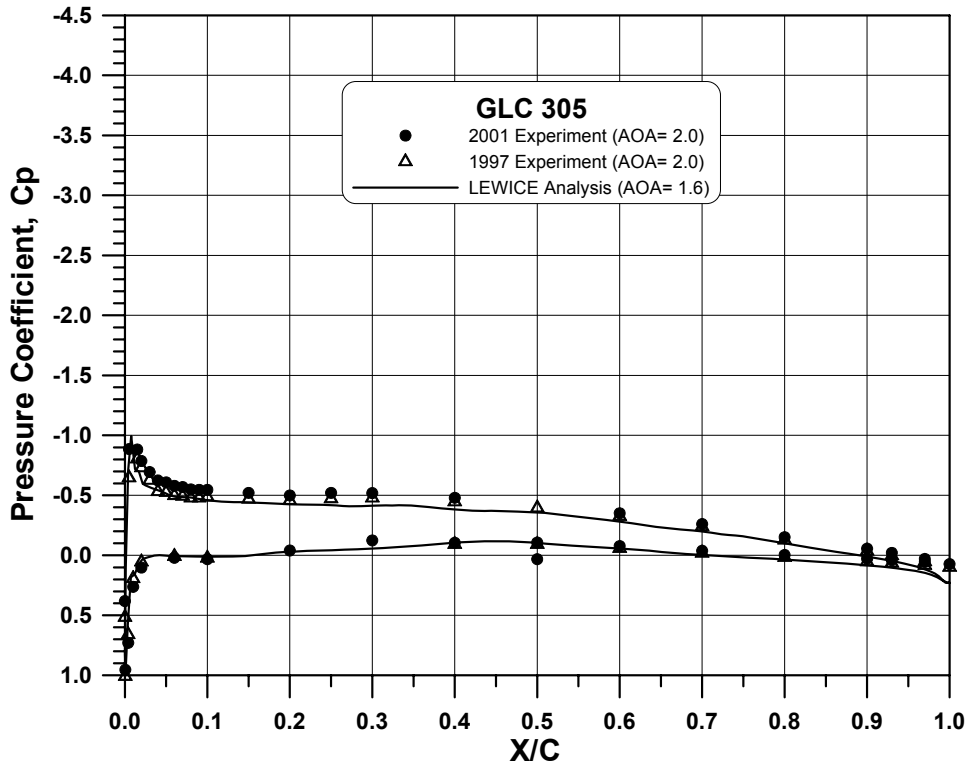


Figure 76.—Comparison of pressure distribution for GLC-305 airfoil with $\alpha = 1.5^\circ$.

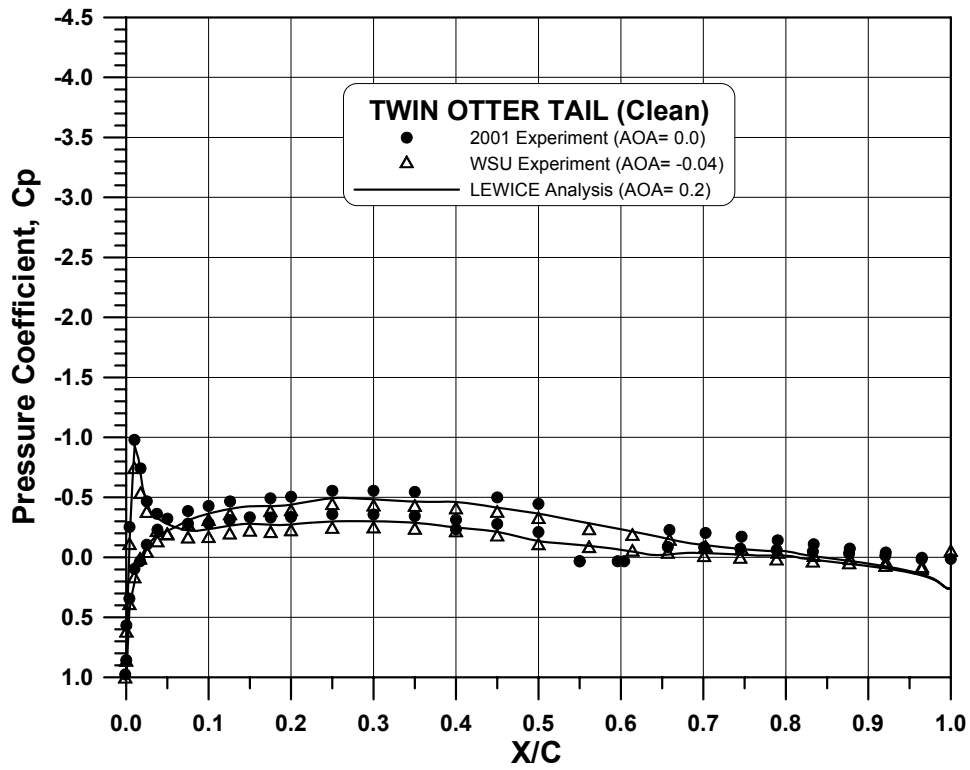


Figure 77.—Comparison of pressure distribution for Twin Otter tail with $\alpha = 0^\circ$.

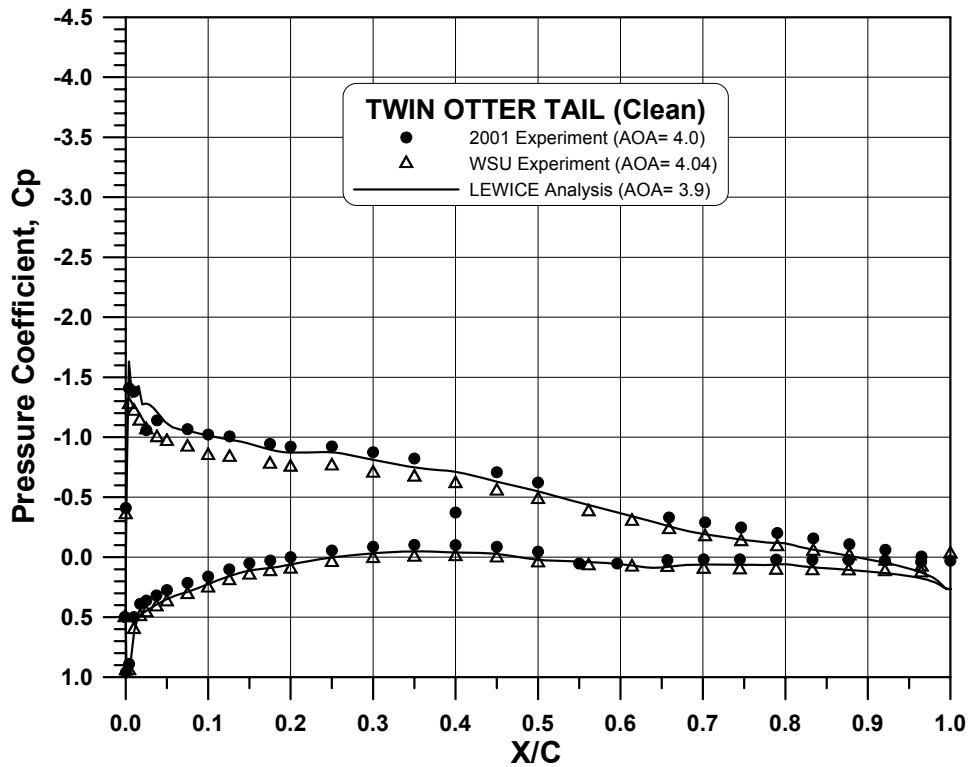


Figure 78.—Comparison of pressure distribution for Twin Otter tail with $\alpha = 4^\circ$.

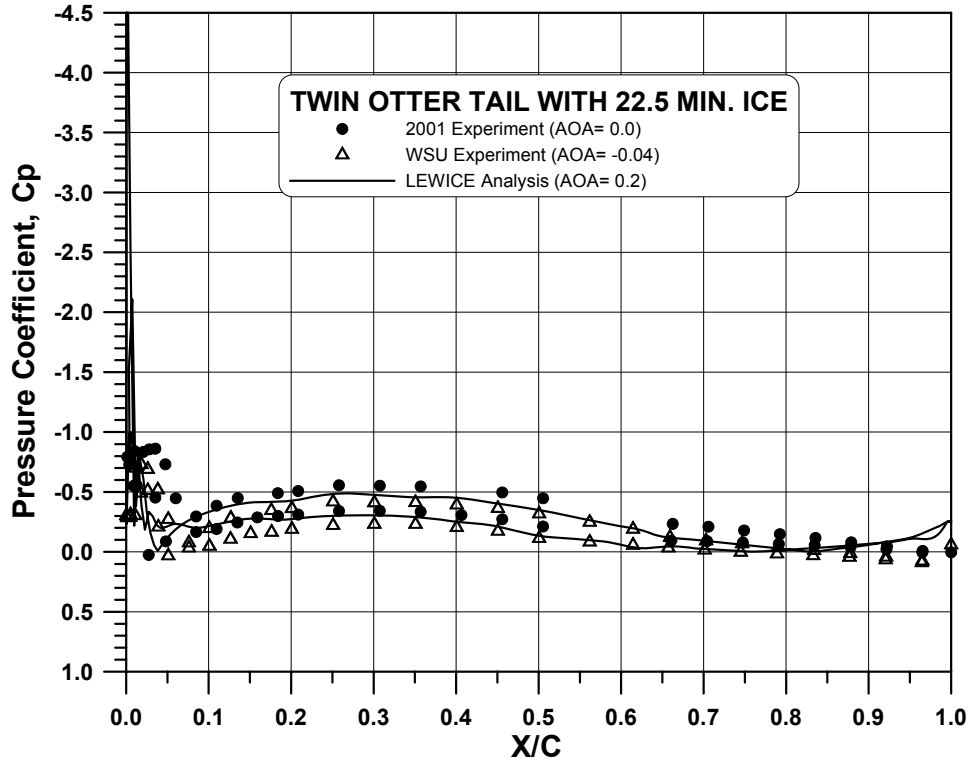


Figure 79.—Comparison of pressure distribution for Twin Otter tail with 22.5-min ice shape at $\alpha = 0^\circ$.

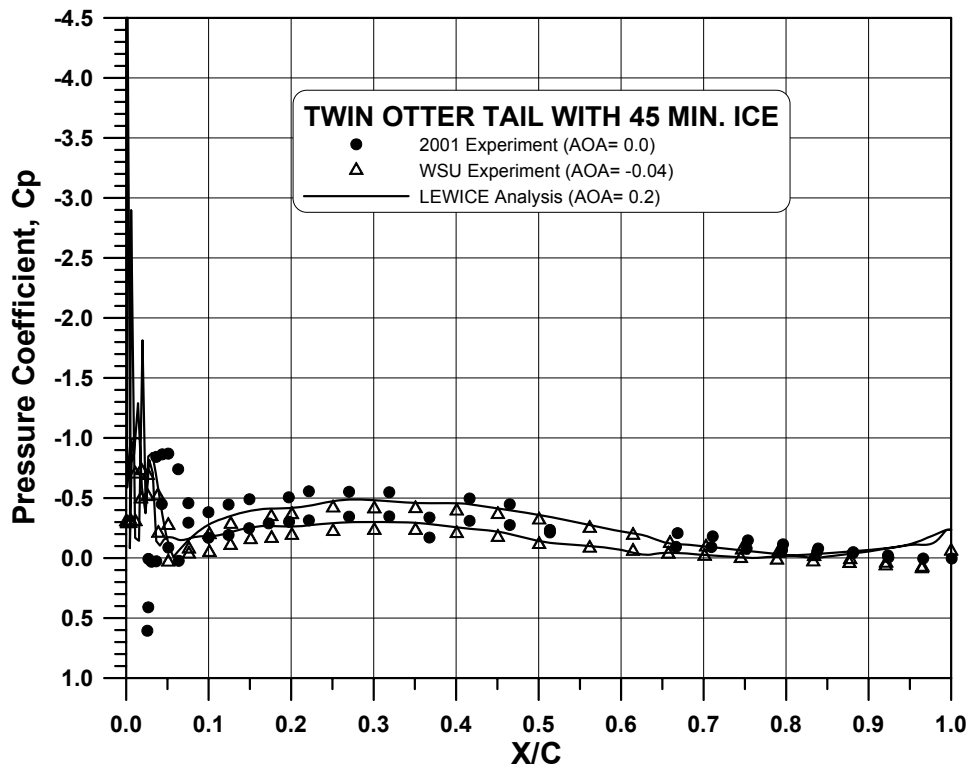


Figure 80.—Comparison of pressure distribution for Twin Otter tail with 45-min ice shape at $\alpha = 0^\circ$.

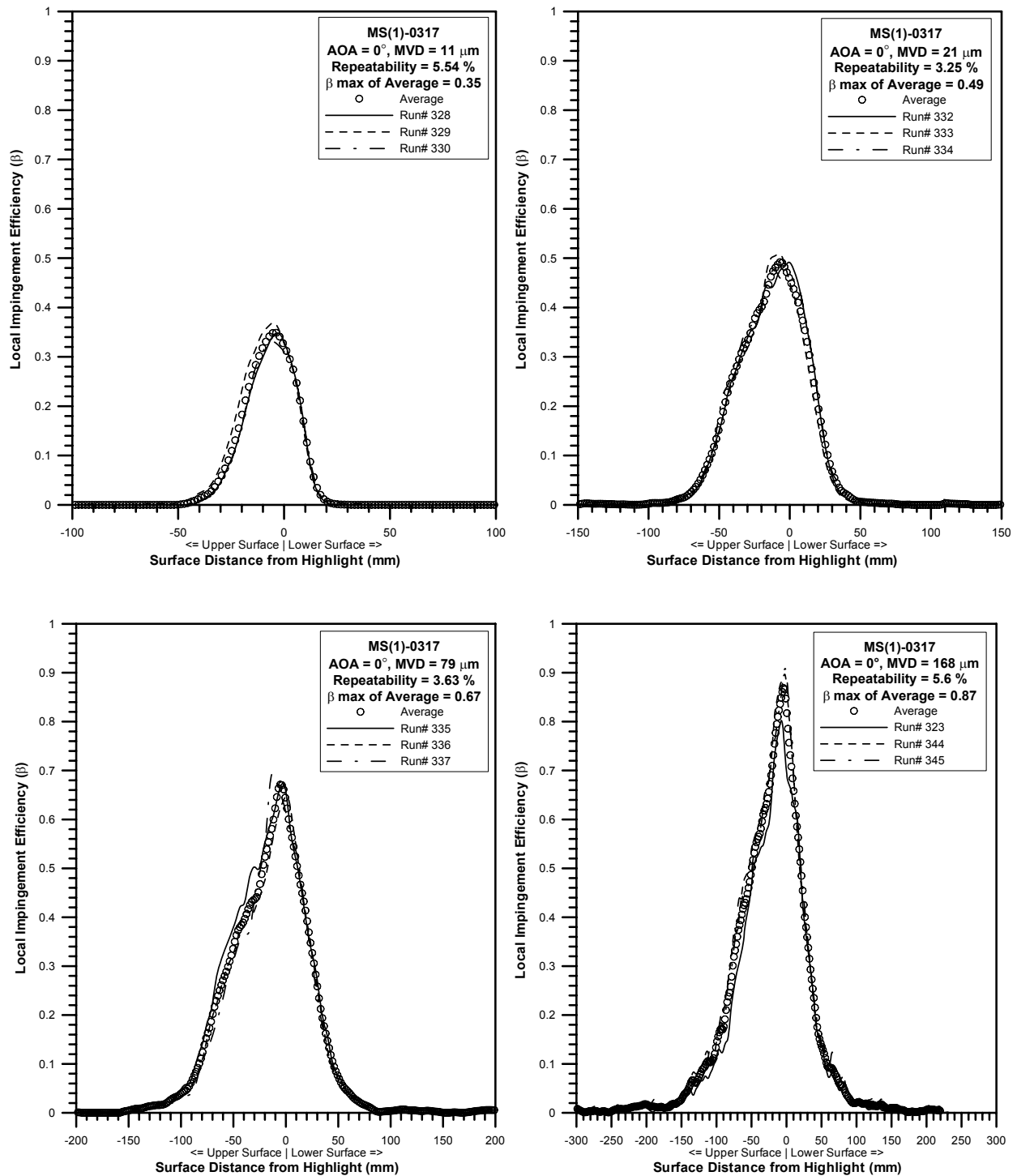


Figure 81.—Test repeatability for MS-317 airfoil at AOA = 0°.

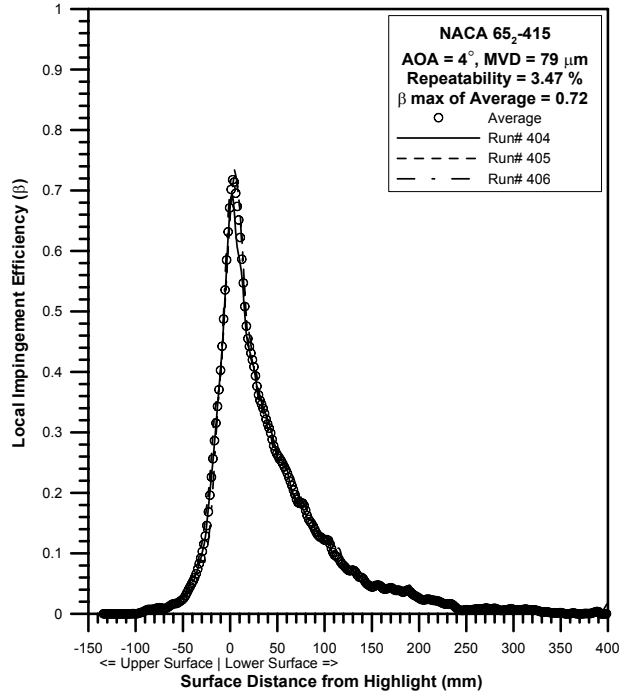
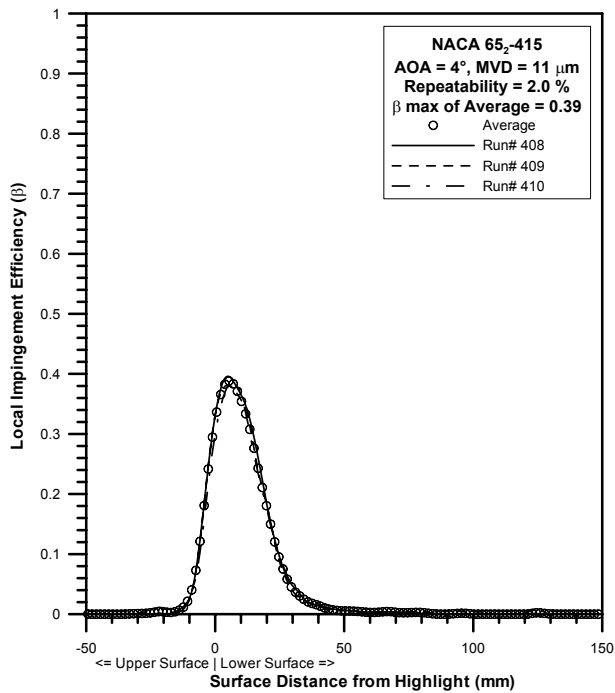
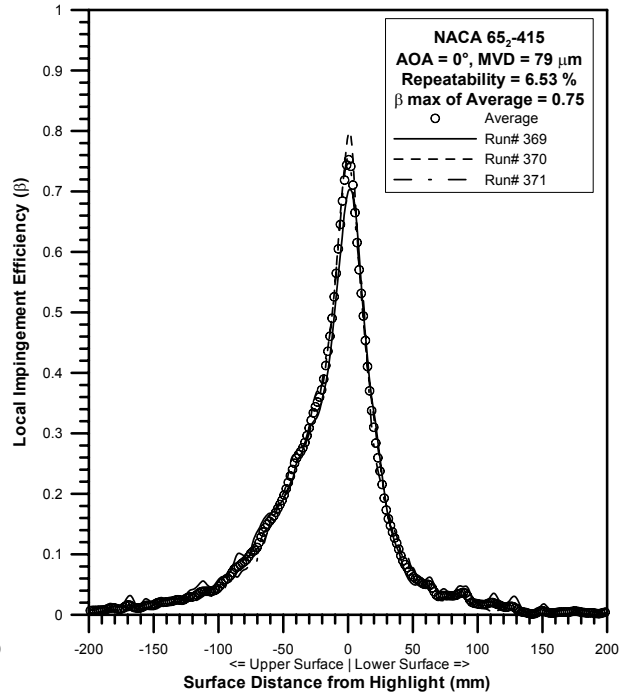
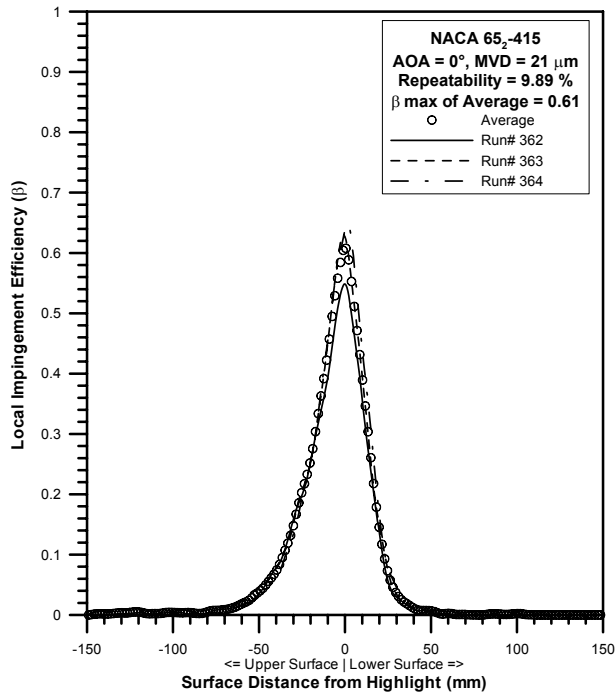


Figure 82.—Test repeatability for NACA 65₂-415 airfoil at AOA = 0° and 4°.

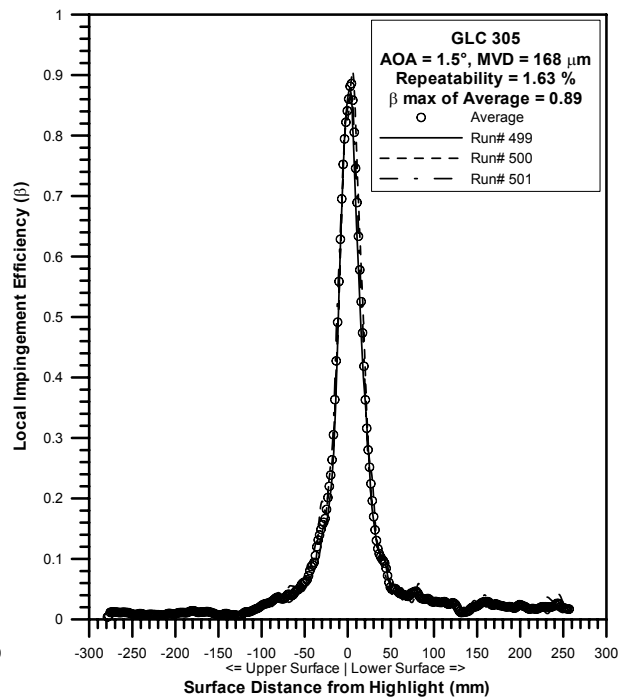
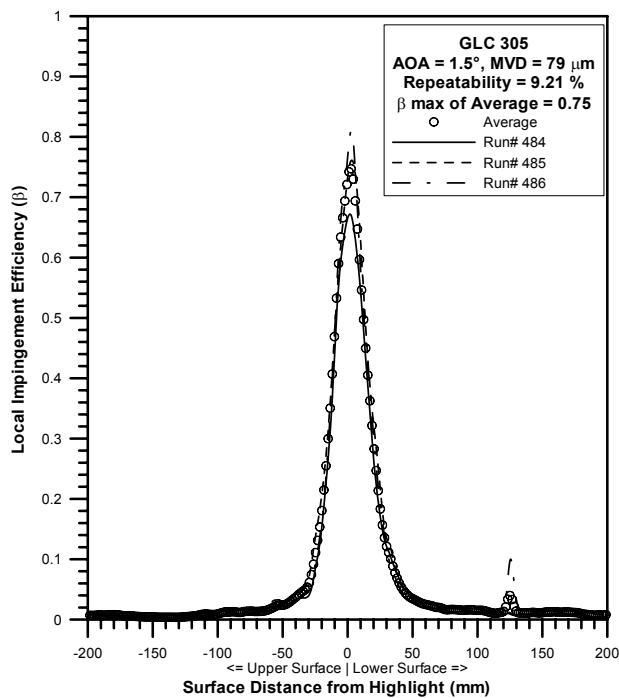
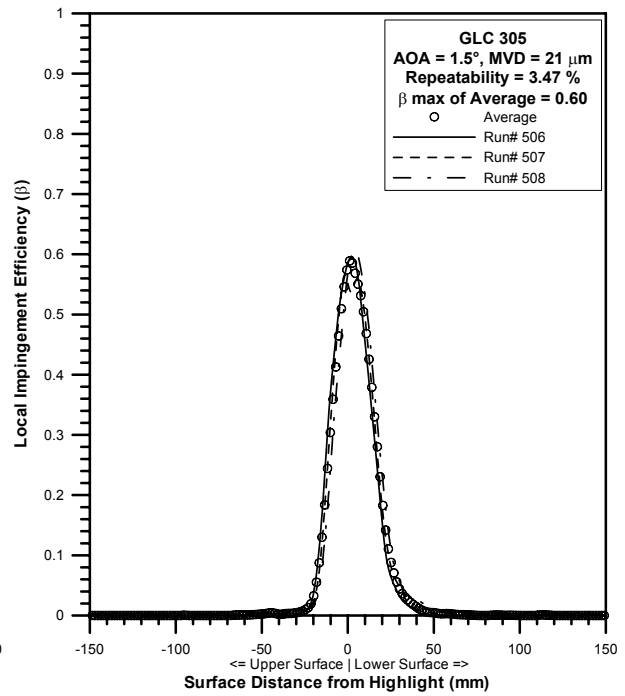
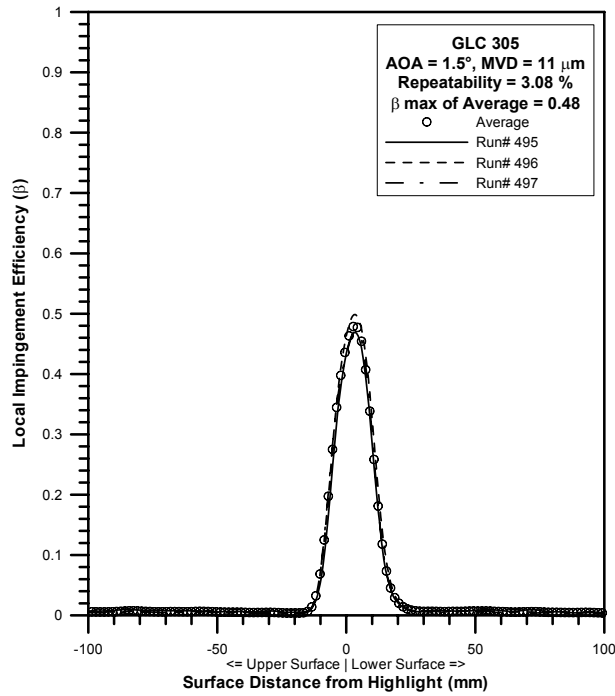


Figure 83.—Test repeatability for GLC–305 airfoil at AOA = 1.5°.

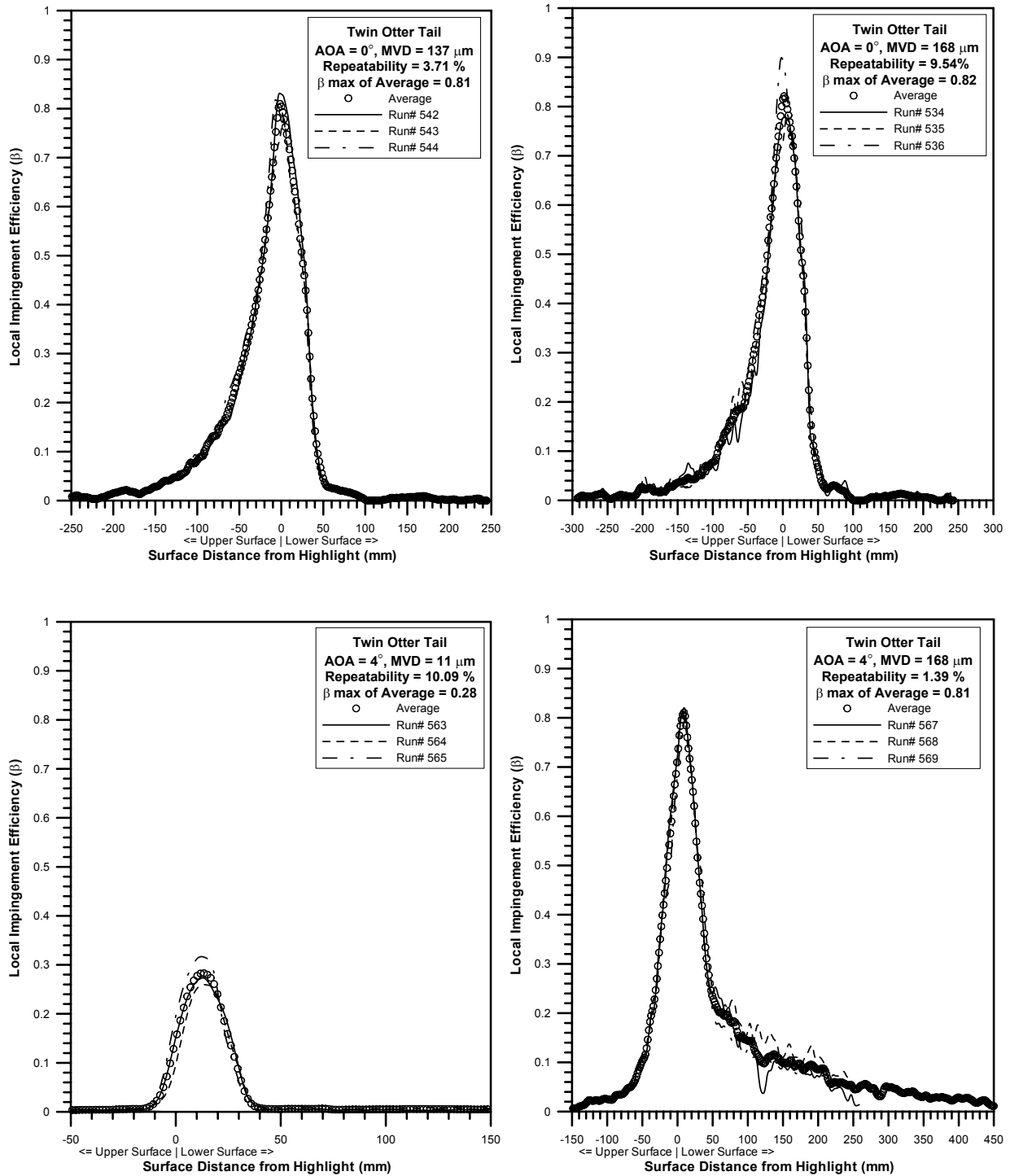


Figure 84.—Test repeatability for Twin Otter tail at AOA = 0° and 4°.

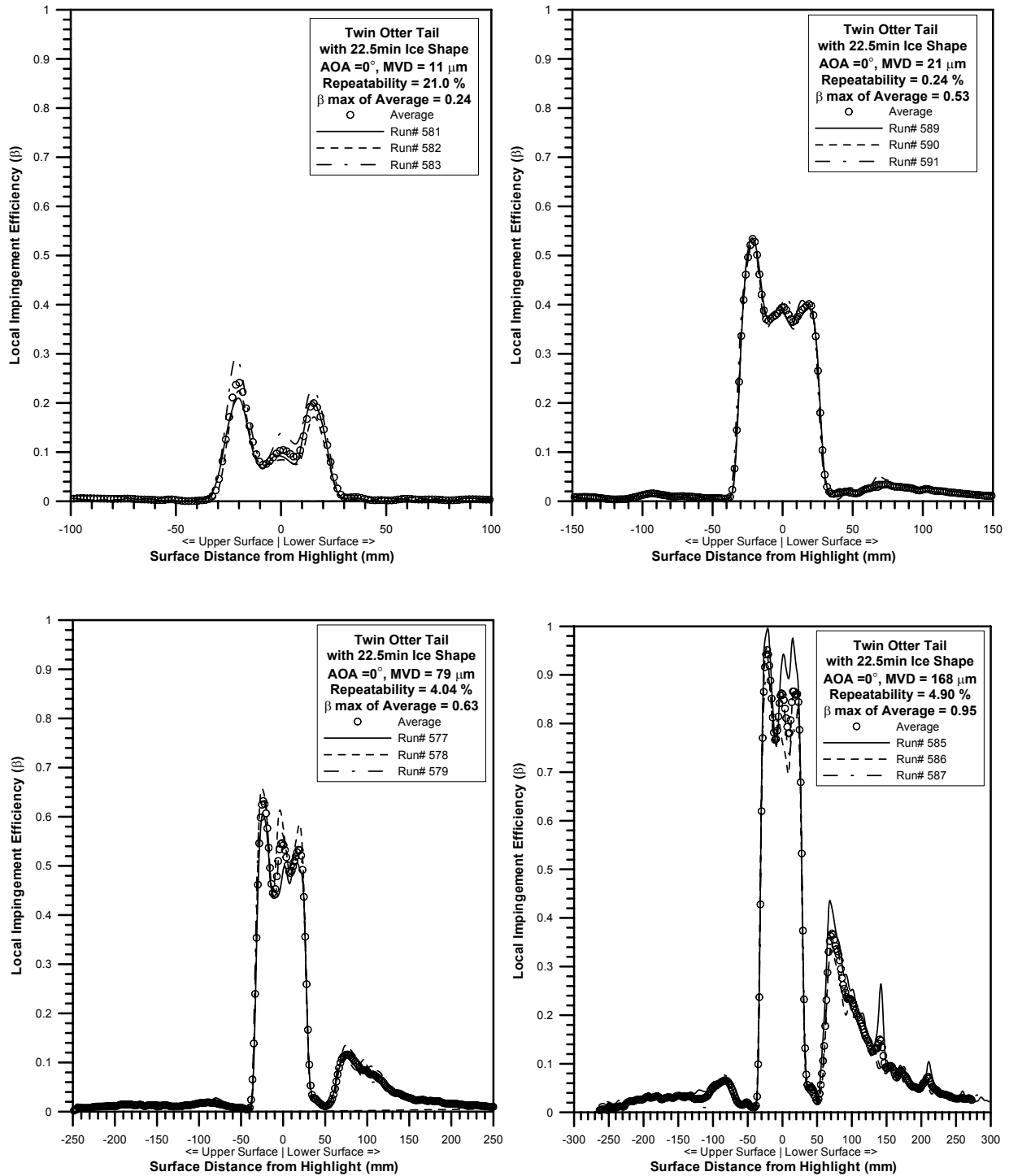


Figure 85.—Test repeatability for Twin Otter tail with 22.5-min ice shape at AOA = 0°.

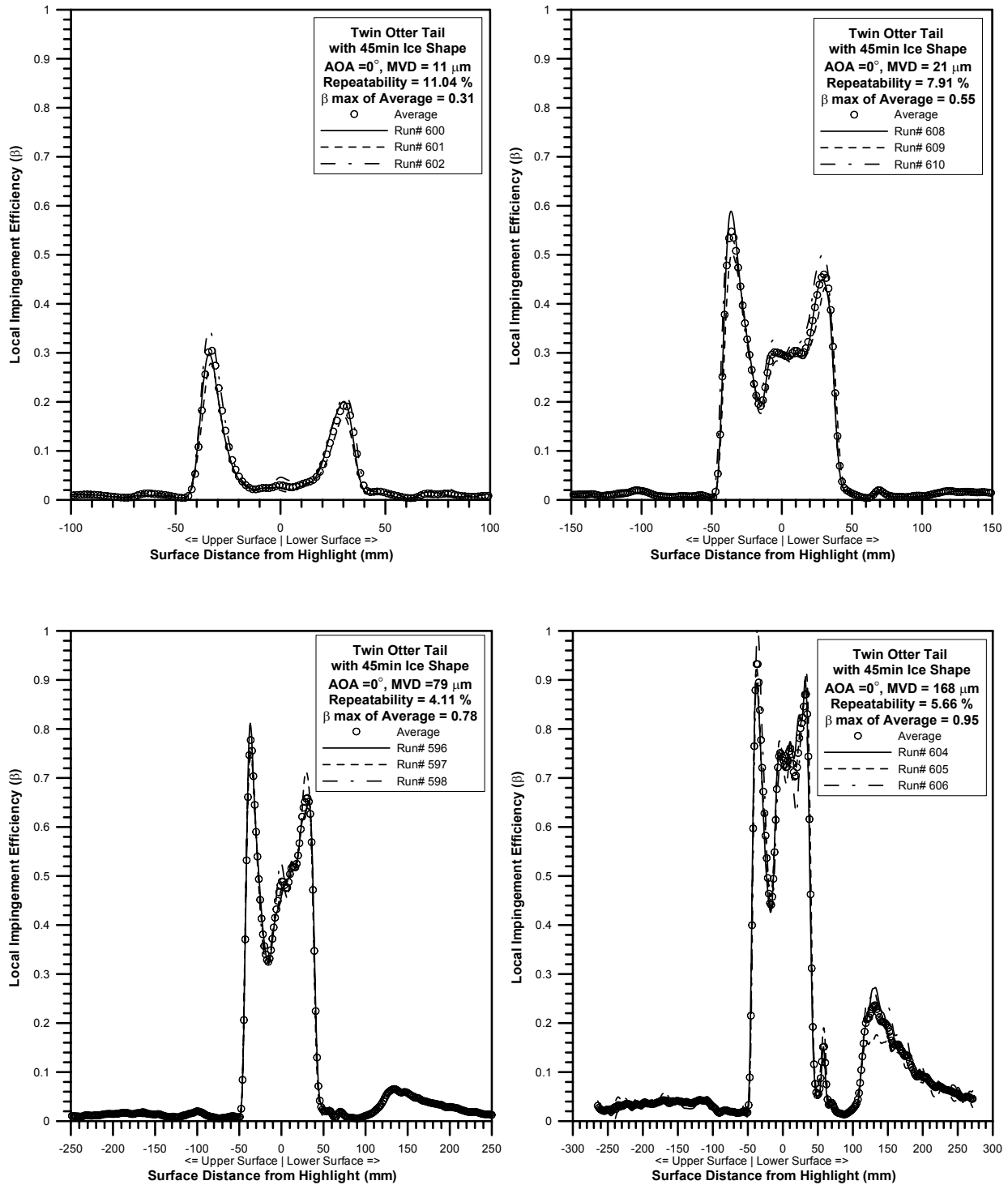


Figure 86.—Test repeatability for Twin Otter tail with 45-min ice shape at AOA = 0°.

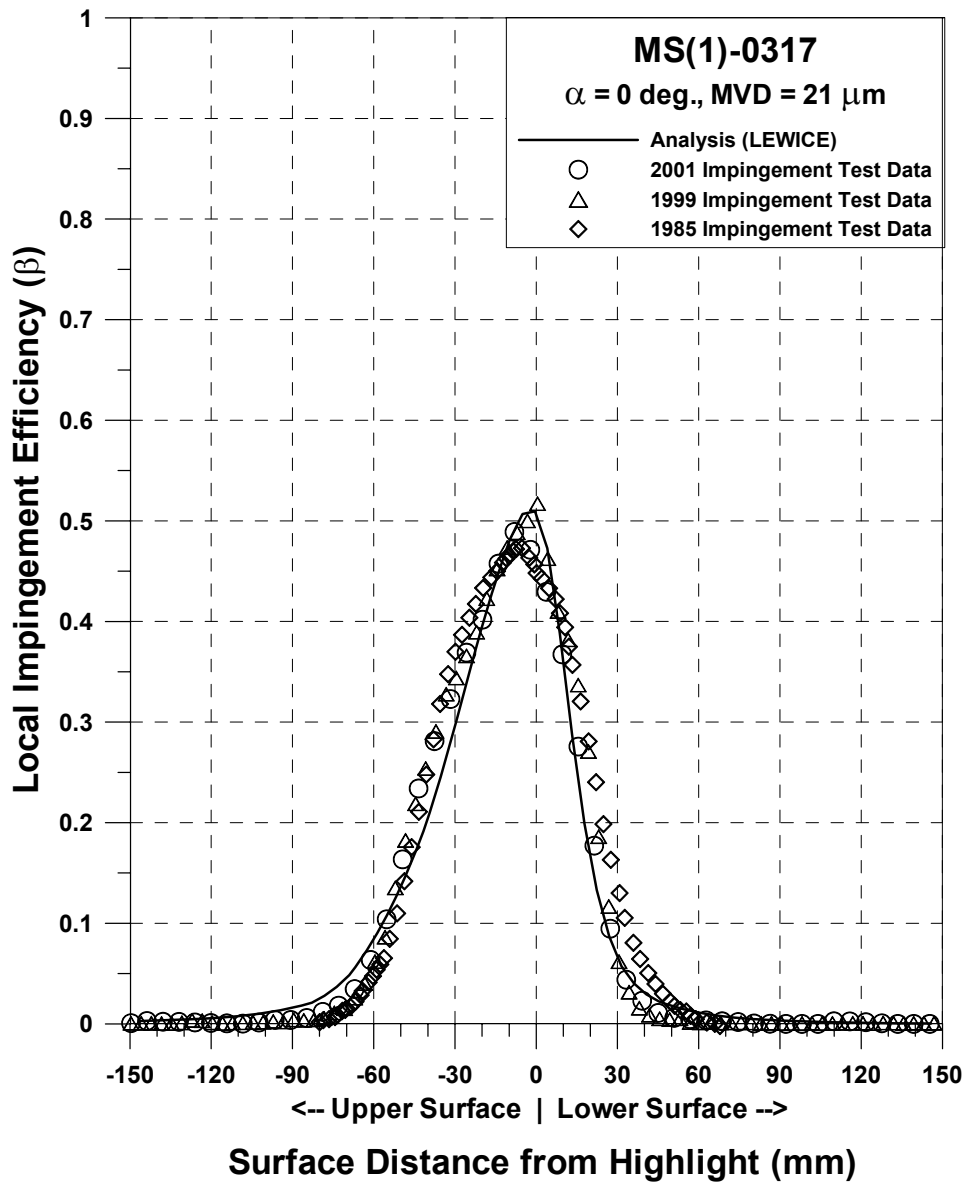


Figure 87a.—Impingement efficiency distribution for MS-317 airfoil from 1985, 1999 and 2001 entries; $c = 36 \text{ in.}$, $V_\infty = 175 \text{ mph}$, $\text{AOA} = 0^\circ$, $\text{MVD} = 21 \mu\text{m}$

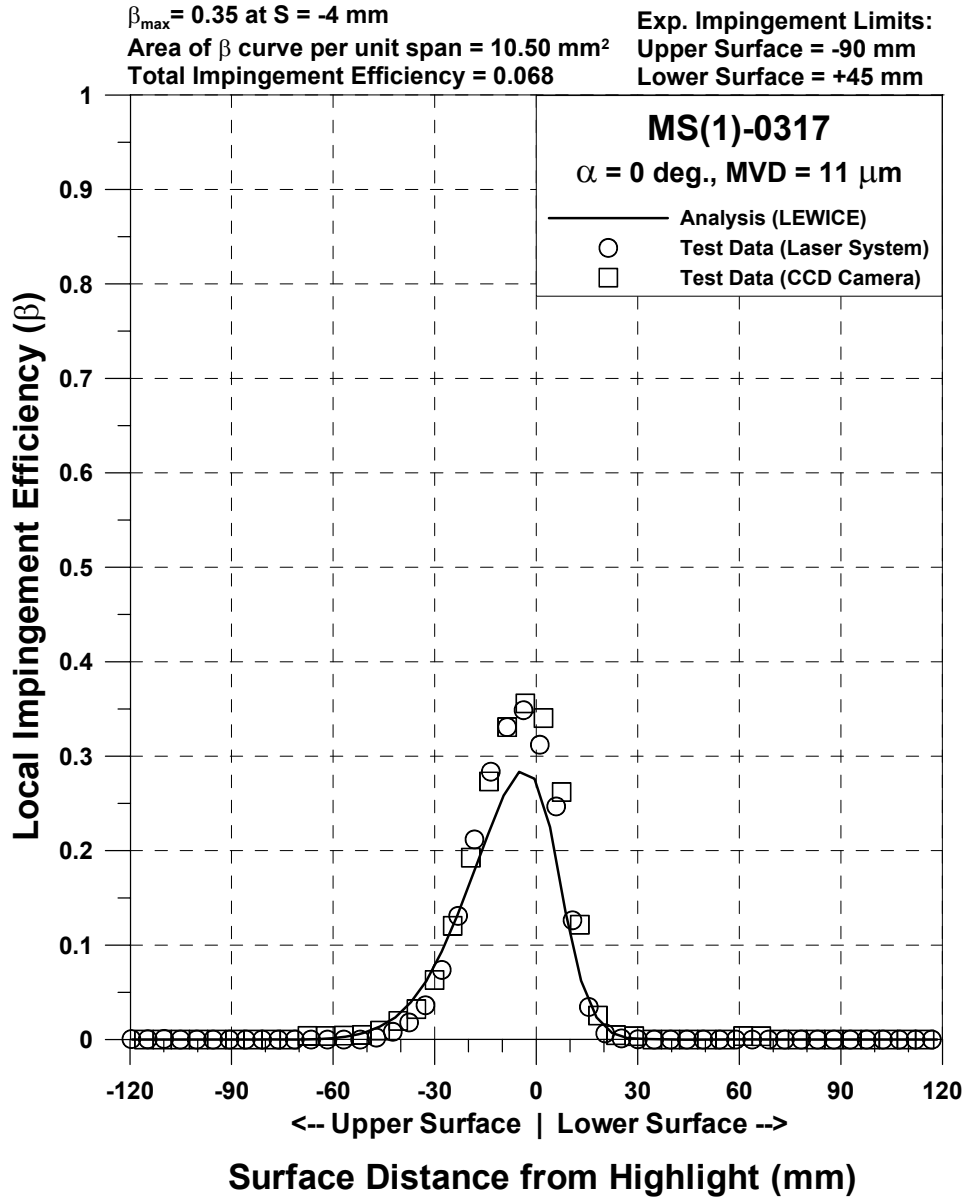


Figure 87b.—Impingement efficiency distribution for MS-317 airfoil;
 $c = 36 \text{ in.}, V_{\infty} = 175 \text{ mph}, \text{AOA} = 0^{\circ}, \text{MVD} = 11 \mu\text{m}.$

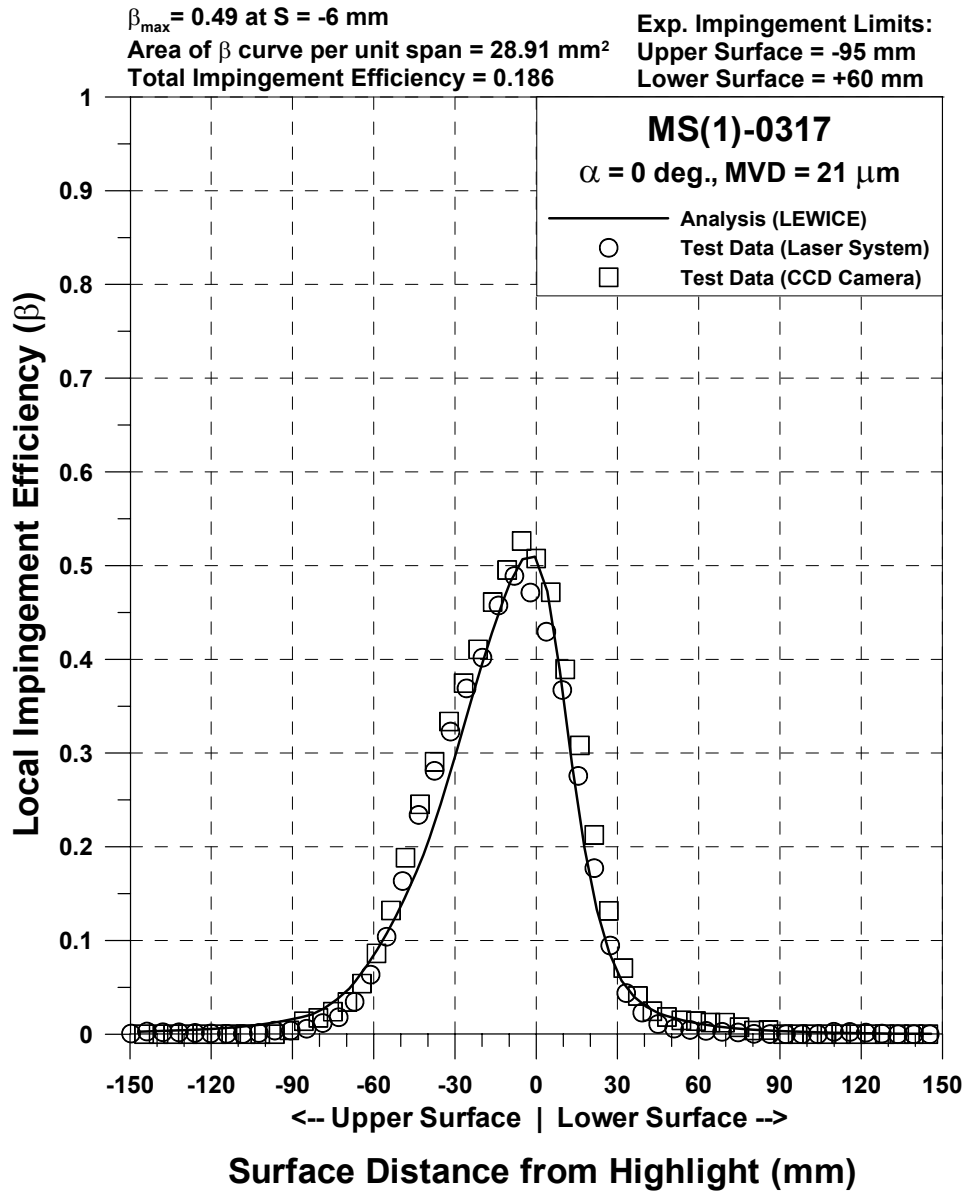


Figure 87c.—Impingement efficiency distribution for MS-317 airfoil;
 $c = 36$ in., $V_{\infty} = 175$ mph, $AOA = 0^{\circ}$, $MVD = 21 \mu\text{m}$

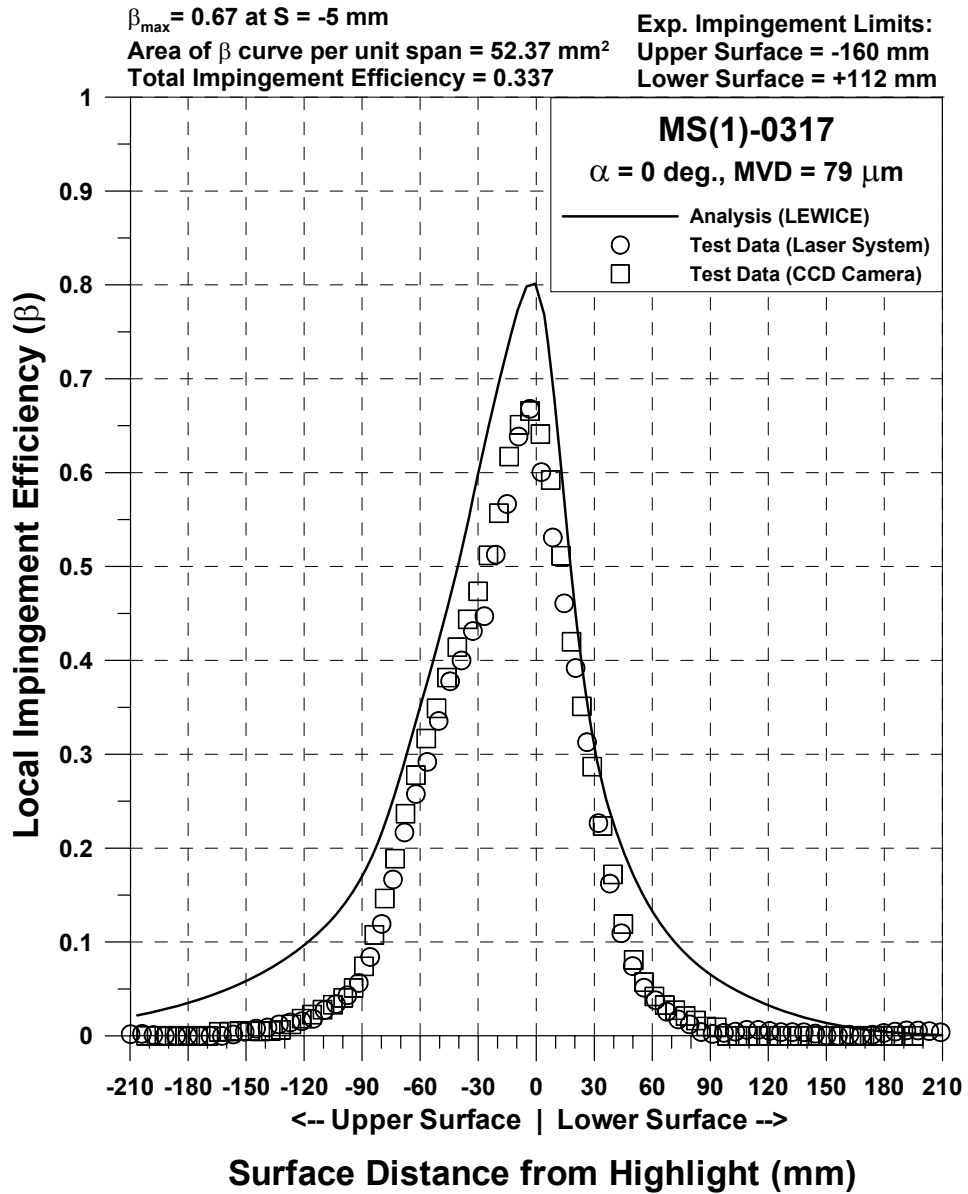


Figure 87d.—Impingement efficiency distribution for MS-317 airfoil;
 $c = 36\text{-in.}$, $V_{\infty} = 175$ mph, $AOA = 0^{\circ}$, $MVD = 79 \mu\text{m}$.

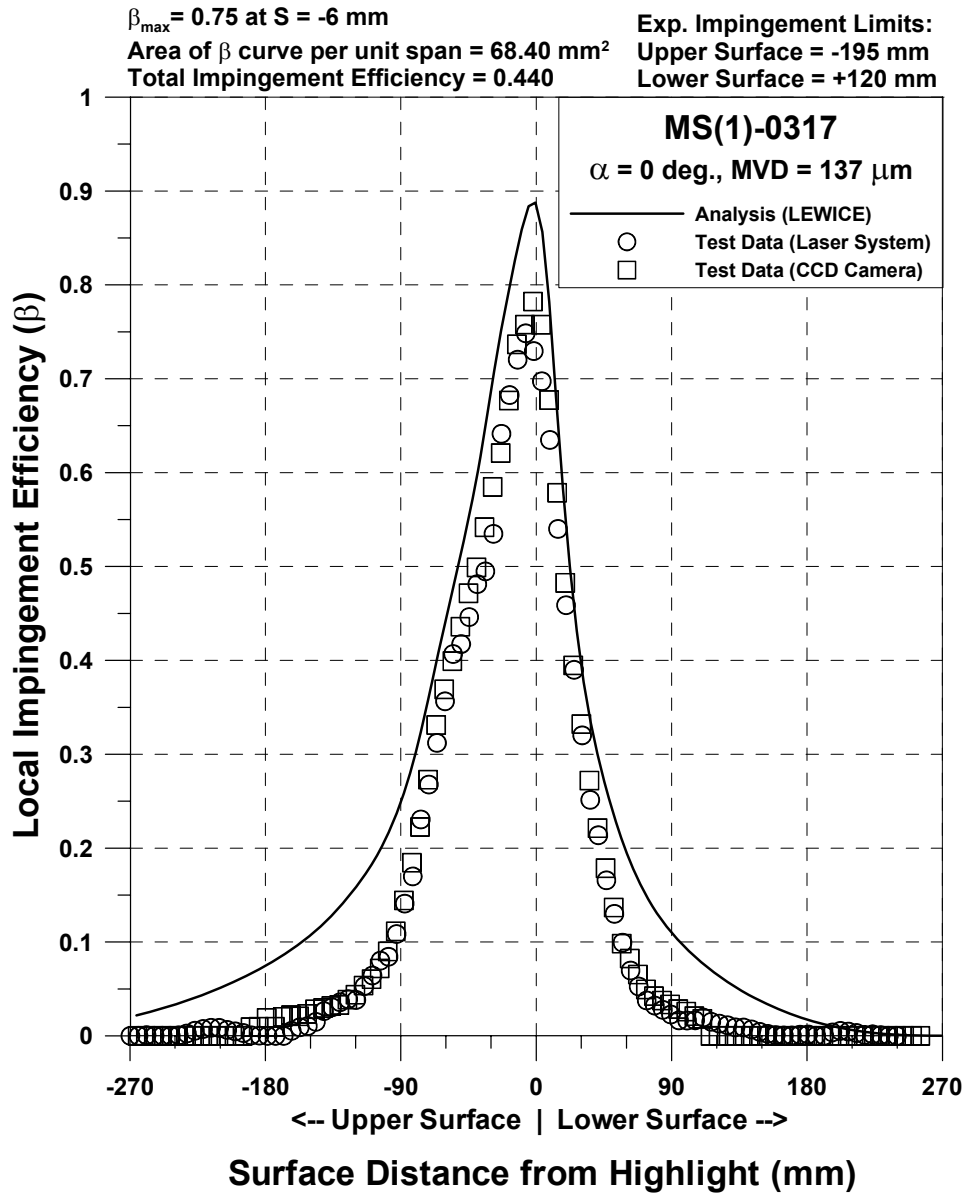


Figure 87e.—Impingement efficiency distribution for MS-317 airfoil;
 $c = 36$ in., $V_{\infty} = 175$ mph, $AOA = 0^{\circ}$, $MVD = 137 \mu\text{m}$.

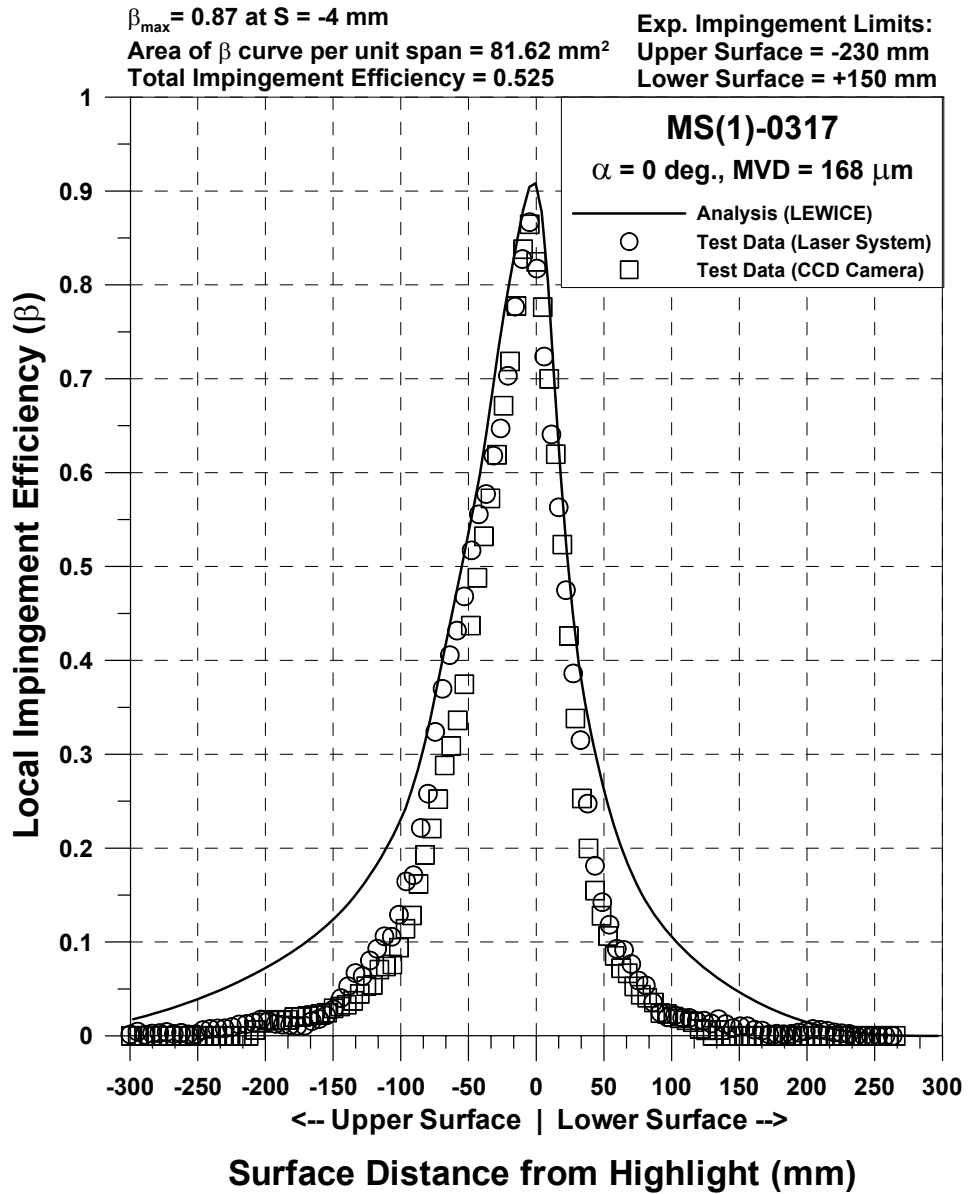


Figure 87f.—Impingement efficiency distribution for MS-317 airfoil;
 $c = 36$ in., $V_{\infty} = 175$ mph, $\text{AOA} = 0^\circ$, $\text{MVD} = 168 \mu\text{m}$.

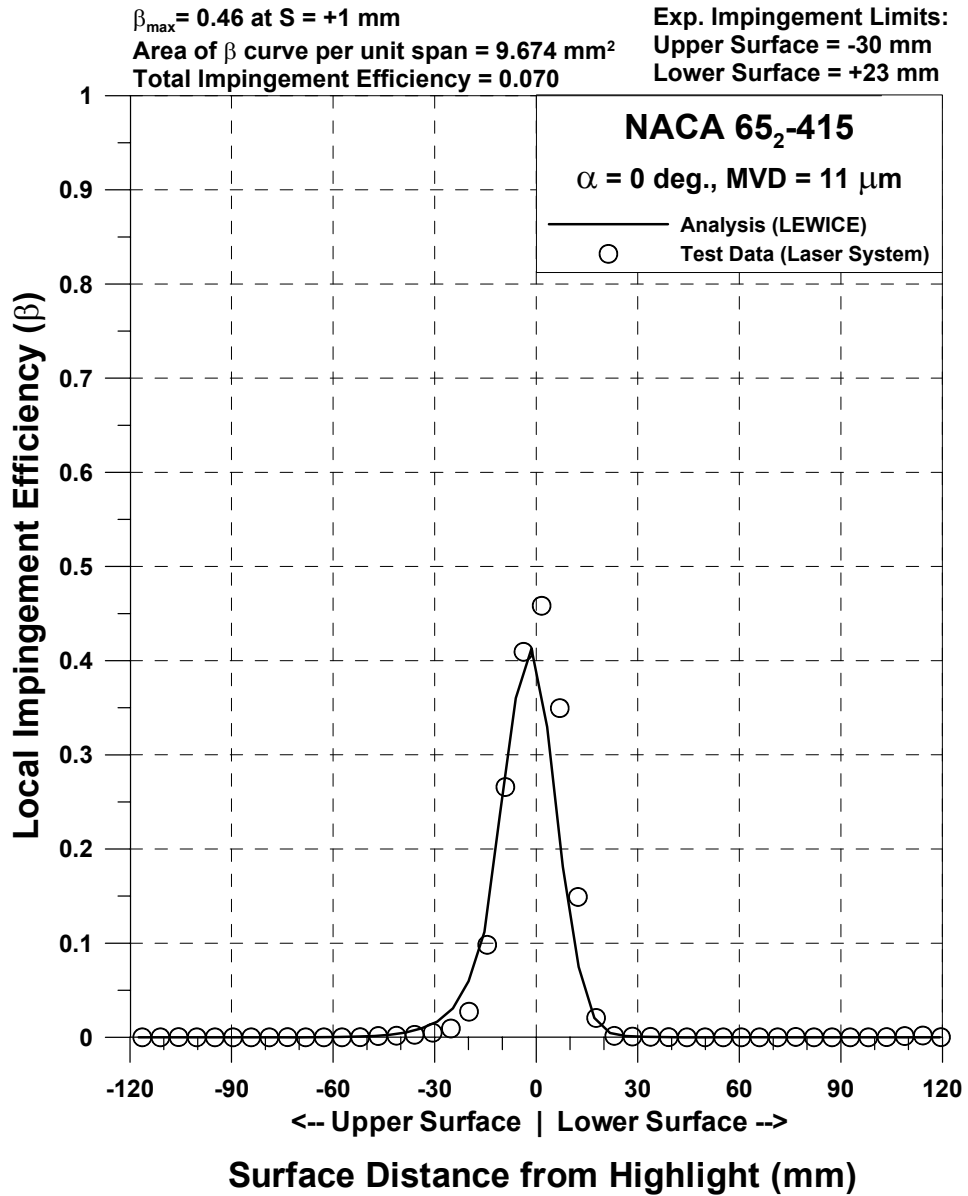


Figure 88a.—Impingement efficiency distribution for NACA 65₂-415 airfoil;
 $c = 36$ in., $V_\infty = 175$ mph, $\text{AOA} = 0^\circ$, $\text{MVD} = 11 \mu\text{m}$.

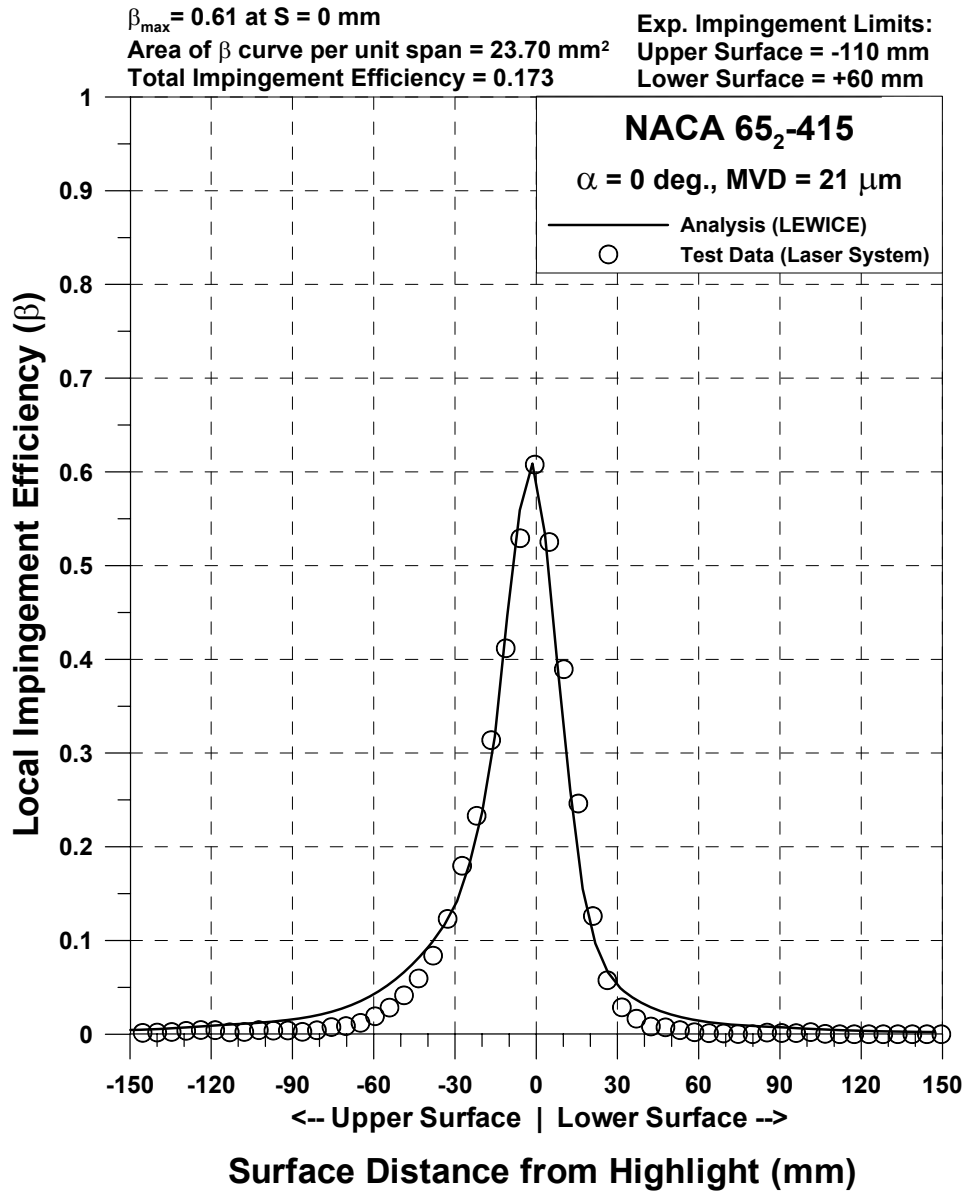


Figure 88b.—Impingement efficiency distribution for NACA 65₂-415 airfoil; $c = 36$ in., $V_\infty = 175$ mph, $\text{AOA} = 0^\circ$, $\text{MVD} = 21 \mu\text{m}$.

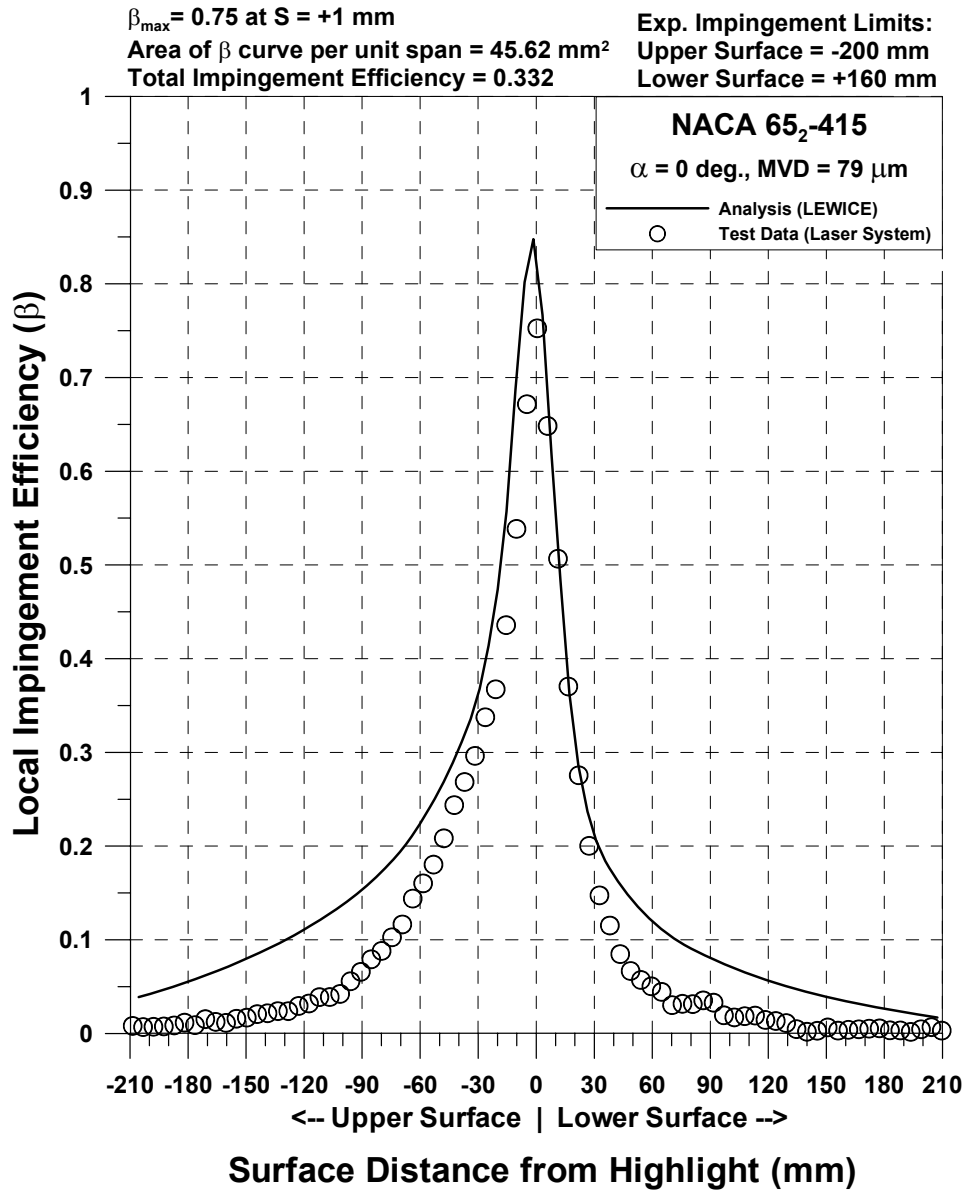


Figure 88c.—Impingement efficiency distribution for NACA 65₂-415 airfoil; $c = 36 \text{ in.}$, $V_{\infty} = 175 \text{ mph}$, $\text{AOA} = 0^\circ$, $\text{MVD} = 79 \text{ }\mu\text{m}$.

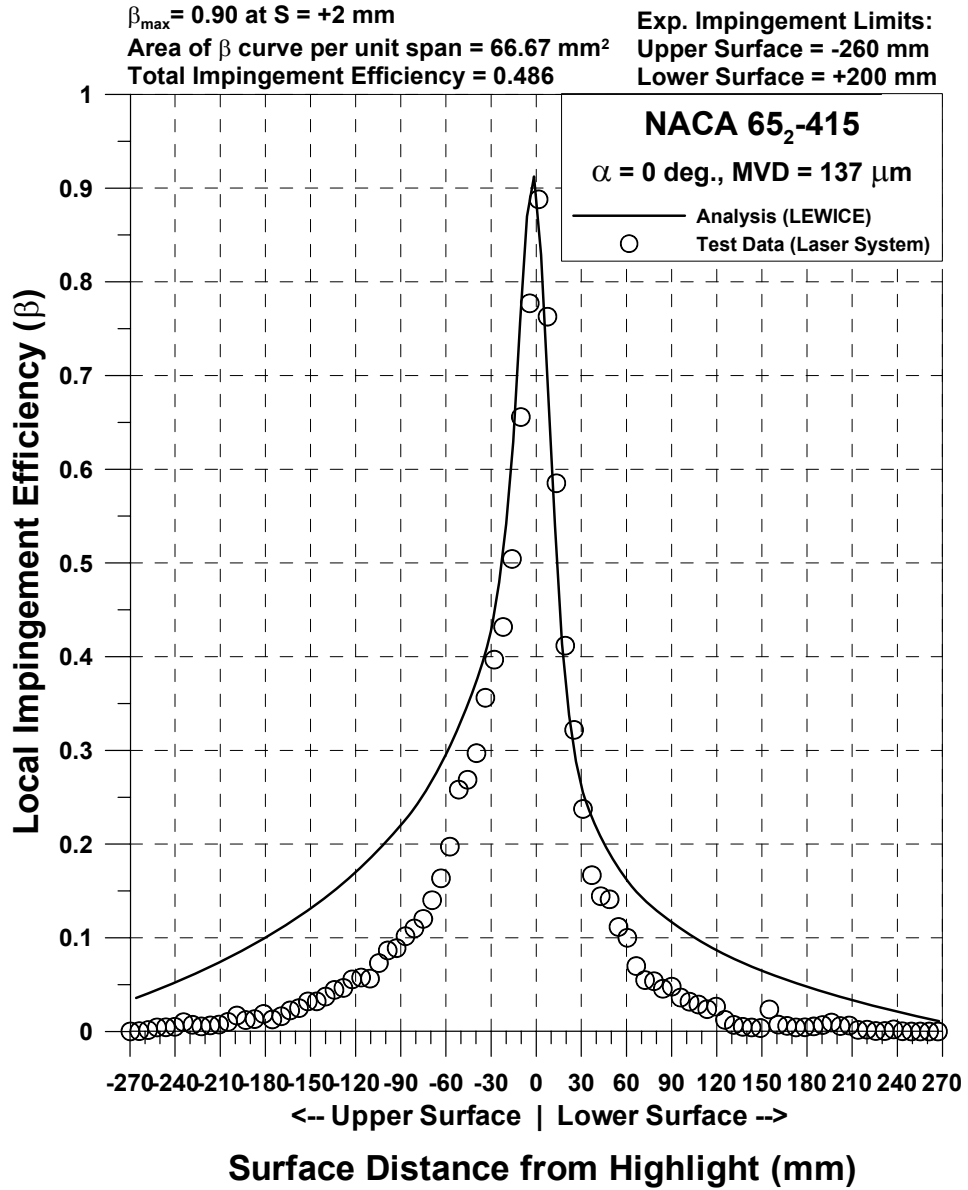


Figure 88d.—Impingement efficiency distribution for NACA 65₂-415 airfoil;
 $c = 36$ in., $V_{\infty} = 175$ mph, $\text{AOA} = 0^\circ$, $\text{MVD} = 137 \mu\text{m}$.

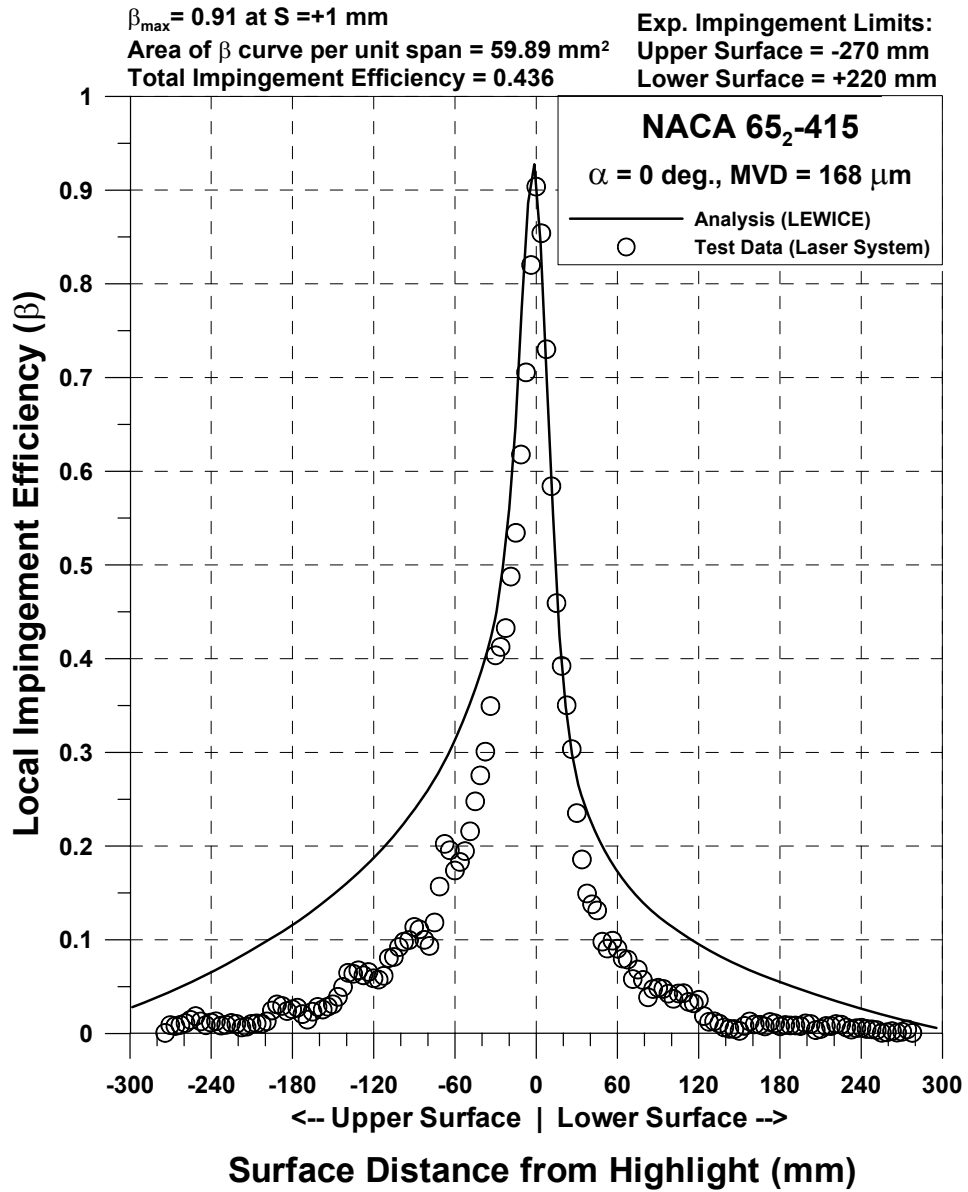


Figure 88e.—Impingement efficiency distribution for NACA 65₂-415 airfoil;
 $c = 36$ in., $V_{\infty} = 175$ mph, $\text{AOA} = 0^\circ$, $\text{MVD} = 168 \mu\text{m}$.

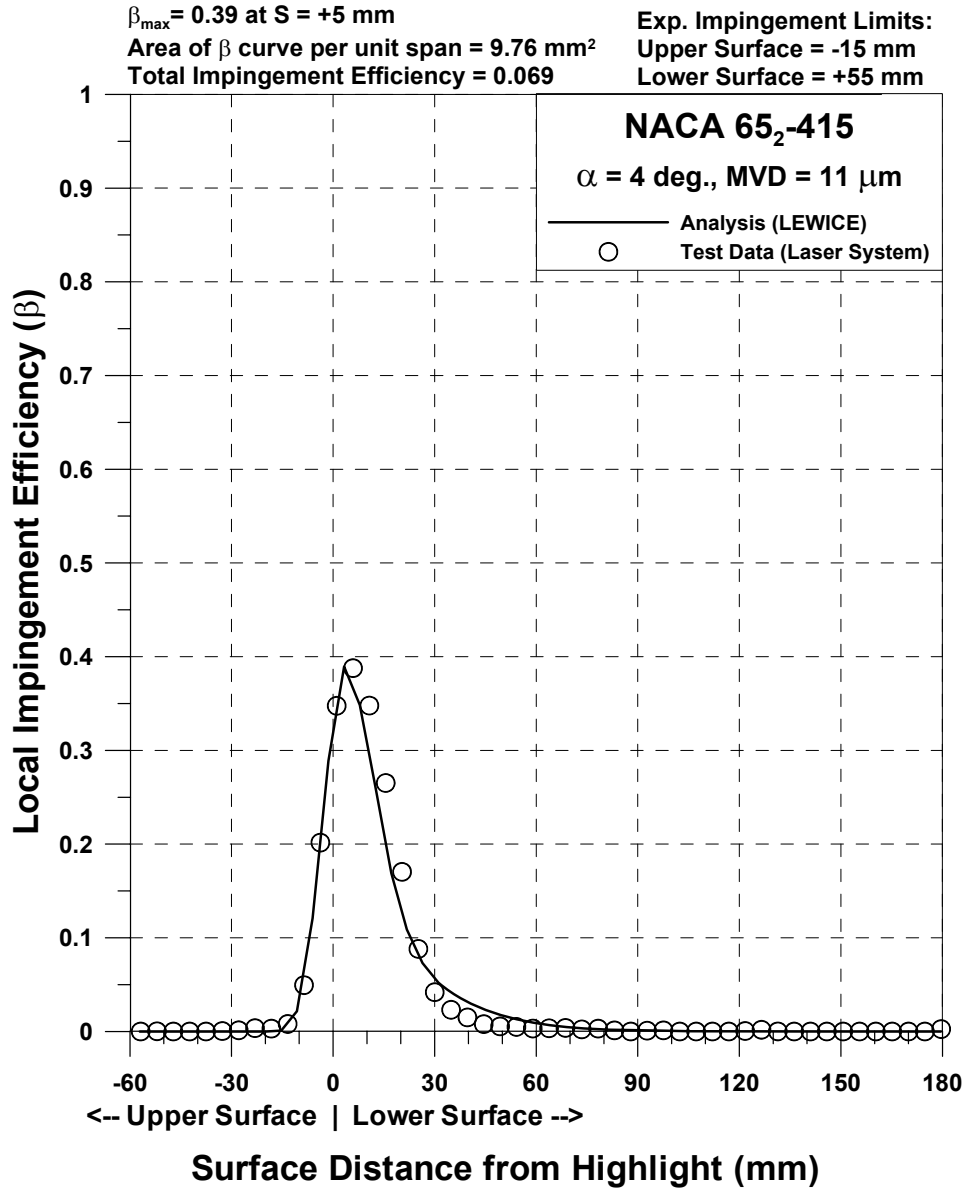


Figure 89a.—Impingement efficiency distribution for NACA 65₂-415 airfoil; $c = 36$ in., $V_\infty = 175$ mph, $\text{AOA} = 4^\circ$, $\text{MVD} = 11 \mu\text{m}$.

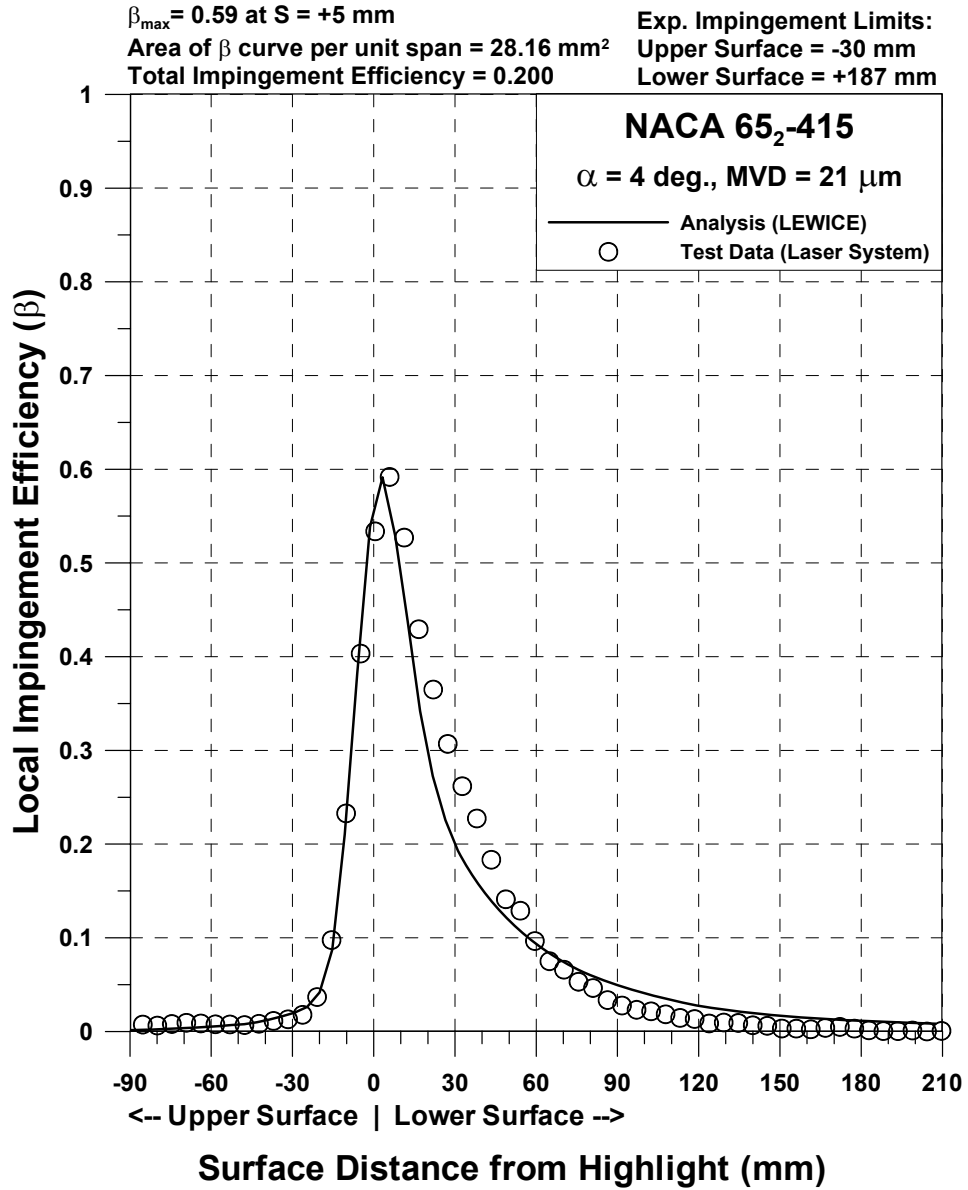


Figure 89b.—Impingement efficiency distribution for NACA 65₂-415 airfoil; $c = 36$ in., $V_{\infty} = 175$ mph, $\text{AOA} = 4^{\circ}$, $\text{MVD} = 21 \mu\text{m}$.

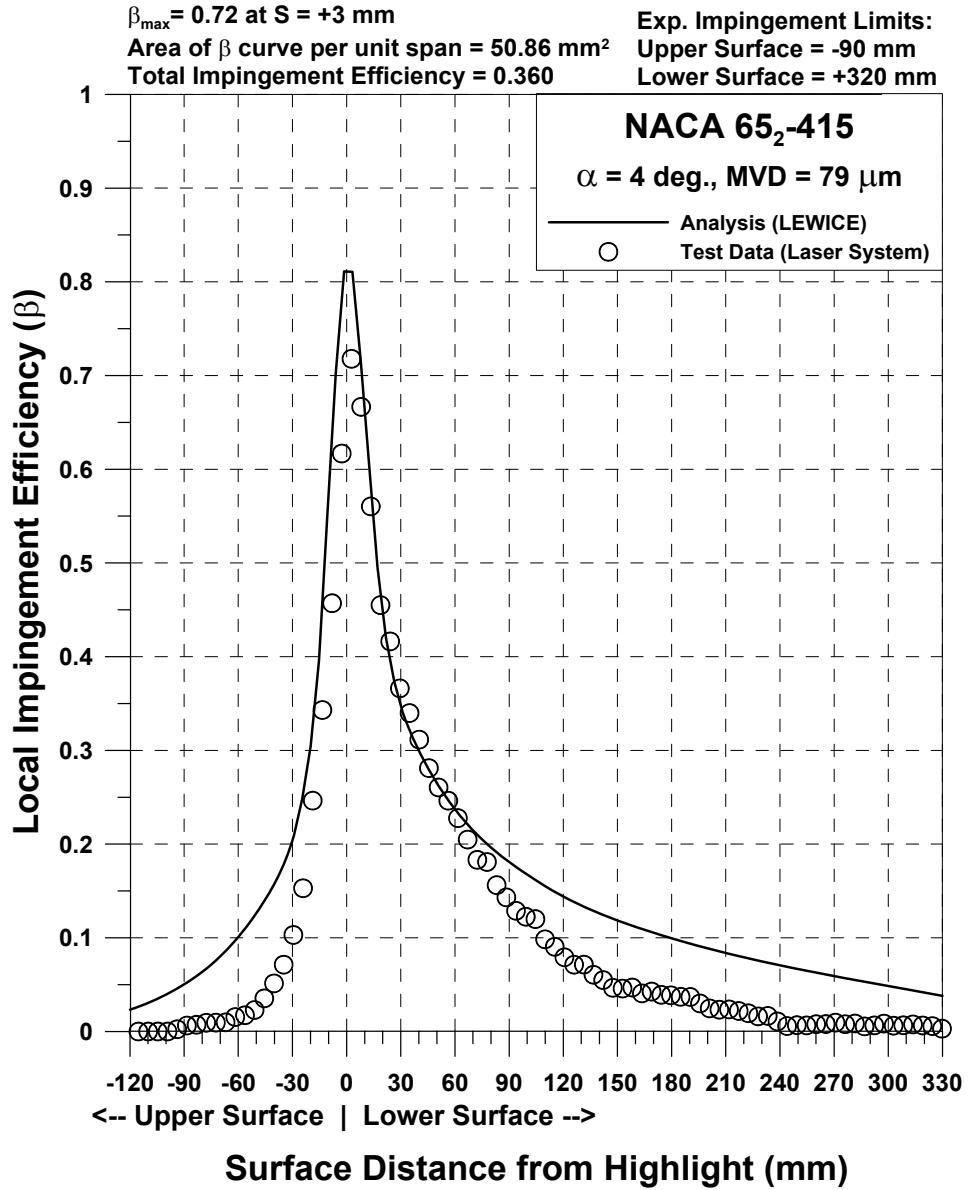


Figure 89c.—Impingement efficiency distribution for NACA 65₂-415 airfoil;
 $c = 36$ in., $V_{\infty} = 175$ mph, $\text{AOA} = 4^{\circ}$, $\text{MVD} = 79 \mu\text{m}$.

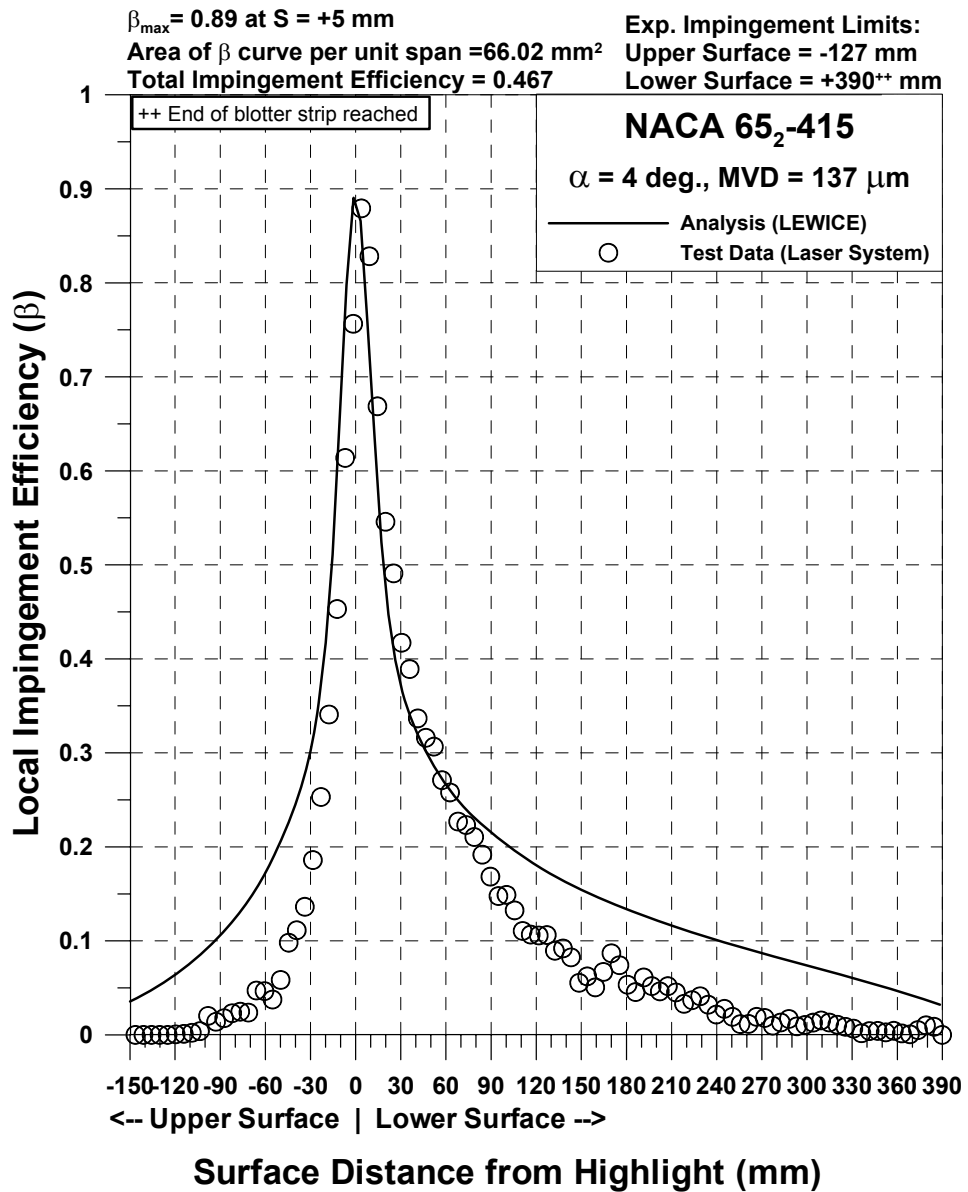


Figure 89d.—Impingement efficiency distribution for NACA 65₂-415 airfoil;
 $c = 36$ in., $V_{\infty} = 175$ mph, $\text{AOA} = 4^\circ$, $\text{MVD} = 137 \mu\text{m}$.

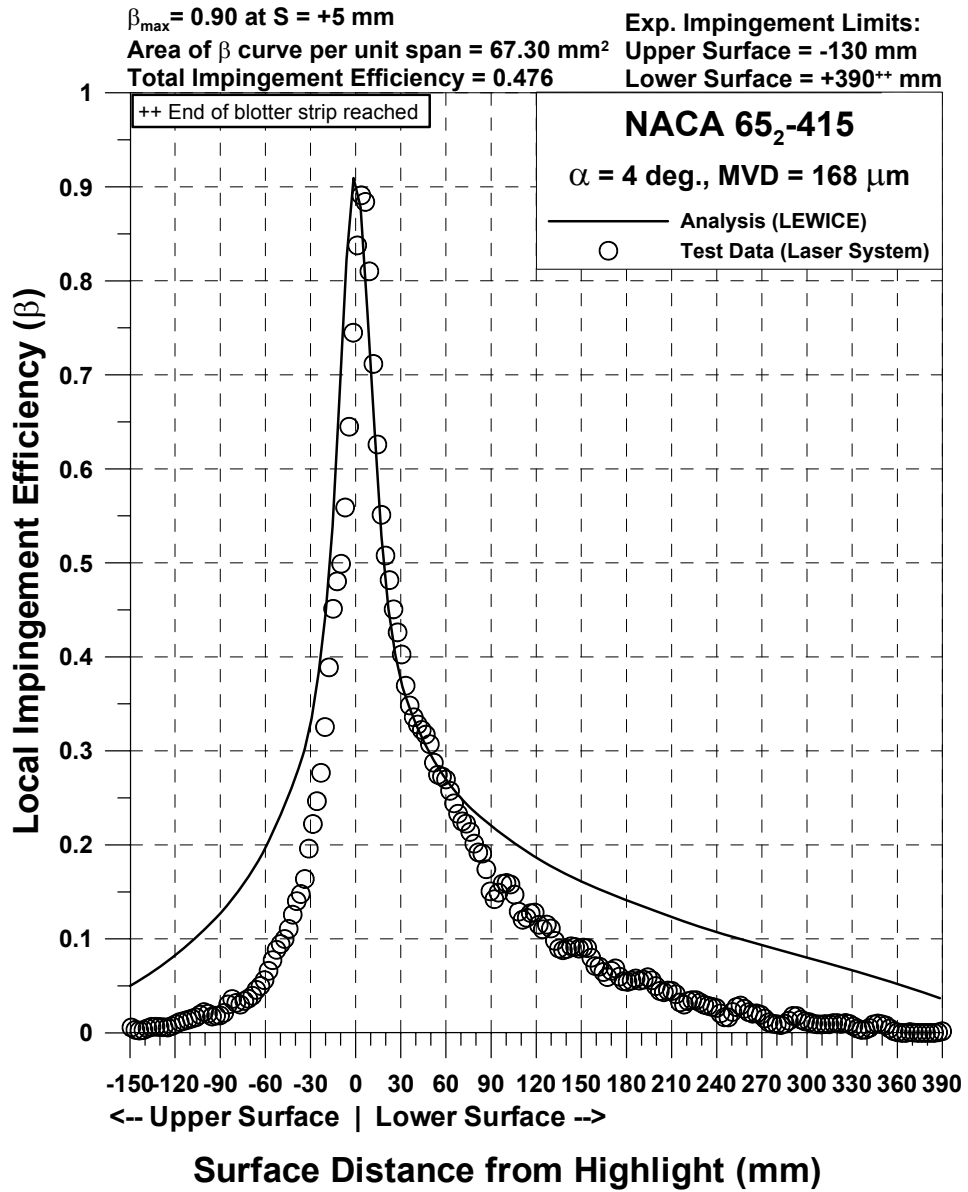


Figure 89e.—Impingement efficiency distribution for NACA 65₂-415 airfoil;
 $c = 36 \text{ in.}$, $V_{\infty} = 175 \text{ mph}$, $AOA = 4^{\circ}$, $MVD = 168 \mu\text{m}$.

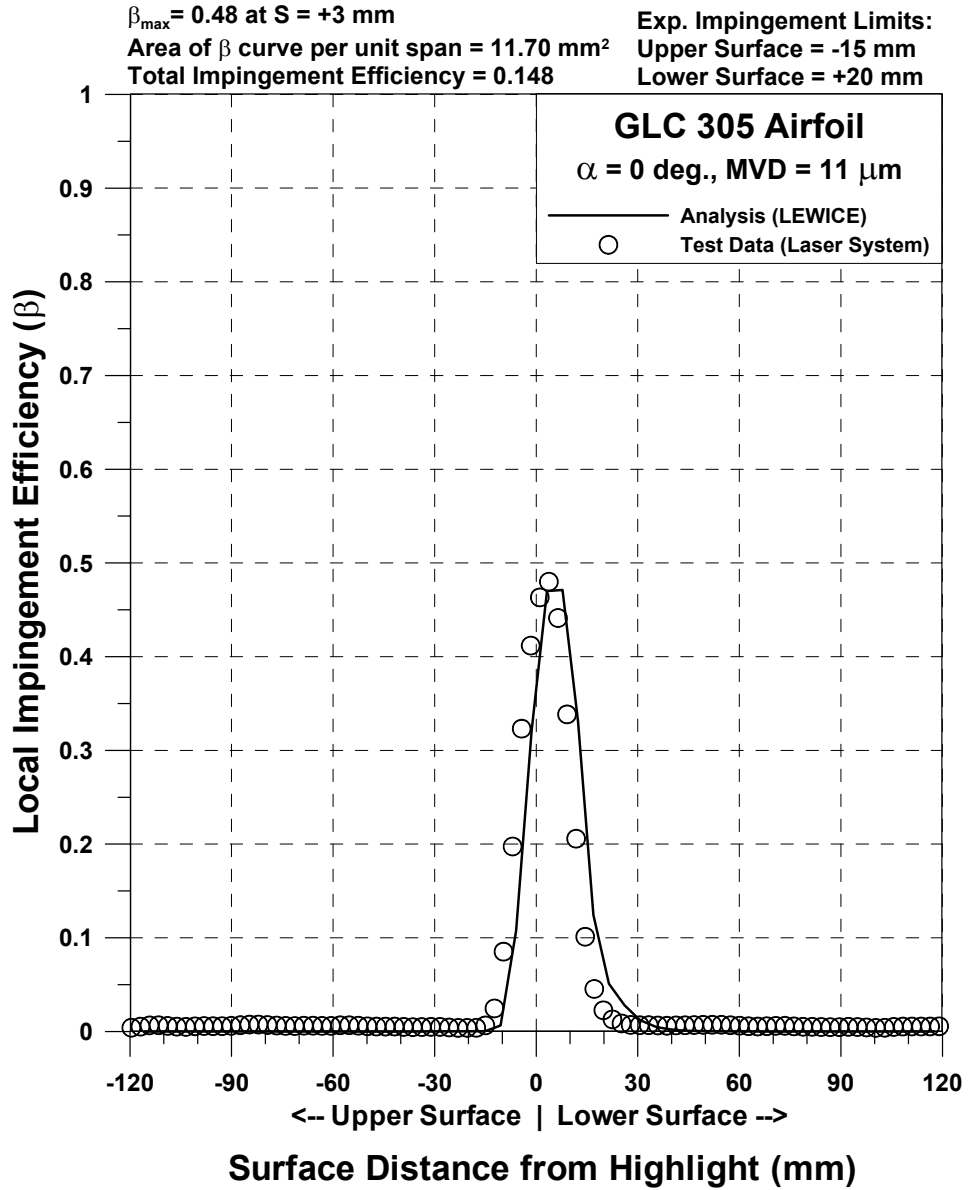


Figure 90a.—Impingement efficiency distribution for GLC-305 airfoil;
 $c = 36$ in., $V_{\infty} = 175$ mph, AOA = 1.5°, MVD = 11 μ m.

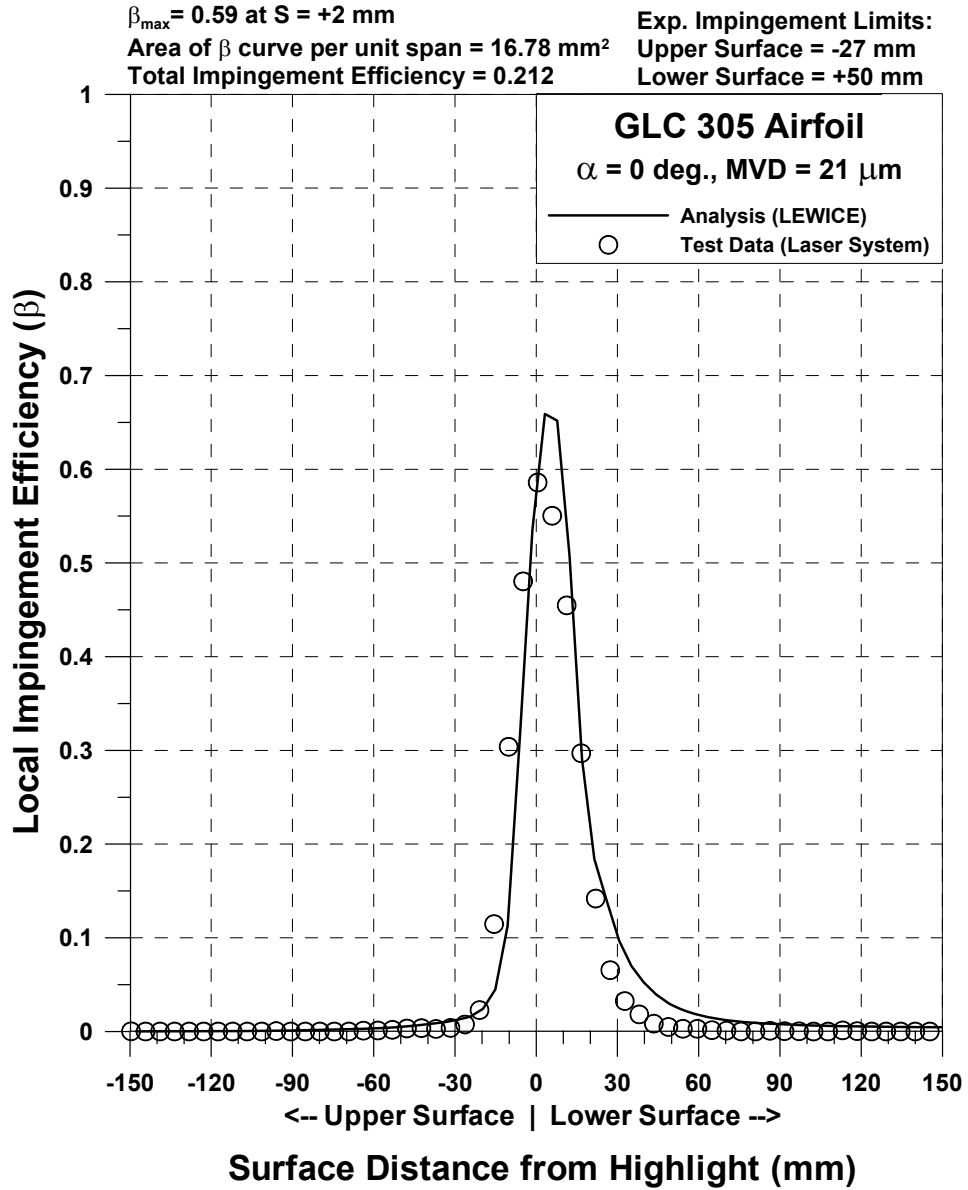


Figure 90b.—Impingement efficiency distribution for GLC-305 airfoil; $c = 36$ in., $V_\infty = 175$ mph, $\text{AOA} = 1.5^\circ$, $\text{MVD} = 21 \mu\text{m}$.

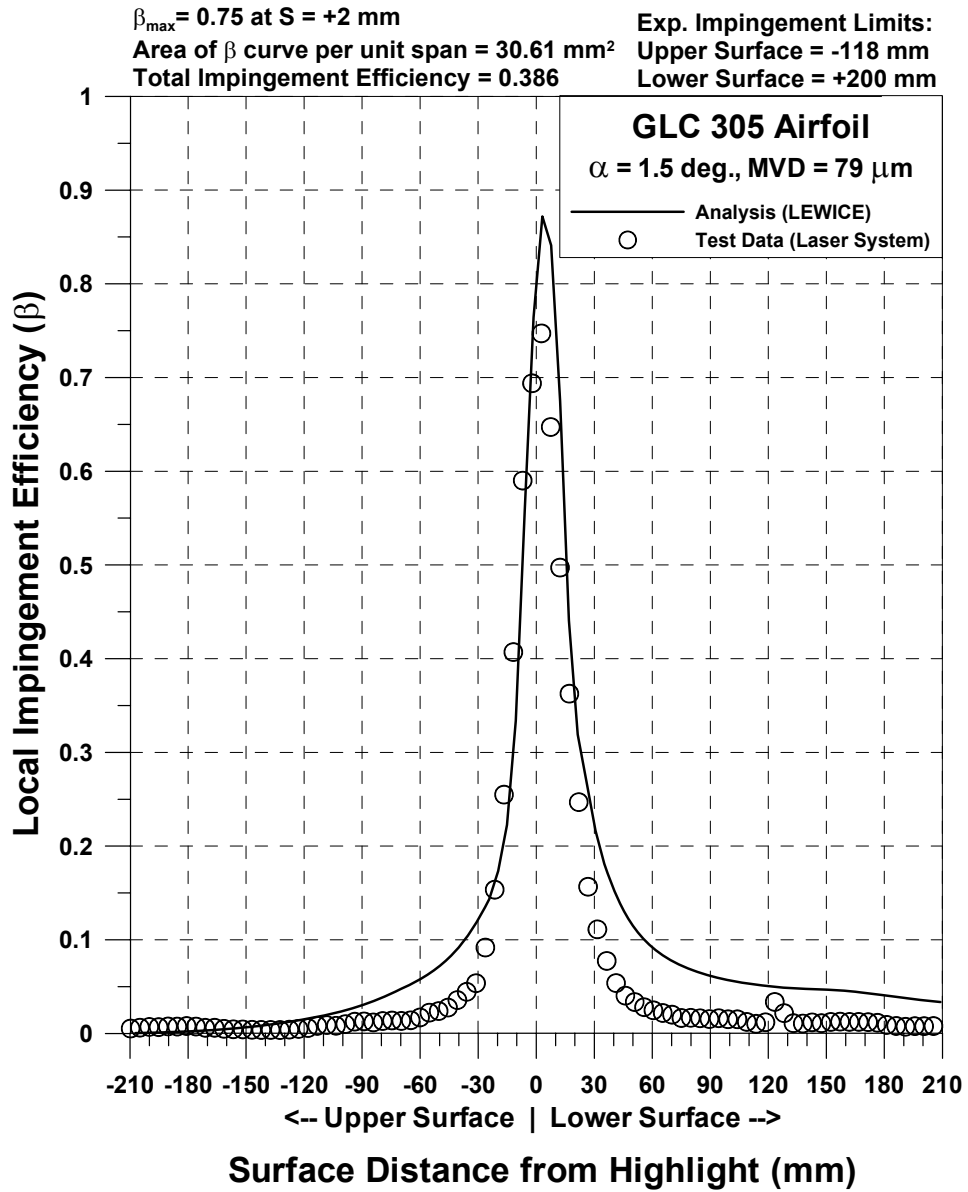


Figure 90c.—Impingement efficiency distribution for GLC-305 airfoil;
 $c = 36$ in., $V_\infty = 175$ mph, AOA = 1.5°, MVD = 79 μ m.

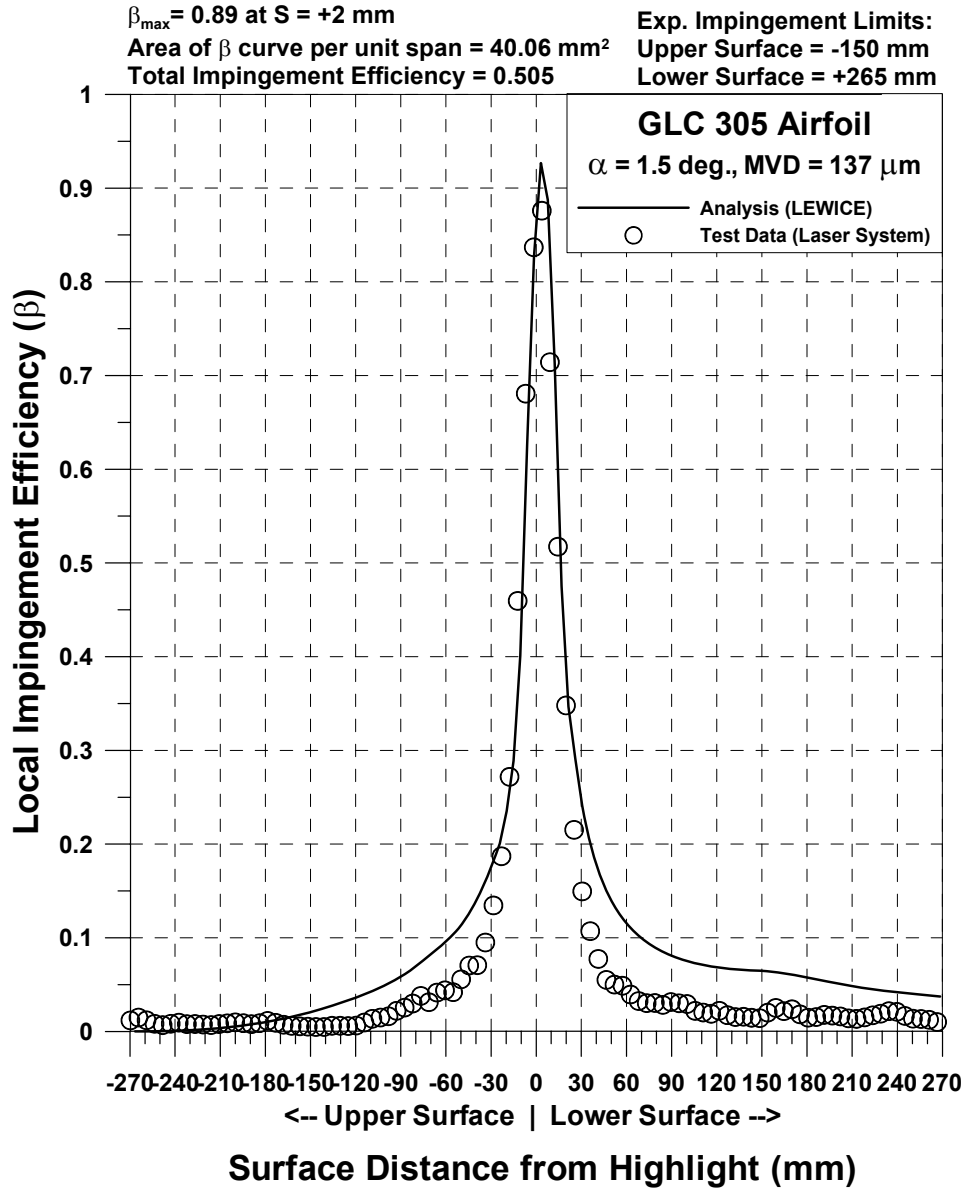


Figure 90d.—Impingement efficiency distribution for GLC-305 airfoil;
 $c = 36$ in., $V_\infty = 175$ mph, $AOA = 1.5^\circ$, $MVD = 137 \mu\text{m}$.

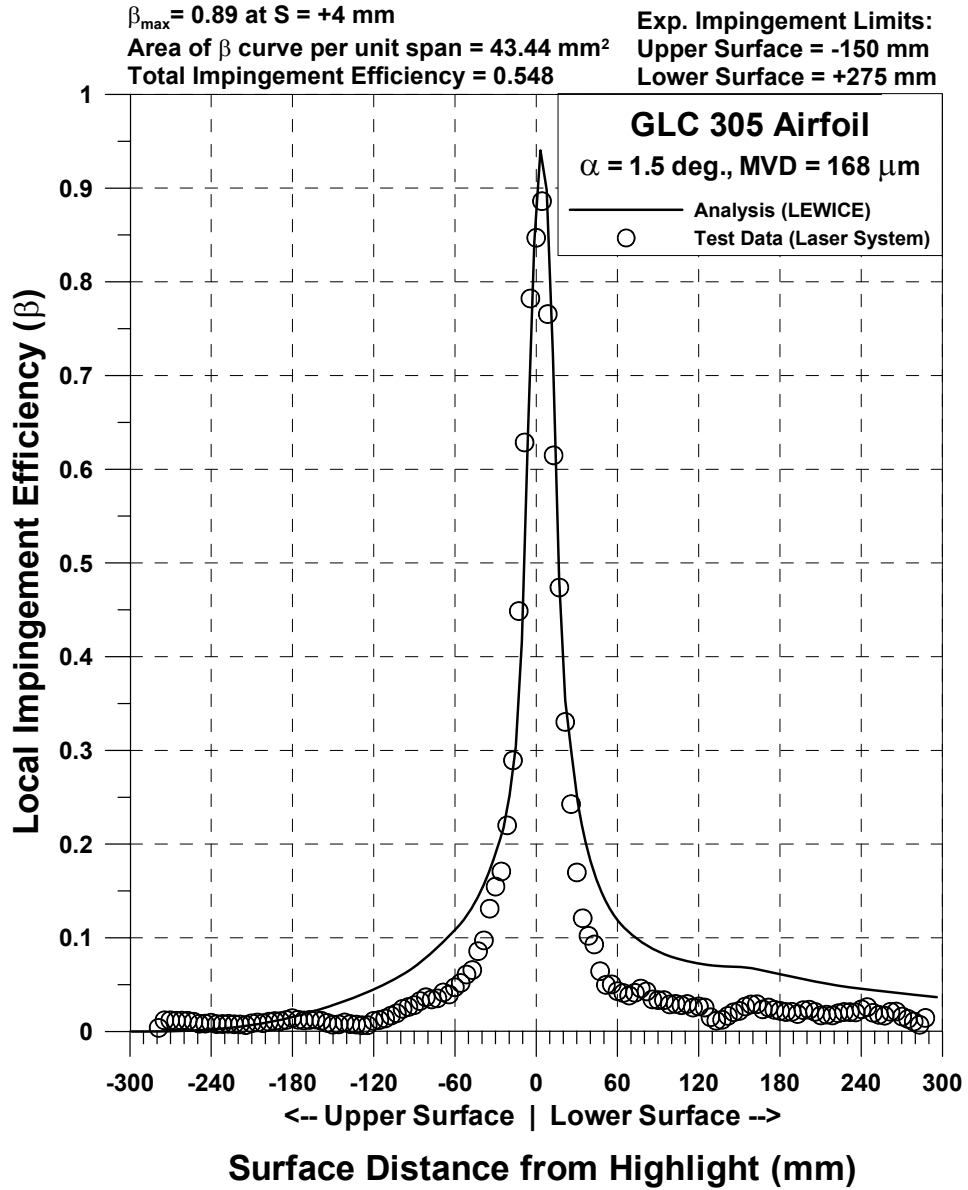


Figure 90e.—Impingement efficiency distribution for GLC-305 airfoil;
 $c = 36$ in., $V_{\infty} = 175$ mph, $AOA = 1.5^{\circ}$, $MVD = 168 \mu\text{m}$.

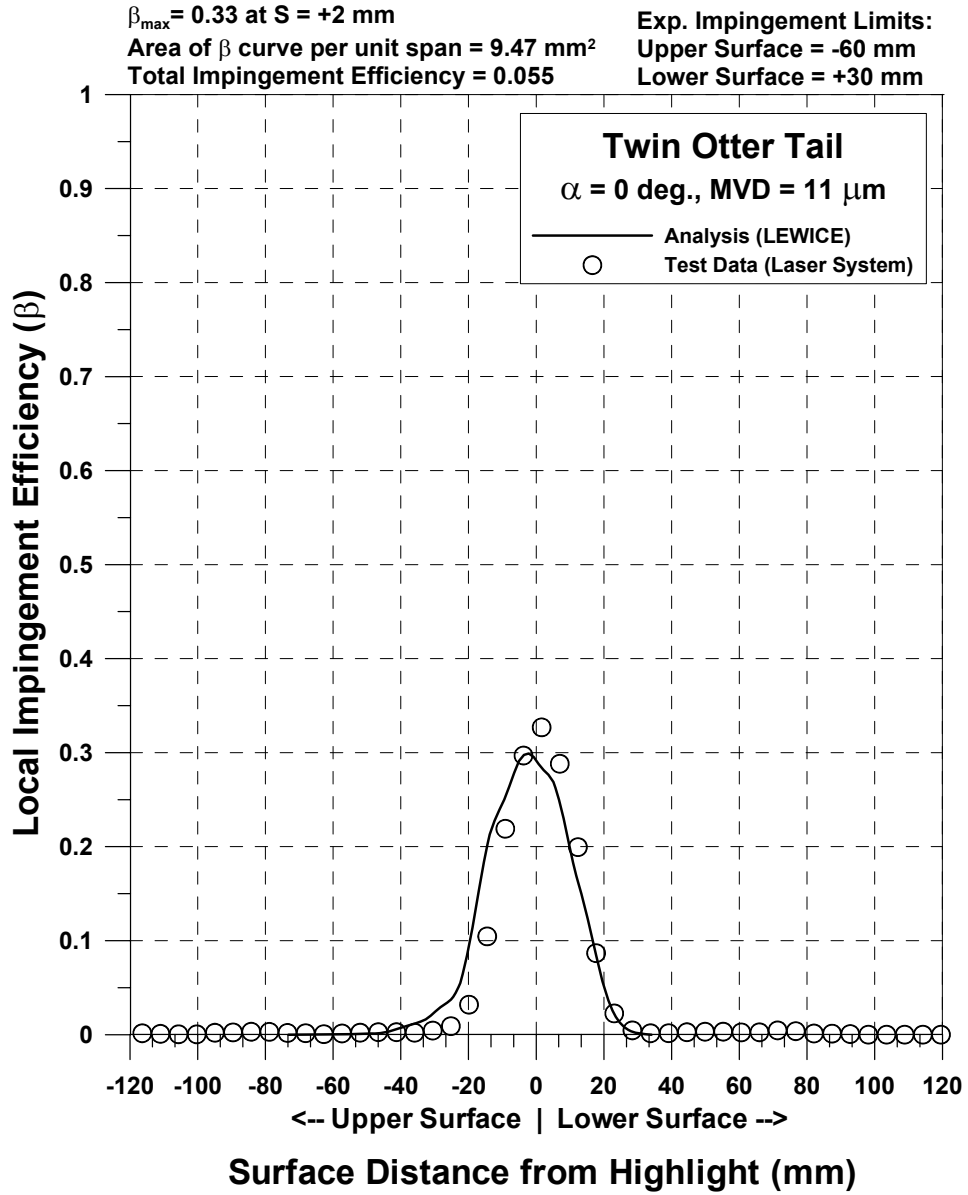


Figure 91a.—Impingement efficiency distribution for Twin Otter tail; $c = 57 \text{ in.}, V_{\infty} = 175 \text{ mph}, \text{AOA} = 0^{\circ}, \text{MVD} = 11 \mu\text{m}.$

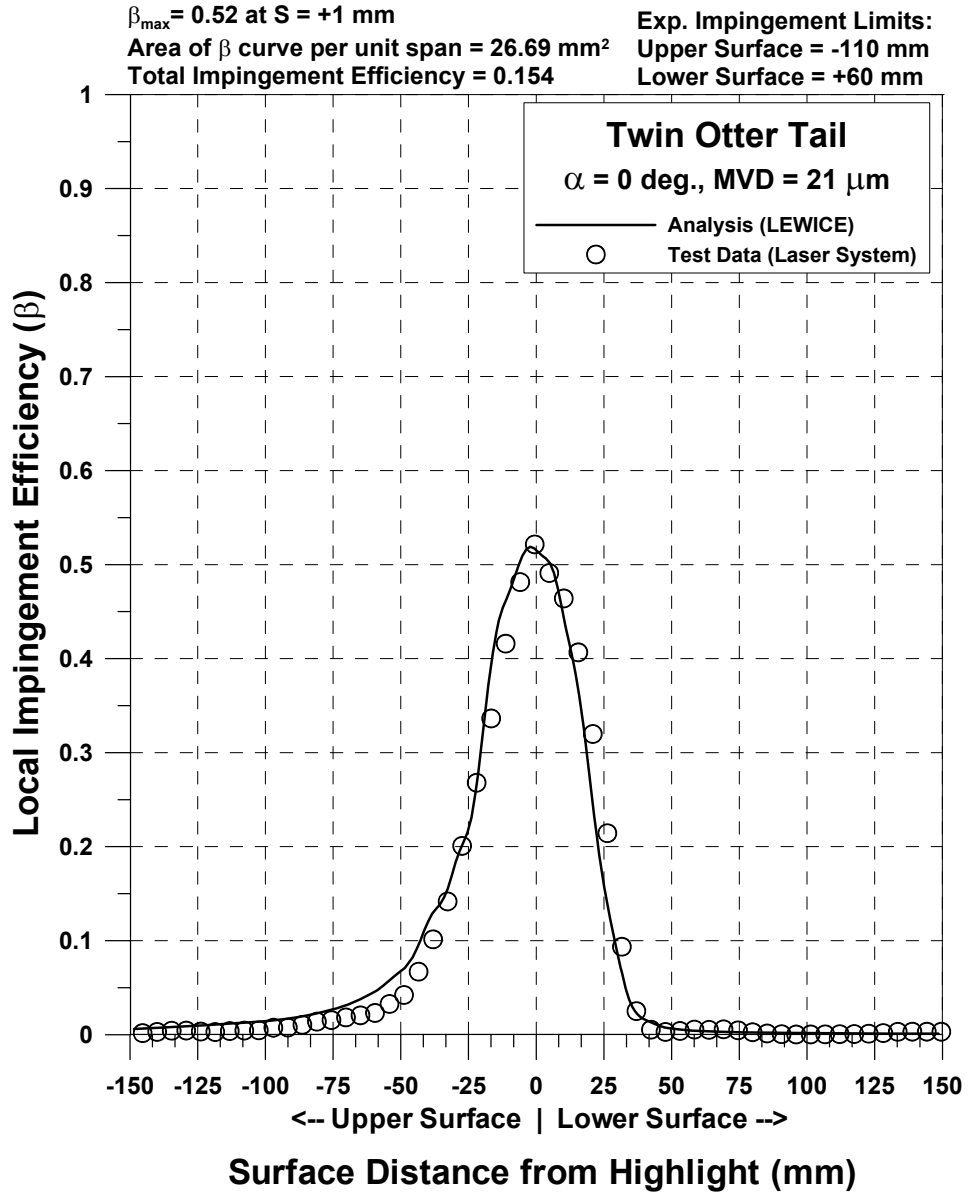


Figure 91b.—Impingement efficiency distribution for Twin Otter tail;
 $c = 57$ in., $V_{\infty} = 175$ mph, $\text{AOA} = 0^\circ$, $\text{MVD} = 21 \mu\text{m}$.

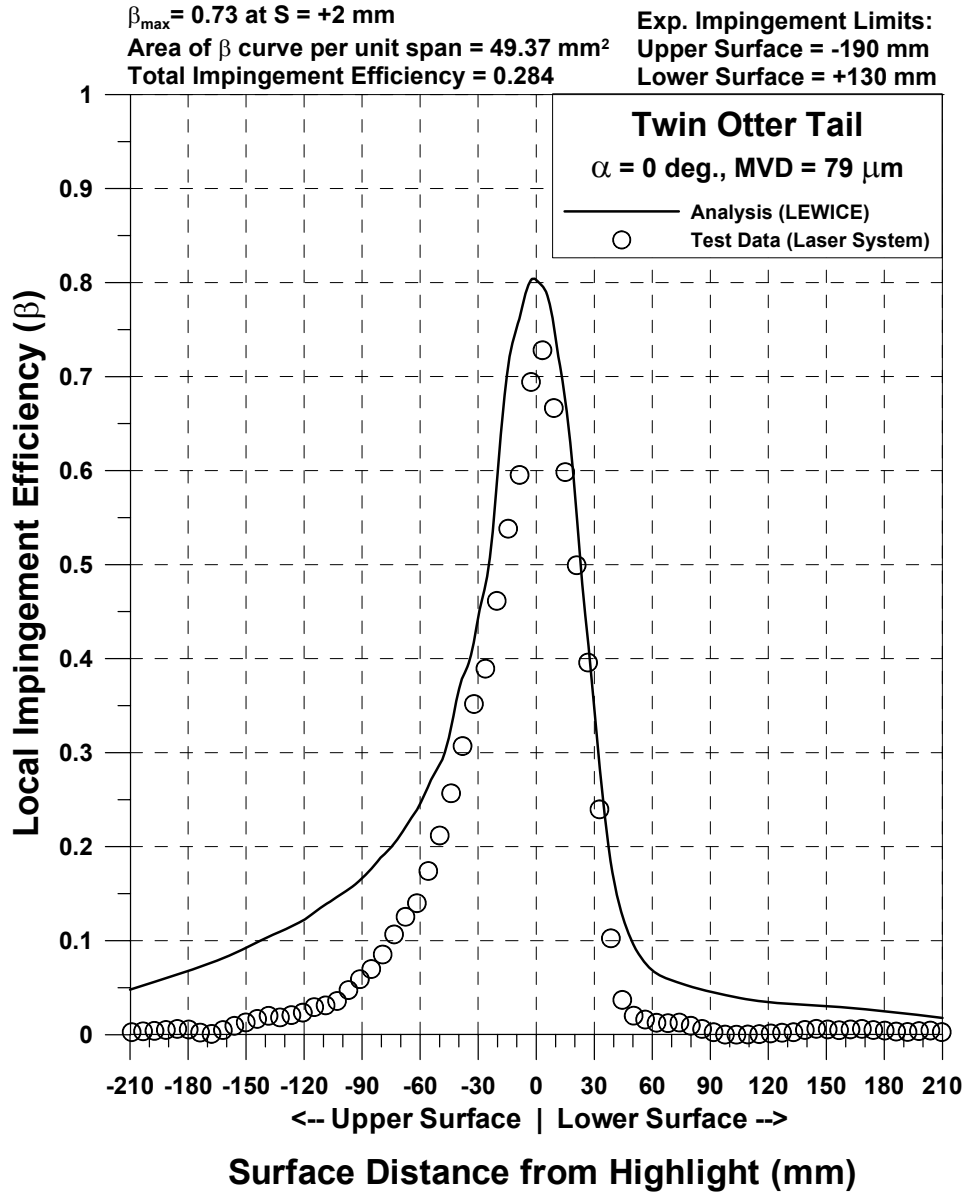


Figure 91c.—Impingement efficiency distribution for Twin Otter tail;
 $c = 57 \text{ in.}$, $V_{\infty} = 175 \text{ mph}$, $AOA = 0^{\circ}$, $MVD = 79 \mu\text{m}$.

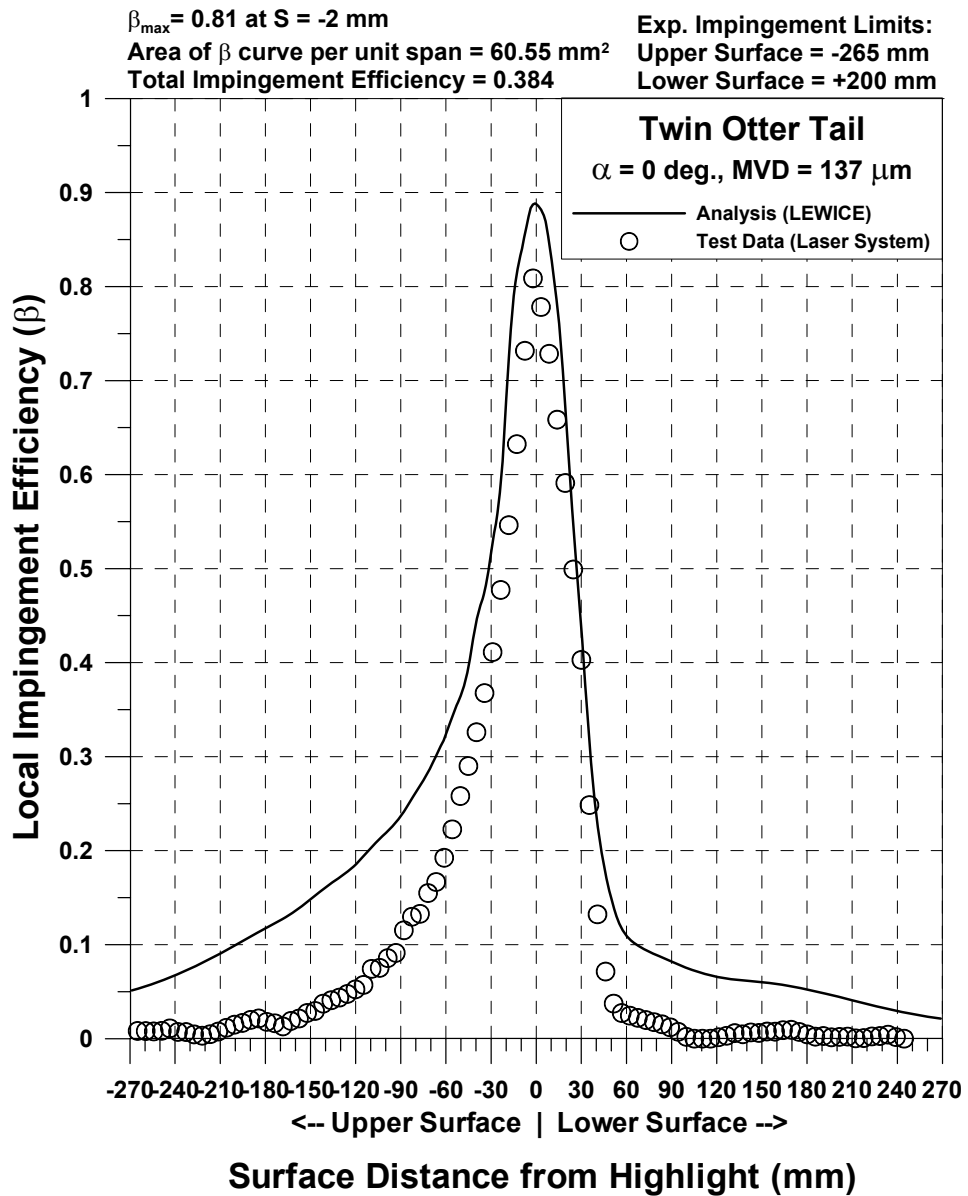


Figure 91d.—Impingement efficiency distribution for Twin Otter tail;
 $c = 57$ in., $V_\infty = 175$ mph, $AOA = 0^\circ$, $MVD = 137 \mu\text{m}$.

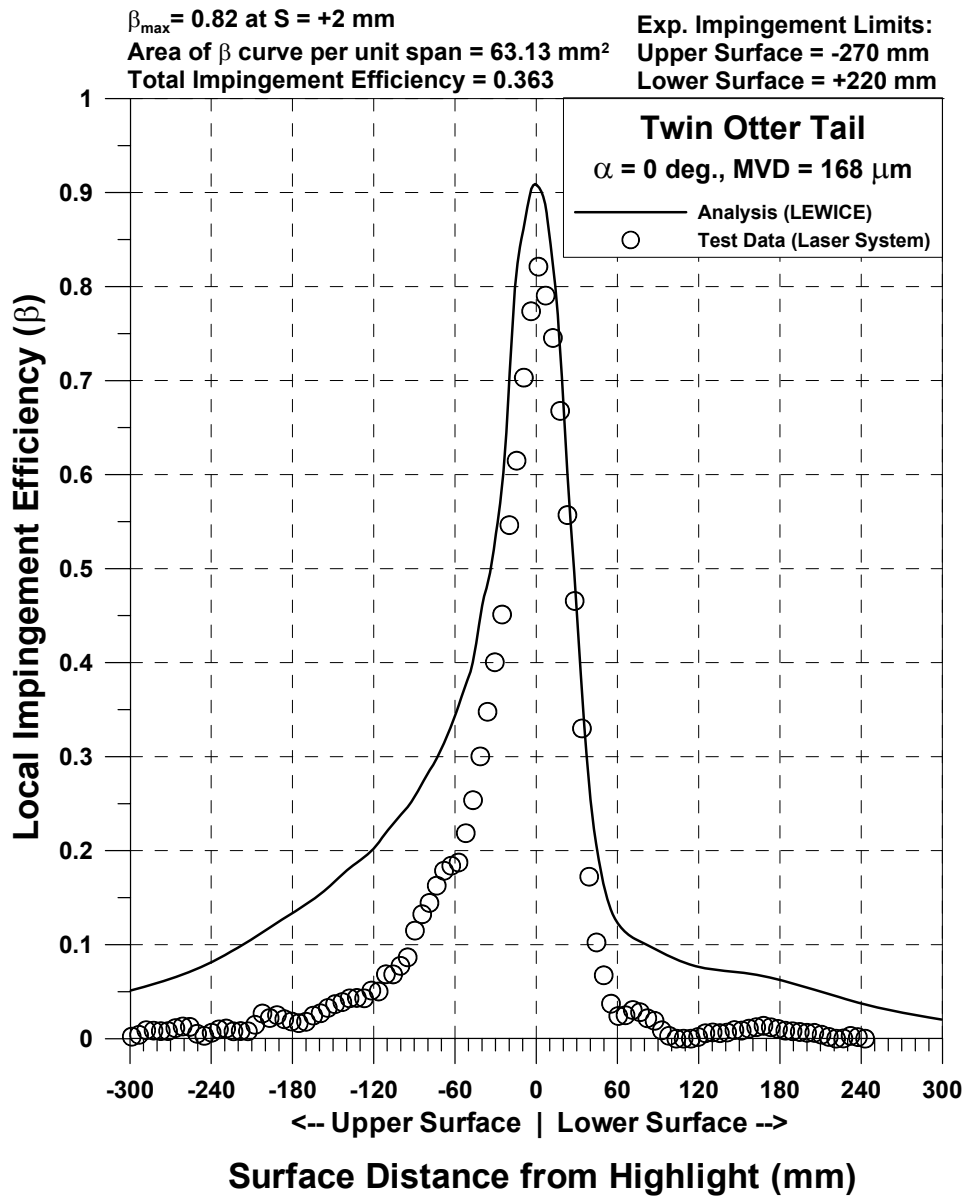


Figure 91e.—Impingement efficiency distribution for Twin Otter tail;
 $c = 57 \text{ in.}$, $V_{\infty} = 175 \text{ mph}$, $\text{AOA} = 0^\circ$, $\text{MVD} = 168 \mu\text{m}$.

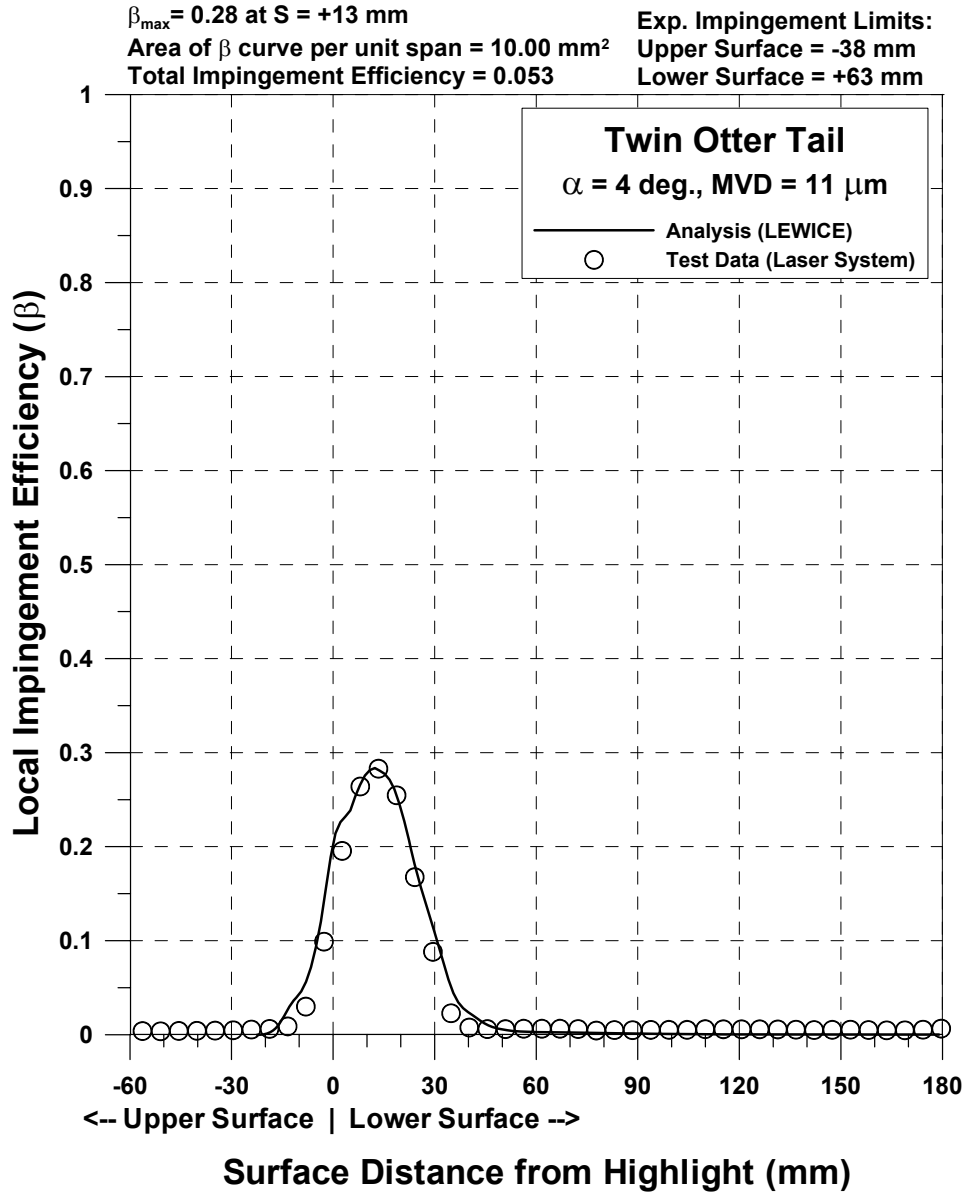


Figure 92a.—Impingement efficiency distribution for Twin Otter tail; $c = 57$ in., $V_{\infty} = 175$ mph, $AOA = 4^{\circ}$, $MVD = 11 \mu\text{m}$.

$\beta_{max} = 0.46$ at $S = +8$ mm

Area of β curve per unit span = 27.96 mm²

Total Impingement Efficiency = 0.148

Exp. Impingement Limits:

Upper Surface = -45 mm

Lower Surface = +210 mm

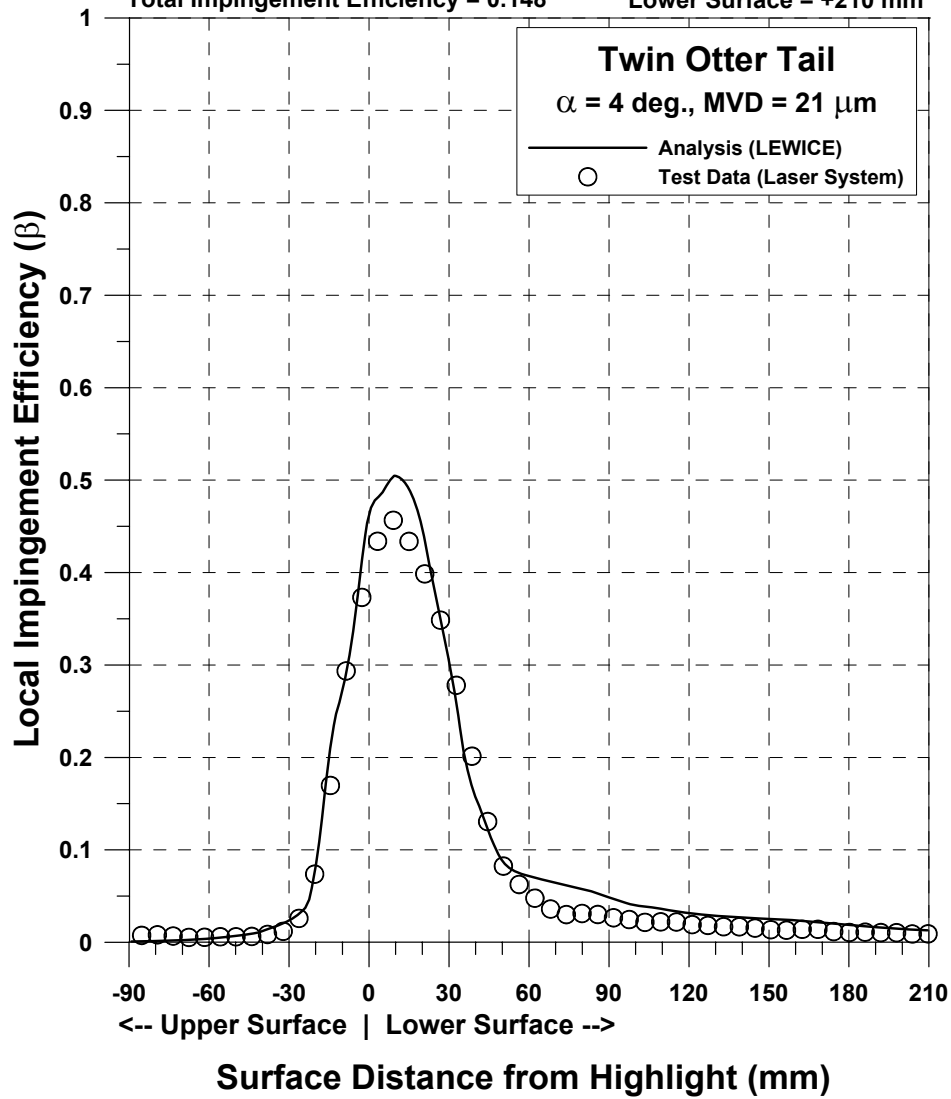


Figure 92b.—Impingement efficiency distribution for Twin Otter tail;
 $c = 57$ in., $V_{\infty} = 175$ mph, AOA = 4°, MVD = 21 μ m

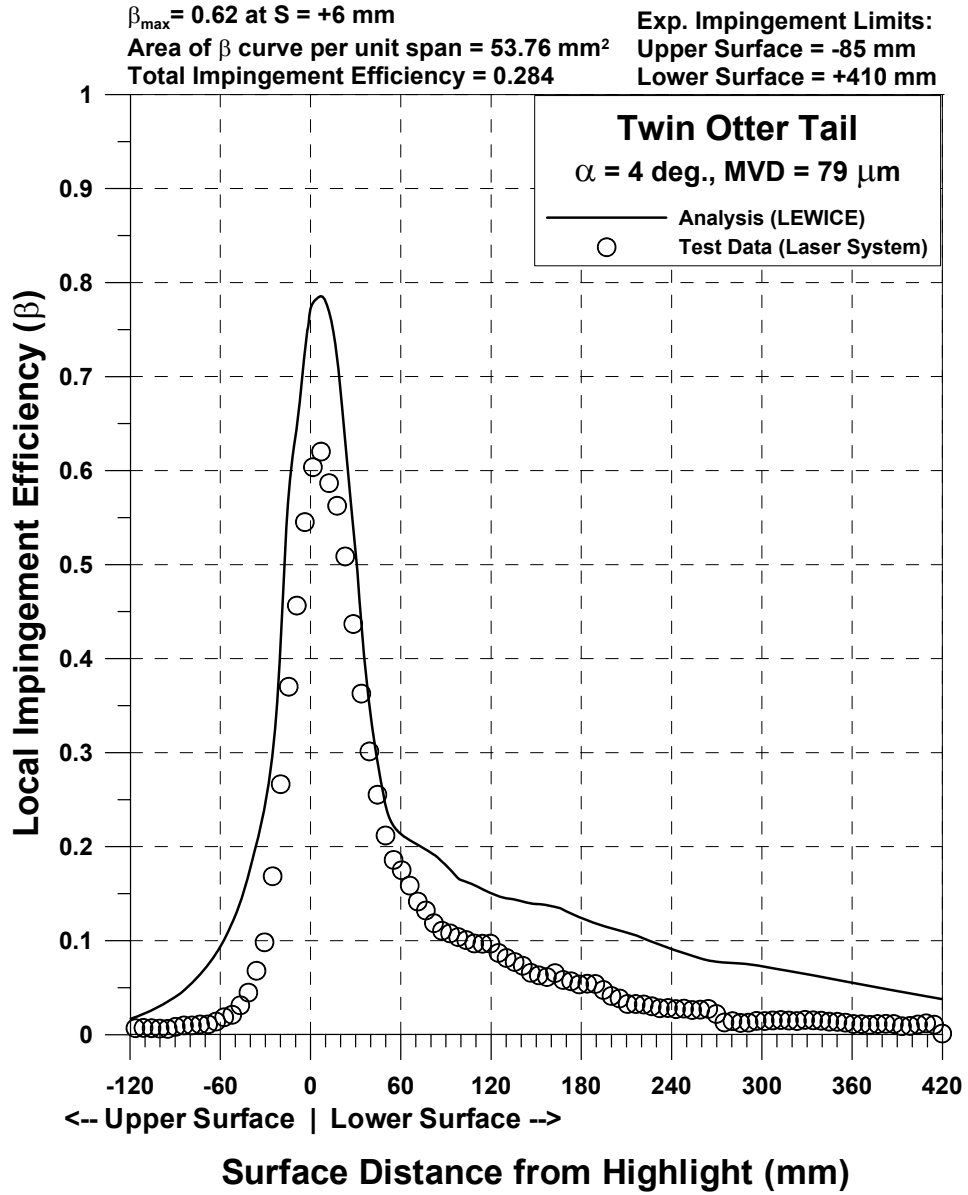


Figure 92c.—Impingement efficiency distribution for Twin Otter tail;
 $c = 57$ in., $V_{\infty} = 175$ mph, $AOA = 4^{\circ}$, $MVD = 79$ μ m.

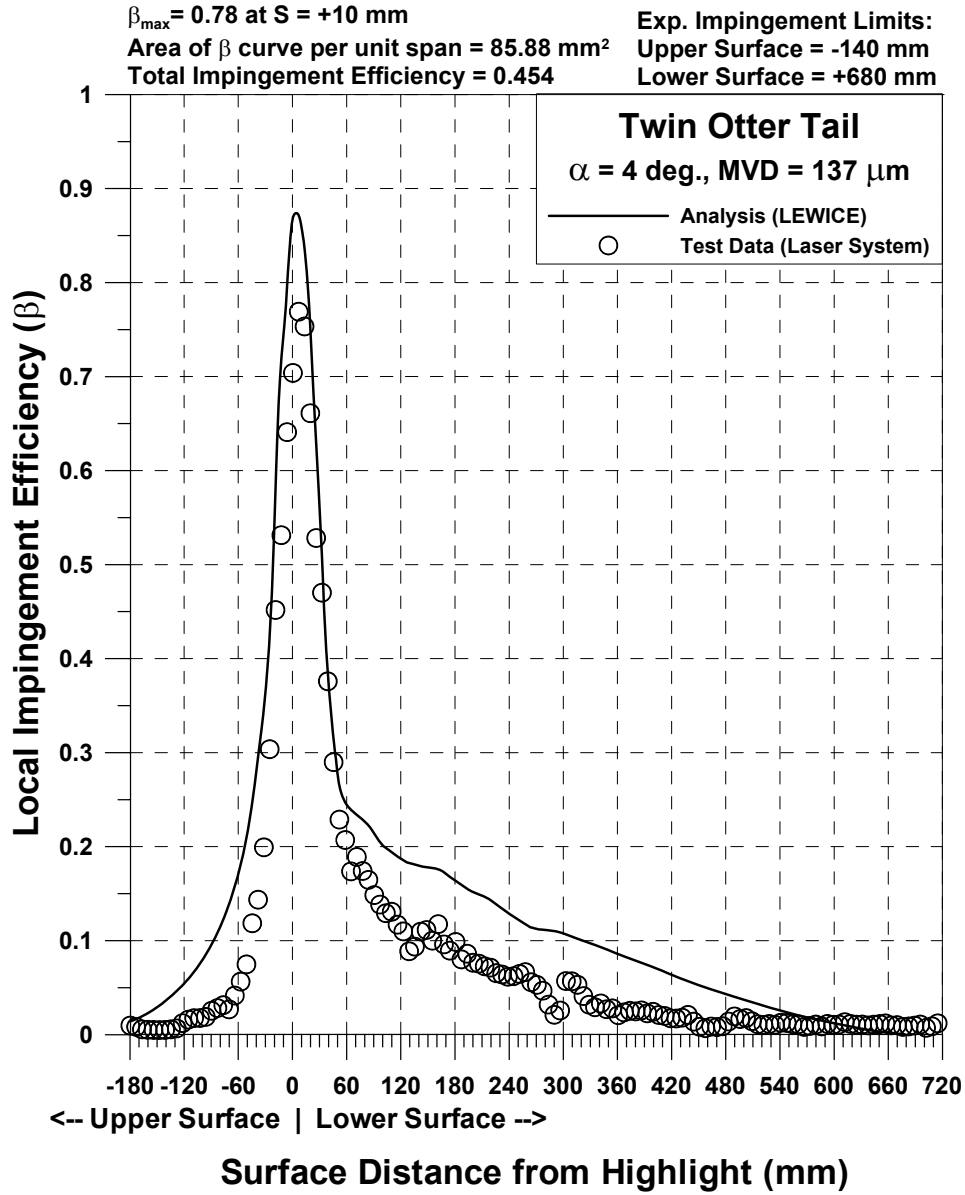


Figure 92d.—Impingement efficiency distribution for Twin Otter tail;
 $c = 57 \text{ in.}$, $V_{\infty} = 175 \text{ mph}$, $AOA = 4^\circ$, $MVD = 137 \mu\text{m}$.

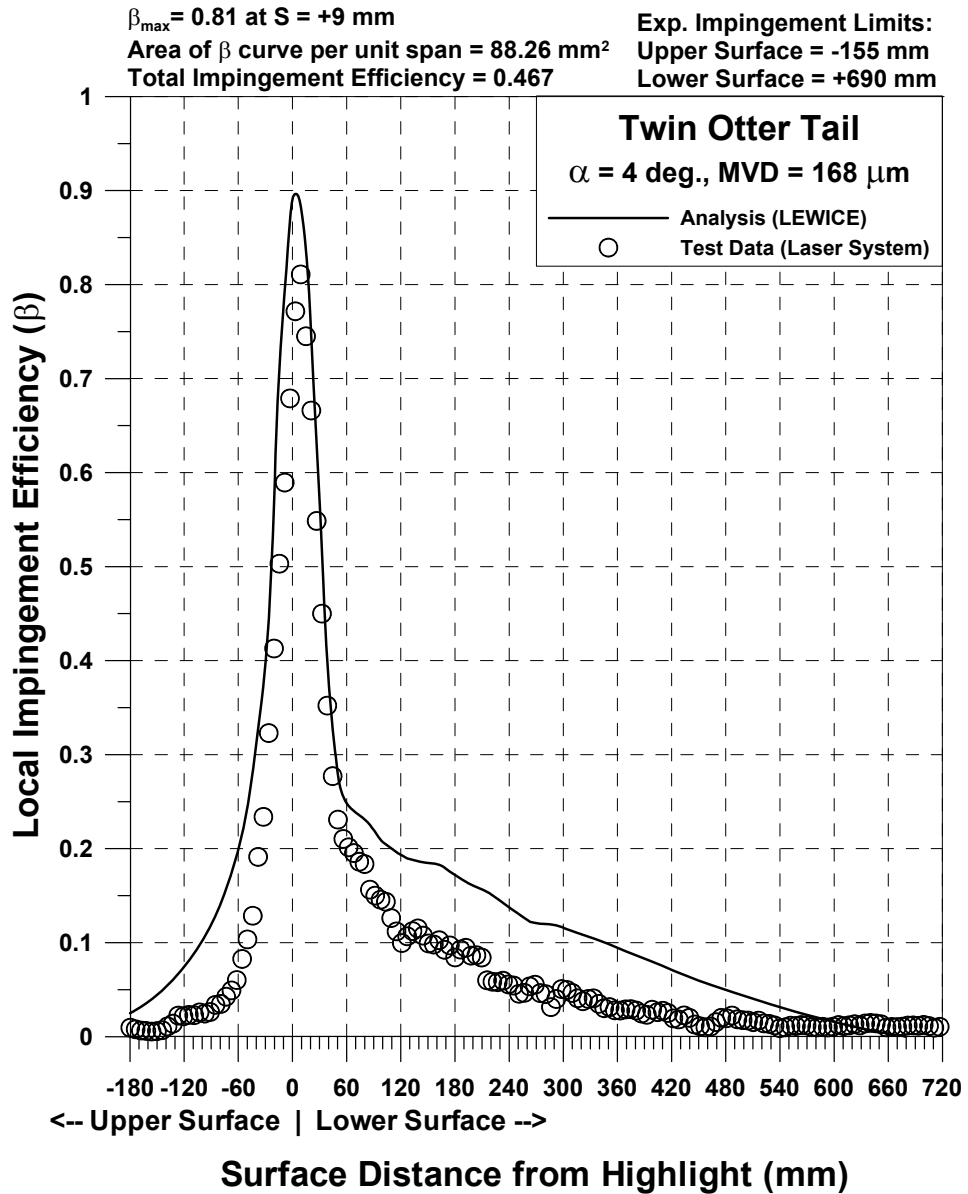


Figure 92e.—Impingement efficiency distribution for Twin Otter tail;
 $c = 57$ in., $V_{\infty} = 175$ mph, AOA = 4°, MVD = 168 μ m.

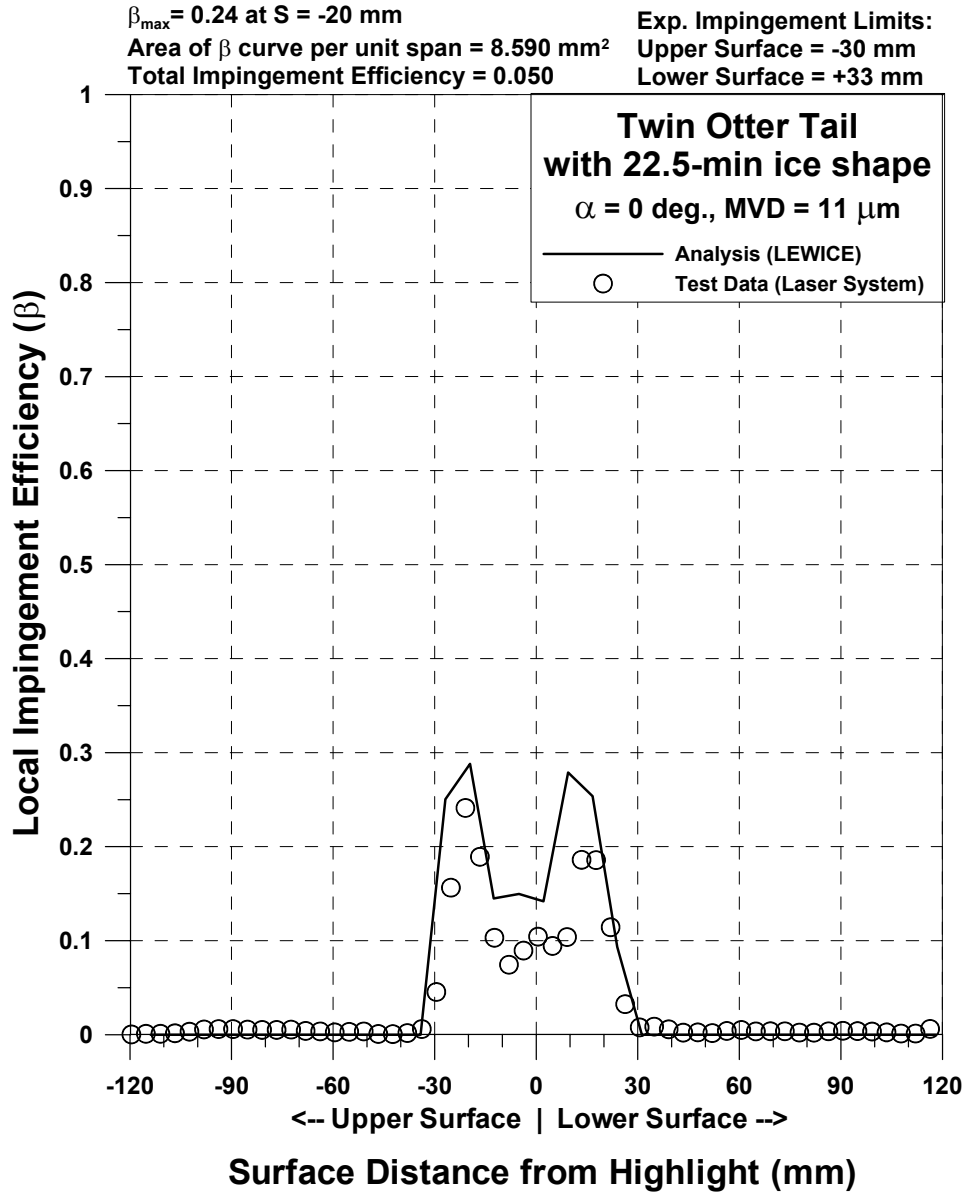


Figure 93a.—Impingement efficiency distribution for Twin Otter tail with 22.5-min ice shape; $c = 57$ in., $V_\infty = 175$ mph, $AOA = 0^\circ$, $MVD = 11 \mu\text{m}$.

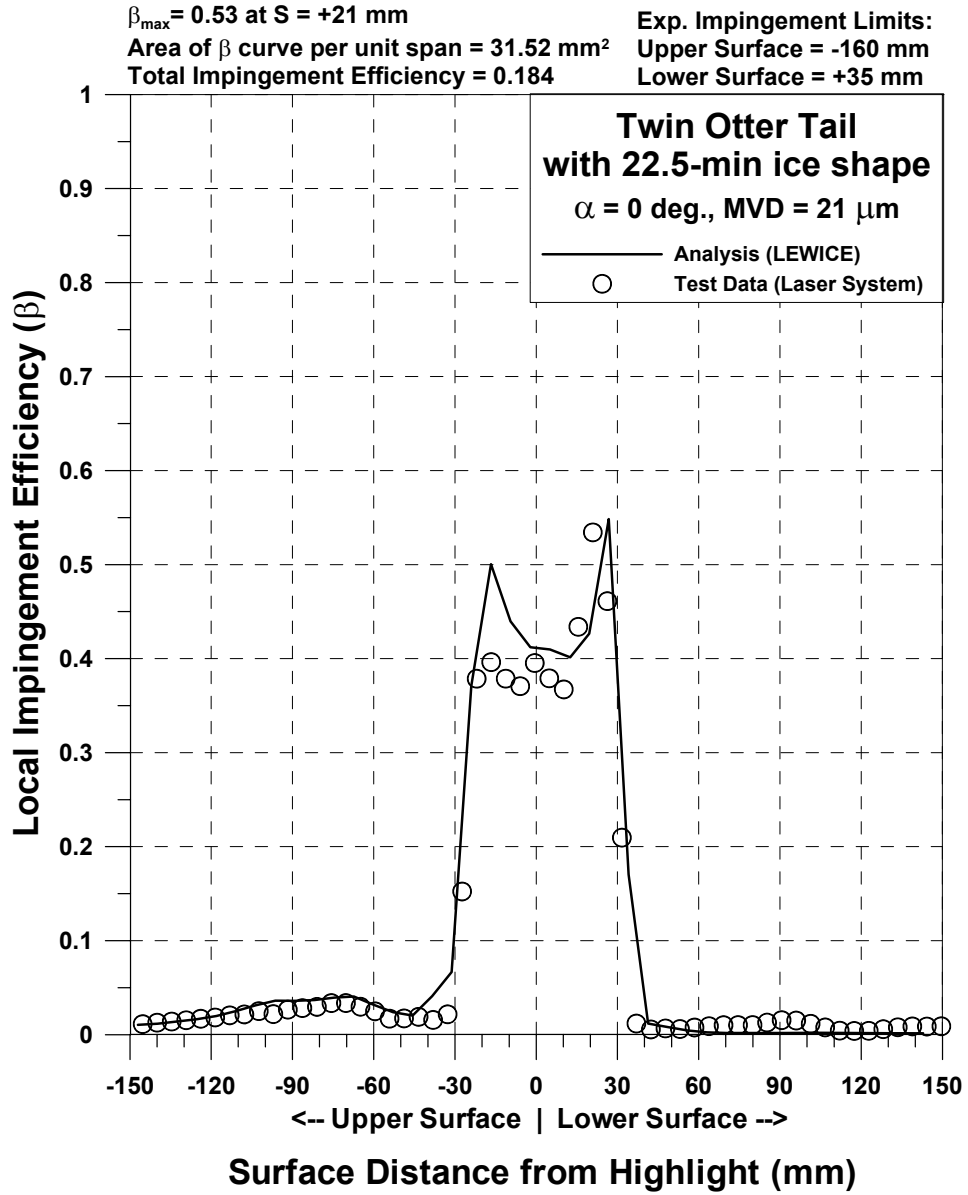


Figure 93b.—Impingement efficiency distribution for Twin Otter tail with 22.5-min ice shape; $c = 57$ in., $V_\infty = 175$ mph, $AOA = 0^\circ$, $MVD = 21 \mu\text{m}$.

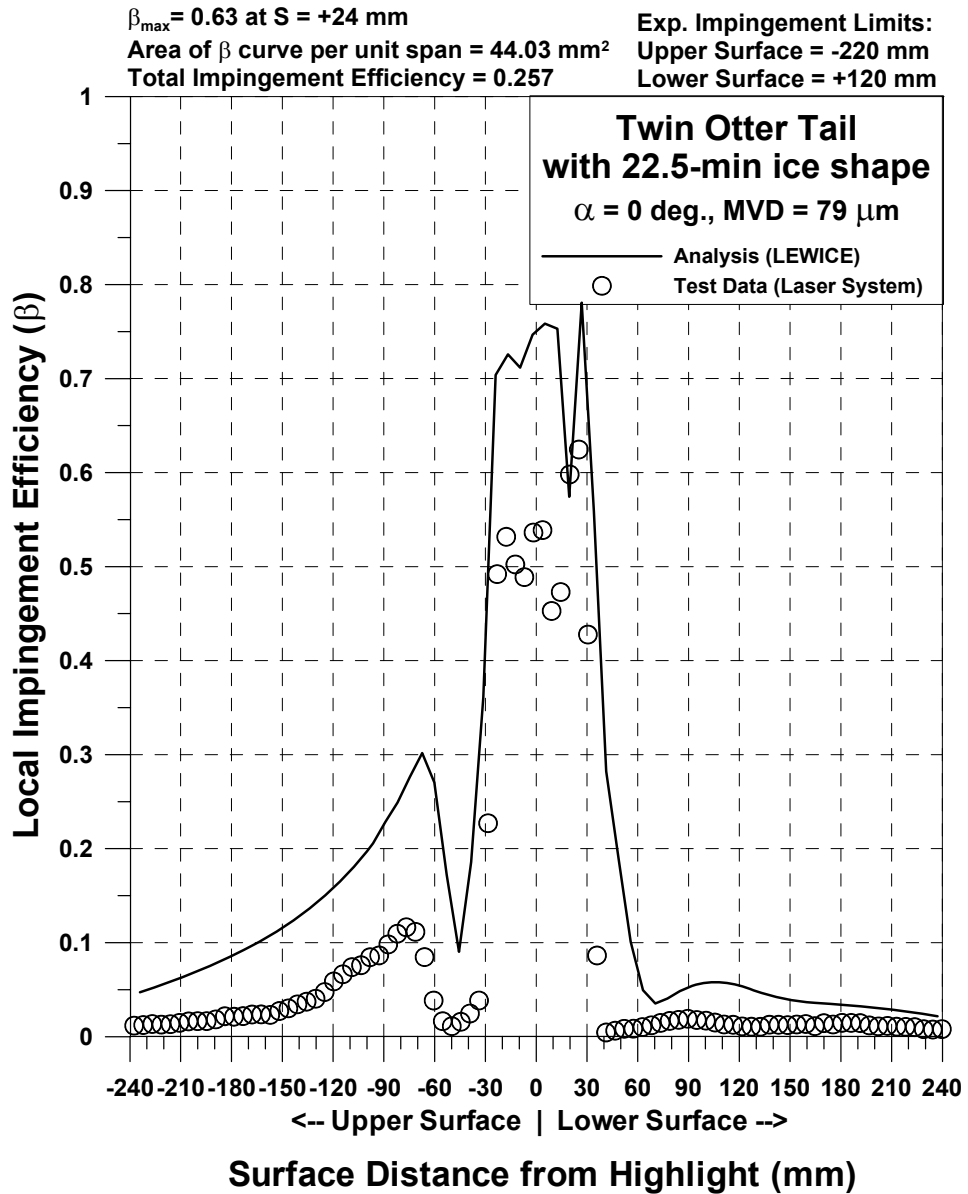


Figure 93c.—Impingement efficiency distribution for Twin Otter tail with 22.5-min ice shape; $c = 57$ in., $V_\infty = 175$ mph, $AOA = 0^\circ$, $MVD = 79 \mu\text{m}$.

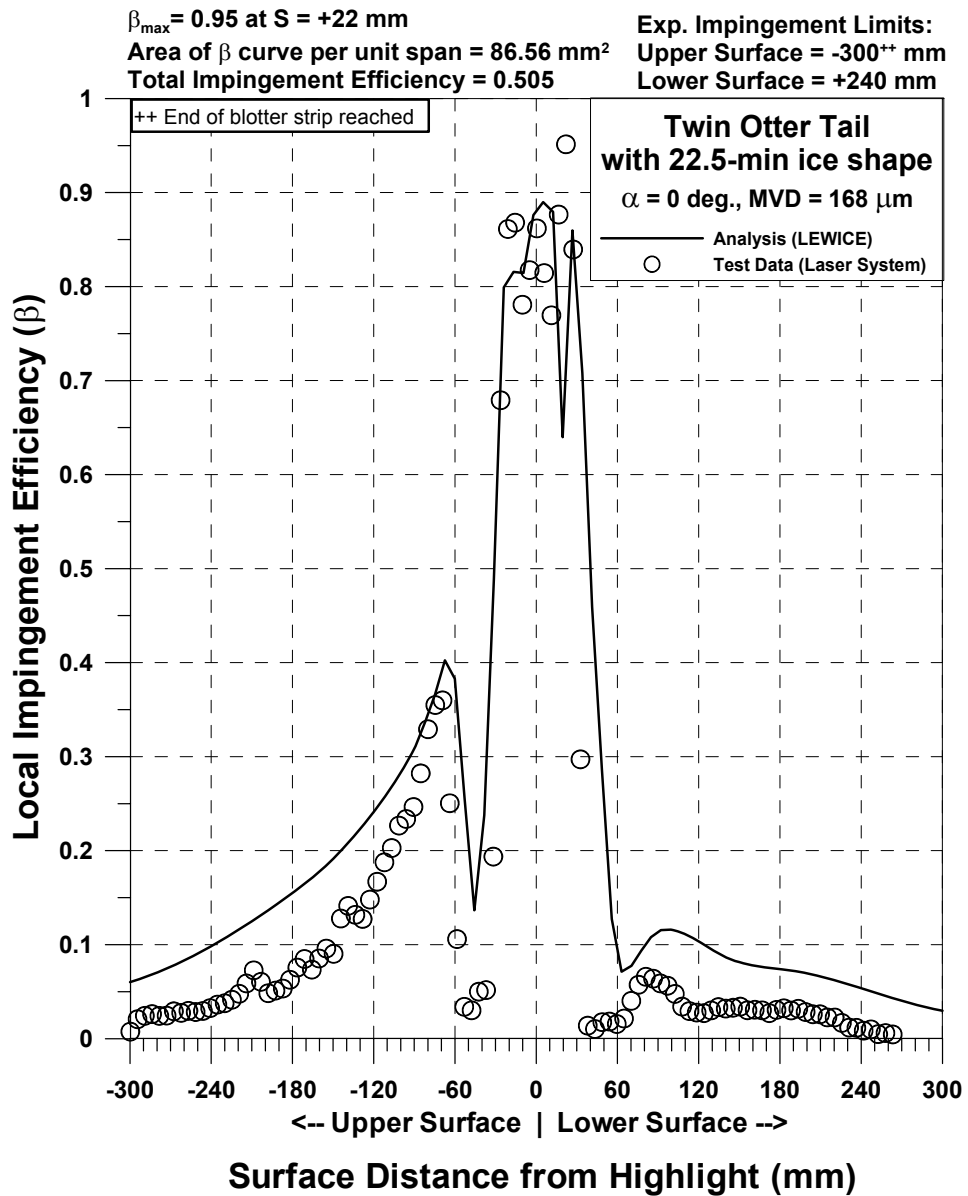


Figure 93d.—Impingement efficiency distribution for Twin Otter tail with 22.5-min ice shape; $c = 57$ in., $V_\infty = 175$ mph, $AOA = 0^\circ$, $MVD = 168 \mu\text{m}$.

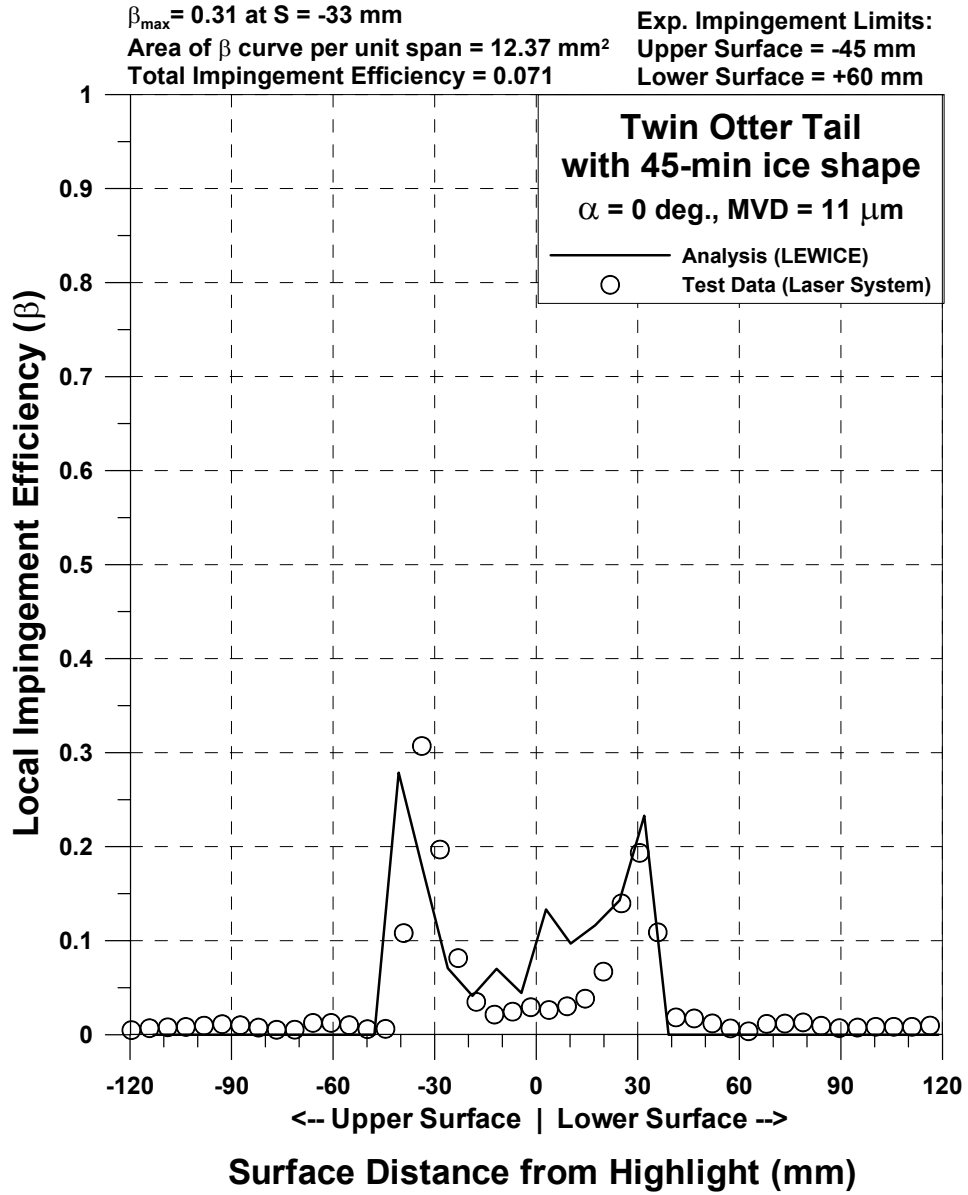


Figure 94a.—Impingement efficiency distribution for Twin Otter tail with 45-min ice shape; $c = 57$ in., $V_\infty = 175$ mph, $AOA = 0^\circ$, $MVD = 11 \mu\text{m}$.

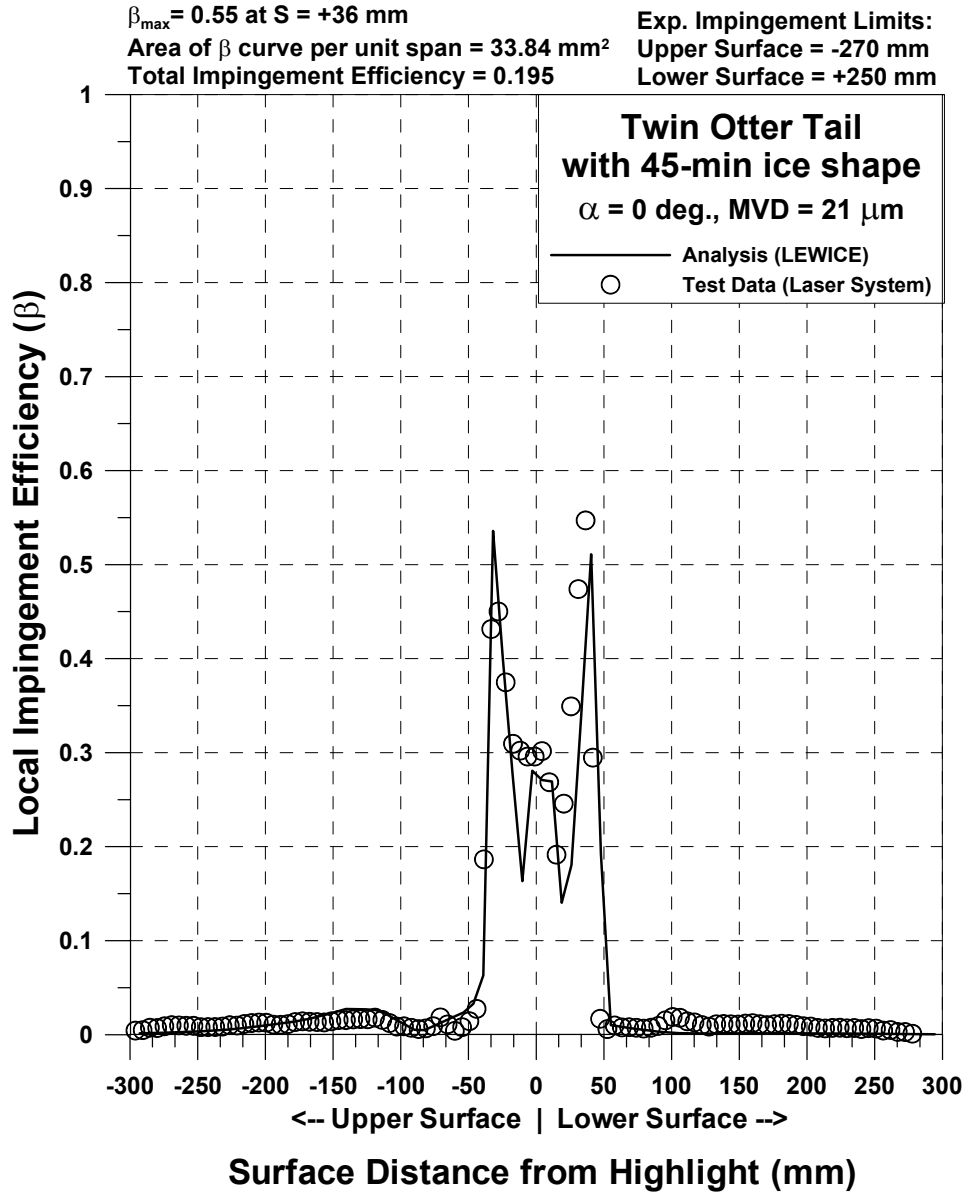


Figure 94b.—Impingement efficiency distribution for Twin Otter tail with 45-min ice shape; $c = 57$ in., $V_\infty = 175$ mph, $AOA = 0^\circ$, $MVD = 21$ μ m.

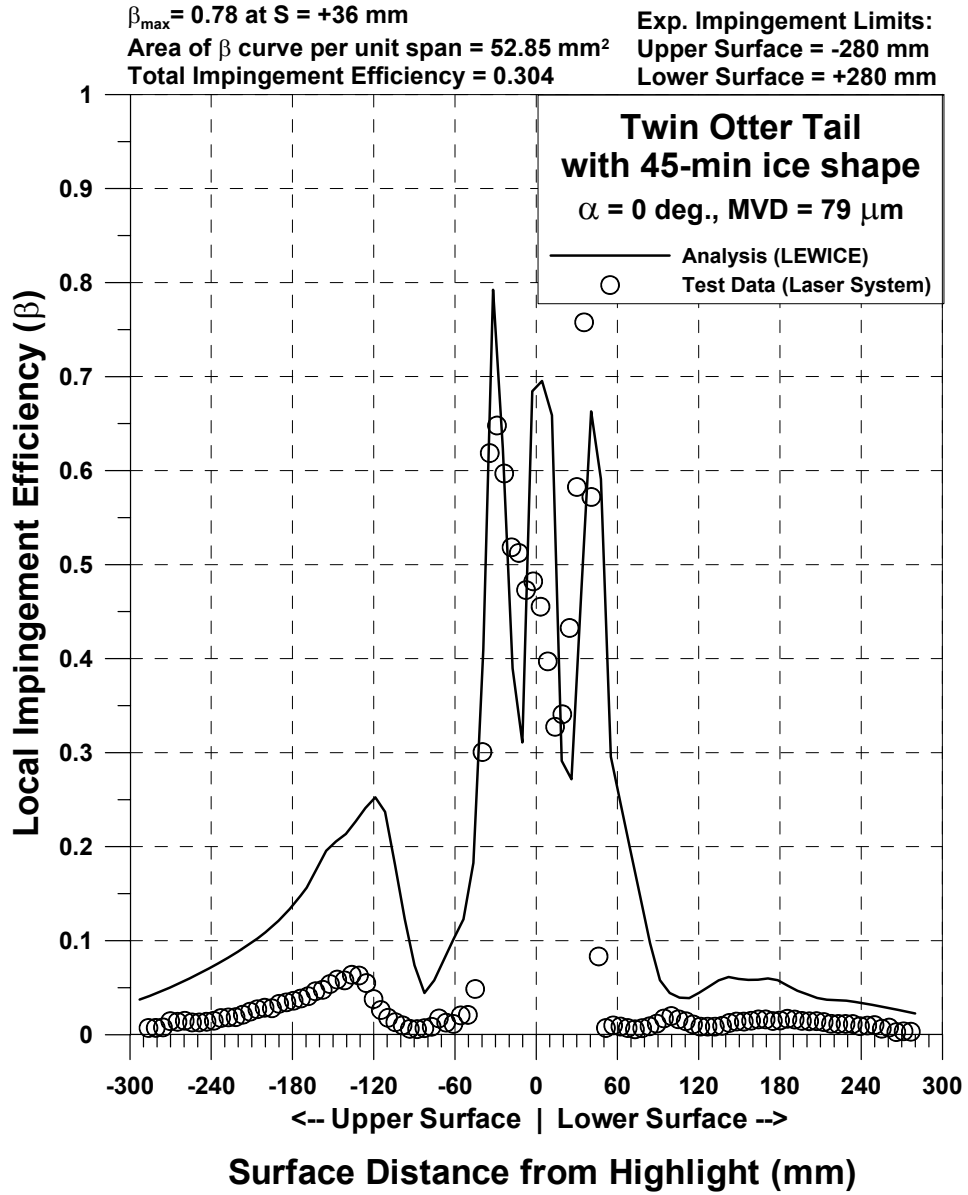


Figure 94c.—Impingement efficiency distribution for Twin Otter tail with 45-min ice shape; $c = 57$ in., $V_\infty = 175$ mph, $AOA = 0^\circ$, $MVD = 79 \mu\text{m}$.

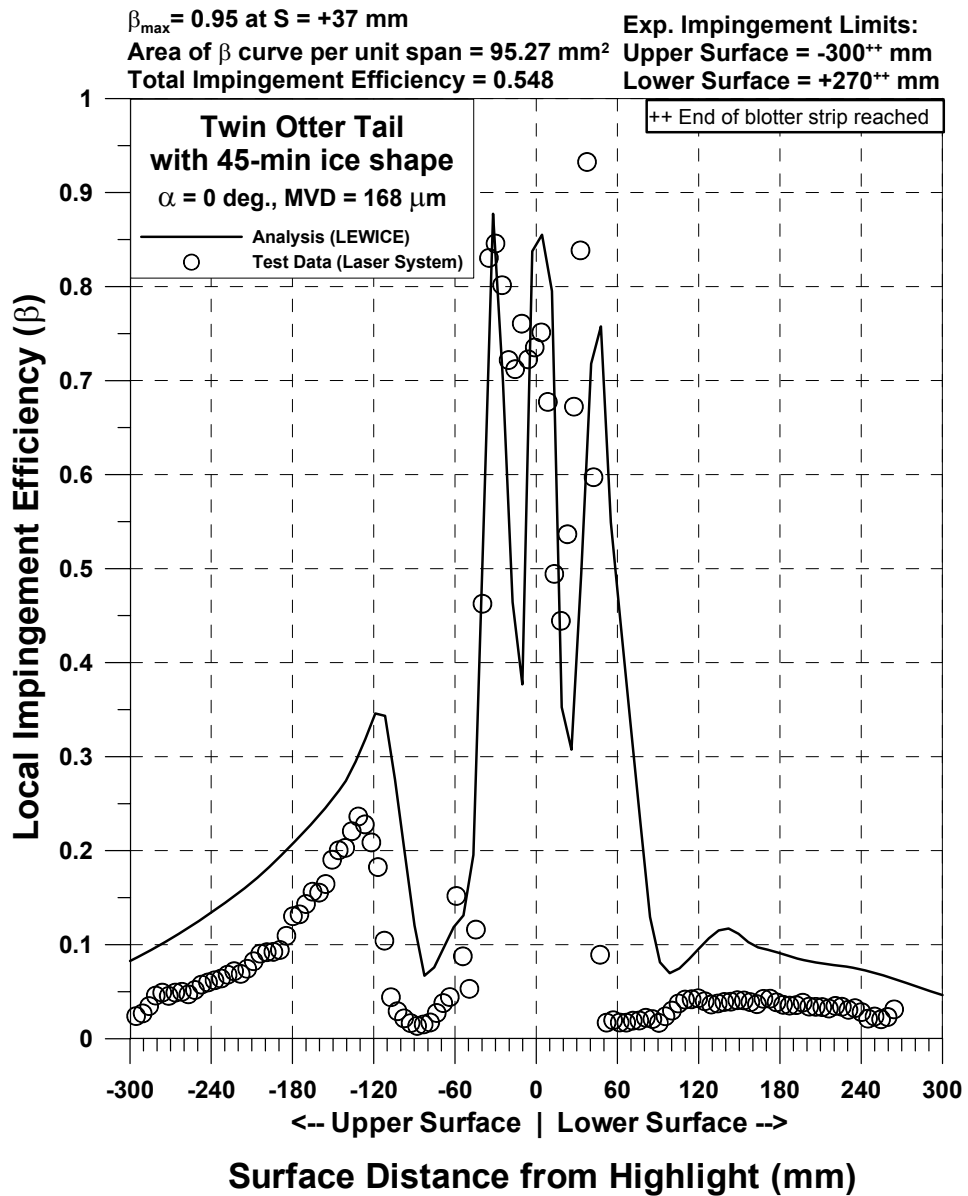


Figure 94d.—Impingement efficiency distribution for Twin Otter tail with 45-min ice shape; $c = 57$ in., $V_{\infty} = 175$ mph, $AOA = 0^\circ$, $MVD = 168 \mu\text{m}$.

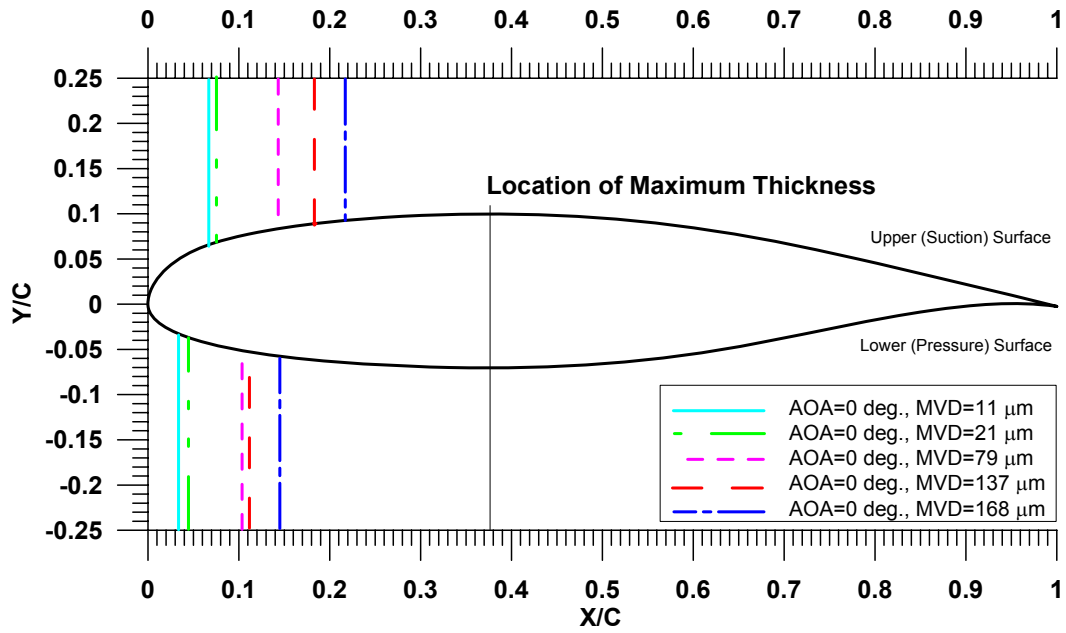


Figure 95.—Experimental impingement limits for MS-317 airfoil at AOA=0°.

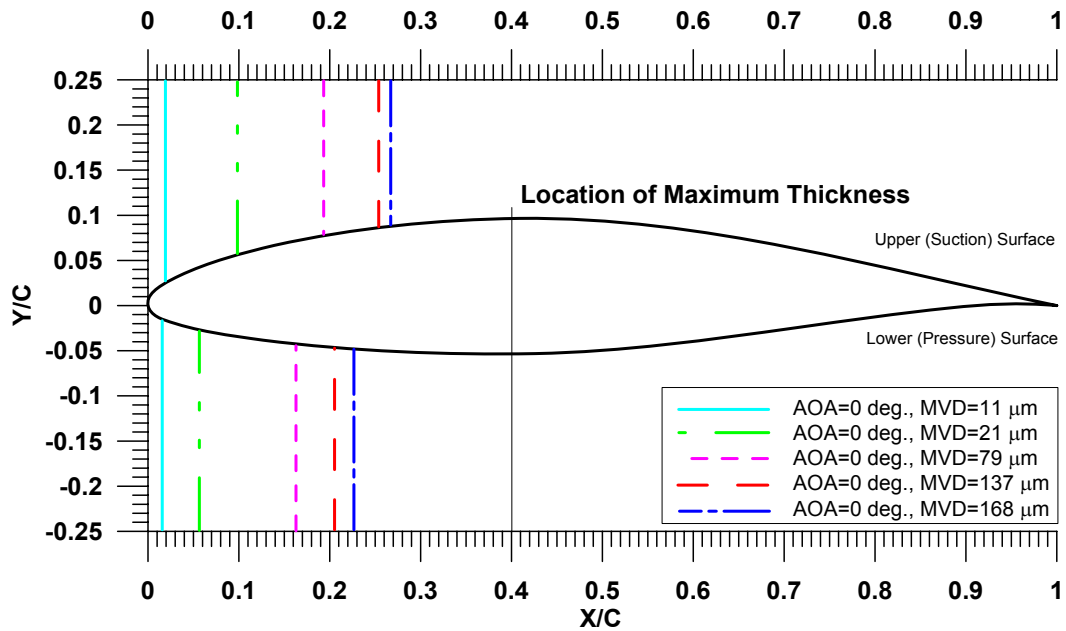


Figure 96.—Experimental impingement limits for NACA 65₂-415 airfoil at AOA=0°.

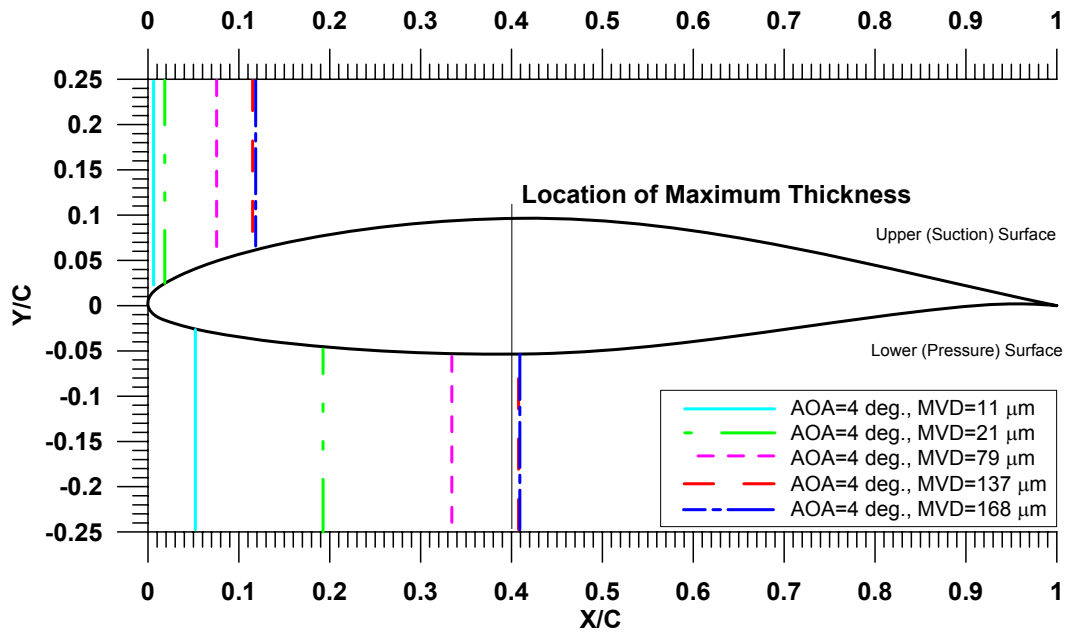


Figure 97.—Experimental impingement limits for NACA 65₂-415 airfoil at AOA=4°.

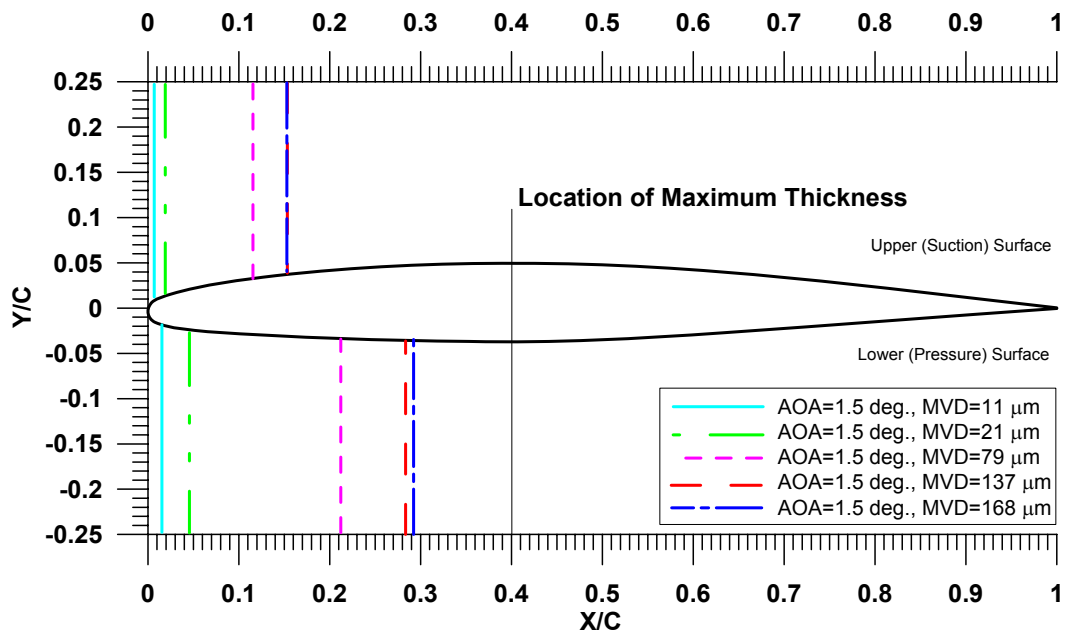


Figure 98.—Experimental impingement limits for GLC-305 airfoil at AOA=1.5°.

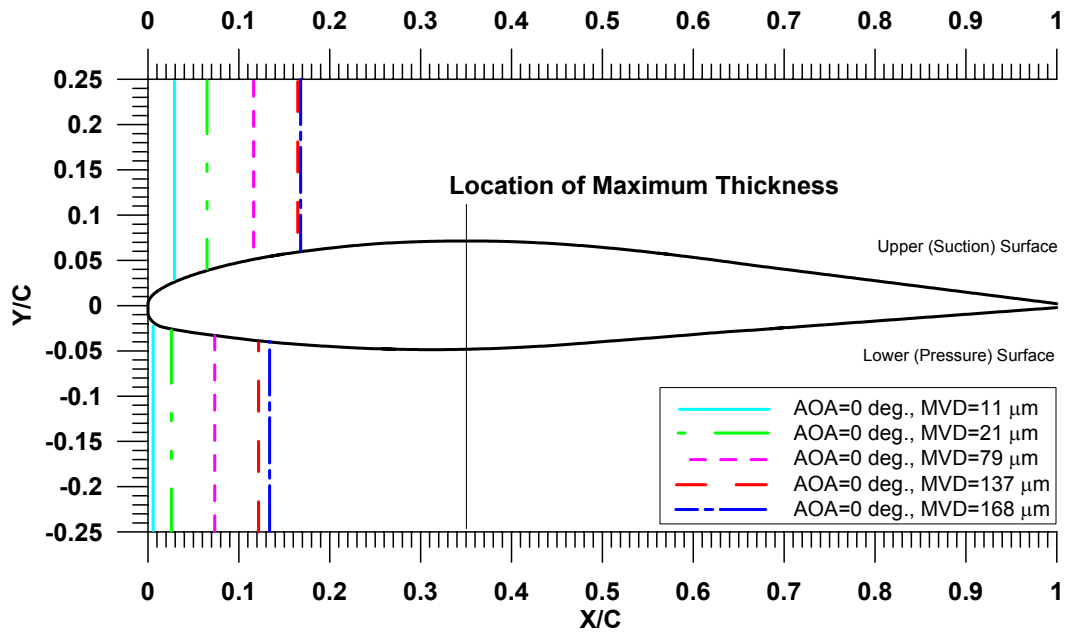


Figure 99.—Experimental impingement limits for Twin Otter tail at AOA=0°.

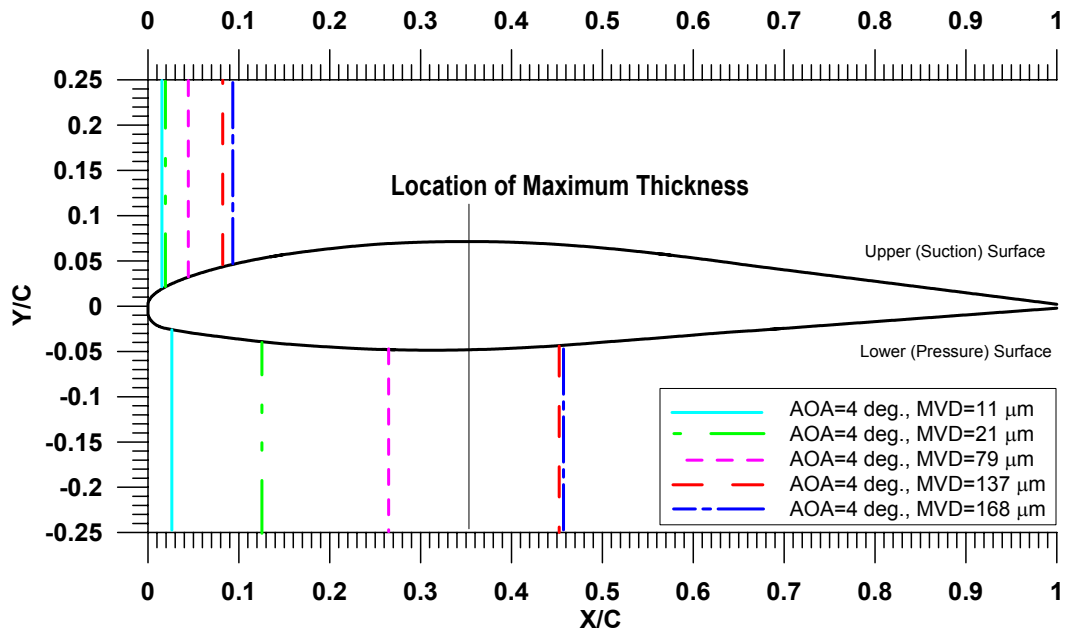


Figure 100.—Experimental impingement limits for Twin Otter tail at AOA=4°.

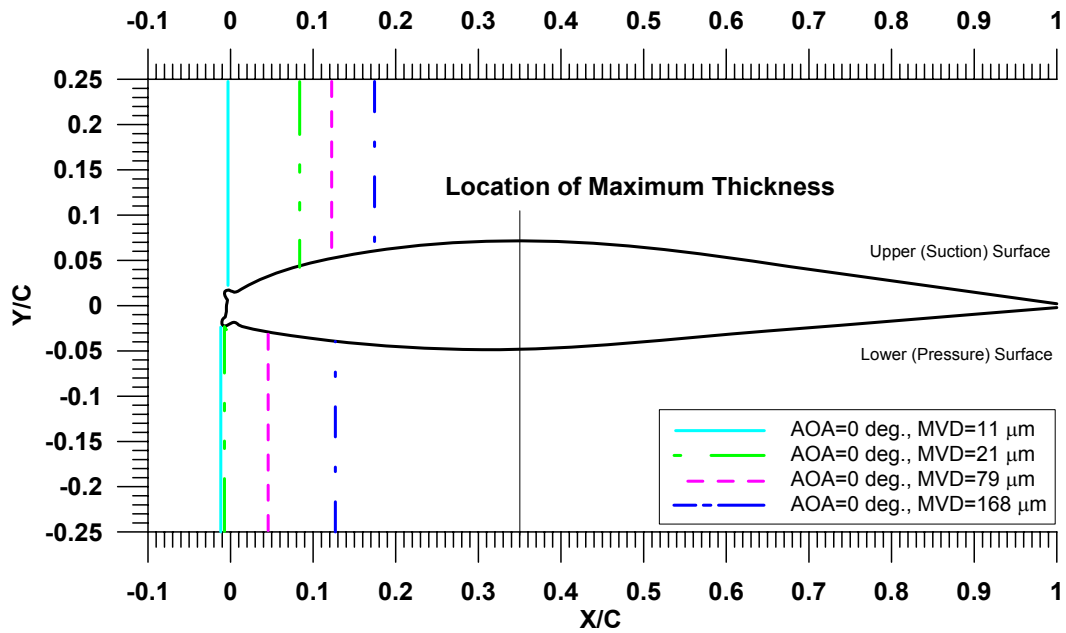


Figure 101.—Experimental impingement limits for Twin Otter tail with 22.5-min ice shape at AOA=0°.

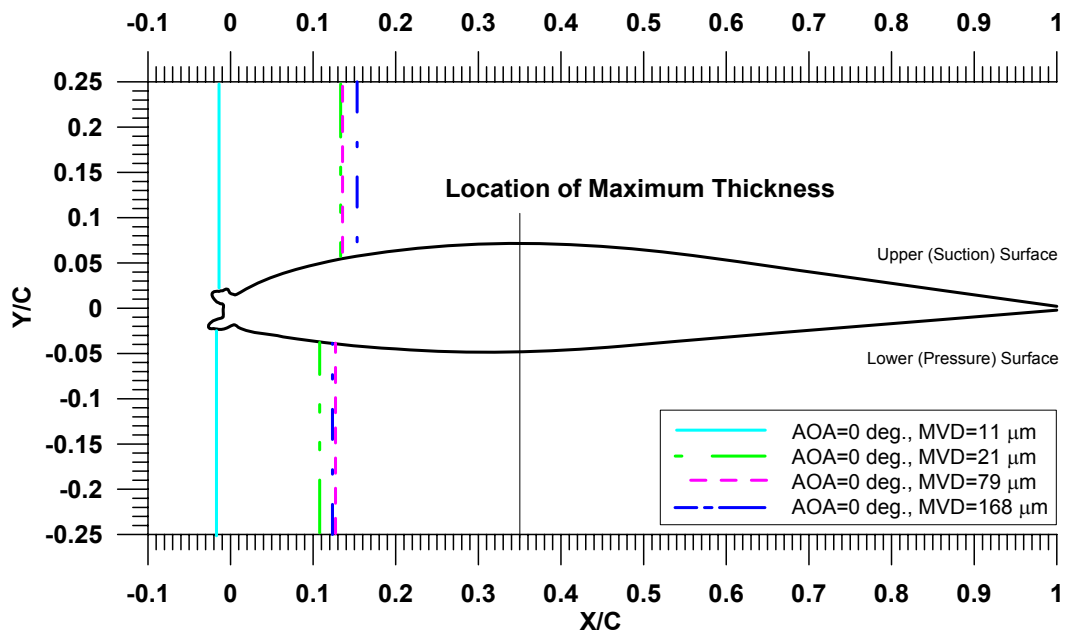


Figure 102.—Experimental impingement limits for Twin Otter tail with 45-min ice shape at AOA=0°.

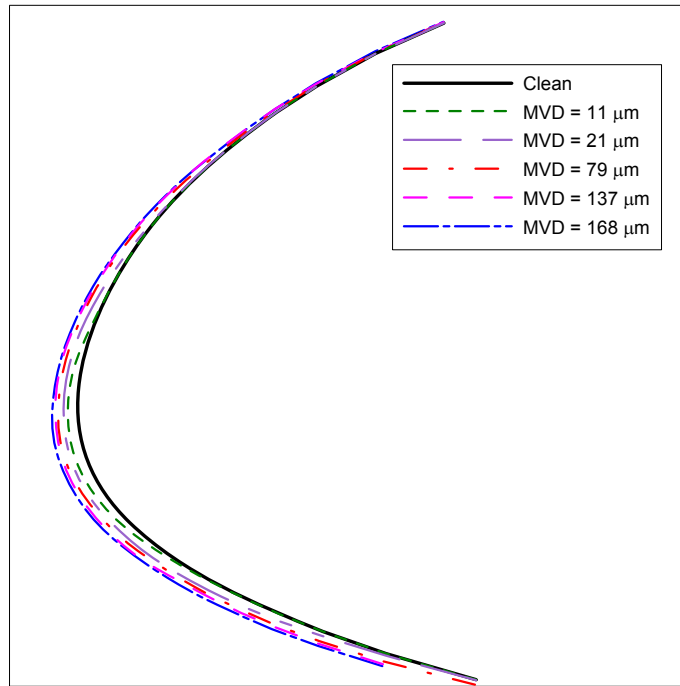


Figure 103.—Experimental impingement efficiency surface distribution for MS-317 airfoil at AOA=0°.

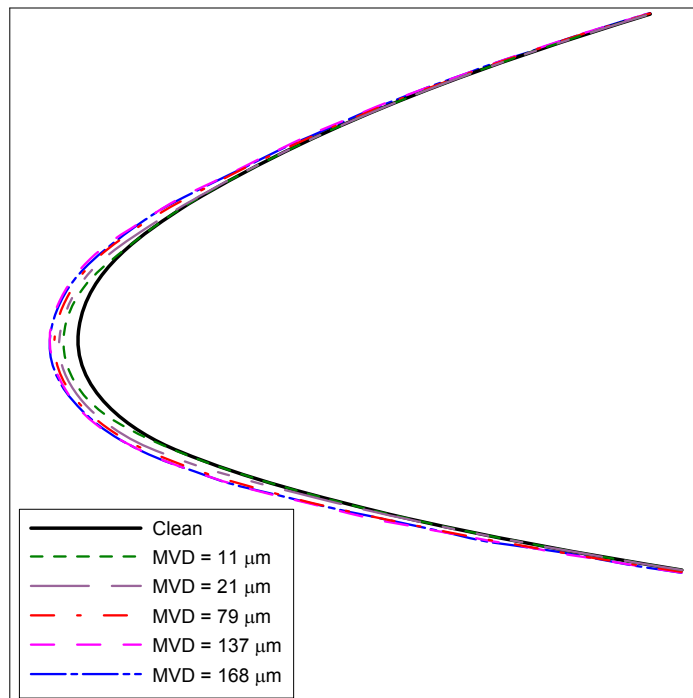


Figure 104.—Experimental impingement efficiency surface distribution for NACA 65₂-415 airfoil at AOA=0°.

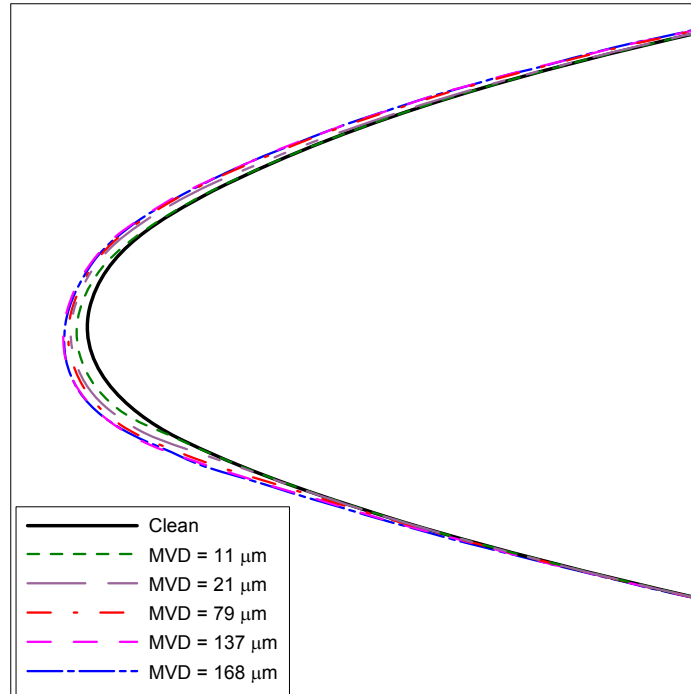


Figure 105.—Experimental impingement efficiency surface distribution for NACA 65₂-415 airfoil at AOA=4°.

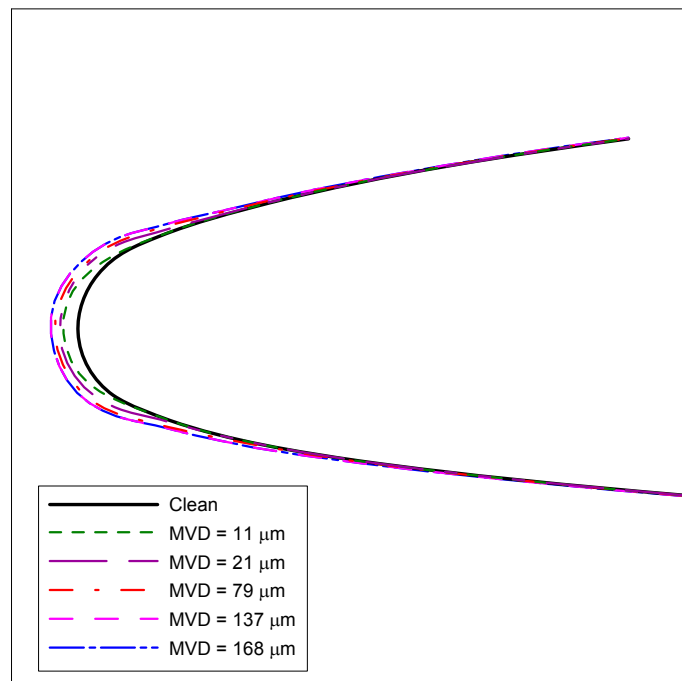


Figure 106.—Experimental impingement efficiency surface distribution for GLC-305 airfoil at AOA=1.5°.

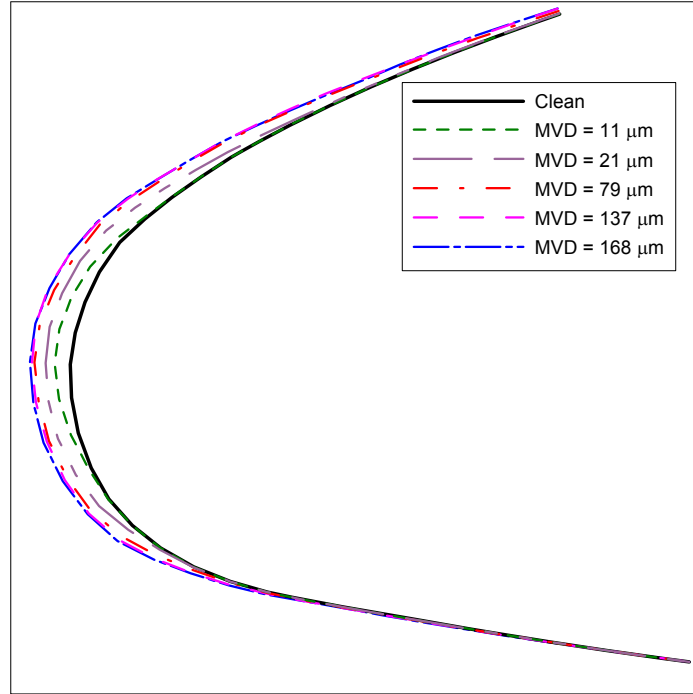


Figure 107.—Experimental impingement efficiency surface distribution for Twin Otter tail at AOA=0°.

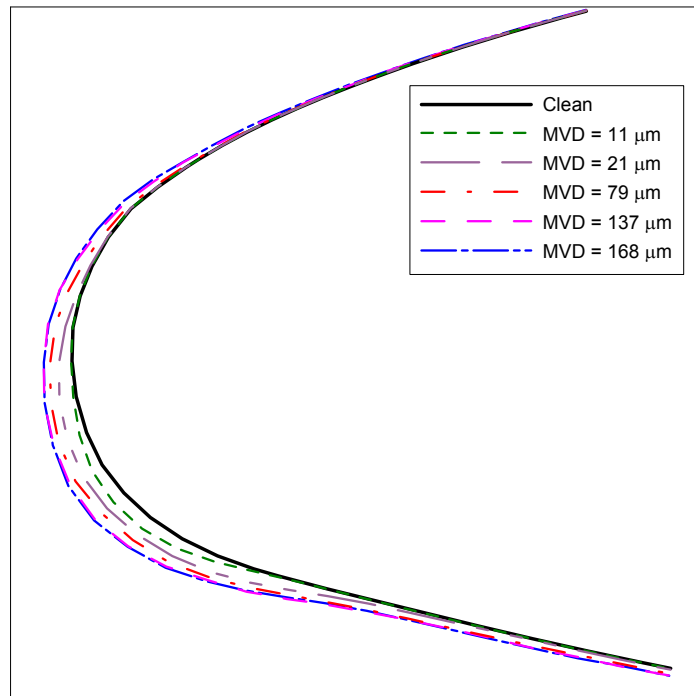


Figure 108.—Experimental impingement efficiency surface distribution for Twin Otter tail at AOA=4°.

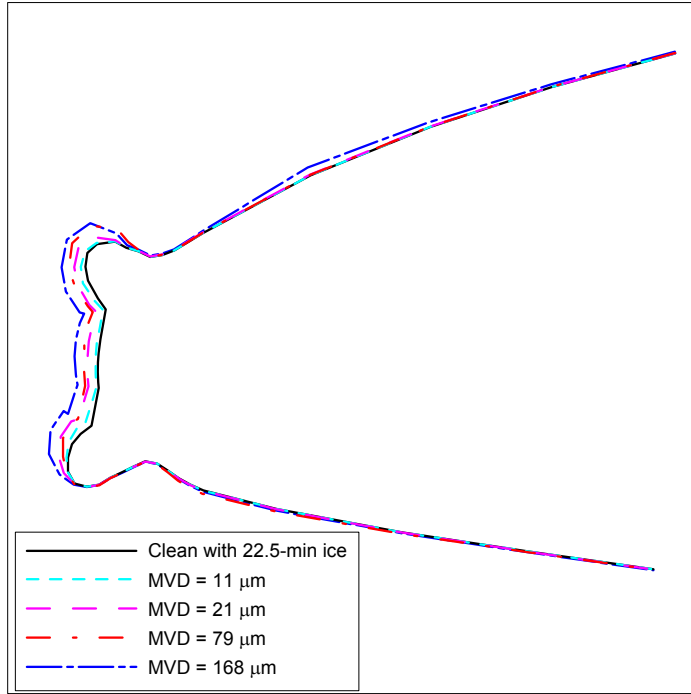


Figure 109.—Experimental impingement efficiency surface distribution for Twin Otter tail with 22.5-min ice shape at AOA=0°.

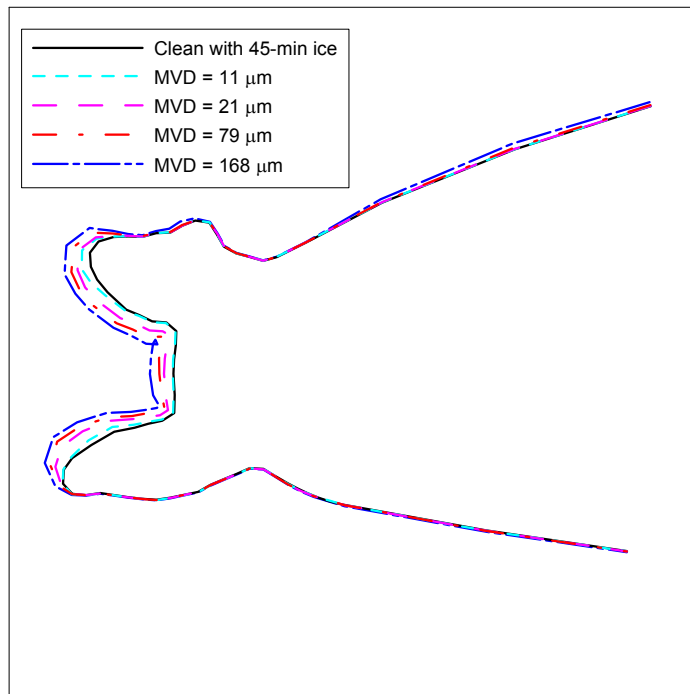


Figure 110.—Experimental impingement efficiency surface distribution for Twin Otter tail with 45-min ice shape at AOA=0°.

Appendix A—General Effects of Large Droplet Dynamics

The material presented in this appendix were taken from AIAA paper 2003–0392 authored by Chiong Tan and Michael Papadakis.

A1. Droplet Transition Regimes

In order to discuss the issues on SLD modeling, it is important to understand the different regimes that a droplet can encounter when traversing a region of varying pressure gradients such as near the stagnation zone of a wing leading edge. Figure A1 shows an illustration of the transition regimes that a single droplet can experience in the vicinity of an airfoil. These regimes can be identified as follows:

A1.1 Regime (a)

Droplet reaches a critical condition where its shape starts to deform due to aerodynamic forces. These forces create surface waves on the droplet and work against the droplet surface tension forces. At the critical moment, surface tension can no longer maintain surface integrity and begins to break-up. There are many criteria to define droplet breakup but the most commonly used are the Weber, Rabin and Bond numbers (refs. A1 to A4). These are defined as follow:

$$\text{Weber number, } We = \frac{\rho_g |V_r|^2 D}{\sigma_d} \quad (\text{A1.1})$$

$$\text{Rabin number, } Ra = We / \sqrt{Re} \quad (\text{A1.2})$$

$$\text{Bond number, } Bo = \frac{\rho_d D^2}{\sigma_d} \left(\frac{dV_r}{dt} \right) \quad (\text{A1.3})$$

$$\text{Reynolds number, } Re = \frac{\rho_g |V_d - V_g| D}{\mu_g} = \frac{\rho_g |V_r| D}{\mu_g} \quad (\text{A1.4})$$

where V_r is the relative velocity between the droplet and surrounding fluid. Other terms are self-explanatory but subscripts g and d refer to air and droplet properties respectively. There are several possible mechanisms of breakup but the following five distinct groups are commonly used (ref. A2):

- $We \leq 12$, vibrational breakup
- $12 < We \leq 50$, bag breakup
- $50 < We \leq 100$, bag and stamen breakup
- $100 < We \leq 350$, sheet stripping
- $We > 350$, wave crest stripping (followed by breakup)

The “bag” type breakup is characterized by a blown film that breaks up eventually while the “sheet stripping” type of breakup is characterized by continual process of water sheets being

shed off. Another commonly used method of defining critical breakup condition is to use the Rabin number (refs. A5 to A8) as follows:

$$\begin{aligned} We/\sqrt{(Re)} = Ra > 0.40, \quad d[We/\sqrt{(Re)}]/dt < 30 \text{ for "bag" breakup} \\ We/\sqrt{(Re)} = Ra > 0.79, \quad d[We/\sqrt{(Re)}]/dt > 30 \text{ for "shear" breakup} \\ We/\sqrt{(Re)} = Ra \geq 1.00, \quad \text{for "shear" breakup} \end{aligned}$$

Most of the critical droplet breakup studies were carried out experimentally where droplets were subjected to aerodynamic forces in test facilities such as a horizontal or vertical tunnel, or shock tubes. The critical Weber number is usually between 12 and 14 for droplets subjected to instantaneous acceleration but in slow moving flows for example, a falling droplet, the critical value can be as large as 22 (ref. A9). Besides the rate of change in the relative velocity, the critical Weber number is also dependent on the fluid viscosity as shown by the three groups below:

$$\begin{aligned} We_c \approx 13.0 - 19.5, \quad 0.01 < Oh < 0.2, \quad \text{drop with slight viscosity} \\ We_c \approx 24.7 - 36.4, \quad 0.2 < Oh < 2.0, \quad \text{drop with great viscosity} \\ Oh > 2.0, \quad \text{no breakup} \end{aligned}$$

The Ohnesorge number, Oh, is defined as follows:

$$Oh = \frac{\mu_d}{\sqrt{\rho_d D \sigma_d}} \quad (A1.5)$$

(e.g., $Oh \approx 0.01$ for 100 μm water droplets at 290 K)

Since fluid viscosity and surface tension tend to vary slowly with temperature in icing conditions, the critical breakup condition becomes a function of the droplet size and droplet relative velocity with respect to the air. Thus, large droplets traversing across a stagnation region (fig. A1) will attain breakup conditions earlier than smaller droplets. Larger droplets also tend to "lag" behind the flow velocity (due to the greater inertia, ref. A10) therefore the relative droplet-air velocities are also greater.

Figure A2 shows an example of the Weber number distribution on a NACA012 airfoil for 20 and 200 μm droplets. It shows that larger droplets, compared to smaller droplets, traversing the stagnation region are more likely to become unstable and breakup before impinging on the airfoil surface. However, droplets do not breakup spontaneously on reaching the critical stage. Instead they initially undergo a transformation from spherical to disk shapes and then droplets start to shed off from the primary droplet. The type of breakup then depends on the prevailing velocity gradients for example, in a shock wave, the explosive type of droplet breakup is common. In accelerating or decelerating flows, shear-stripping type of droplet breakup occurs. In general, droplet breakup can take different forms as discussed earlier. The whole process from start to achieving complete breakup can take several milliseconds (see section A1.3).

If a droplet should break-up prior to impingement (on a solid surface), then a different kind of ice accretion may form since the water impingement characteristics have changed. It is not known if this type of icing phenomenon exists but the potential for large droplets to reach critical breakup condition is quite high in some cases. However, it is possible for droplet to deform but without any breakup.

A1.2 Regime (b)

When a droplet has exceeded the critical breakup condition, its shape begins to deviate from a spherical shape and the drag coefficient of the droplet increases. In discrete trajectory models, such as the ones used in most icing codes, the application of the drag coefficient based on a sphere no longer holds true. Past researchers have also used the droplet shape to define the critical breakup condition. Hinze (ref. A9), for example, derived a simple breakup expression using the lateral diameter of a liquid droplet as follows:

$$(\delta/D)_c = 0.085 We \text{ (suddenly exposed to a steady velocity airstream)}$$

and,

$$(\delta/D)_c = 0.0475 We \text{ (for continuously increasing flow)}$$

where δ is the lateral diameter of the deformed droplet, and D is the initial droplet diameter. Correlation of the above equations with experimental data from Merrington and Richardson (ref. A11) suggests the critical value is approximately unity for breakup. Wierzba (ref. A3) found the value varies between 1.5 and 1.62 at (critical) Weber number of 12.51 (initial droplet diameter of 2.6 mm). The experimental data in reference A12 indicated critical values of between 1.4 and 2.0.

Numerical models have also been developed to predict the drop deformation. A rigorous treatment of the droplet distortion can be found in the empirical (TAB) model of O'Rourke and Amsden (ref. A13), later modified by Clark (ref. A14), which employed the Talyor (ref. A15) analogy between an oscillating and distorting droplet and a spring-mass system. The equation is written as:

$$\left(\frac{\rho_d}{\rho_g} + 1 \right) \frac{d^2 y}{dt^2} + \frac{9\pi^2}{2Re} \left(\frac{\mu_d}{\mu_g} + 1 \right) \frac{dy}{dt} + \frac{9\pi^2}{2We} \left(y - \frac{4}{3\pi} \right) = \frac{2}{\pi} \quad (\text{A1.6})$$

where y is the non-dimensional distance between the center of the deformed half droplet and the equator of the drop. The solution of the above equation can be obtained using a fourth-order Runge-Kutta technique with the following initial conditions:

$$y = 4/(3\pi), \quad dy/dt = 0 \quad \text{at } t = 0.$$

As the droplet shape changes, which usually involves the increase in the lateral diameter, the drag coefficient can change from 0.9 to 4.4 (ref. A4). A proposed equation for a droplet or sphere subjected to an accelerating flow is given by Wolfe and Andersen (ref. A4), and is written as:

$$C_D = \frac{4\rho_d D_o^3}{3\rho_g (V_g - V_d)^2 D_i^2} \frac{dV_d}{dt} \quad (\text{A1.7})$$

where D_o and D_i are the original droplet diameter and lateral diameter of a deformed droplet respectively.

The effect on the ice accretion modeling due to an increased drag is that the local catch efficiency and impingement limits may be altered slightly as shown in figure A3. Smaller droplets

of the appendix C sizes are less affected due to the greater surface tension and low Weber number hence the effect of shape distortion can be largely ignored.

A1.3 Regime (c)

In this regime, droplets are in close proximity to a wall surface and can either remained intact or break-up into smaller droplets prior to reaching a solid surface. When droplets are near the wall boundary layer or in regions where shearing flows exist, they can experience the near-wall and Saffman forces besides the aerodynamic drag force. The near-wall force tends to “push” a droplet away from the wall and the Saffman force provides additional “lift” to a droplet. In a generalized droplet equation of motion written as follows:

$$m_d \frac{dV_d}{dt} = F_{drag} + F_{wall} + F_{saffman} \quad (A1.8)$$

The Saffman lift force can be defined as follow (ref. A16):

$$F_{saffman} = 1.615 D_d^2 (\rho_g \mu_g)^{0.5} \left[\frac{1}{|\vec{\omega}_g|} \right]^{0.5} \left[(\vec{V}_g - \vec{V}_d) \times \vec{\omega}_g \right] f(Re_d, Re_s) \quad (A1.9)$$

$$\vec{\omega}_g = \nabla \times \vec{V}_g \quad (A1.10)$$

$$Re_s = \frac{\rho_g D_d^2 |\vec{\omega}_g|}{\mu_g} \quad (A1.11)$$

$$Re_d = \frac{\rho_g D_d |V_g - V_d|}{\mu_g} \quad (A1.12)$$

At the stagnation region, these forces have a greater influence on smaller rather than larger droplets since the aerodynamic drag force is the predominant force (for large droplets). The effect of these forces on large droplets is felt at the limits of impingement hence it can affect the extent of ice accretion.

As discussed in section “Regime (a),” droplets take a finite time to achieve complete breakup when they have reached critical value. Wolfe and Andersen (ref. A4) derived an empirical equation of the total breakup times for droplets subjected to shock waves in the following form:

$$t = \frac{D}{\sqrt{\frac{256 \mu_d^2}{\rho_d^2 D^2} + \frac{2P}{\rho_d} - \frac{16 \mu_d}{\rho_d D}}} \quad (A1.13)$$

$$P = \left[\frac{1}{2} \rho_g V_r^2 C_D - k \frac{\sigma}{D} \right] \quad (\text{A1.14})$$

The suggested value for the drag coefficient (C_D) in equation A1.14 is between 1 and 2, and the value for k is 2. Figure A4 shows the total breakup time for water droplet sizes in the range of 100 to 1000 μm using the above equation. It must be noted that the short breakup times in figure A4 are for droplets subjected to severe pressure gradients from a shock wave. In the stagnation region of a wing leading edge, for example, it may take longer due to a relatively slower decelerating flow.

A more rigorous treatment of the breakup times is given by Pilch (ref. A2, also adopted for use in a commercial CFD code) who defined three characteristic breakup times;

- i) initiation time is when the characteristic “bag” breakup starts to form,
- ii) primary breakup time is when a coherent drop ceases to exist, and
- iii) total breakup time is when all its fragments no longer undergo further breakup.

If a droplet should break-up completely before reaching the local wall surface, then a breakup size can also be computed using the following empirical correlations: Wolfe and Andersen’s equation (ref. A4),

$$D_{30} = \left[\frac{136 \mu_d \sigma_d^{1.5} D_0^{0.5}}{\rho_g^2 \rho_d^{0.5} |V_d - V_g|^4} \right]^{1/3} \quad (\text{A1.15})$$

or, Pilch’s equation,

$$d_{\max} = We_c \frac{\sigma_d}{\rho_g V_r} \left(1 - \frac{V_{frag}}{V_r} \right)^{-2} \quad (\text{A1.16})$$

where V_{frag} is the fragment cloud velocity.

A1.4 Regime (d)

When a droplet impinges on a solid surface, droplet can either splash on impact (refs. A17 and A18) or “bounce” off without breakup at very shallow impact angles (refs. A19 to A21). Incipient splash can be quantified by an impact parameter, K , defined as follows:

$$K = Oh \cdot Re^{1.25} \quad (\text{A1.17})$$

Recent research by Mundo (ref. A18) has shown that the limit between splashing and deposition is about 57.7, and splashing will occur when this limit is exceeded.

Droplet splashing is particularly important to icing codes because of the mass loss due to splashing that could not be accounted for in existing codes. As a result, the impingement characteristics and the predicted ice shapes do not correlate well with experimental data at the large drop regime where splashing occurs. In addition, there is also a possibility of ice accretion from splash-back droplets re-impinging on aft surfaces which typically are not protected by anti- or de-icing devices. The possibility of droplet splashing during flight in SLD conditions is quite

high due to the large droplet size (greater than 40 μm) and high relative droplet velocity (greater than 100 m/s) encountered.

Figure A5 shows the distribution of the impact parameter on a NACA 0012 airfoil based on a relative droplet-air velocity of 100 m/s and droplet diameter of 100 μm . It shows that a significant part of the airfoil is likely to experience droplet splash due to the high impact parameters.

The parameters that affect the splash mechanism include droplet impact velocity, impact angle, droplet size, viscosity, surface tension and surface roughness (refs. A10, A18). In order to characterize the splash phenomena and develop suitable correlations between impact and rebound conditions, the following non-dimensional terms have been commonly used (refs. A18, A19, A21):

$$\text{Reynolds number, } Re = \frac{\rho d_o w}{\mu} \quad (\text{A1.18})$$

$$\text{Ohnesorge number, } Oh = \frac{\mu}{\sqrt{\rho \sigma d_o}} \quad (\text{A1.19})$$

$$\text{Surface roughness, } S_t = \frac{R_t}{d_o} \quad (\text{A1.20})$$

$$\text{Film thickness, } \delta_t = \frac{f_t}{d_o} \quad (\text{A1.21})$$

$$\text{Weber number, } We = (Oh \cdot Re)^2 = \frac{\rho d_o w^2}{\sigma} \quad (\text{A1.22})$$

where w is the normal component of the droplet impact velocity. The term d_o , ρ , μ , σ represents the water droplet diameter, density, viscosity, surface tension respectively. Notice the difference in the definition of the Weber and Reynolds numbers here that use the liquid density and normal component of droplet impact velocity compared to that in section "Regime (a)". Recent experimental tests using mono-dispersed droplets and a horizontal wind tunnel have provided some data on splash-back size and velocity (ref. A10). Figure A6 shows the effect of the impact parameter and surface roughness on splash-back droplet sizes distribution from the tests.

However there is little or no published data, to the knowledge of the authors, on the amount of mass loss due to splashing. This kind of information is important to the calculation of the water catch efficiency, and hence, to the amount of ice accreted. Experimental tests to determine the distribution of water impingement using different airfoils have shown some interesting results as shown in figures A7 to A9 (ref. A22). These figures show a reduced water impingement distribution near the airfoil leading edge as droplet sizes are increased. The most likely explanation for this is the mass loss due to droplet splashing.

Droplet splashing is also a complicated process because it involves a large distribution of droplet sizes impinging on a water film, typical of SLD icing conditions. In order to understand the mechanism of splashing, a large number of experiments have been performed using high-speed visual imaging system and a single droplet (ref. A18). However, most of the data are not applicable to droplet impingement for an aircraft due to their low impact velocity and limited film heights and surface roughness. These three parameters are considered to be the most important factors that influence the outcome of a droplet splash event. A parametric study relevant to in-flight conditions is quite a difficult challenge. However, direct numerical simulation techniques such as the volume of fluid methodology (VOF) can be used to study the splash

mechanism during droplet impingement. Figure A10 (ref. A23) shows an example of a transient computation using the VOF technique to simulate a single droplet impinging on a stationary water film (130 μm diameter, 50 μm depth, impact velocity of 60 m/s).

The results show the various stages of droplet disintegration into the water film and resulting splash droplets generated from the water stems. It is possible to estimate the amount of mass loss numerically and compared with experimental data.

A1.5 Regime (e)

In section A1.4, it was indicated that the possibility of droplet splashing from large droplets (SLD conditions) in flight icing condition is quite high. The splash-back droplets can re-impinge on aft surfaces and cause aft ice accretion. The dynamics of the rebound droplets are governed by the (splash-back) droplet size, velocity and angle, the geometry and configuration of the sections e.g. wing and stabilizer, intakes. Geometrical shape can include ice shape and water film on an airfoil. Small droplets tend to be entrained near the surface forming a “fog-like” appearance over the body itself. Large splash droplets, with sufficient energy, can escape the boundary layer and may re-impinge on aft surface.

A2. LWC Measurement For SLD Conditions

The currently available instrumentation for measuring LWC include the icing blade, rotating cylinder and hot-wire probes such as the Johnson-William probe, CSIRO-king probe and Nevzorov probe (ref. A24). These instruments have been optimized for measuring appendix C droplet sizes but significant errors have been reported for SLD sizes. Droplet splashing is considered to be the main source of error for these intrusive devices. As mentioned earlier, droplet splash only needs a few microseconds (see fig. A10) therefore it is conceivable that the mass loss (due to splash droplets) is the cause for these measurement errors. Non-intrusive probes such as the Phase Doppler Particle Analyzer (PDPA) have also been used to measure the mass flux, but data quality depends heavily on the skill and experience of the experimentalist with the PDPA probe (ref. A25). A possible method of minimizing this is to collect all the droplets in the probe to give a direct measurement in the so-called iso-kinetic technique. In the design, an air stream tube (laden with poly-dispersed droplets) equivalent to the suction probe diameter (i.e. captured area-ratio of unity) is collected and measured directly (gravimetric or water depth) to give the LWC.

References

- A1. Lane, W.R., “Shatter of drops in Stream of Air,” *Ind. Eng. Chem.*, 43, no 4, 1312–1317, 1951.
- A2. Pilch, M. and Erdman, C.A., “Use of Breakup Time Data and Velocity History data to Predict the Maximum Size of Stable Fragments for Acceleration-Induced Breakup of a Liquid Drop,” *Int. J. Multiphase Flow*, 13, no. 6, 741–757, 1987.
- A3. Wierzba, A., “Deformation and breakup of liquid drops in a gas stream at nearly critical Weber numbers,” *Experiments in Fluids* 9, 59–64, 1990.
- A4. Wolfe, H.E. and Andersen, W.H., “Kinetics, Mechanism, and Resultant Droplet Sizes of the Aerodynamic Breakup of Liquid Drops,” Aerojet-General Corporation research and engineering Division Report no. 0395–04 (18)SP, 1964.
- A5. Borisov, A.A., “Droplet Breakup Regimes and Criteria for their Existence,” *J. Eng. Physics*, 40, 1, 1981 [AIAA–90–2309].

- A6. Kennedy, J.B. and Roberts, J., "Rain Ingestion in a Gas Turbine Engine," ILASS-AMERICAS, Inst. of Liquid Atomisation and Spray Systems, 4th Annual Conference, Hartford, USA, 154–186, 1990.
- A7. Dickerson, R.A. and Coultas, T.A., "Breakup of droplets in an Accelerating Gas flow," AIAA-66-611, 1966.
- A8. Rabin, E.A., Schallennmuller, A.R. and Lawhead, R.B., "Displacement and shattering of Propellant Droplet," Final Summary Report, Washington DC, US Airforce Office of Scientific Research, AFOSR TR 60-75, March 1960.
- A9. Hinze, J.O., "Fundamentals of the Hydrodynamic Mechanism of Splitting in Dispersion Processes," A.I.Ch.E. Journal, vol. 1, no. 3, 289–295, 1955.
- A10. Tan, S.C. and Bartlett, P.G., "Droplet Dynamics," ICECREMO Project Task 1.3, Contractor Report, ICECREMO/TR/CRAN1/JT970531/1, June 1997.
- A11. Merrington, A.C., and Richardson, E.G., Proc. Phys. Society, 59, 1, 1947.
- A12. Krzeczkowski, S.A., "Measurement of Liquid Droplet Disintegration Mechanism," Int. J. Multiphase Flow, vol. 6, 227–239, 1980.
- A13. O'Rourke, P.J. and Amsden, A.A., "The TAB Method for Numerical Calculation of Spray Droplet Breakup," Society of Automotive Engineers Paper 87-2089, 1987.
- A14. Clark, M.M., "Drop Breakup in a Turbulent Flow—I, Conception and Modelling Considerations," Chemical Engineering Science, vol. 43, no. 3, 671–679, 1988.
- A15. Talyor, G.I., "The Shape and Acceleration of a Drop in a High Speed Airstream," The Scientific Paper of G.I. Talyor, edited by G.K. Batchelor, vol. III, Univ. Press, Cambridge, UK, 1963.
- A16. Sommerfeld M., "Theoretical and Experimental Modeling of Particulate Flow—Overview and Fundamentals," Lecture series 2000-06, April 3–7, 2000, Von Karman Institute.
- A17. Parker, G.J. and Bruen, E., "The collision of drops with dry and wet surfaces in an air atmosphere," Proc. Inst. Mech. Eng.(London), 184, Paper 23, 1969.
- A18. Mundo, Chr., Sommerfeld, M. and Tropea, C., "Droplet-wall collisions: Experimental studies of the deformation and Breakup process," Int. J. Multiphase Flow, vol. 21, no. 2, p. 151–173, 1995.
- A19. Fielding, S.E., "Experimental study of water droplets at high speeds and low incidence," RAE report C2450/FR, 1986.
- A20. Rein, M., "Phenomena of a liquid drop impact on solid and liquid surfaces," Fluid Dynamics Res. 12, 61–93, 1993.
- A21. Stow, C.D., and Hadfield, M.G., "An experimental investigation of fluid flow resulting from an impact from a water drop with an unyielding dry surface," Proc. R. Soc. London A 373, pp. 419–441, 1981.
- A22. Papadakis, M., Hung, K.E., and Yeong, H.W., "Experimental investigation of water impingement on single and multi-element airfoils," AIAA 2000-0100.
- A23. Tan, C.S., Papadakis, M., "General effects of large droplet dynamics on ice accretion modeling," AIAA-03-0392, Reno, 2003.
- A24. Ide, R.F., "Comparison of Liquid Water Content Measurement Techniques in an Icing Wind Tunnel," NASA/TM—1999-209643, 1999.
- A25. Rudoff, R.C., Bachalo, E.J., and Bachalo, W.D., "Liquid Water Content Measurement Using the Phase Doppler Particle Analyser in the NASA Lewis Icing Research Tunnel," AIAA 93-0298, Reno, 1993.

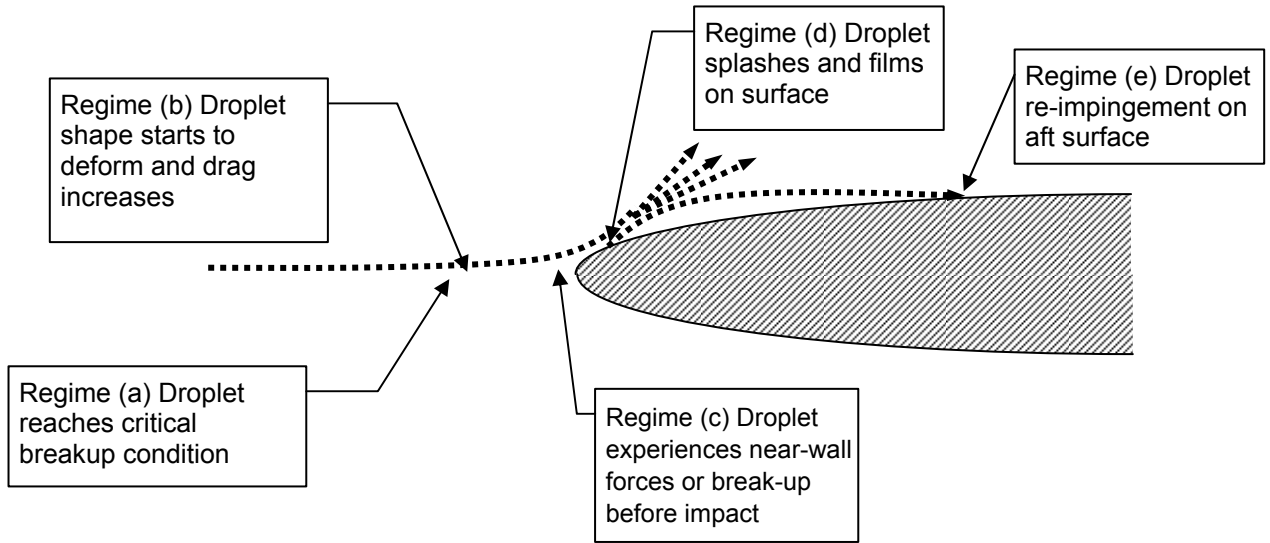


Figure A1.—Potential droplet transition regimes.

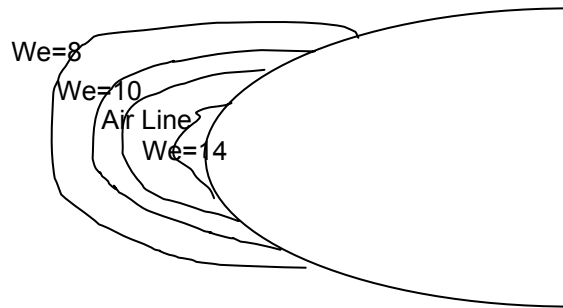


Figure A2(a).—Weber number distribution, $d = 200 \mu\text{m}$, $V_r = 100 \text{m/s}$.

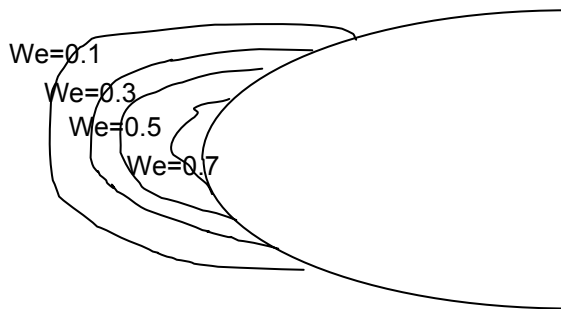


Figure A2(b).—Weber number distribution, $d = 20 \mu\text{m}$, $V_r = 100 \text{m/s}$.

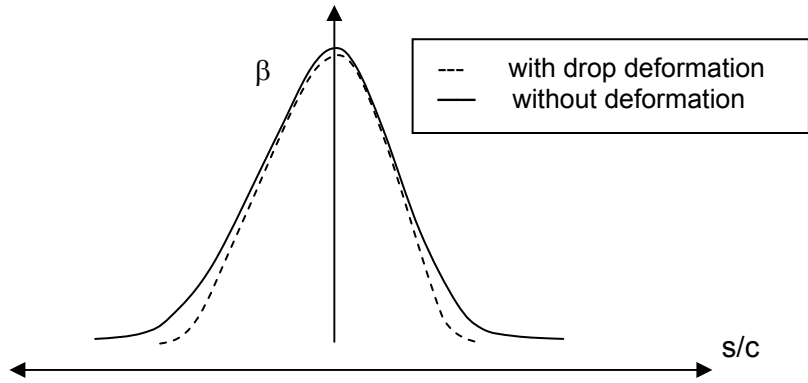


Figure A3.—Effects of droplet deformation on the local catch efficiency.

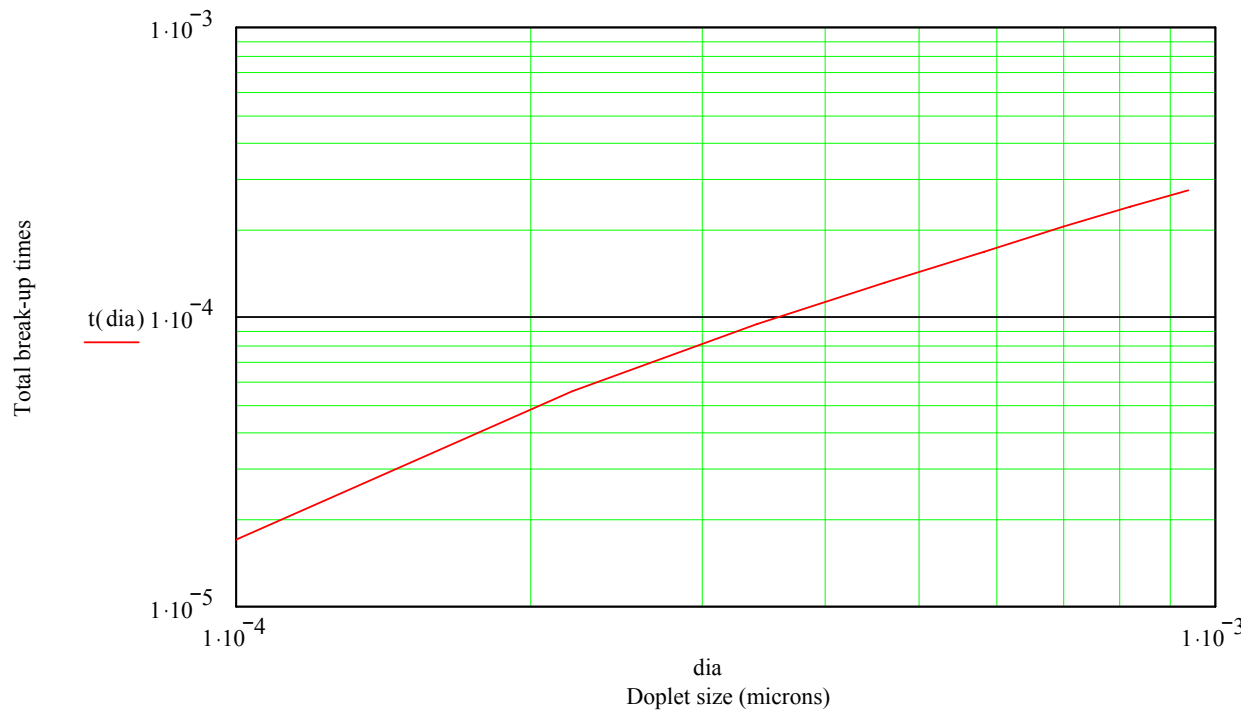


Figure A4.—Total Breakup times ($V_r = 100$ m/s).

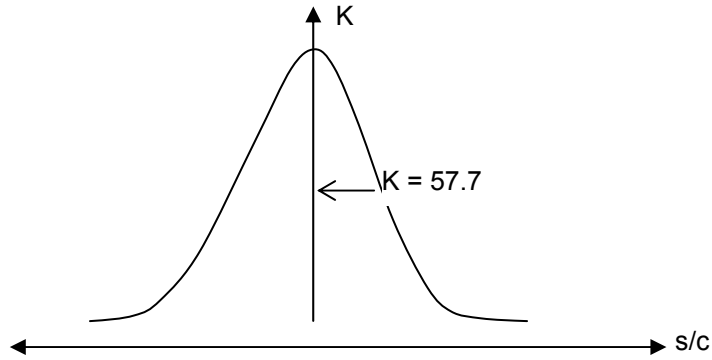


Figure A5.—Distribution of the K parameter on an airfoil.

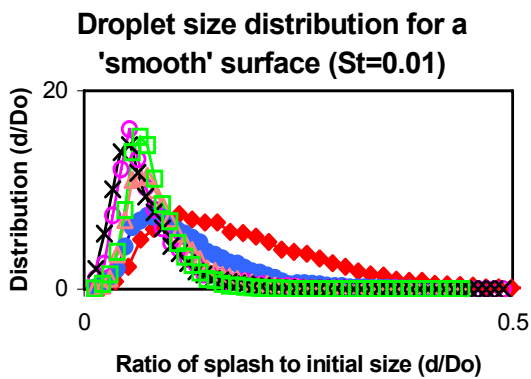


Figure A6(a).—Splash-back sizes from smooth surface.

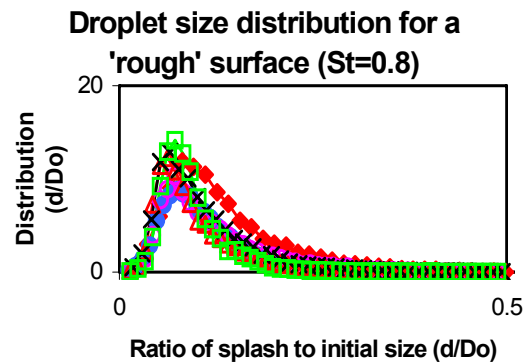


Figure A6(b).—Splash-back sizes from rough surface.

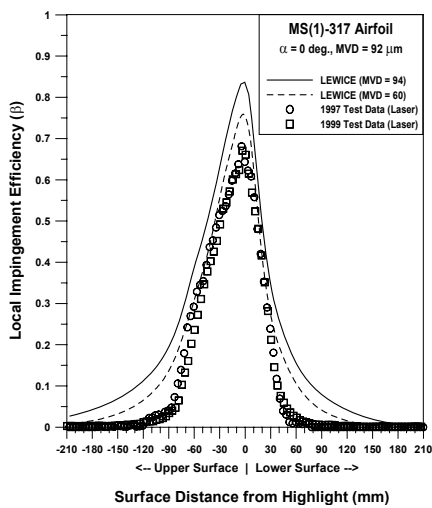
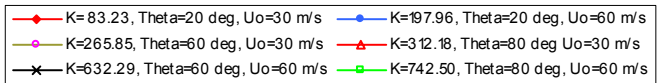
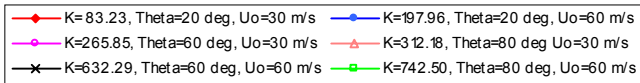


Figure A7.—SLD impingement on an MS-317 airfoil (LEWICE vs. Experiment).

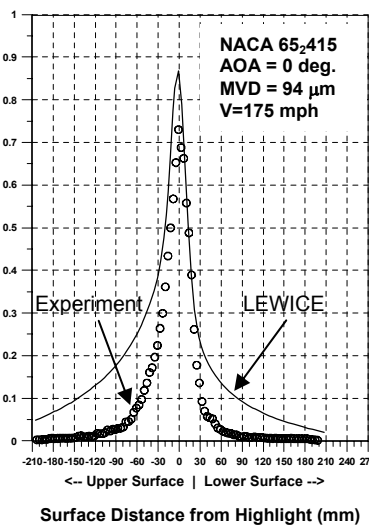


Figure A8.—SLD Impingement on a NACA 65₂-415 airfoil (LEWICE vs. Experiment).

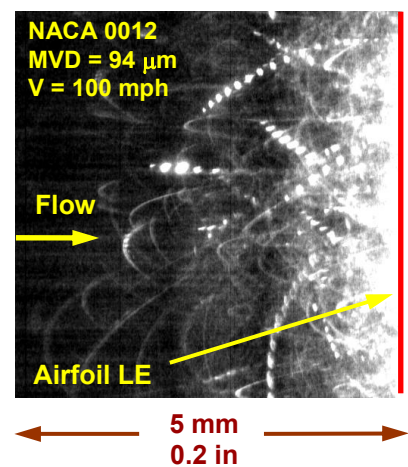


Figure A9.—Droplet Splashing on a NACA 0012 airfoil.

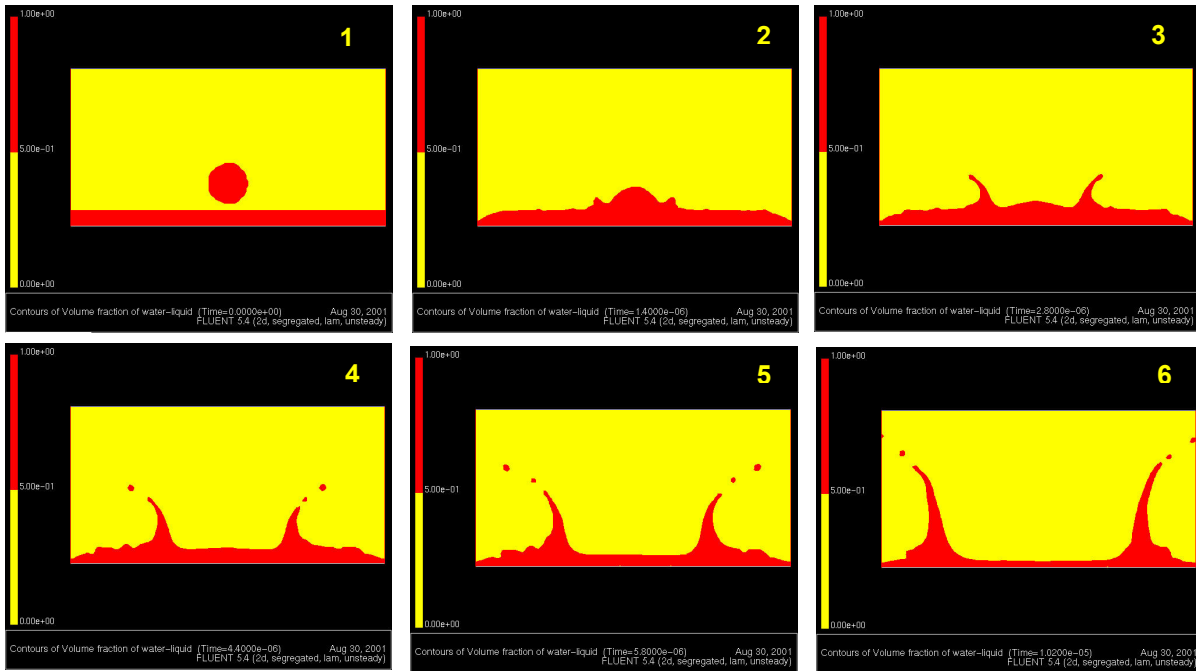


Figure A10.—Single droplet impinging on a stationary water film; 130 μm diameter, 50 μm depth, impact velocity of 60 m/s.

Appendix B—Summary of Impingement Results Data

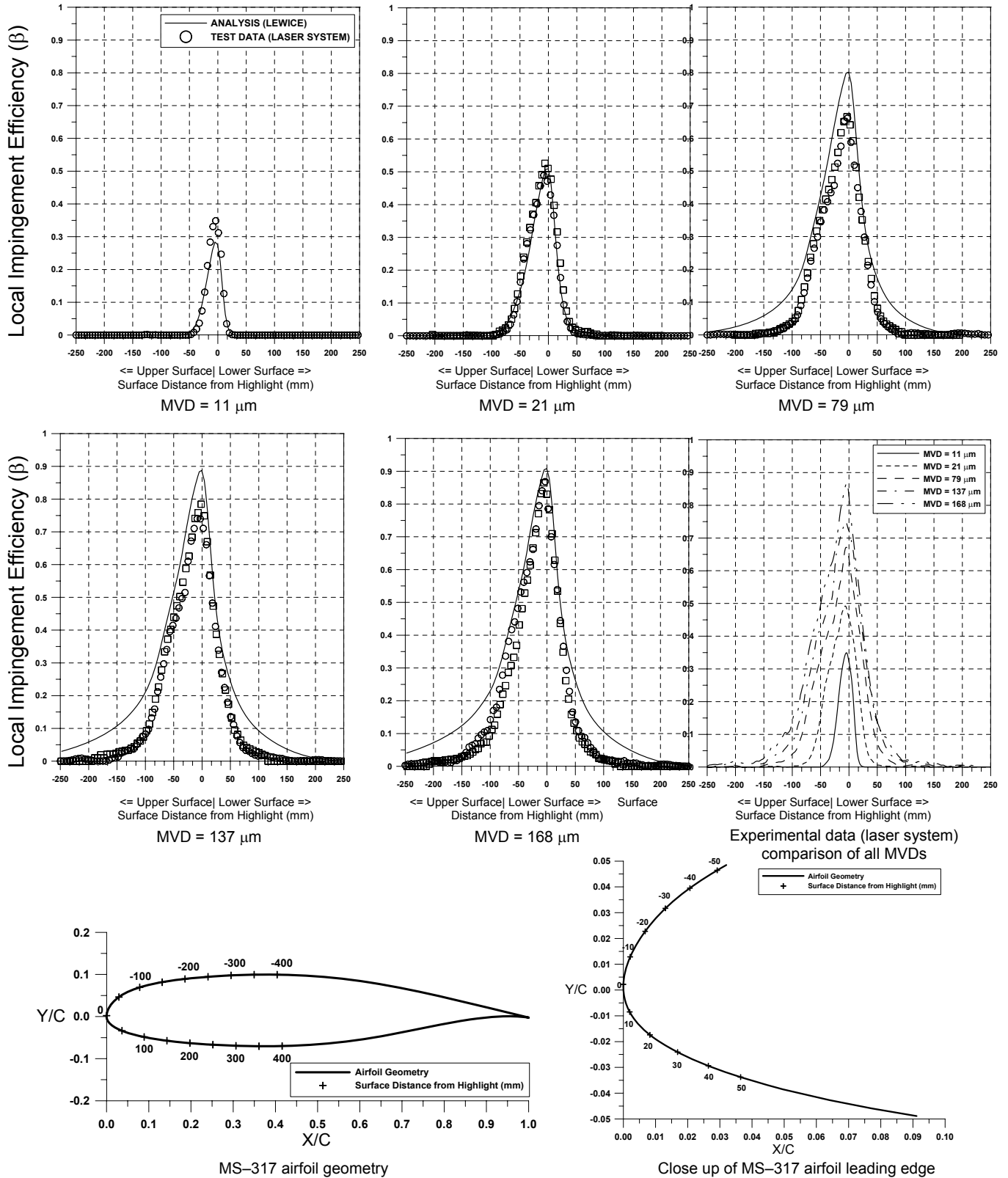
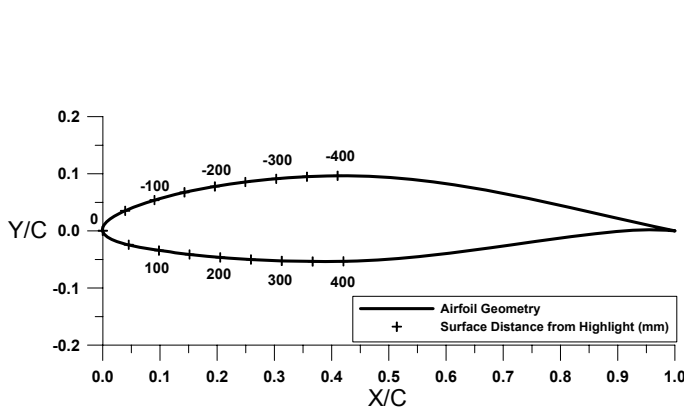
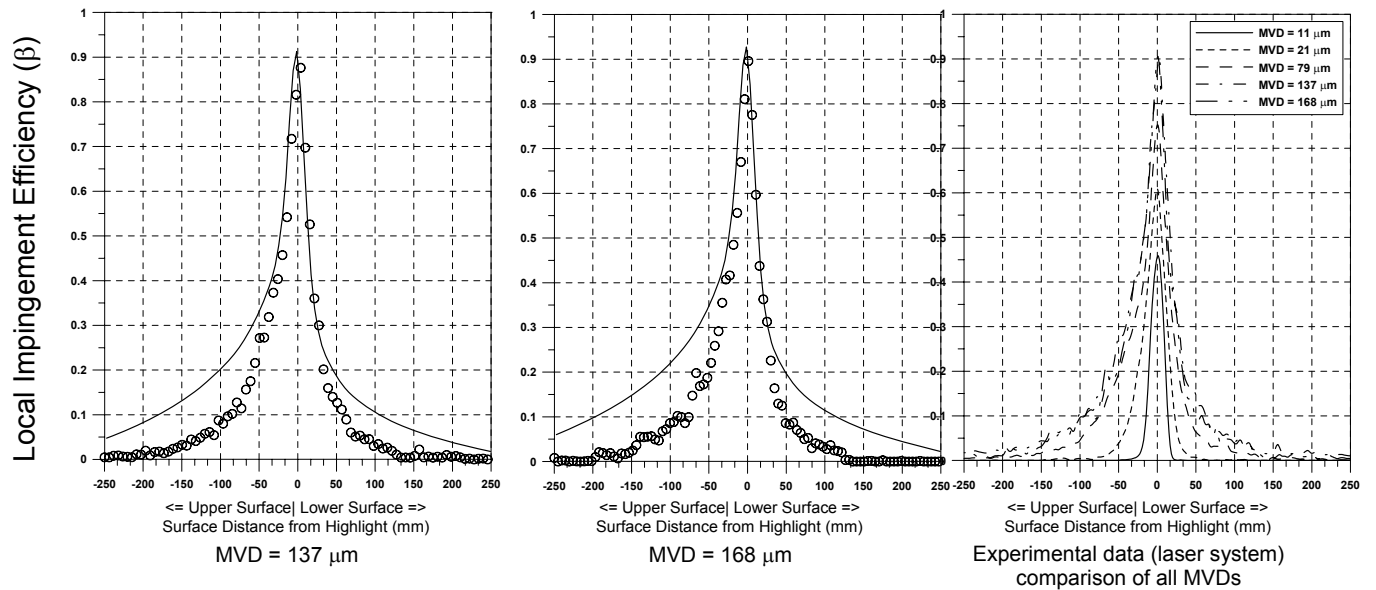
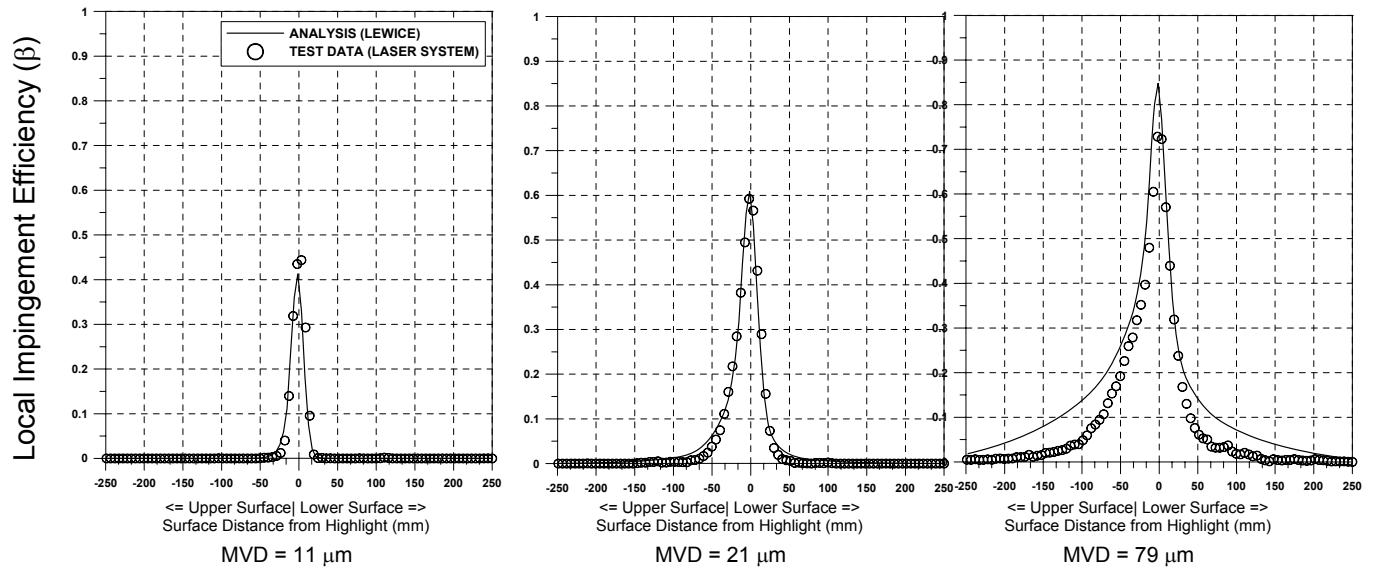
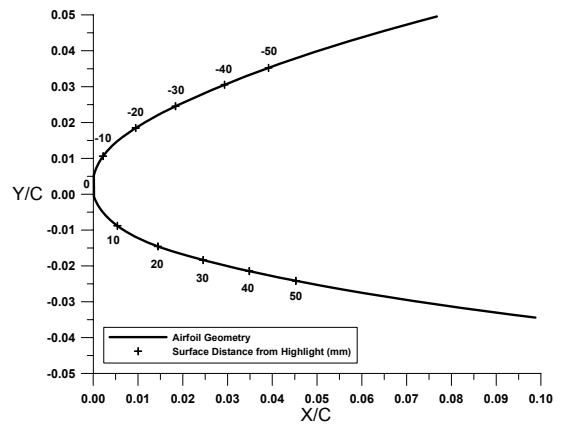


Figure B1.—Summary of MS-317 airfoil impingement data, AOA = 0°.



NACA 65₂-415 airfoil geometry



Close up of NACA 65₂-415 airfoil leading edge

Figure B2.—Summary of NACA 65₂-415 airfoil impingement data, AOA = 0°.

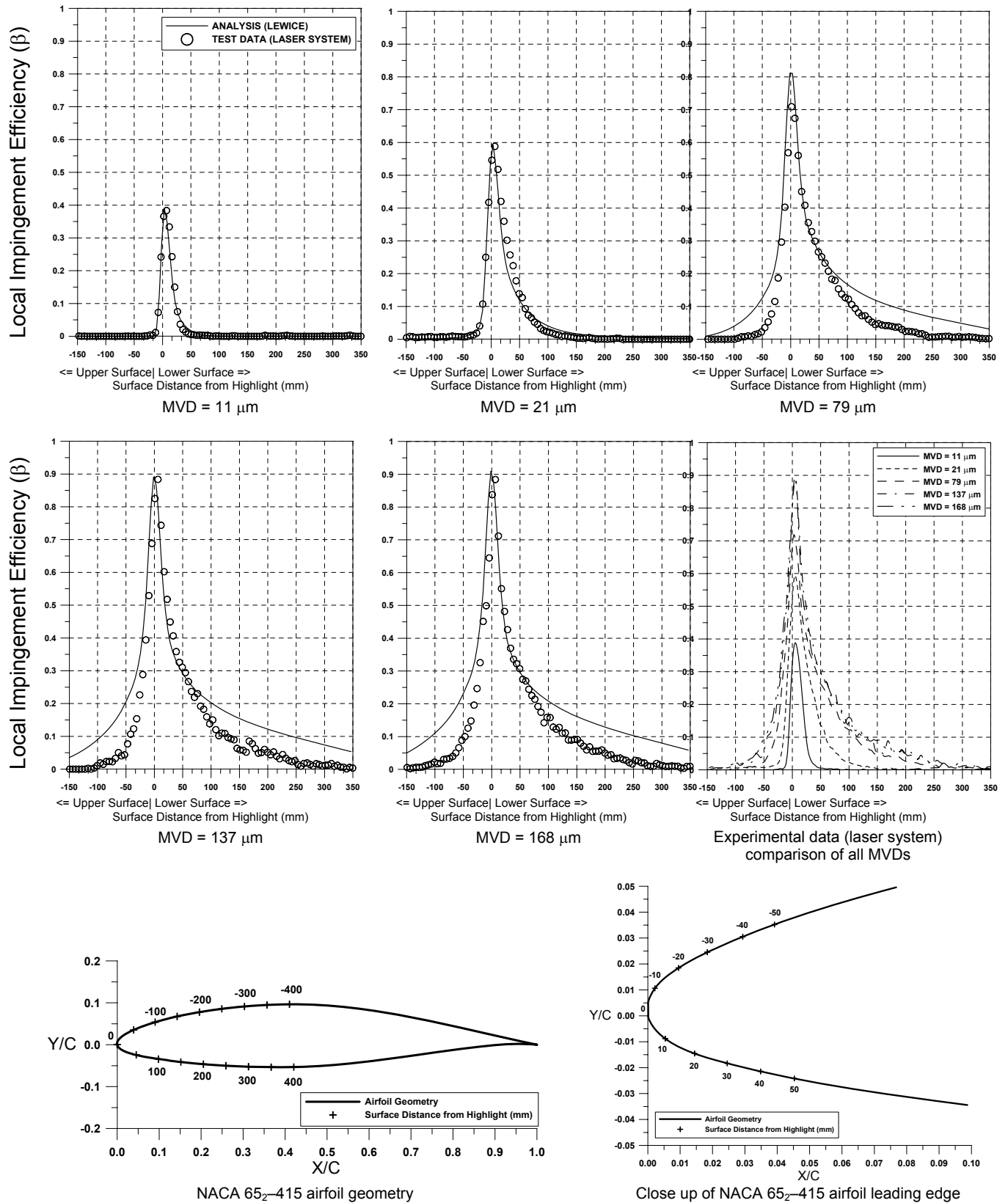


Figure B3.—Summary of NACA 652-415 airfoil impingement data, AOA = 4°.

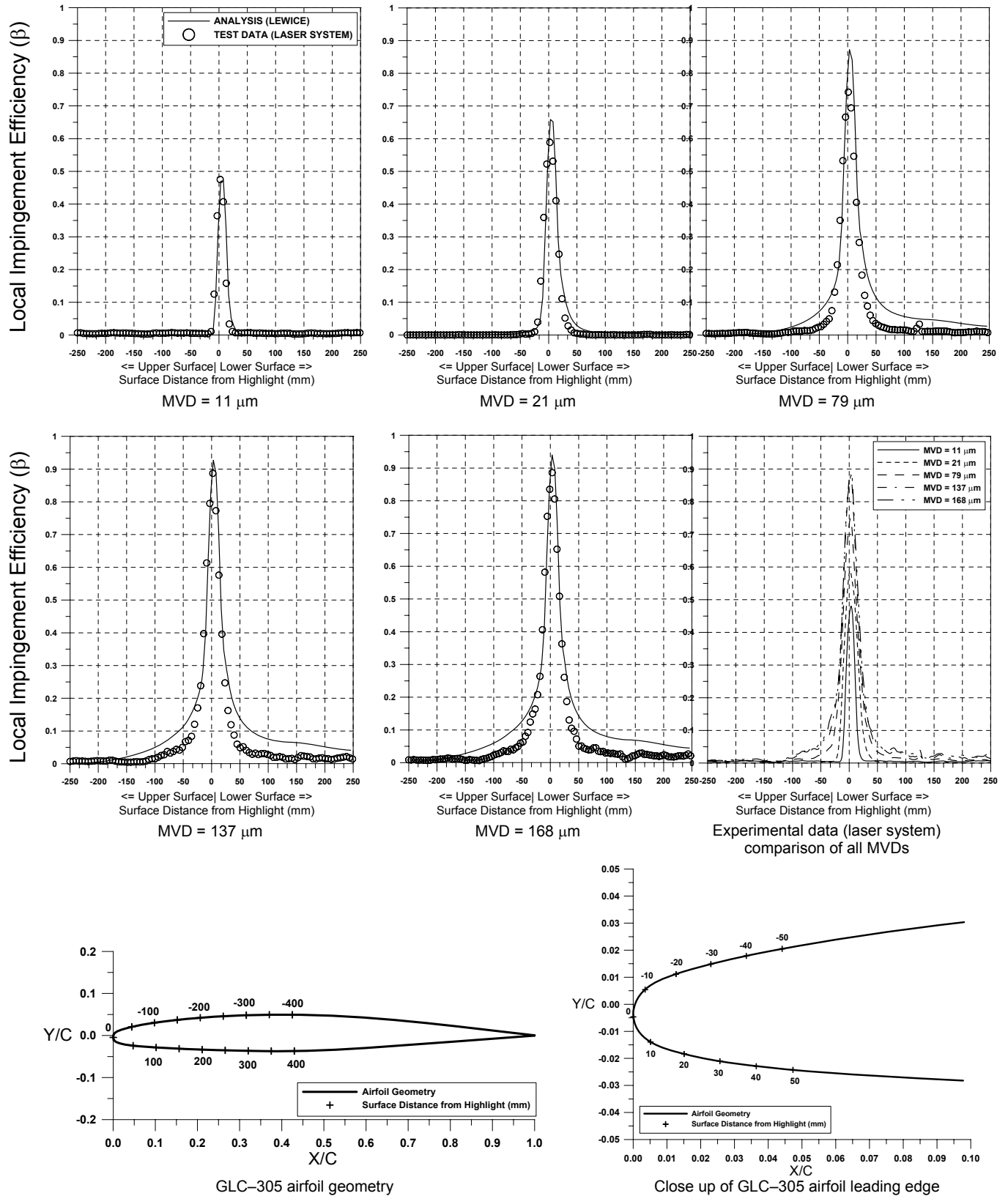


Figure B4.—Summary of GLC-305 airfoil impingement data, AOA = 1.5°.

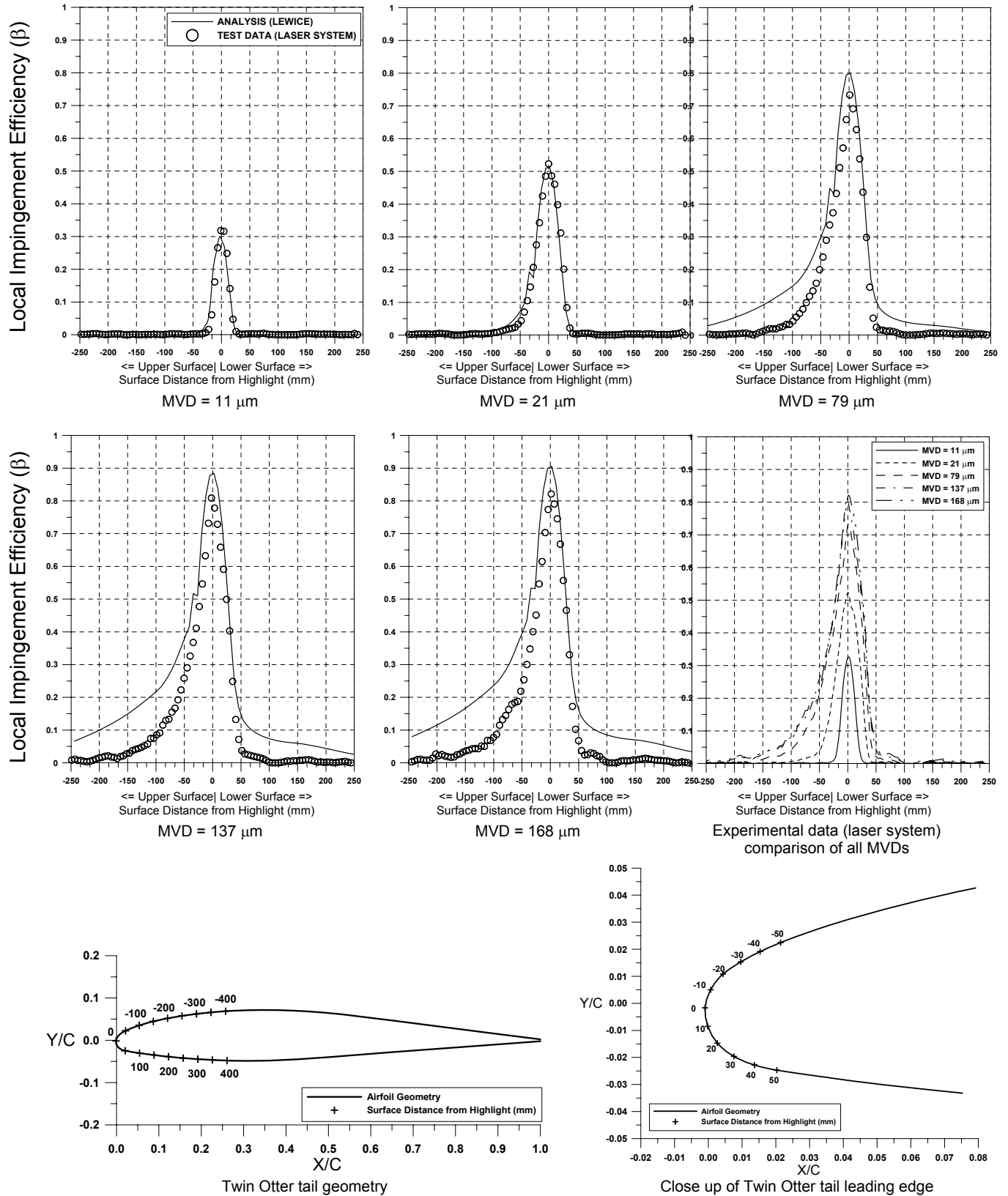


Figure B5.—Summary of Twin Otter tail impingement data, AOA = 0°.

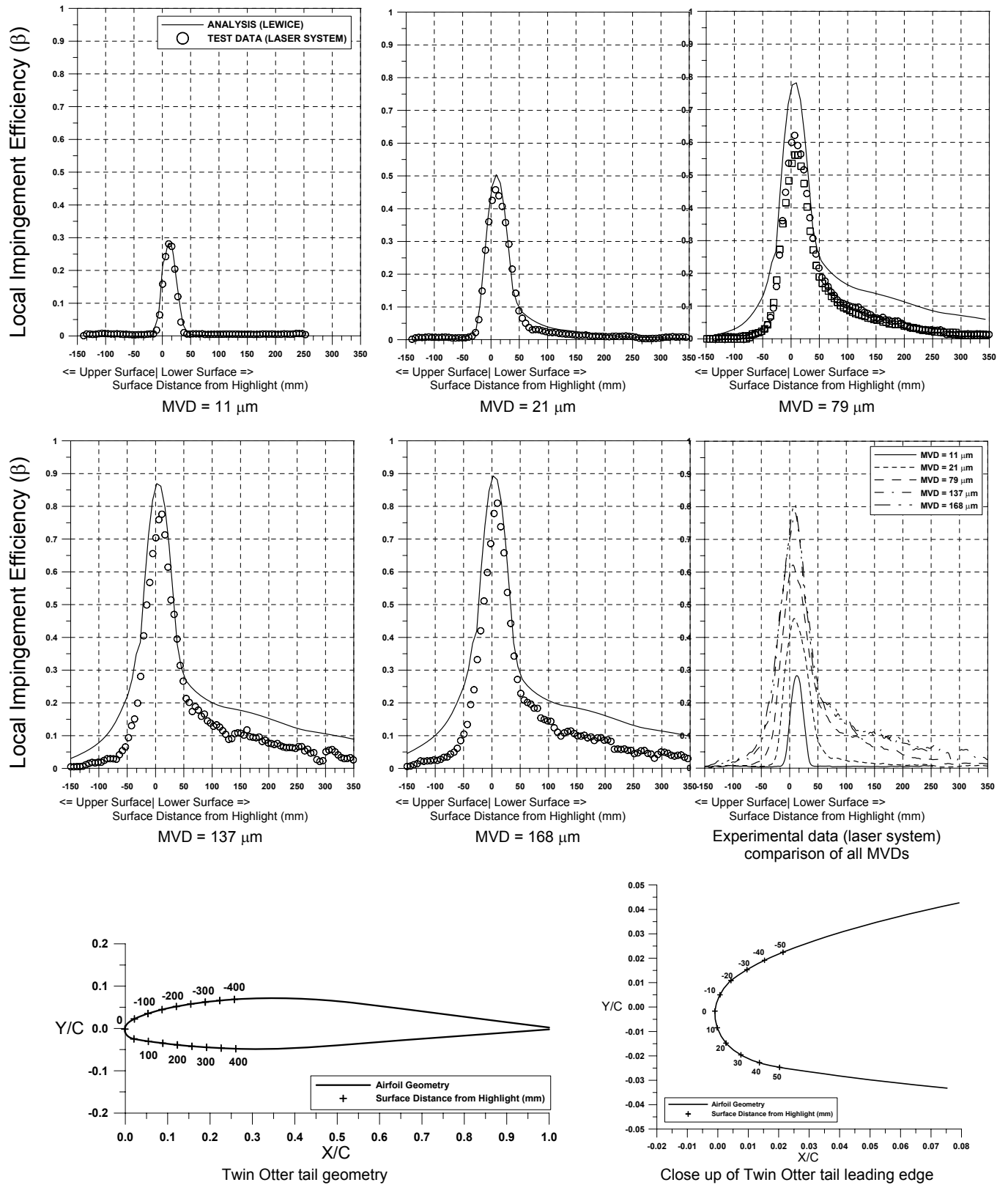
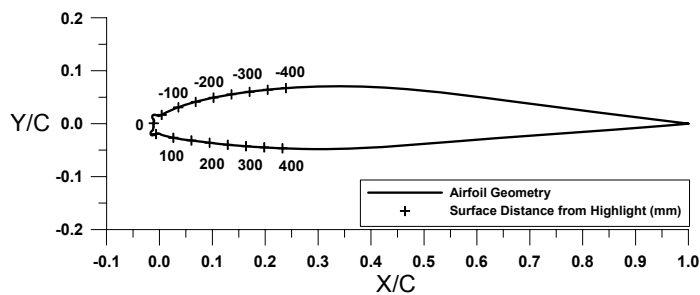
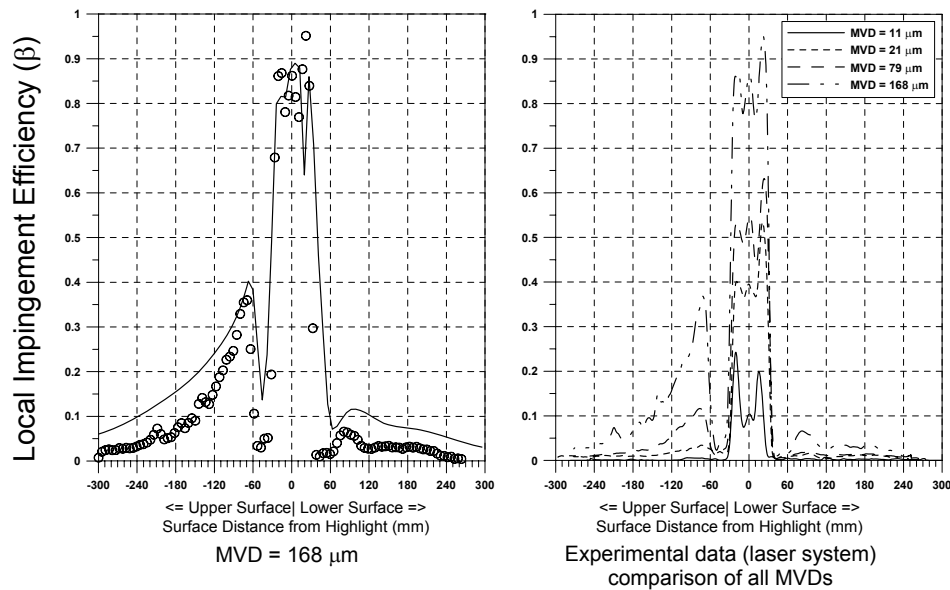
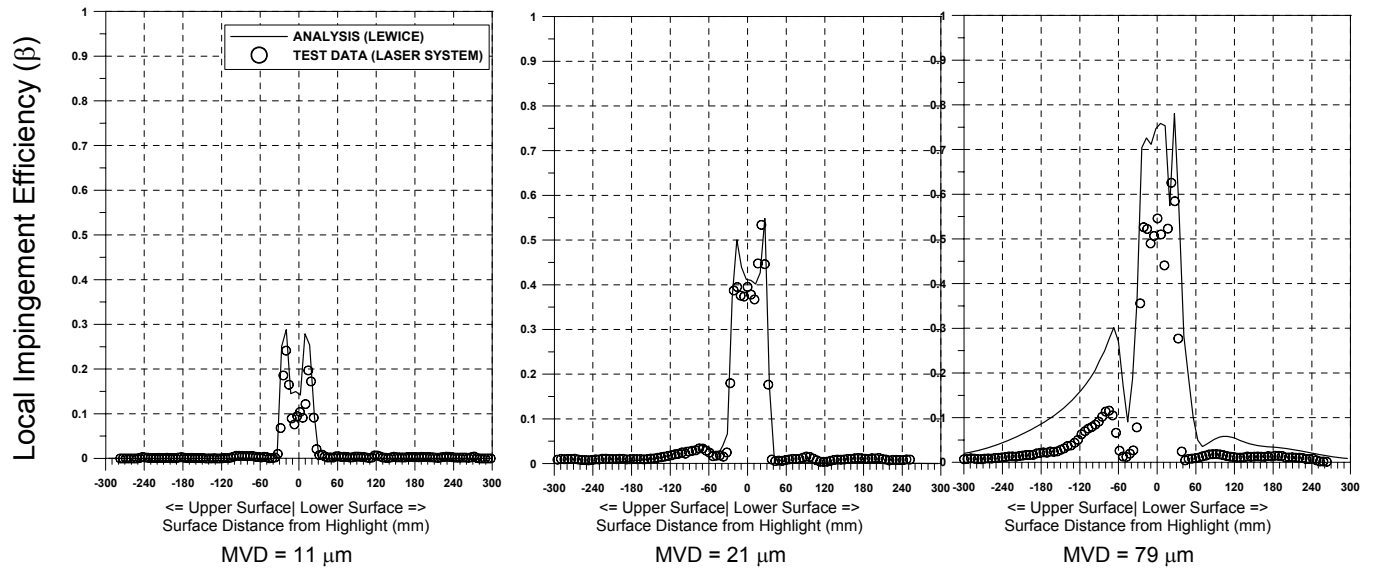
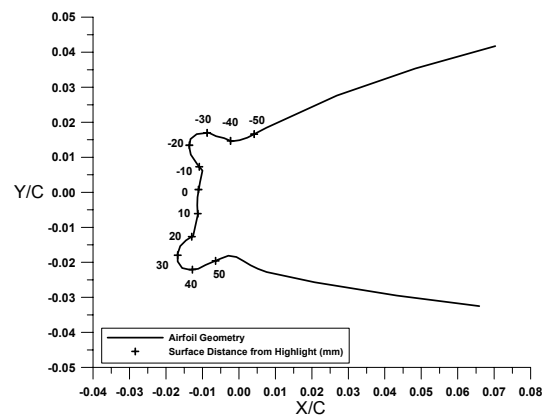


Figure B6.—Summary of Twin Otter tail impingement data, AOA = 4°.



Twin Otter tail with 22.5-min ice shape geometry



Close up of Twin Otter tail with 22.5-min ice shape leading edge

Figure B7.—Summary of Twin Otter tail with 22.5-min ice shape impingement data, AOA = 0°.

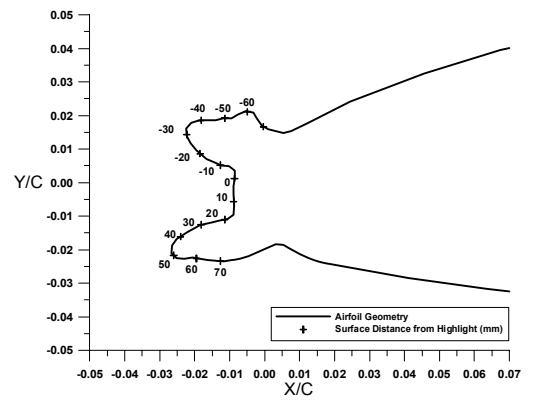
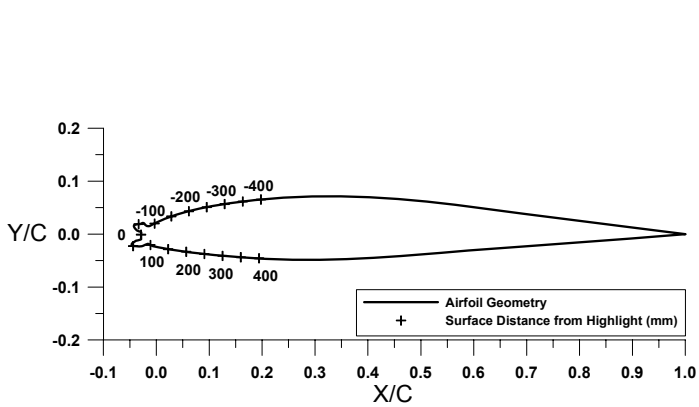
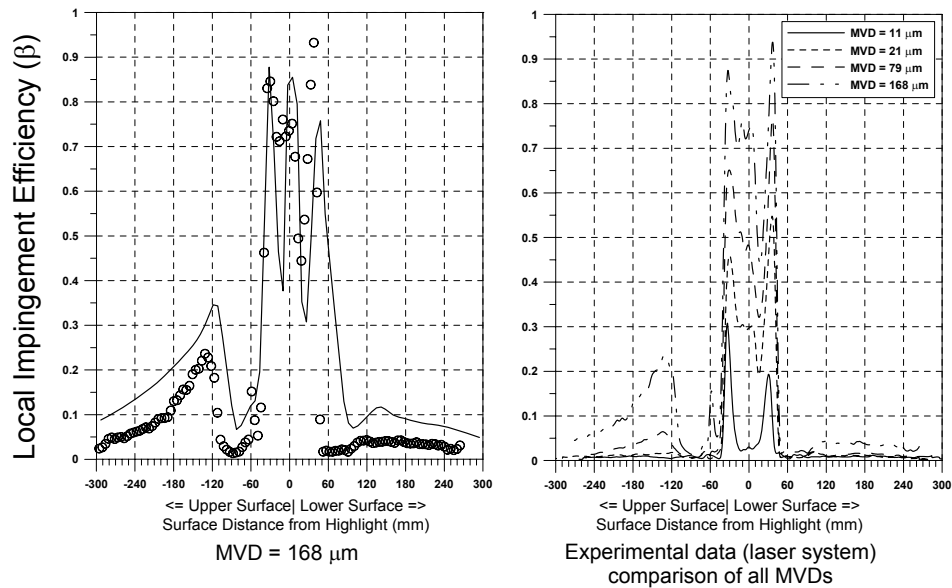
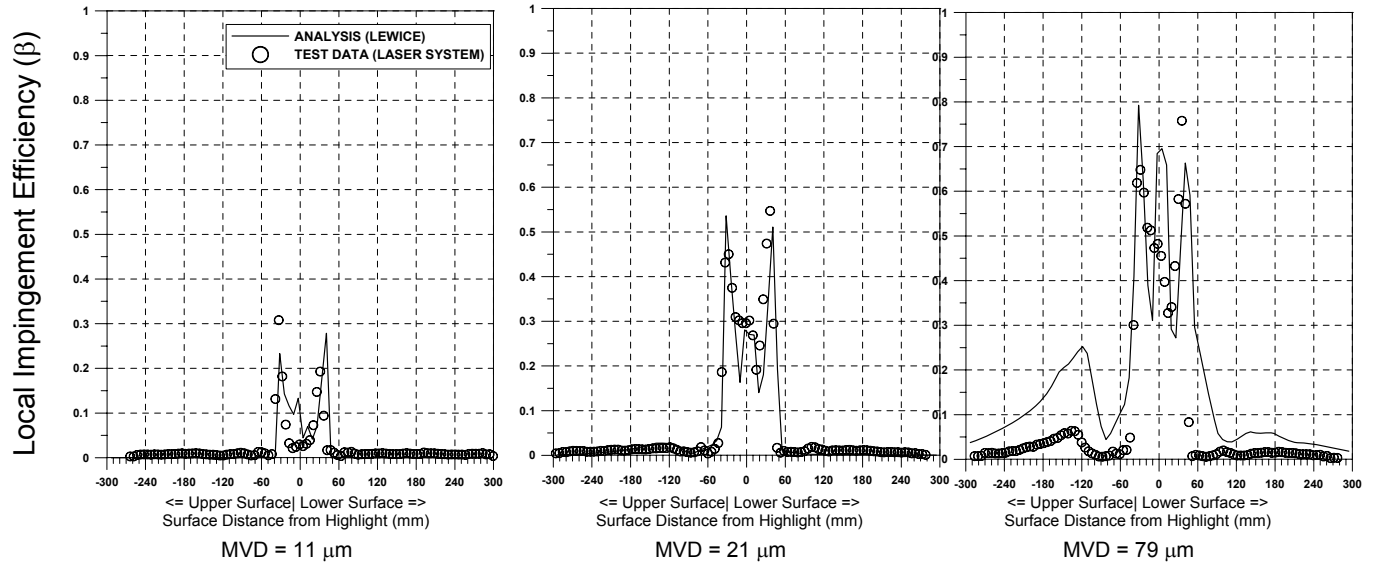


Figure B8.—Summary of Twin Otter tail with 45-min ice shape impingement data, AOA = 0°.

Appendix C—Coordinates of Airfoil Sections and Pressure Ports

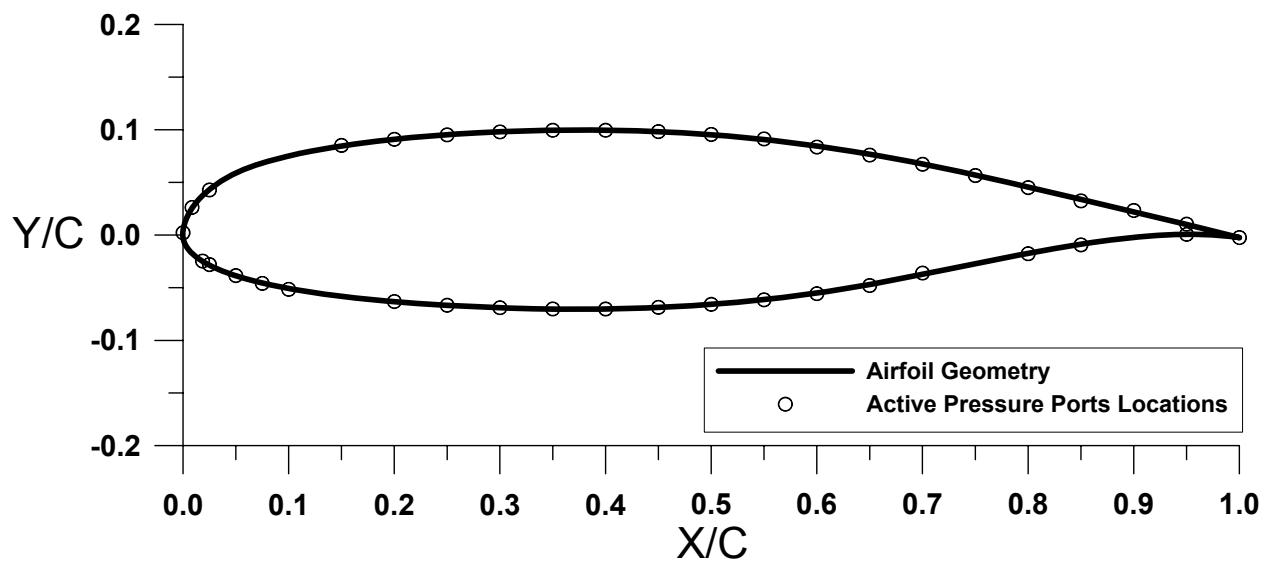


Figure C1.—MS(1)—0317 Airfoil

TABLE C1.1.—COORDINATES OF MS(1)–0317 AIRFOIL

Lower Surface						Upper Surface					
x/c	y/c	x/c	y/c	x/c	y/c	x/c	y/c	x/c	y/c	x/c	y/c
1	-0.0024	0.3147	-0.0695			0.0000	0.0022	0.2795	0.0972	1	-0.0024
0.9848	-0.0007	0.2977	-0.0690			0.0001	0.0042	0.2959	0.0980		
0.9725	0.0002	0.2811	-0.0684			0.0004	0.0062	0.3118	0.0986		
0.9603	0.0007	0.2643	-0.0676			0.0008	0.0081	0.3251	0.0990		
0.9469	0.0007	0.2473	-0.0667			0.0013	0.0101	0.3375	0.0993		
0.9332	0.0002	0.2306	-0.0657			0.0018	0.0120	0.3527	0.0996		
0.9193	-0.0006	0.2145	-0.0645			0.0025	0.0139	0.3690	0.0997		
0.9051	-0.0017	0.1982	-0.0631			0.0032	0.0157	0.3854	0.0997		
0.8907	-0.0032	0.1814	-0.0616			0.0040	0.0176	0.4020	0.0995		
0.8760	-0.0050	0.1657	-0.0600			0.0049	0.0193	0.4183	0.0992		
0.8612	-0.0070	0.1502	-0.0582			0.0059	0.0211	0.4341	0.0988		
0.8460	-0.0093	0.1348	-0.0562			0.0068	0.0229	0.4498	0.0983		
0.8304	-0.0119	0.1199	-0.0540			0.0079	0.0246	0.4658	0.0975		
0.8145	-0.0147	0.1055	-0.0516			0.0090	0.0262	0.4818	0.0966		
0.7981	-0.0177	0.0911	-0.0489			0.0101	0.0279	0.4971	0.0956		
0.7812	-0.0210	0.0772	-0.0459			0.0113	0.0295	0.5129	0.0943		
0.7640	-0.0244	0.0640	-0.0427			0.0126	0.0311	0.5290	0.0929		
0.7443	-0.0283	0.0496	-0.0385			0.0138	0.0326	0.5446	0.0913		
0.7249	-0.0323	0.0394	-0.0350			0.0152	0.0341	0.5601	0.0896		
0.7061	-0.0361	0.0323	-0.0321			0.0165	0.0355	0.5755	0.0877		
0.6903	-0.0392	0.0273	-0.0298			0.0180	0.0370	0.5908	0.0857		
0.6732	-0.0425	0.0238	-0.0280			0.0194	0.0383	0.6063	0.0836		
0.6576	-0.0454	0.0213	-0.0267			0.0209	0.0397	0.6223	0.0812		
0.6433	-0.0479	0.0196	-0.0257			0.0224	0.0410	0.6383	0.0787		
0.6273	-0.0507	0.0179	-0.0247			0.0245	0.0428	0.6545	0.0760		
0.6112	-0.0533	0.0162	-0.0236			0.0276	0.0453	0.6713	0.0730		
0.5956	-0.0557	0.0145	-0.0225			0.0320	0.0485	0.6871	0.0701		
0.5802	-0.0578	0.0129	-0.0213			0.0384	0.0527	0.7018	0.0673		
0.5648	-0.0597	0.0113	-0.0201			0.0479	0.0579	0.7178	0.0639		
0.5488	-0.0615	0.0098	-0.0188			0.0588	0.0628	0.7353	0.0602		
0.5328	-0.0632	0.0083	-0.0175			0.0708	0.0671	0.7518	0.0565		
0.5172	-0.0646	0.0070	-0.0160			0.0835	0.0709	0.7687	0.0528		
0.5014	-0.0658	0.0056	-0.0145			0.0967	0.0743	0.7858	0.0489		
0.4851	-0.0669	0.0044	-0.0129			0.1103	0.0774	0.8025	0.0451		
0.4690	-0.0679	0.0034	-0.0112			0.1245	0.0802	0.8211	0.0407		
0.4529	-0.0687	0.0024	-0.0095			0.1391	0.0828	0.8389	0.0365		
0.4367	-0.0693	0.0016	-0.0076			0.1541	0.0852	0.8565	0.0324		
0.4202	-0.0698	0.0010	-0.0057			0.1690	0.0873	0.8758	0.0278		
0.4061	-0.0701	0.0005	-0.0038			0.1843	0.0892	0.8946	0.0233		
0.3966	-0.0702	0.0002	-0.0018			0.2001	0.0910	0.9130	0.0189		
0.3824	-0.0703	0.0000	0.0002			0.2156	0.0925	0.9312	0.0145		
0.3655	-0.0703					0.2313	0.0939	0.9486	0.0103		
0.3487	-0.0702					0.2473	0.0952	0.9658	0.0062		
0.3317	-0.0699					0.2633	0.0962	0.9827	0.0020		

TABLE C1.2.—COORDINATES OF ACTIVE PRESSURE PORTS OF MS(1)–0317 AIRFOIL

Lower Surface		Upper Surface	
x/c	y/c	x/c	y/c
1	-0.00236	0.00E+00	0.002182
0.95	0.00065	8.50E-03	0.02624
0.85	-0.00932	2.50E-02	0.042818
0.8	-0.01772	0.15	0.085152
0.7	-0.03612	0.2	0.090967
0.65	-0.04792	0.25	0.095164
0.6	-0.05566	0.3	0.097974
0.55	-0.06151	0.35	0.099557
0.5	-0.06581	0.4	0.099534
0.45	-0.06868	0.45	0.098267
0.4	-0.07023	0.5	0.095566
0.35	-0.07019	0.55	0.091311
0.3	-0.06901	0.6	0.083582
0.25	-0.0667	0.65	0.075956
0.2	-0.06314	0.7	0.067262
0.1	-0.05157	0.75	0.056542
7.50E-02	-0.04592	0.8	0.045093
5.00E-02	-0.03851	0.85	0.032429
2.50E-02	-0.02804	0.9	0.023332
1.85E-02	-0.02472	0.95	0.010347

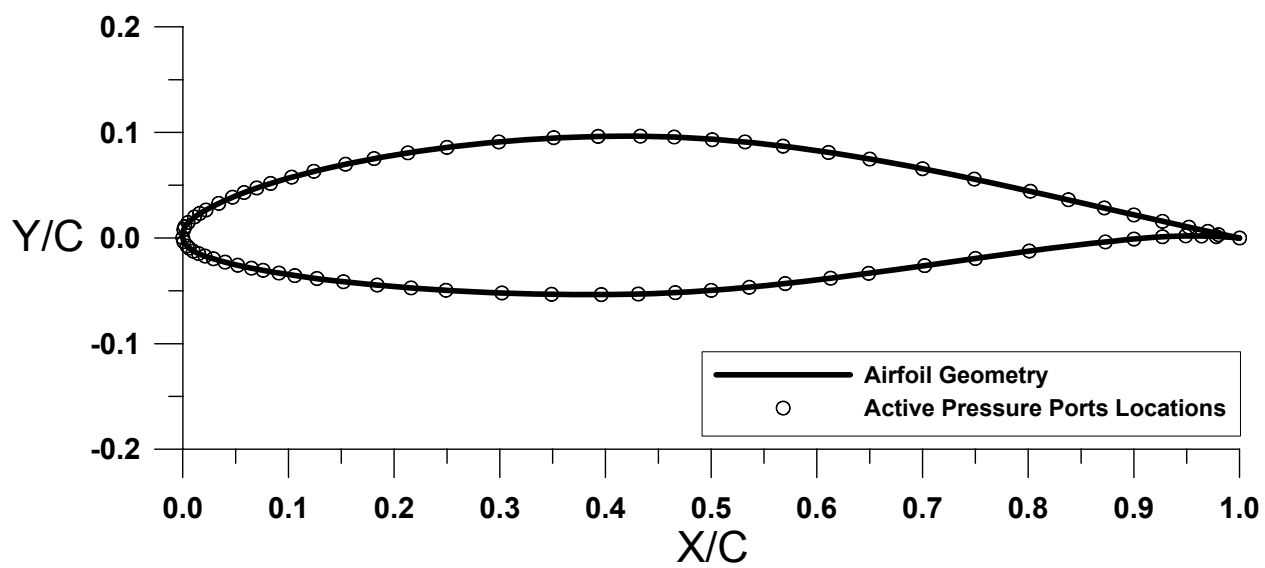


Figure C2.—NACA 65₂-415 Airfoil.

TABLE C2.1.—COORDINATES OF NACA 65₂-415 AIRFOIL

Lower Surface						Upper Surface					
x/c	y/c	x/c	y/c	x/c	y/c	x/c	y/c	x/c	y/c	x/c	y/c
1	0.0000	0.8358	-0.0078	0.6080	-0.0387	0.0000	0.0003	0.0416	0.0363	0.1891	0.0767
0.9942	0.0004	0.8311	-0.0084	0.6030	-0.0393	-0.0002	0.0013	0.0443	0.0375	0.1931	0.0774
0.9898	0.0007	0.8264	-0.0090	0.5981	-0.0399	-0.0002	0.0023	0.0470	0.0386	0.1971	0.0781
0.9856	0.0009	0.8215	-0.0096	0.5939	-0.0404	-0.0002	0.0033	0.0497	0.0398	0.2011	0.0787
0.9816	0.0011	0.8164	-0.0103	0.5902	-0.0408	-0.0001	0.0043	0.0525	0.0409	0.2052	0.0794
0.9779	0.0013	0.8112	-0.0110	0.5849	-0.0414	0.0001	0.0053	0.0554	0.0420	0.2093	0.0800
0.9742	0.0015	0.8061	-0.0117	0.5830	-0.0417	0.0003	0.0062	0.0582	0.0431	0.2133	0.0807
0.9708	0.0017	0.8011	-0.0123	0.5817	-0.0418	0.0006	0.0072	0.0612	0.0442	0.2174	0.0813
0.9674	0.0018	0.7960	-0.0130	0.5805	-0.0420	0.0010	0.0081	0.0642	0.0453	0.2216	0.0819
0.9641	0.0019	0.7906	-0.0137	0.5786	-0.0422	0.0014	0.0090	0.0672	0.0464	0.2257	0.0825
0.9612	0.0020	0.7851	-0.0145	0.5739	-0.0427	0.0018	0.0099	0.0704	0.0474	0.2298	0.0831
0.9582	0.0020	0.7798	-0.0152	0.5701	-0.0431	0.0023	0.0108	0.0735	0.0485	0.2339	0.0837
0.9551	0.0021	0.7741	-0.0160	0.5661	-0.0436	0.0028	0.0117	0.0768	0.0496	0.2381	0.0843
0.9520	0.0021	0.7685	-0.0168	0.5617	-0.0440	0.0034	0.0125	0.0800	0.0506	0.2422	0.0848
0.9490	0.0021	0.7618	-0.0177	0.5574	-0.0445	0.0040	0.0133	0.0833	0.0517	0.2464	0.0853
0.9460	0.0020	0.7555	-0.0186	0.5533	-0.0449	0.0047	0.0140	0.0866	0.0527	0.2504	0.0858
0.9432	0.0019	0.7498	-0.0194	0.5492	-0.0453	0.0054	0.0147	0.0899	0.0537	0.2544	0.0863
0.9404	0.0019	0.7438	-0.0202	0.5447	-0.0458	0.0061	0.0155	0.0933	0.0547	0.2585	0.0868
0.9372	0.0017	0.7377	-0.0211	0.5401	-0.0462	0.0068	0.0161	0.0967	0.0557	0.2626	0.0873
0.9340	0.0016	0.7317	-0.0219	0.5355	-0.0467	0.0075	0.0168	0.1000	0.0567	0.2667	0.0878
0.9307	0.0014	0.7257	-0.0227	0.5310	-0.0471	0.0083	0.0175	0.1034	0.0577	0.2708	0.0882
0.9274	0.0012	0.7196	-0.0236	0.5266	-0.0475	0.0091	0.0181	0.1069	0.0586	0.2749	0.0887
0.9239	0.0010	0.7136	-0.0244	0.5221	-0.0479	0.0098	0.0187	0.1103	0.0596	0.2790	0.0891
0.9204	0.0007	0.7076	-0.0253	0.5177	-0.0482	0.0106	0.0194	0.1138	0.0605	0.2832	0.0895
0.9167	0.0005	0.7016	-0.0261	0.5133	-0.0486	0.0114	0.0200	0.1173	0.0614	0.2873	0.0899
0.9129	0.0002	0.6955	-0.0270	0.5090	-0.0489	0.0122	0.0205	0.1209	0.0623	0.2913	0.0903
0.9090	-0.0002	0.6895	-0.0278	0.5046	-0.0493	0.0131	0.0211	0.1244	0.0632	0.2951	0.0907
0.9047	-0.0006	0.6841	-0.0286	0.5004	-0.0496	0.0139	0.0217	0.1280	0.0641	0.2992	0.0910
0.9003	-0.0010	0.6796	-0.0292	0.4960	-0.0499	0.0147	0.0222	0.1316	0.0649	0.3034	0.0914
0.8956	-0.0014	0.6742	-0.0300	0.4917	-0.0502	0.0155	0.0228	0.1353	0.0658	0.3077	0.0918
0.8914	-0.0018	0.6695	-0.0306	0.4874	-0.0505	0.0164	0.0233	0.1389	0.0666	0.3119	0.0921
0.8865	-0.0023	0.6651	-0.0312	0.4830	-0.0507	0.0172	0.0239	0.1426	0.0674	0.3162	0.0924
0.8818	-0.0027	0.6614	-0.0317	0.4786	-0.0510	0.0181	0.0244	0.1463	0.0683	0.3205	0.0928
0.8773	-0.0032	0.6574	-0.0323	0.4743	-0.0512	0.0190	0.0249	0.1500	0.0691	0.3248	0.0931
0.8726	-0.0037	0.6529	-0.0329	0.4699	-0.0515	0.0202	0.0256	0.1539	0.0699	0.3291	0.0934
0.8679	-0.0042	0.6490	-0.0334	0.4655	-0.0517	0.0219	0.0266	0.1577	0.0707	0.3333	0.0936
0.8632	-0.0047	0.6438	-0.0341	0.4612	-0.0519	0.0243	0.0279	0.1615	0.0715	0.3376	0.0939
0.8586	-0.0052	0.6390	-0.0347	0.4568	-0.0521	0.0266	0.0291	0.1654	0.0723	0.3419	0.0942
0.8540	-0.0057	0.6341	-0.0354	0.4524	-0.0523	0.0290	0.0304	0.1693	0.0730	0.3462	0.0944
0.8495	-0.0062	0.6289	-0.0361	0.4481	-0.0525	0.0315	0.0316	0.1732	0.0738	0.3505	0.0947
0.8462	-0.0066	0.6237	-0.0367	0.4438	-0.0526	0.0340	0.0328	0.1772	0.0745	0.3548	0.0949
0.8425	-0.0070	0.6183	-0.0374	0.4395	-0.0528	0.0365	0.0340	0.1811	0.0753	0.3590	0.0951
0.8398	-0.0074	0.6132	-0.0380	0.4351	-0.0529	0.0390	0.0352	0.1851	0.0760	0.3633	0.0953

TABLE C2.1.—(CONTINUED) COORDINATES OF NACA 65₂-415 AIRFOIL

Lower Surface						Upper Surface					
x/c	y/c	x/c	y/c	x/c	y/c	x/c	y/c	x/c	y/c	x/c	y/c
0.4307	-0.0530	0.2296	-0.0483	0.0520	-0.0258	0.3676	0.0955	0.5400	0.0902	0.7255	0.0606
0.4263	-0.0531	0.2249	-0.0479	0.0489	-0.0250	0.3718	0.0956	0.5440	0.0898	0.7295	0.0598
0.4219	-0.0532	0.2202	-0.0476	0.0458	-0.0243	0.3761	0.0958	0.5481	0.0894	0.7335	0.0590
0.4175	-0.0533	0.2155	-0.0473	0.0428	-0.0236	0.3803	0.0959	0.5522	0.0889	0.7389	0.0579
0.4132	-0.0534	0.2109	-0.0469	0.0399	-0.0228	0.3845	0.0961	0.5564	0.0884	0.7427	0.0571
0.4087	-0.0535	0.2062	-0.0465	0.0370	-0.0220	0.3886	0.0962	0.5603	0.0880	0.7452	0.0566
0.4043	-0.0535	0.2017	-0.0462	0.0341	-0.0213	0.3928	0.0963	0.5646	0.0874	0.7489	0.0558
0.4001	-0.0536	0.1971	-0.0458	0.0313	-0.0205	0.3969	0.0964	0.5681	0.0870	0.7536	0.0548
0.3957	-0.0536	0.1926	-0.0454	0.0286	-0.0196	0.4009	0.0964	0.5723	0.0865	0.7583	0.0538
0.3912	-0.0536	0.1880	-0.0450	0.0259	-0.0188	0.4050	0.0965	0.5766	0.0859	0.7630	0.0528
0.3866	-0.0536	0.1835	-0.0446	0.0234	-0.0180	0.4090	0.0965	0.5810	0.0854	0.7678	0.0518
0.3820	-0.0536	0.1789	-0.0441	0.0208	-0.0171	0.4130	0.0965	0.5854	0.0848	0.7721	0.0509
0.3774	-0.0536	0.1744	-0.0437	0.0189	-0.0164	0.4170	0.0966	0.5898	0.0842	0.7770	0.0498
0.3727	-0.0536	0.1699	-0.0433	0.0176	-0.0159	0.4210	0.0966	0.5943	0.0835	0.7820	0.0487
0.3680	-0.0536	0.1654	-0.0428	0.0167	-0.0155	0.4251	0.0965	0.5987	0.0829	0.7870	0.0476
0.3633	-0.0535	0.1609	-0.0423	0.0158	-0.0151	0.4291	0.0965	0.6029	0.0823	0.7920	0.0465
0.3585	-0.0535	0.1564	-0.0419	0.0149	-0.0147	0.4331	0.0965	0.6071	0.0817	0.7970	0.0454
0.3537	-0.0534	0.1520	-0.0414	0.0139	-0.0143	0.4371	0.0964	0.6114	0.0810	0.8021	0.0443
0.3489	-0.0533	0.1477	-0.0409	0.0130	-0.0139	0.4411	0.0964	0.6158	0.0804	0.8071	0.0432
0.3441	-0.0532	0.1433	-0.0404	0.0121	-0.0134	0.4451	0.0963	0.6201	0.0797	0.8121	0.0420
0.3395	-0.0531	0.1390	-0.0399	0.0113	-0.0130	0.4491	0.0962	0.6243	0.0790	0.8171	0.0409
0.3348	-0.0530	0.1348	-0.0394	0.0104	-0.0125	0.4531	0.0961	0.6287	0.0783	0.8221	0.0398
0.3301	-0.0529	0.1306	-0.0389	0.0095	-0.0120	0.4570	0.0960	0.6329	0.0777	0.8272	0.0387
0.3253	-0.0528	0.1265	-0.0383	0.0087	-0.0114	0.4609	0.0958	0.6369	0.0770	0.8322	0.0375
0.3206	-0.0527	0.1224	-0.0378	0.0079	-0.0109	0.4649	0.0957	0.6412	0.0763	0.8377	0.0363
0.3158	-0.0525	0.1183	-0.0373	0.0071	-0.0102	0.4689	0.0955	0.6457	0.0755	0.8434	0.0350
0.3110	-0.0524	0.1143	-0.0367	0.0063	-0.0096	0.4729	0.0953	0.6500	0.0748	0.8486	0.0338
0.3063	-0.0522	0.1103	-0.0362	0.0056	-0.0090	0.4769	0.0951	0.6544	0.0740	0.8547	0.0324
0.3015	-0.0520	0.1064	-0.0356	0.0048	-0.0083	0.4809	0.0949	0.6590	0.0732	0.8600	0.0312
0.2968	-0.0519	0.1025	-0.0350	0.0041	-0.0075	0.4849	0.0947	0.6635	0.0724	0.8655	0.0299
0.2920	-0.0517	0.0987	-0.0344	0.0035	-0.0068	0.4888	0.0945	0.6680	0.0716	0.8715	0.0285
0.2872	-0.0515	0.0949	-0.0338	0.0028	-0.0060	0.4928	0.0942	0.6726	0.0708	0.8787	0.0268
0.2824	-0.0512	0.0911	-0.0332	0.0023	-0.0052	0.4967	0.0940	0.6772	0.0700	0.8845	0.0255
0.2775	-0.0510	0.0873	-0.0326	0.0017	-0.0044	0.5006	0.0937	0.6818	0.0691	0.8899	0.0243
0.2727	-0.0508	0.0835	-0.0319	0.0012	-0.0035	0.5045	0.0934	0.6865	0.0682	0.8952	0.0230
0.2678	-0.0505	0.0797	-0.0312	0.0008	-0.0026	0.5084	0.0931	0.6909	0.0674	0.9003	0.0219
0.2630	-0.0503	0.0759	-0.0306	0.0004	-0.0017	0.5122	0.0928	0.6955	0.0665	0.9055	0.0207
0.2582	-0.0500	0.0722	-0.0299	0.0002	-0.0007	0.5161	0.0925	0.7002	0.0656	0.9108	0.0195
0.2534	-0.0498	0.0686	-0.0292	0.0000	0.0003	0.5201	0.0921	0.7048	0.0647	0.9164	0.0182
0.2486	-0.0495	0.0651	-0.0285			0.5240	0.0918	0.7089	0.0639	0.9218	0.0170
0.2439	-0.0492	0.0618	-0.0279			0.5280	0.0914	0.7132	0.0631	0.9270	0.0158
0.2391	-0.0489	0.0584	-0.0272			0.5320	0.0910	0.7172	0.0623	0.9321	0.0146
0.2344	-0.0486	0.0552	-0.0265			0.5361	0.0906	0.7217	0.0614	0.9370	0.0135

TABLE C2.1.—(CONTINUED) COORDINATES OF NACA 65₂-415 AIRFOIL

Lower Surface						Upper Surface					
x/c	y/c	x/c	y/c	x/c	y/c	x/c	y/c	x/c	y/c	x/c	y/c
						0.9421	0.0124				
						0.9472	0.0113				
						0.9519	0.0103				
						0.9562	0.0093				
						0.9607	0.0083				
						0.9654	0.0073				
						0.9701	0.0063				
						0.9745	0.0054				
						0.9796	0.0043				
						0.9850	0.0032				
						0.9911	0.0019				
						0.9964	0.0007				
						1	0.0000				

TABLE C2.2.—COORDINATES OF ACTIVE PRESSURE PORTS OF NACA 65₂-415 AIRFOIL

Lower Surface		Upper Surface	
x/c	y/c	x/c	y/c
1	0	1.00E-03	0.008118
0.978	0.001346	2.00E-03	0.010808
0.964	0.001907	5.00E-03	0.014744
0.949	0.002054	1.10E-02	0.019957
0.927	0.001213	1.60E-02	0.023324
0.9	-0.00097	2.20E-02	0.026553
0.873	-0.00369	3.40E-02	0.032812
0.801	-0.01231	4.70E-02	0.038637
0.75	-0.01937	5.80E-02	0.04309
0.702	-0.02614	7.00E-02	0.047436
0.649	-0.03342	8.30E-02	0.051689
0.613	-0.03804	0.103	0.057663
0.57	-0.04313	0.124	0.06318
0.536	-0.04667	0.154	0.069898
0.5	-0.04959	0.181	0.075261
0.466	-0.0517	0.213	0.080682
0.431	-0.05302	0.25	0.085845
0.396	-0.05359	0.299	0.091031
0.349	-0.05331	0.351	0.095086
0.302	-0.05204	0.393	0.096268
0.249	-0.04948	0.433	0.096479
0.216	-0.04725	0.465	0.095669
0.184	-0.04457	0.501	0.093115
0.152	-0.04139	0.532	0.091032
0.127	-0.03834	0.568	0.087005
0.106	-0.03558	0.611	0.08103
9.10E-02	-0.0332	0.65	0.074801
7.60E-02	-0.03057	0.7	0.065612
6.50E-02	-0.02854	0.749	0.055821
5.20E-02	-0.02576	0.802	0.044293
4.00E-02	-0.02282	0.838	0.036263
2.90E-02	-0.01963	0.872	0.028497
2.10E-02	-0.01708	0.9	0.021854
1.50E-02	-0.01473	0.927	0.015786
1.00E-02	-0.01249	0.952	0.010256
6.00E-03	-0.00961	0.97	0.006321
4.00E-03	-0.00754	0.98	0.003166
1.00E-03	-0.00349		
0.00E+00	0.000281		

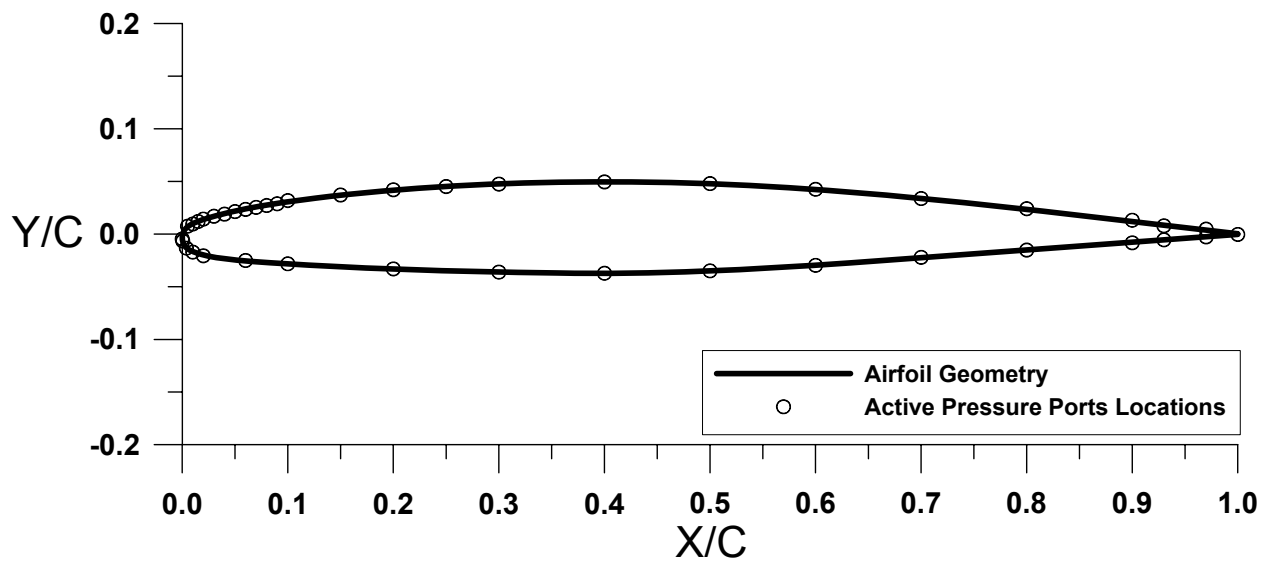


Figure C3.—GLC 305 Airfoil.

TABLE C3.1.—COORDINATES OF GLC 305 AIRFOIL

Lower Surface						Upper Surface					
x/c	y/c	x/c	y/c	x/c	y/c	x/c	y/c	x/c	y/c	x/c	y/c
1	-0.0003	0.4008	-0.0372	0.0030	-0.0119	0.0000	-0.0026	0.3178	0.0484	0.8092	0.0224
0.9832	-0.0016	0.3893	-0.0372	0.0019	-0.0103	0.0003	-0.0007	0.3288	0.0487	0.8206	0.0211
0.9676	-0.0027	0.3778	-0.0371	0.0010	-0.0085	0.0009	0.0012	0.3398	0.0490	0.8345	0.0195
0.9491	-0.0041	0.3662	-0.0370	0.0003	-0.0066	0.0018	0.0030	0.3506	0.0493	0.8488	0.0178
0.9304	-0.0054	0.3542	-0.0369	0.0000	-0.0046	0.0029	0.0047	0.3614	0.0494	0.8627	0.0162
0.9106	-0.0069	0.3421	-0.0367			0.0042	0.0062	0.3726	0.0495	0.8749	0.0148
0.8918	-0.0083	0.3299	-0.0365			0.0057	0.0075	0.3841	0.0496	0.8892	0.0132
0.8726	-0.0097	0.3177	-0.0363			0.0074	0.0086	0.3955	0.0496	0.9061	0.0112
0.8535	-0.0111	0.3052	-0.0361			0.0092	0.0096	0.4069	0.0495	0.9209	0.0095
0.8370	-0.0123	0.2930	-0.0358			0.0110	0.0104	0.4187	0.0495	0.9351	0.0078
0.8242	-0.0133	0.2809	-0.0356			0.0128	0.0112	0.4303	0.0494	0.9495	0.0062
0.8114	-0.0142	0.2689	-0.0353			0.0147	0.0120	0.4414	0.0493	0.9621	0.0047
0.7985	-0.0152	0.2565	-0.0350			0.0165	0.0127	0.4524	0.0491	0.9801	0.0026
0.7857	-0.0161	0.2437	-0.0347			0.0184	0.0134	0.4637	0.0489	1	0.0003
0.7664	-0.0175	0.2314	-0.0343			0.0211	0.0142	0.4753	0.0486		
0.7492	-0.0188	0.2197	-0.0339			0.0248	0.0154	0.4868	0.0483		
0.7325	-0.0201	0.2079	-0.0335			0.0301	0.0170	0.4979	0.0480		
0.7200	-0.0210	0.1958	-0.0331			0.0375	0.0189	0.5090	0.0476		
0.7048	-0.0221	0.1841	-0.0326			0.0480	0.0214	0.5202	0.0471		
0.6889	-0.0233	0.1728	-0.0321			0.0580	0.0235	0.5314	0.0465		
0.6729	-0.0244	0.1610	-0.0315			0.0678	0.0254	0.5428	0.0459		
0.6576	-0.0255	0.1476	-0.0308			0.0776	0.0271	0.5535	0.0453		
0.6448	-0.0265	0.1338	-0.0301			0.0876	0.0288	0.5642	0.0447		
0.6329	-0.0273	0.1214	-0.0295			0.0980	0.0304	0.5748	0.0441		
0.6214	-0.0281	0.1094	-0.0289			0.1085	0.0319	0.5859	0.0433		
0.6096	-0.0289	0.0977	-0.0282			0.1191	0.0333	0.5968	0.0426		
0.5976	-0.0297	0.0865	-0.0275			0.1298	0.0346	0.6083	0.0417		
0.5854	-0.0304	0.0758	-0.0268			0.1405	0.0359	0.6200	0.0408		
0.5733	-0.0312	0.0655	-0.0260			0.1512	0.0371	0.6319	0.0399		
0.5611	-0.0319	0.0553	-0.0251			0.1620	0.0382	0.6441	0.0389		
0.5492	-0.0326	0.0457	-0.0241			0.1726	0.0393	0.6563	0.0378		
0.5375	-0.0332	0.0366	-0.0229			0.1828	0.0402	0.6681	0.0368		
0.5256	-0.0338	0.0290	-0.0217			0.1938	0.0412	0.6795	0.0358		
0.5136	-0.0344	0.0236	-0.0206			0.2051	0.0421	0.6910	0.0348		
0.5019	-0.0349	0.0198	-0.0197			0.2164	0.0430	0.7022	0.0338		
0.4906	-0.0354	0.0171	-0.0190			0.2274	0.0438	0.7139	0.0326		
0.4793	-0.0358	0.0152	-0.0184			0.2383	0.0445	0.7261	0.0314		
0.4680	-0.0362	0.0133	-0.0178			0.2492	0.0452	0.7381	0.0302		
0.4568	-0.0365	0.0114	-0.0171			0.2605	0.0458	0.7494	0.0291		
0.4456	-0.0368	0.0095	-0.0164			0.2721	0.0464	0.7601	0.0279		
0.4345	-0.0369	0.0077	-0.0156			0.2838	0.0470	0.7710	0.0267		
0.4234	-0.0371	0.0060	-0.0146			0.2952	0.0475	0.7823	0.0255		
0.4122	-0.0372	0.0044	-0.0134			0.3064	0.0480	0.7942	0.0241		

TABLE C3.2.—COORDINATES OF ACTIVE PRESSURE PORTS OF GLC-305 AIRFOIL

Lower Surface		Upper Surface	
x/c	y/c	x/c	y/c
1	-0.00033	5.00E-03	0.00752
0.97	-0.00271	1.00E-02	0.00959
0.93	-0.00544	1.50E-02	0.011984
0.9	-0.00829	2.00E-02	0.014231
0.8	-0.01517	3.00E-02	0.016962
0.7	-0.02209	4.00E-02	0.018941
0.6	-0.02968	5.00E-02	0.021401
0.5	-0.03493	6.00E-02	0.023476
0.4	-0.03718	7.00E-02	0.025391
0.3	-0.03608	8.00E-02	0.027147
0.2	-0.03306	9.00E-02	0.028798
0.1	-0.0282		
6.00E-02	-0.02508		
2.00E-02	-0.02061		
1.00E-02	-0.01709		
4.00E-03	-0.01336		
5.00E-04	-0.00662		
0.00E+00	-0.00464		

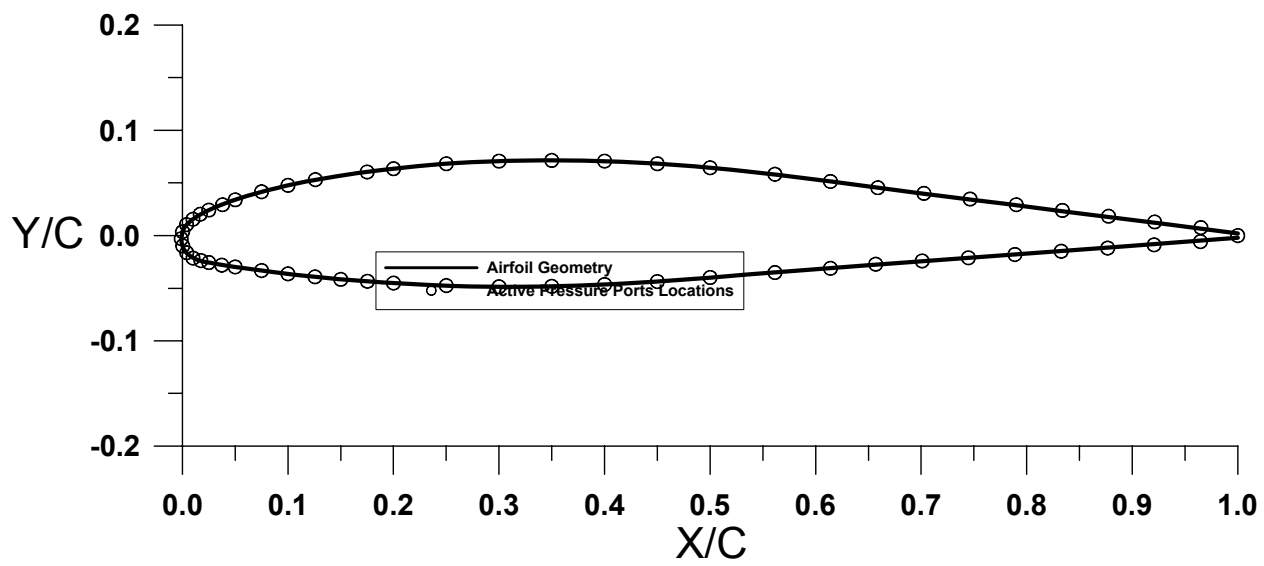


Figure C4.—Twin Otter tail.

TABLE C4.1.—COORDINATES OF TWIN OTTER

Lower Surface						Upper Surface					
x/c	y/c	x/c	y/c	x/c	y/c	x/c	y/c	x/c	y/c	x/c	y/c
-0.001	-0.0017	0.2213	-0.0463	0.8052	-0.0167	1	0.0022	0.3121	0.071	0.0286	0.0258
-0.0008	-0.005	0.2294	-0.0467	0.8251	-0.0152	1	-0.0022	0.3024	0.0708	0.025	0.0242
-0.0002	-0.0085	0.2376	-0.0471	0.8455	-0.0137	0.9767	0.0051	0.293	0.0705	0.0216	0.0225
0.0011	-0.012	0.246	-0.0474	0.8662	-0.0121	0.9538	0.008	0.2837	0.0701	0.0183	0.0208
0.0029	-0.0151	0.2545	-0.0477	0.8874	-0.0106	0.9314	0.0109	0.2746	0.0697	0.0151	0.019
0.0052	-0.0177	0.2633	-0.048	0.909	-0.009	0.9095	0.0137	0.2657	0.0693	0.0121	0.017
0.0081	-0.02	0.2722	-0.0482	0.9311	-0.0073	0.888	0.0164	0.257	0.0687	0.0092	0.015
0.0113	-0.0219	0.2813	-0.0484	0.9536	-0.0056	0.8669	0.0191	0.2484	0.0681	0.0065	0.0128
0.015	-0.0233	0.2905	-0.0485	0.9766	-0.0039	0.8463	0.0217	0.2401	0.0675	0.004	0.0105
0.0187	-0.0244	0.3	-0.0486			0.826	0.0242	0.2319	0.0668	0.0019	0.0076
0.0225	-0.0252	0.3097	-0.0486			0.8062	0.0268	0.2239	0.066	0.0005	0.0045
0.0264	-0.0259	0.3195	-0.0486			0.7867	0.0292	0.216	0.0652	-0.0005	0.0015
0.0304	-0.0266	0.3296	-0.0486			0.7677	0.0316	0.2083	0.0644		
0.0345	-0.0273	0.3398	-0.0484			0.749	0.034	0.2008	0.0636		
0.0386	-0.028	0.3503	-0.0482			0.7307	0.0363	0.1934	0.0627		
0.0429	-0.0287	0.361	-0.048			0.7128	0.0386	0.1862	0.0619		
0.0472	-0.0294	0.3719	-0.0476			0.6952	0.0408	0.1791	0.061		
0.0516	-0.0301	0.383	-0.0472			0.678	0.043	0.1722	0.0601		
0.0562	-0.0307	0.3944	-0.0467			0.6611	0.0452	0.1654	0.0592		
0.0608	-0.0313	0.406	-0.0462			0.6446	0.0475	0.1587	0.0583		
0.0655	-0.032	0.4178	-0.0456			0.6284	0.0497	0.1522	0.0573		
0.0703	-0.0326	0.4298	-0.045			0.6126	0.0517	0.1458	0.0564		
0.0753	-0.0332	0.4421	-0.0442			0.597	0.0537	0.1396	0.0554		
0.0803	-0.0338	0.4546	-0.0434			0.5817	0.0556	0.1335	0.0543		
0.0854	-0.0345	0.4674	-0.0424			0.5668	0.0574	0.1275	0.0533		
0.0906	-0.0351	0.4805	-0.0414			0.5521	0.0591	0.1216	0.0522		
0.096	-0.0358	0.4938	-0.0403			0.5377	0.0606	0.1159	0.0511		
0.1014	-0.0365	0.5073	-0.0392			0.5236	0.0621	0.1103	0.0499		
0.107	-0.0372	0.5212	-0.0382			0.5098	0.0635	0.1048	0.0488		
0.1127	-0.0378	0.5353	-0.0371			0.4962	0.0647	0.0995	0.0476		
0.1185	-0.0385	0.5498	-0.036			0.4829	0.0659	0.0942	0.0464		
0.1244	-0.0391	0.5645	-0.0348			0.4699	0.0669	0.0891	0.0452		
0.1304	-0.0397	0.5795	-0.0336			0.4571	0.0678	0.0841	0.044		
0.1366	-0.0404	0.5948	-0.0324			0.4445	0.0686	0.0792	0.0427		
0.1429	-0.041	0.6105	-0.031			0.4323	0.0693	0.0744	0.0414		
0.1493	-0.0415	0.6264	-0.0297			0.4202	0.0699	0.0697	0.0401		
0.1558	-0.0421	0.6427	-0.0285			0.4084	0.0704	0.0651	0.0388		
0.1625	-0.0426	0.6594	-0.0275			0.3968	0.0708	0.0607	0.0375		
0.1694	-0.0431	0.6763	-0.0262			0.3855	0.0711	0.0563	0.0361		
0.1764	-0.0435	0.6936	-0.025			0.3743	0.0713	0.052	0.0347		
0.1835	-0.044	0.7113	-0.0236			0.3634	0.0714	0.0479	0.0333		
0.1907	-0.0445	0.7293	-0.0223			0.3527	0.0714	0.0438	0.0319		
0.1982	-0.045	0.7477	-0.0209			0.3423	0.0714	0.0398	0.0304		
0.2057	-0.0454	0.7665	-0.0195			0.332	0.0713	0.036	0.0289		
0.2134	-0.0459	0.7856	-0.0181			0.3219	0.0712	0.0322	0.0274		

TABLE C4.2.—COORDINATES OF ACTIVE PRESSURE PORTS OF TWIN OTTER AIRFOIL

Lower Surface		Upper Surface	
x/c	y/c	x/c	y/c
1	0	0.0001	0.0037
0.9646	-0.0057	0.0039	0.0104
0.9207	-0.0088	0.01	0.0155
0.8767	-0.0119	0.0169	0.0203
0.8327	-0.0149	0.025	0.0242
0.7888	-0.018	0.038	0.0293
0.7448	-0.0211	0.05	0.034
0.7009	-0.0241	0.075	0.0416
0.6569	-0.0272	0.1	0.0477
0.614	-0.0311	0.126	0.0531
0.5614	-0.0351	0.175	0.0604
0.5	-0.0398	0.2	0.0635
0.45	-0.0437	0.25	0.0682
0.4	-0.0465	0.3	0.0707
0.35	-0.0482	0.35	0.0714
0.3	-0.0486	0.4	0.0707
0.25	-0.0475	0.45	0.0682
0.2	-0.0451	0.5	0.0644
0.1753	-0.0434	0.5614	0.0582
0.15	-0.0416	0.614	0.0514
0.1256	-0.0392	0.6589	0.0455
0.1	-0.0363	0.7026	0.0401
0.075	-0.0332	0.7463	0.0347
0.05	-0.0298	0.7901	0.0293
0.0373	-0.0281	0.8338	0.0239
0.025	-0.0256	0.8775	0.0184
0.0175	-0.0238	0.9212	0.013
0.01	-0.0214	0.965	0.0076
0.0041	-0.0163		
0.0003	-0.0098		
-0.0011	-0.003		

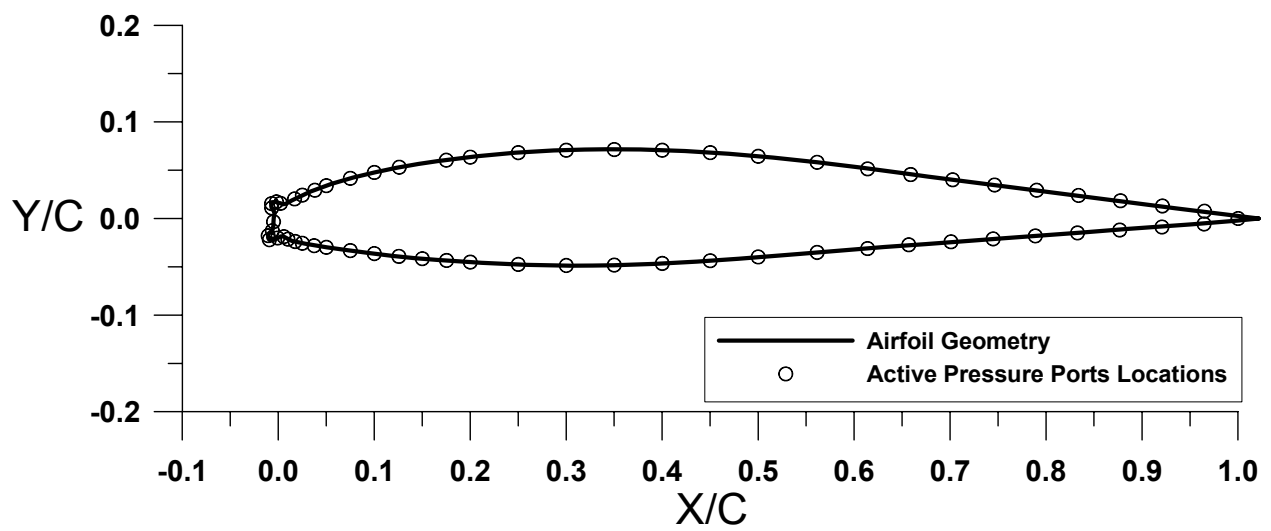


Figure C5.—Twin Otter with 22.5-min ice shape.

TABLE C5.1.—COORDINATES OF TWIN OTTER WITH 22.5-MIN ICE SHAPE

Lower Surface						Upper Surface					
x/c	y/c	x/c	y/c	x/c	y/c	x/c	y/c	x/c	y/c	x/c	y/c
-0.0113	-0.0016	0.5899	-0.0311			1	0	0.0024	0.0156		
-0.0114	-0.0041	0.6127	-0.0292			0.9775	0.0025	0.0002	0.0149		
-0.0113	-0.0064	0.6354	-0.0276			0.9549	0.0054	-0.0020	0.0146		
-0.0125	-0.0124	0.6582	-0.0261			0.9322	0.0083	-0.0041	0.0155		
-0.0145	-0.0137	0.6810	-0.0244			0.9096	0.0111	-0.0063	0.0160		
-0.0161	-0.0154	0.7038	-0.0227			0.8869	0.0140	-0.0083	0.0170		
-0.0168	-0.0175	0.7265	-0.0210			0.8643	0.0169	-0.0116	0.0166		
-0.0168	-0.0198	0.7493	-0.0193			0.8416	0.0197	-0.0133	0.0152		
-0.0156	-0.0216	0.7721	-0.0176			0.8189	0.0226	-0.0136	0.0130		
-0.0134	-0.0222	0.7949	-0.0159			0.7963	0.0255	-0.0132	0.0108		
-0.0112	-0.0218	0.8176	-0.0142			0.7736	0.0284	-0.0114	0.0080		
-0.0092	-0.0207	0.8404	-0.0126			0.7510	0.0312	-0.0100	0.0062		
-0.0071	-0.0199	0.8632	-0.0109			0.7283	0.0341	-0.0106	0.0032		
-0.0050	-0.0190	0.8860	-0.0092			0.7057	0.0370	-0.0111	0.0008		
-0.0029	-0.0181	0.9087	-0.0075			0.6830	0.0398				
-0.0007	-0.0185	0.9315	-0.0058			0.6604	0.0427				
0.0013	-0.0196	0.9543	-0.0041			0.6377	0.0457				
0.0032	-0.0208	0.9771	-0.0024			0.6151	0.0488				
0.0052	-0.0219	1	0			0.5924	0.0518				
0.0076	-0.0228					0.5698	0.0546				
0.0207	-0.0257					0.5471	0.0573				
0.0433	-0.0295					0.5244	0.0598				
0.0659	-0.0325					0.5017	0.0621				
0.0886	-0.0354					0.4789	0.0642				
0.1112	-0.0380					0.4562	0.0660				
0.1340	-0.0403					0.4334	0.0676				
0.1567	-0.0422					0.4106	0.0689				
0.1795	-0.0438					0.3878	0.0698				
0.2023	-0.0452					0.3650	0.0703				
0.2251	-0.0463					0.3421	0.0704				
0.2479	-0.0472					0.3193	0.0703				
0.2708	-0.0477					0.2964	0.0699				
0.2936	-0.0480					0.2736	0.0692				
0.3164	-0.0479					0.2508	0.0680				
0.3393	-0.0476					0.2280	0.0664				
0.3621	-0.0469					0.2053	0.0642				
0.3849	-0.0460					0.1826	0.0617				
0.4077	-0.0449					0.1599	0.0589				
0.4305	-0.0436					0.1373	0.0556				
0.4533	-0.0420					0.1148	0.0517				
0.4761	-0.0402					0.0925	0.0471				
0.4988	-0.0384					0.0703	0.0417				
0.5216	-0.0366					0.0483	0.0353				
0.5444	-0.0349					0.0269	0.0276				
0.5671	-0.0330					0.0075	0.0184				

TABLE C5.2.—COORDINATES OF ACTIVE PRESSURE PORTS OF TWIN OTTER WITH 22.5-MIN ICE SHAPE

Lower Surface		Upper Surface	
x/c	y/c	x/c	y/c
1	0	0.0169	0.0203
0.9646	-0.0057	0.025	0.0242
0.9207	-0.0088	0.038	0.0293
0.8767	-0.0119	0.05	0.034
0.8327	-0.0149	0.075	0.0416
0.7888	-0.018	0.1	0.0477
0.7448	-0.0211	0.126	0.0531
0.7009	-0.0241	0.175	0.0604
0.6569	-0.0272	0.2	0.0635
0.614	-0.0311	0.25	0.0682
0.5614	-0.0351	0.3	0.0707
0.5	-0.0398	0.35	0.0714
0.45	-0.0437	0.4	0.0707
0.4	-0.0465	0.45	0.0682
0.35	-0.0482	0.5	0.0644
0.3	-0.0486	0.5614	0.0582
0.25	-0.0475	0.614	0.0514
0.2	-0.0451	0.6589	0.0455
0.1753	-0.0434	0.7026	0.0401
0.15	-0.0416	0.7463	0.0347
0.1256	-0.0392	0.7901	0.0293
0.1	-0.0363	0.8338	0.0239
0.075	-0.0332	0.8775	0.0184
0.05	-0.0298	0.9212	0.013
0.0373	-0.0281	0.965	0.0076
0.025	-0.0256	-0.00693	0.01095
0.0175	-0.0238	-0.00703	0.01545
0.01	-0.0214	-0.00195	0.0173
0.005737	-0.018758	0.002306	0.0157
-0.00073	-0.020161		
-0.00936	-0.021963		
-0.01059	-0.017767		
-0.00628	-0.012605		
-0.00506	-0.003343		

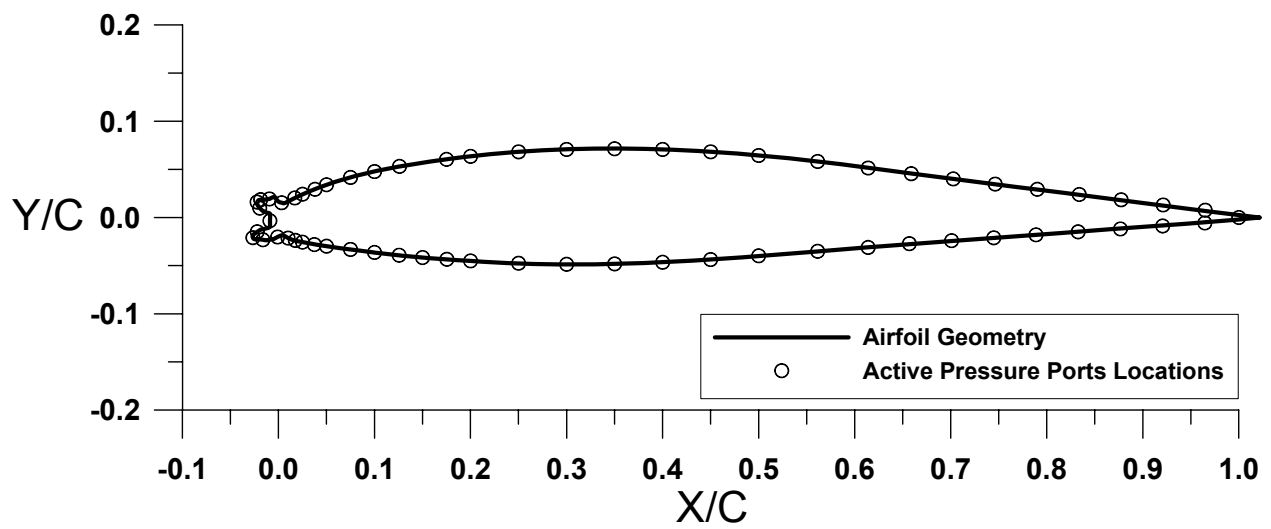


Figure C6.—Twin Otter with 45-min ice shape.

TABLE C6.1.—COORDINATES OF TWIN OTTER WITH 45-MIN ICE SHAPE

Lower Surface						Upper Surface					
x/c	y/c	x/c	y/c	x/c	y/c	x/c	y/c	x/c	y/c	x/c	y/c
-0.0289	-0.0011	0.3169	-0.0485			1	0	-0.0078	0.0176		
-0.029	-0.0033	0.3397	-0.048			0.9771	0.0025	-0.0124	0.0153		
-0.0288	-0.0067	0.3625	-0.0472			0.9544	0.0054	-0.0146	0.0147		
-0.0289	-0.0096	0.3853	-0.0462			0.9318	0.0083	-0.0168	0.0153		
-0.0308	-0.0109	0.4081	-0.0451			0.9091	0.0112	-0.019	0.0159		
-0.033	-0.0114	0.4309	-0.0436			0.8865	0.0141	-0.0209	0.017		
-0.0352	-0.012	0.4537	-0.0419			0.8638	0.0169	-0.022	0.0189		
-0.0384	-0.0126	0.4765	-0.0401			0.8411	0.0198	-0.0232	0.0208		
-0.0421	-0.0147	0.4992	-0.0383			0.8185	0.0227	-0.0255	0.0212		
-0.0452	-0.0169	0.522	-0.0366			0.7958	0.0255	-0.0275	0.0203		
-0.0465	-0.0187	0.5448	-0.0348			0.7731	0.0284	-0.0295	0.0192		
-0.0466	-0.0209	0.5676	-0.033			0.7505	0.0313	-0.0317	0.0191		
-0.0452	-0.0225	0.5903	-0.031			0.7278	0.0342	-0.0339	0.0185		
-0.0429	-0.0227	0.6131	-0.0292			0.7052	0.037	-0.0362	0.0186		
-0.0407	-0.0224	0.6359	-0.0277			0.6825	0.0399	-0.0386	0.0185		
-0.0384	-0.0228	0.6587	-0.0261			0.6599	0.0428	-0.041	0.0178		
-0.0362	-0.0231	0.6814	-0.0244			0.6372	0.0457	-0.0423	0.016		
-0.034	-0.0233	0.7042	-0.0227			0.6146	0.0488	-0.0422	0.0138		
-0.0317	-0.0235	0.727	-0.021			0.5919	0.0518	-0.0412	0.0117		
-0.0295	-0.0232	0.7498	-0.0193			0.5693	0.0547	-0.0395	0.0097		
-0.0273	-0.0227	0.7725	-0.0176			0.5466	0.0574	-0.0365	0.0069		
-0.025	-0.0222	0.7953	-0.0159			0.5239	0.06	-0.0344	0.006		
-0.0231	-0.0211	0.8181	-0.0142			0.5012	0.0624	-0.0324	0.005		
-0.021	-0.0202	0.8409	-0.0125			0.4785	0.0645	-0.0301	0.0049		
-0.0189	-0.0194	0.8636	-0.0108			0.4557	0.0664	-0.0285	0.0035		
-0.0168	-0.0184	0.8864	-0.0091			0.4329	0.0681	-0.0286	0.0012		
-0.0146	-0.0186	0.9092	-0.0075			0.4101	0.0694				
-0.0126	-0.0197	0.932	-0.0058			0.3873	0.0705				
-0.0107	-0.0209	0.9548	-0.0041			0.3645	0.0711				
-0.0086	-0.022	0.9775	-0.0024			0.3416	0.0714				
-0.0065	-0.0229	1	0			0.3188	0.0714				
-0.0015	-0.0243					0.296	0.0711				
0.021	-0.0284					0.2731	0.0705				
0.0436	-0.0317					0.2503	0.0695				
0.0662	-0.0346					0.2275	0.0681				
0.0889	-0.0374					0.2048	0.0661				
0.1116	-0.0399					0.1821	0.0637				
0.1343	-0.0419					0.1594	0.061				
0.1571	-0.0436					0.1367	0.058				
0.1799	-0.0451					0.1142	0.0545				
0.2027	-0.0464					0.0917	0.0502				
0.2255	-0.0474					0.0694	0.0453				
0.2483	-0.0481					0.0474	0.0394				
0.2712	-0.0485					0.0256	0.0325				
0.294	-0.0486					0.0044	0.024				

TABLE C6.2.—COORDINATES OF ACTIVE PRESSURE PORTS OF TWIN OTTER AIRFOIL WITH 45-MIN ICE SHAPE

Lower Surface		Upper Surface	
x/c	y/c	x/c	y/c
1	0	0.0169	0.0203
0.9646	-0.0057	0.025	0.0242
0.9207	-0.0088	0.038	0.0293
0.8767	-0.0119	0.05	0.034
0.8327	-0.0149	0.075	0.0416
0.7888	-0.018	0.1	0.0477
0.7448	-0.0211	0.126	0.0531
0.7009	-0.0241	0.175	0.0604
0.6569	-0.0272	0.2	0.0635
0.614	-0.0311	0.25	0.0682
0.5614	-0.0351	0.3	0.0707
0.5	-0.0398	0.35	0.0714
0.45	-0.0437	0.4	0.0707
0.4	-0.0465	0.45	0.0682
0.35	-0.0482	0.5	0.0644
0.3	-0.0486	0.5614	0.0582
0.25	-0.0475	0.614	0.0514
0.2	-0.0451	0.6589	0.0455
0.1753	-0.0434	0.7026	0.0401
0.15	-0.0416	0.7463	0.0347
0.1256	-0.0392	0.7901	0.0293
0.1	-0.0363	0.8338	0.0239
0.075	-0.0332	0.8775	0.0184
0.05	-0.0298	0.9212	0.013
0.0373	-0.0281	0.965	0.0076
0.025	-0.0256	-0.01955	0.00971
0.0175	-0.0238	-0.02237	0.01603
0.01	-0.0214	-0.01858	0.01855
-0.00095	-0.020254	-0.00948	0.01926
-0.01623	-0.023114	0.003243	0.01533
-0.02667	-0.020965		
-0.02214	-0.014762		
-0.00898	-0.003343		

Appendix D—Run Tables

Date: 09/24/2001
 Concentration: 0.0003 grams/cc
 P_{∞} = 13.74 psi
 Geometry: Collector Mechanism

Run I.D.	TAS (mph)	AOA (deg.)	TOTAL TEMP. (°F)	STATIC TEMP. (°F)	R.H. (%)	P_{air} (psi)	P_{water} (psi)	MVD (µm)	Spray Time (sec)	Clock Time (EST)	IRT Air (psi)	Remark
256	176	0	50.76	45.22	68.6	43	67	11	9	19:03	30	
257	175	0	50.48	45.04	73.2	43	67	11	9	19:18	30	Open both vent doors 32", steam on
258	175	0	50.53	45.08	70.0	22	77	21	3.8	19:25	30	Doors stay open, steam on
259	176	0	51.77	46.20	76.1	22	77	21	3	19:35	30	Doors shut, steam on
260	176	0	49.71	44.22	78.0	18	90	40	2.5	19:51	40	Doors open, steam on
261	176	0	48.68	43.17	71.8	18	90	40	1.5	19:57	40	Doors open, steam on
262	175	0	49.05	43.59	73.2	18	90	40	1.8	20:04	40	Doors open, steam on
263	176	0	51.09	45.56	76.2	18	90	40	1.5	20:13	40	Doors open, steam off
264	175	0	49.83	44.35	69.6	8.2	40.2	70	1.5	20:20	40	Doors open, steam on
265	175	0	48.42	42.97	67.5	8.2	40.2	70	2	20:26	40	Doors open, steam on
266	175	0	48.60	43.14	73.7	8.2	40.2	70	2	20:33	40	Doors open, steam on
267	175	0	50.30	44.77	76.1	6	37	79	2	20:42	40	Doors open, steam off
268	175	0	48.16	42.71	74.7	6	37	79	2	20:49	40	Doors open, steam on
269	176	0	49.86	44.36	77.2	5	33	120	2	21:01	40	Doors shut, steam off
270	175	0	49.42	43.96	70.0	5	33	120	2	21:10	40	Doors shut, steam on
271	175	0	49.69	44.23	74.1	5	70	168	1.5	21:23	40	Doors shut, steam on
272	175	0	48.86	43.39	68.9	5	70	168	1.25	21:30	40	Doors shut, steam on
273	175	0	48.57	43.12	74.2	5	70	168	1	21:38	40	Doors open, steam on
274	175	0	50.42	44.91	76.2	5	70	168	0.75	21:59	40	Doors shut, steam on
275	175	0	48.07	42.59	70.9	5	70	168	0.75	22:16	40	Doors shut, steam on
276	176	0	50.46	44.92	76.1	43	67	11	6	22:27	30	Doors shut, steam off
277	175	0	48.50	43.03	70.5	22	77	21	3	22:33	30	Doors shut, steam on

Date: 09/25/2001 Tuesday
 Concentration: 0.0003 grams/cc
 P_o = 14.07 psi
 Geometry: Collector Mechanism

Run I.D.	TAS (mph)	AOA (deg.)	TOTAL TEMP. (°F)	STATIC TEMP. (°F)	R.H. (%)	P _{air} (psi)	P _{water} (psi)	MVD (µm)	Spray Time (sec)	Clock Time (EST)	IRT Air (psi)	Remark
278	175	0	44.85	39.35	71.9	43	67	11	4.5	18:01	30	Doors open, steam on
279	176	0	43.71	38.20	73.8	43	67	11	4.5	18:08	30	Doors open, steam on
280	175	0	44.69	39.25	73.2	22	77	21	2.0	18:14	30	Doors open, steam on
281	175	0	45.34	39.83	72.0	22	77	21	2.0	18:21	30	Doors open, steam on
282	175	0	42.39	36.90	73.8	22	77	21	2.5	18:31	30	Previous 2 runs sparse/spotty spray-patterns on strips, increases spray time
283	175	0	43.12	37.67	75.9	22	77	21	2.5	18:37	30	Doors open, steam on
284	175	0	43.81	38.34	71.7	8	40	40	1.5	18:47	40	Doors open, steam on
285	175	0	42.53	37.06	73.3	8	40	40	2.0	18:55	40	Doors open, steam on
286	175	0	41.71	36.22	72.4	8	40	40	2.0	19:03	40	Doors open, steam on
287	175	0	43.34	37.88	70.4	5	33	80	1.5	19:19	40	Doors open, steam on
288	175	0	39.95	34.45	75.1	5	33	80	2.0	19:27	40	Doors open, steam on
289	175	0	41.13	35.62	77.6	5	33	80	2.0	19:34	40	WSU air nozzle on before tunnel started to prevent spitting from WSU nozzles onto strip. Doors shut, steam on
290	175	0	42.54	37.05	75.0	5	40	100	2.0	19:43	40	Doors shut, steam on
291	175	0	42.32	36.83	69.4	5	40	100	2.0	19:54	40	Doors shut, steam on
292	175	0	40.97	35.47	72.2	5	55	137	1	20:03	40	Doors open, steam on
293	175	0	42.34	36.89	78.1	5	55	137	1	20:09	40	Doors open, steam on
294	175	0	42.20	36.73	71.3	5	70	168	0.75	20:15	40	Doors open, steam on
295	175	0	41.63	36.13	72.1	5	70	168	0.75	20:22	40	Doors open, steam on
296	175	0	38.87	33.43	71.6	22	77	21	2.8	20:30	30	Doors open, steam on
297	175	0	42.78	37.23	74.4	22	77	21	1	20:41	30	Doors shut, steam off
298	175	0	39.94	34.44	72.1	22	77	21	1.8	20:49	30	Doors open, steam on
299	175	0	42.61	37.09	76.0	22	77	21	1.8	20:58	30	Doors shut, steam off
300	175	0	43.06	37.64	72.1	22	77	21	1.8	21:43	30	ALL blades (a-g) Doors shut, steam on
301	175	0	44.45	38.87	74.5	5	70	168	0.75	21:43	40	ALL blades (a-g) Doors shut, steam off

Date: 09/26/2001
 Concentration: 0.0003 grams/cc
 $P_{\infty} = 14.07$ psi
 Geometry: MS(1)-0317 Airfoil

Run I.D.	TAS (mph)	AOA (deg.)	TOTAL TEMP. (°F)	STATIC TEMP. (°F)	R.H. (%)	P_{air} (psi)	P_{water} (psi)	MVD (μm)	Spray Time (sec)	Clock Time (EDT)	IRT Air (psi)	Remark
302		8										Surface Pressure RDG=9265
		6										Surface Pressure RDG=9266
		4										Surface Pressure RDG=9267
		2										Surface Pressure RDG=9268
		1										Surface Pressure RDG=9269
		0.5										Surface Pressure RDG=9270
		0										Surface Pressure RDG=9271
		-0.5										Surface Pressure RDG=9272
		-1										Surface Pressure RDG=9273
		-1.5										Surface Pressure RDG=9274
		-2										Surface Pressure RDG=9275
		0										Surface Pressure RDG=9276
306	175	0	49.20	43.70	73.1	22	77	21	4	18:47	30	Doors open, steam on
307	176	0	49.46	43.93	76.0	22	77	21	2	18:54	30	Doors open, steam off
308	175	0	55.96	50.47	74.6	8	40	40	4	19:12	40	Doors shut, steam off
309	175	0	52.48	47.05	74.5	8	40	40	2	19:21	40	Doors open, steam on
310	176	0	55.39	49.84	76.0	8	40	40	3	19:40	40	Doors shut, steam off
311	175	0	53.78	48.33	72.2	6	37	79	2	19:52	40	Doors shut, steam on
312	175	0	53.80	48.34	72.2	6	37	79	4	20:04	40	Doors shut, steam off
313	174	0	52.58	47.18	73.2	5	33	80	4	20:17	40	Doors shut, steam on
314	175	0	53.29	47.82	74.3	5	33	80	4	20:23	40	Doors shut, steam on
315	175	0	54.06	48.60	73.3	5	33	80	2	20:29	40	Doors shut, steam on
316	175	0	53.37	47.92	72.2	5	40	100	4	20:39	40	Doors shut, steam on
317	175	0	52.53	47.05	72.4	5	40	100	2	20:45	40	Doors shut, steam on
318	175	0	54.61	49.10	72.2	5	40	100	8	20:54	40	Doors shut, steam off
319	175	0	53.25	47.78	72.1	5	55	137	4	21:06	40	Doors shut, steam on
320	175	0	53.37	47.94	71.1	5	55	137	1	21:11	40	Doors shut, steam on
321	175	0	44.71	39.22	74.1	5	70	168	4	21:19	40	Doors shut, steam off
322	175	0	43.25	37.79	78.4	5	70	168	0.75	21:26	40	Doors shut, steam off
323	175	0	52.75	47.25	73.8	5	70	168	0.75	21:39	40	Doors shut, steam off
324	175	0	52.73	47.24	74.7	5	70	168	0.75	21:49	40	Doors shut, steam on
325	175	0	55.42	49.90	75.7	22	77	21	1.8	22:04	30	Doors shut, steam on
326	175	0	52.04	46.58	74.8	22	77	21	2	22:15	30	Doors open, steam on
327	175	0	54.51	49.00	75.2	22	77	21	1.8	22:26	30	Doors shut, steam off

Date: 09/27/2001
 Concentration: 0.0003 grams/cc
 P_o = 14.34 psi
 Geometry: MS(1)-0317 Airfoil

Run I.D.	TAS (mph)	AOA (deg.)	TOTAL TEMP. (°F)	STATIC TEMP. (°F)	R.H. (%)	P _{air} (psi)	P _{water} (psi)	MVD (µm)	Spray Time (sec)	Clock Time (EDT)	IRT Air (psi)	Remark
331	176	0	52.73	47.16	71.6	22	77	21	4	17:34	30	Doors shut, steam off
332	175	0	51.71	46.22	72.5	22	77	21	2	17:40	30	Doors open, steam on
333	175	0	50.72	45.29	72.4	22	77	21	2	17:52	30	Doors open, steam on
334	175	0	50.66	45.21	75.0	22	77	21	2	17:58	30	Doors open, steam on
335	175	0	51.55	46.05	73.7	6	37	79	2	18:05	40	Doors open, steam on
336	175	0	49.79	44.28	74.2	6	37	79	2	18:11	40	Doors open, steam on
337	175	0	51.85	46.35	73.5	6	37	79	2	18:20	40	Doors open, steam off
338	175	0	50.68	45.23	74.1	6	37	79	4	18:26	40	Doors open, steam off
339	175	0	51.87	46.34	61.7	5	55	137	4	18:35	40	Splashes on strip before spray (from puddle on floor). Doors shut, steam off
340	173	0	50.29	44.92	72.9	5	55	137	1	18:57	40	Doors shut, steam off
341	175	0	50.93	45.44	75.0	5	55	137	1	19:05	40	Doors open, steam on
342	175	0	52.61	47.09	73.9	5	55	137	1	19:13	40	Doors open, steam on
343	176	0	51.69	46.16	73.6	5	70	168	0.75	19:28	40	Doors open, steam on
344	175	0	48.88	43.44	72.8	5	70	168	0.75	20:02	40	Doors open, steam on
345	175	0	47.78	42.32	73.5	5	70	168	0.75	20:11	40	Doors open, steam on
346	174	0	45.81	40.43	76.3	5	70	168	4	20:17	30	Doors open, steam on
347	175	0	49.80	44.28	73.6	22	77	21	2.5	20:55	40	Doors open, steam on-wrong IRT air
348	174	0	47.24	41.83	73.1	22	77	21	2.5	21:03	30	Doors open, steam on
349	175	0	49.58	44.09	73.3	22	77	21	2.5	21:11	30	Doors shut, steam off
350	175	0	48.81	43.30	72.2	5	55	137	1.5	21:27	40	Doors open, steam on
351	175	0	46.77	41.32	72.3	5	55	137	1.5	21:33	40	Doors open, steam on
352	175	0	48.65	43.14	74.3	5	55	137	1.5	21:40	40	Doors open, steam off
353	175	0	47.67	42.28	73.6	5	70	168	1	21:47	40	Doors open, steam on
354	175	0	48.57	43.10	73.3	5	70	168	1	21:53	40	Doors open, steam off
355	175	0	48.43	42.99	73.8	5	70	168	1	21:01	40	Doors open, steam on

Date: 09/28/2001

Concentration: 0.0003 grams/cc

P_o = 14.3 psi

Geometry: NACA 65₂-415 Airfoil

AOA (IRT) 2, 1.5, 1, 0.5, 0, -0.5, -1, -1.5, -2, -4, -5, -6, -7, -8, -9, -10

AOA(airfoil) -2, -1.5, -1, -0.5, 0, 0.5, 1, 1.5, 2, 4, 5, 6, 7, 8, 9, 10

Run I.D.	TAS (mph)	AOA (deg.)	TOTAL TEMP. (°F)	STATIC TEMP. (°F)	R.H. (%)	P _{air} (psi)	P _{water} (psi)	MVD (µm)	Spray Time (sec)	Clock Time (EDT)	IRT Air (psi)	Remark
356		10										Surface Pressure RDG= 9278
		9										Surface Pressure RDG= 9279
		8										Surface Pressure RDG= 9280
		7										Surface Pressure RDG= 9281
		6										Surface Pressure RDG= 9282
		5										Surface Pressure RDG= 9283
		4										Surface Pressure RDG= 9284
		3										Surface Pressure RDG= 9285
		2										Surface Pressure RDG= 9286
		1.5										Surface Pressure RDG= 9287
		1										Surface Pressure RDG= 9288
		0.4										Surface Pressure RDG= 9289
		0										Surface Pressure RDG= 9290
		-0.5										Surface Pressure RDG= 9291
		-1										Surface Pressure RDG= 9292
		-1.5										Surface Pressure RDG= 9293
		-1.9										Surface Pressure RDG= 9294
		0										Surface Pressure RDG= 9295
		3.5										Surface Pressure RDG= 9296
		4										Surface Pressure RDG= 9297
357	174	0	55.34	49.91	48.2	5	70	168	4	17:48	40	Doors open, steam on
359	175	0	48.60	43.17	74.1	43	67	11	4.5	18:54	30	Doors open, steam on
360	175	0	47.95	42.49	74.3	43	67	11	4.5	19:05	30	Doors open, steam on
361	175	0	49.38	43.91	73.9	43	67	11	4.5	19:12	30	Doors open, steam off
362	174	0	48.88	43.45	72.3	22	77	21	2	19:28	30	Doors open, steam on
363	175	0	46.41	40.97	72.6	22	77	21	2	19:34	30	Doors open, steam on
364	175	0	48.69	43.20	72.6	22	77	21	2	19:41	30	Doors shut, steam off
365	175	0	47.78	42.32	72.5	22	77	21	2.5	20:20	30	Doors open, steam on
366	175	0	49.33	43.86	73.0	22	77	21	2.5	20:37	30	Doors open, steam off
367	175	0	51.72	46.22	72.9	22	77	21	2.5	22:41	30	Doors shut, steam off
368	175	0	48.17	42.73	73.1	22	77	21	2.5	22:28	30	Doors open, steam off
369	175	0	49.68	44.15	73.1	6	37	79	2	22:57	40	Doors shut, steam off
370	175	0	47.10	41.63	72.4	6	37	79	2	23:02	40	Doors shut, steam off
371	175	0	48.70	43.16	73.4	6	37	79	2	23:09	40	Doors shut, steam off

Date: 10/01/2001 Monday
 Concentration: 0.0003 grams/cc
 P_o = 14.31 psi
 Geometry: NACA 65₂-415 Airfoil

Run I.D.	TAS (mph)	AOA (deg.)	TOTAL TEMP. (°F)	STATIC TEMP. (°F)	R.H. (%)	P _{air} (psi)	P _{water} (psi)	MVD (µm)	Spray Time (sec)	Clock Time (EST)	IRT Air (psi)	Remark
372	176	0	53.96	48.44	74.5	6	37	79	2	17:48	40	Doors shut, steam off
373	175	0	53.13	47.65	73.4	6	37	79	2	17:56	40	Doors open, steam on
374	175	0	52.51	47.03	73.2	6	37	79	2	18:04	40	Doors open, steam on
375	175	0	51.45	45.99	73.2	6	37	79	4	18:11	40	Doors open, steam on
376	175	0	53.17	47.68	74.2	5	55	137	1	18:17	40	Doors open, steam off
377	175	0	49.28	43.81	75.0	5	55	137	1	18:23	40	Doors open, steam on
378	175	0	53.28	47.81	71.7	5	55	137	1	18:32	40	Doors shut, steam off
379	175	0	50.07	44.59	73.7	5	55	137	1.5	18:38	40	Doors open, steam on
380	175	0	53.60	48.11	73.9	5	55	137	1.5	18:46	40	Doors shut, steam off
381	175	0	52.81	47.36	71.2	5	55	137	1.5	18:53	40	Doors open, steam on
382	175	0	48.43	43.01	75.8	5	55	137	4	18:59	40	Doors open, steam on
383	175	0	52.78	47.30	73.4	5	70	168	0.75	19:10	40	Doors shut, steam off
384	174	0	49.92	44.50	73.5	5	70	168	0.75	19:17	40	Doors open, steam on
385	176	0	53.39	47.83	73.6	5	70	168	0.75	19:25	40	Doors shut, steam off
386	176	0	51.44	45.91	73.0	5	70	168	1	19:36	40	Doors open, steam on
387	175	0	52.86	47.37	73.7	5	70	168	1	19:41	40	Doors open, steam on
388	175	0	49.83	33.34	73.6	5	70	168	1	19:47	40	Doors open, steam on
389	175	0	50.88	45.42	76.9	5	70	168	4	19:52	40	Doors open, steam on
390	175	4	50.06	44.57	73.5	5	70	168	4	20:03	40	Doors open, steam on, double-length strip
391	175	4	52.51	47.02	73.5	5	70	168	1	20:15	40	Doors shut, steam off
392	175	4	51.27	45.77	73.1	5	70	168	1	20:24	40	Doors shut, steam on
393	175	4	51.51	46.01	70.6	5	70	168	1	20:30	40	Doors shut, steam on
394	175	4	49.64	44.16	71.1	5	70	168	0.75	20:35	40	Doors shut, steam on
395	175	4	52.48	46.99	72.3	5	70	168	0.75	20:44	40	Doors shut, steam off

Run I.D.	TAS (mph)	AOA (deg.)	TOTAL TEMP. (°F)	STATIC TEMP. (°F)	R.H. (%)	P _{air} (psi)	P _{water} (psi)	MVD (µm)	Spray Time (sec)	Clock Time (EST)	IRT Air (psi)	Remark
396	175	4	51.47	45.98	73.7	5	70	168	0.75	20:50	40	Doors open, steam on
397	175	4	50.77	45.30	72.3	5	55	137	1	20:56	40	Doors open, steam on
398	176	4	51.70	46.20	73.7	5	55	137	1	21:03	40	Doors shut, steam off
399	175	4	50.35	44.86	73.7	5	55	137	1	21:09	40	Doors open, steam on
400	175	4	51.05	45.60	77.8	5	55	137	4	21:14	40	Doors open, steam on
401	175	4	50.86	45.40	73.4	5	55	137	1.5	21:19	40	Doors open, steam on
402	176	4	52.35	46.82	74.2	5	55	137	1.5	21:26	40	Doors shut, steam off
403	175	4	51.65	46.19	72.1	5	55	137	1.5	21:29	40	Doors shut, steam off
404	175	4	51.31	45.85	73.3	6	37	79	2	21:37	40	Doors open, steam on
405	176	4	52.85	47.33	74.1	6	37	79	2	21:45	40	Doors shut, steam off
406	175	4	51.16	45.69	73.6	6	37	79	2	21:52	40	Doors open, steam on
407	176	4	52.51	46.98	73.5	6	37	79	4	21:57	40	Doors shut, steam off
408	175	4	49.86	44.42	73.8	43	67	11	4.5	22:03	30	Doors open, steam on
409	175	4	53.08	47.60	72.8	43	67	11	4.5	22:17	30	Doors shut, steam off
410	175	4	51.49	46.04	74.2	43	67	11	4.5	22:23	30	Doors open, steam on
411	174	4	49.86	44.43	70.2	22	77	21	2	22:31	30	Doors shut, steam off
412	175	4	49.65	44.22	74.1	22	77	21	2.5	22:36	30	Doors open, steam on
413	175	4	50.66	45.17	74.8	22	77	21	2.5	22:41	30	Doors shut, steam off
414	175	4	51.11	45.66	71.3	22	77	21	2	22:46	30	Doors shut, steam on
415	175	4	49.22	43.79	71.1	22	77	21	4	22:51	30	Doors open, steam on
416	175	4	49.43	43.98	74.4	22	77	21	2.5	22:57	30	Doors shut, steam off
417	175	4	50.96	45.50	74.2	22	77	21	2	23:02	30	Doors shut, steam off

Date: 10/02/2001 Tuesday
 Concentration: 0.0003 grams/cc
 P_o = 14.31 psi
 Geometry: Collector Mechanism

Run I.D.	TAS (mph)	AOA (deg.)	TOTAL TEMP. (°F)	STATIC TEMP. (°F)	R.H. (%)	P _{air} (psi)	P _{water} (psi)	MVD (µm)	Spray Time (sec)	Clock Time (EST)	IRT Air (psi)	Remark
418	178	4	52.60	46.95	73.0	6	37	79	4	17:17	40	Doors open, steam on
419	175	4	53.61	48.15	72.5	6	37	79	2	17:31	40	Doors open, steam on
420	175	4	52.86	47.39	72.1	6	37	79	2	17:36	40	Doors open, steam on
421	175	4	51.84	46.40	72.2	6	37	79	2	17:42	40	Doors open, steam on
422	176	4	53.82	48.30	72.3	5	55	137	4	17:50	40	Doors open, steam on
423	175	4	50.42	44.97	72.4	5	55	137	1	17:56	40	Doors open, steam on
424	176	4	52.72	47.21	71.1	5	55	137	1	18:02	40	Doors shut, steam off
425	175	4	49.83	44.35	72.8	5	55	137	1	18:08	40	Doors shut, steam off
426	176	4	52.00	46.47	70.7	5	55	137	1.5	18:14	40	Doors shut, steam off
427	175	4	50.77	45.32	72.5	5	55	137	1.5	18:19	40	Doors shut, steam off
428	175	4	52.03	46.55	73.6	5	55	137	1.5	18:25	40	Doors shut, steam on
429	174	4	49.31	43.91	74.1	43	67	11	4.5	18:32	30	Doors shut, steam on
430	176	4	52.50	46.70	73.5	43	67	11	4.5	18:39	30	Doors shut, steam off
431	174	4	50.31	44.91	73.7	43	67	11	4.5	18:45	30	Doors shut, steam off
432	177	4	52.15	46.59	72.5	5	70	168	4	18:52	40	Doors shut, steam off
433	175	4	49.74	44.29	73.3	5	70	168	0.75	18:58	40	Doors shut, steam off
434	176	4	52.53	46.99	73.1	5	70	168	0.75	19:05	40	Doors shut, steam off
435	175	4	49.93	44.45	73.7	5	70	168	0.75	19:12	40	Doors shut, steam off
436	176	4	53.22	47.68	73.4	5	70	168	1	19:21	40	Doors shut, steam off
437	175	4	49.62	44.15	73.4	5	70	168	1	19:28	40	Doors shut, steam off
438	176	4	53.28	47.74	73.7	5	70	168	1	19:37	40	Doors shut, steam off
439	175	4	52.21	46.75	73.1	22	77	21	4	19:45	30	Doors open, steam on
440	175	4	51.68	46.24	73.5	22	77	21	2	19:53	30	Doors open, steam on

Run I.D.	TAS (mph)	AOA (deg.)	TOTAL TEMP. (°F)	STATIC TEMP. (°F)	R.H. (%)	P _{air} (psi)	P _{water} (psi)	MVD (µm)	Spray Time (sec)	Clock Time (EST)	IRT Air (psi)	Remark
441	176	4	52.42	46.91	73.0	22	77	21	2	20:02	30	Doors open, steam on
442	175	4	49.98	44.54	73.7	22	77	21	2	20:07	30	Doors open, steam on
443	175	4	51.27	45.84	74.2	22	77	21	2.5	20:14	30	Doors open, steam on
444	175	4	51.31	45.82	73.6	22	77	21	2.5	20:23	30	Doors open, steam off
445	175	4	51.06	45.65	73.5	22	77	21	2.5	20:33	30	Doors open, steam off
446	175	0	51.40	45.92	73.5	22	77	21	4	20:58	30	Doors open, steam off
447	175	0	51.68	46.19	72.5	22	77	21	2.5	21:05	30	Doors open, steam off
448	176	0	50.79	45.29	75.2	22	77	21	2.5	21:12	30	Doors open, steam on
449	175	0	51.11	45.63	72.1	22	77	21	2.5	21:17	30	Doors open, steam on
450	176	0	52.25	46.73	72.7	22	77	21	2	21:25	30	Doors open, steam on
451	176	0	49.75	44.24	73.9	22	77	21	2	21:32	30	Doors open, steam on
452	177	0	51.57	46.00	73.7	22	77	21	2	21:38	30	Doors open, steam on
453	176	0	48.35	42.80	72.3	6	37	79	4	21:46	40	Doors open, steam on
454	177	0	51.34	45.72	73.1	6	37	79	2	21:55	40	Doors shut, steam off
455	176	0	49.23	43.67	73.1	6	37	79	2	22:01	40	Doors open, steam on
456	178	0	51.27	45.61	73.9	6	37	79	2	22:08	40	Doors open, steam on
457	176	0	50.49	44.95	73.3	5	55	137	1	22:16	40	Doors open, steam on
458	178	0	38.86	33.19	73.4	5	55	137	1	22:23	40	Doors open, steam on

The Collector was adjusted as follows:

The leading edge location is at 53" from RHS wall (looking downstream), that corresponding to 4° of the NACA-65 airfoil. It has shifted by 1 in. to the right looking downstream from the previous configuration (AOA=0° runs), to compensate for the uniformity area offset at AOA=4°. The adjustment was only applied up to Run no. 445.

Date: 10/03/2001 Wednesday
 Concentration: 0.0003 grams/cc
 P_o = 14.28 psi

Geometry: Collector Mechanism

Run I.D.	TAS (mph)	AOA (deg.)	TOTAL TEMP. (°F)	STATIC TEMP. (°F)	R.H. (%)	P _{air} (psi)	P _{water} (psi)	MVD (µm)	Spray Time (sec)	Clock Time (EST)	IRT Air (psi)	Remark
459	175	0	41.80	36.36	75.9	5	55	137	1	18:03	40	Doors open, steam on
460	178	0	42.14	36.56	72.8	5	55	137	1	18:13	40	Doors open, steam on
461	175	0	42.12	36.55	73.0	5	55	137	1	18:23	40	Doors open, steam on
462	175	0	41.74	36.19	74.4	5	55	137	1	18:35	40	Doors open, steam on
463	175	0	40.16	34.60	72.6	5	55	137	1.5	18:41	40	Doors open, steam on
464	175	0	40.66	35.12	71.2	5	55	137	1.5	18:45	40	Doors open, steam on
465	175	0	40.63	35.08	72.4	5	55	137	1.5	18:51	40	Doors open, steam on
466	175	0	40.94	35.44	73.5	43	67	11	4.5	18:58	30	Doors open, steam on
467	175	0	41.18	35.70	73.5	43	67	11	4.5	19:04	30	Doors open, steam on
468	174	0	40.12	34.70	73.1	43	67	11	4.5	19:09	30	Doors open, steam on
469	177	0	41.77	36.19	73.6	5	70	168	1	19:14	40	Doors open, steam on
470	177	0	40.91	35.36	73.4	5	70	168	1	19:27	40	Doors open, steam on
471	176	0	40.05	34.55	73.0	5	70	168	1	19:33	40	Doors open, steam on
472	176	0	41.23	35.68	72.7	5	70	168	0.75	19:42	40	Doors open, steam on
473	177	0	40.69	35.10	73.5	5	70	168	0.75	19:47	40	Doors open, steam on
474	176	0	40.42	34.89	73.1	5	70	168	0.75	19:58	40	Doors open, steam on
475	75	0	39.78	38.77	72.3	5	55	137	1.5	20:11	40	Doors open, steam on, speed test
476	75	0	41.45	40.46	72.9	5	55	137	1.5	20:18	40	Doors open, steam off, speed test
477	100	0	39.53	37.77	71.4	5	55	137	1.5	20:24	40	Doors open, steam on, speed test
478	100	0	41.44	39.58	72.8	5	55	137	1.5	20:24	40	Doors shut, steam off, speed test
479	125	0	40.07	37.31	72.5	5	55	137	1.5	20:40	40	Doors shut, steam off, speed test
480	125	0	41.41	38.56	73.2	5	55	137	1.5	20:45	40	Doors shut, steam on, speed test
481	150	0	40.64	36.59	72.5	5	55	137	1.5	20:50	40	Doors shut, steam on, speed test
482	150	0	40.05	35.96	70.3	5	55	137	1.5	20:55	40	Doors shut, steam on, speed test

Date: 10/04/2001 Thursday
 Concentration: 0.0003 grams/cc
 P_o = 14.32 psi
 Geometry: GLC-305 Airfoil

Run I.D.	TAS (mph)	AOA (deg.)	TOTAL TEMP. (°F)	STATIC TEMP. (°F)	R.H. (%)	P _{air} (psi)	P _{water} (psi)	MVD (µm)	Spray Time (sec)	Clock Time (EST)	IRT Air (psi)	Remark
483		-2										Surface Pressure, α sweep RDG=9299
		-1.5										RDG=9300
		-1										RDG=9301
		-0.5										RDG=9302
		0										RDG=9303
		0.5										RDG=9304
		1										RDG=9305
		1.5										RDG=9306
		2										RDG=9307
		3										RDG=9308
		4										RDG=9309
		5										RDG=9310
		6										RDG=9311
		7										RDG=9312
		8										RDG=9313
		1.5										RDG=9314
484	176	1.5	64.30	58.77	74.0	6	37	79	2	17:38	40	Impingement tests begin, doors open, steam on
485	175	1.5	64.51	59.06	73.1	6	37	79	2	17:48	40	Doors shut, steam on
486	176	1.5	66.98	61.45	73.7	6	37	79	2	17:58	40	Doors shut, steam on
487	175	1.5	67.75	62.26	74.3	6	37	79	4	18:10	40	Doors shut, steam on
488	175	1.5	68.41	62.93	74.0	5	55	137	1	18:18	40	Doors shut, steam on
489	175	1.5	68.72	63.24	73.0	5	55	137	1	18:23	40	Doors open, steam on
490	176	1.5	66.09	60.59	72.7	5	55	137	1	19:00	40	Doors open, steam on
491	176	1.5	65.79	60.29	72.9	5	55	137	1.5	19:07	40	Doors open, steam off

Run I.D.	TAS (mph)	AOA (deg.)	TOTAL TEMP. (°F)	STATIC TEMP. (°F)	R.H. (%)	P _{air} (psi)	P _{water} (psi)	MVD (µm)	Spray Time (sec)	Clock Time (EST)	IRT Air (psi)	Remark
492	175	1.5	66.14	60.67	74.4	5	55	137	1.5	19:12	40	Doors open, steam off
493	175	1.5	66.31	60.85	73.8	5	55	137	1.5	19:23	40	Doors open, steam off
494	175	1.5	66.34	60.87	71.3	5	55	137	4	19:29	40	Doors open, steam off
495	175	1.5	66.57	61.14	74.7	43	67	11	4.5	19:36	30	Doors open, steam off
496	176	1.5	64.04	58.59	74.7	43	67	11	4.5	19:43	30	Doors open, steam off
497	175	1.5	64.57	59.14	75.7	43	67	11	4.5	19:49	30	Doors open, steam off
498	175	1.5	64.93	59.46	73.2	43	67	11	18	19:55	30	North Door open, steam off
499	177	1.5	67.09	61.49	72.7	5	70	168	0.75	20:08	40	Doors open, steam off
500	177	1.5	67.26	61.65	73.7	5	70	168	0.75	20:34	40	Doors shut, steam off
501	176	1.5	65.01	59.50	73.0	5	70	168	0.75	20:41	40	Doors open, steam on
502	175	1.5	64.60	59.14	72.3	5	70	168	1	20:49	40	Doors open, steam on
503	176	1.5	66.32	60.80	73.1	5	70	168	1	20:58	40	Doors shut, steam off
504	175	1.5	65.07	59.60	73.1	5	70	168	1	21:06	40	Doors open, steam on
505	175	1.5	65.21	59.80	72.8	5	70	168	4	21:12	40	Doors open, steam on
506	175	1.5	65.08	59.62	71.9	22	77	21	2	21:19	30	Doors open, steam on
507	175	1.5	65.24	59.81	73.4	22	77	21	2	21:24	30	Doors open, steam on
508	175	1.5	66.25	60.73	72.4	22	77	21	2	21:31	30	Doors open, steam on
509	176	1.5	63.88	58.40	73.1	22	77	21	2.5	21:39	30	Doors open, steam on
510	175	1.5	65.26	59.77	73.7	22	77	21	2.5	21:47	30	Doors closed, steam on
511	175	1.5	66.29	60.75	74.1	22	77	21	2.5	21:53	30	Doors closed, steam on
512	175	1.5	64.66	59.17	71.3	22	77	21	4	22:00	30	Doors closed, steam on
513	75	1.5	64.39	63.37	72.3	5	55	137	1.5	22:08	0	Doors closed, steam on, speed test
514	75	1.5	64.12	63.11	73.1	5	55	137	1.5	22:12	0	Doors closed, steam on, speed test
515	100	1.5	63.75	61.97	71.3	5	55	137	1.5	22:19	40	Doors closed, steam on, speed test
516	100	1.5	63.49	61.73	72.5	5	55	137	1.5	22:26	40	Doors closed, steam off, speed test
517	125	1.5	64.30	61.50	75.0	5	55	137	1.5	22:35	40	Doors closed, steam off, speed test
518	125	1.5	64.77	61.96	74.2	5	55	137	1.5	22:40	40	Doors closed, steam on, speed test
519	150	1.5	64.25	60.95	73.7	5	55	137	1.5	22:52	40	Doors closed, steam on, speed test
520	150	1.5	65.53	61.56	74.2	5	55	137	1.5	22:59	40	Doors closed, steam, speed test

Date: 10/05/2001 Friday
 Concentration: 0.0003 grams/cc
 P_∞ = 14.22 psi

Geometry: Uniformity Grid

Run I.D.	TAS (mph)	AOA (deg.)	TOTAL TEMP. (°F)	STATIC TEMP. (°F)	R.H. (%)	P _{air} (psi)	P _{water} (psi)	MVD (µm)	Spray Time (sec)	Clock Time (EST)	IRT Air (psi)	Remark
521	176	N.A.	64.41	58.92	69.9	6	37	79	2	17:54	40	Doors open, steam on, Strips
522	175	N.A.	63.01	57.49	70.6	6	37	79	2	19:18	40	Doors open, steam on, Strips
523												Skipped
524	175	N.A.	59.51	54.03	73.5	43	67	11	4.5	21:53	30	Doors shut, steam off, Strips
525	175	N.A.	53.68	48.22	72.1	5	70	168	1	22:09	40	Doors open, steam on, Strips
526	176	N.A.	57.95	52.46	71.8	22	77	21	2	22:29	30	Doors shut, steam off, Strips
527												
528	176	N.A.	58.83	53.40	70.1	6	37	79	5.5	20:51	40	Doors open, steam on, Uniform square
529	175	N.A.	56.48	51.00	71.2	5	55	137	1	19:56	40	Doors open, steam on, Uniform square
530	175	N.A.	57.71	52.26	73.0	43	67	11	1	20:11	30	Doors open, steam on, Uniform square
531	175	N.A.	59.01	53.54	72.1	5	70	168	1	20:22	40	Doors open, steam on, Uniform square
532	175	N.A.	58.75	53.33	70.9	22	77	21	2	20:39	30	Doors open, steam on, Uniform square
533	176	N.A.	55.73	50.27	72.4	6	37	79	2	21:08	40	Doors open, steam on, Uniform square

Date: 10/09/2001 Tuesday
 Concentration: 0.0003 grams/cc
 P_∞ = 14.5 psi

Geometry: Twin-Otter

Run I.D.	TAS (mph)	AOA (deg.)	TOTAL TEMP. (°F)	STATIC TEMP. (°F)	R.H. (%)	P _{air} (psi)	P _{water} (psi)	MVD (µm)	Spray Time (sec)	Clock Time (EST)	IRT Air (psi)	Remark
534	175	0	52.03	46.57	72.1	5	70	168	0.75	20:43	40	Doors open, steam on
535	174	0	50.38	44.97	72.1	5	70	168	0.75	21:00	40	Doors open, steam on
536	175	0	49.36	43.91	72.2	5	70	168	0.75	21:13	40	Doors open, steam on
537	175	0	48.63	43.19	72.8	5	70	168	4	21:30	40	Doors open, steam on
538	174	0	50.26	44.84	71.4	6	37	79	2	21:38	40	Doors open, steam on
539	175	0	50.72	45.25	72.3	6	37	79	2	21:49	40	Doors open, steam on
540	175	0	50.76	45.31	72.2	6	37	79	2	22:06	40	Doors open, steam on
541	175	0	49.25	43.79	72.5	6	37	79	4	22:22	40	Doors open, steam on
542	175	0	48.84	43.38	72.9	5	55	137	1	22:31	40	Doors open, steam off
543	176	0	45.14	39.59	72.4	5	55	137	1	22:50	40	Doors open, steam on
544	176	0	47.32	41.78	72.5	5	55	137	1	22:57	40	Doors open, steam off
545	176	0	45.63	40.12	71.8	5	55	137	4	23:02	40	Doors open, steam on

Date: 10/10/2001 Wednesday
 Concentration: 0.0003 grams/cc
 P_o = 14.5 psi
 Geometry: Twin-Otter

Airfoil AOA: -3, -2, -1.5, -1, -0.5, 0, 0.5, 1, 1.5, 2, 3, 3.5, 4, 4.5, 5, 5.5, 6, 6.5
 IRT AOA: 4.5, 3.5, 3, 2.5, 2, 1.5, 1, 0.5, 0, -0.5, -1.5, -2, -2.5, -3, -3.5, -4, -4.5, -5

Run I.D.	TAS (mph)	AOA (deg.)	TOTAL TEMP. (°F)	STATIC TEMP. (°F)	R.H. (%)	P _{air} (psi)	P _{water} (psi)	VD (µm)	Spray Time (sec)	Clock Time (EST)	IRT Air (psi)	Remark
546	175	-3			73.2					16:44		Surface Pressures, AOA Sweep, RDG=9315
	174	-2			59.1					16:45		RDG = 9316
	175	-1.5			65.5					16:46		RDG = 9317
	175	-1			58.7					16:47		RDG = 9318
	175	-0.5			56.3					16:48		RDG = 9319
	175	0			58.4					16:49		RDG = 9320
	175	0.5			63.7					16:49		RDG = 9321
	175	1			69.1					16:50		RDG = 9322
	175	1.5			72.8					16:51		RDG = 9323
	175	2			74.8					16:51		RDG = 9324
	175	3			61.4					16:56		RDG = 9324
	174	3.5			72.8					16:57		RDG = 9325
	174	4			78.6					16:59		RDG = 9326
	175	4.5			66.0					17:00		RDG = 9327
	175	5			60.8					17:01		RDG = 9328
	174	5.5			65.2					17:02		RDG = 9329
	175	6			75.0					17:04		RDG = 9330
	175	6.5			77.1					17:05		RDG = 9331
	175	0			59.1					17:08		RDG = 9332
547	174	0	58.52	53.12	72.8	43	67	11	4.5	17:22	30	Doors shut, steam on
548	176	0	61.29	55.77	71.7	43	67	11	4.5	17:28	30	Doors shut, steam off

Run I.D.	TAS (mph)	AOA (deg.)	TOTAL TEMP. (°F)	STATIC TEMP. (°F)	R.H. (%)	P _{air} (psi)	P _{water} (psi)	MVD (µm)	Spray Time (sec)	Clock Time (EST)	IRT Air (psi)	Remark
549	173	0	54.70	49.35	72.7	43	67	11	4.5	17:49	30	Doors open, steam on
550	176	0	56.34	50.83	72.1	43	67	11	18	17:57	30	Doors open, steam off
551	175	0	56.38	50.90	73.0	22	77	21	2	18:05	30	Doors open, steam off
552	175	0	56.78	51.31	72.5	22	77	21	2	18:13	30	Doors open, steam on
553	175	0	54.30	48.85	72.9	22	77	21	2	18:19	30	Doors open, steam on
554	174	0	55.01	49.60	72.3	22	77	21	4	18:24	30	Doors open, steam on
555	174	4	57.55	52.16	72.5	6	37	79	2	18:35	40	Doors open, steam on
556	175	4	52.76	47.31	72.3	6	37	79	2	18:44	40	Doors open, steam on
557	175	4	56.93	51.48	71.5	6	37	79	2	18:52	40	Doors open, steam off
558	176	4	55.26	49.75	73.6	6	37	79	4	18:57	40	Doors open, steam on
559	176	4	57.74	52.23	74.1	5	55	137	4	19:24	40	Doors open, steam on
560	176	4	56.63	51.12	71.0	5	55	137	1	19:39	40	Doors shut, steam off
561	175	4	54.99	49.51	72.4	5	55	137	1	19:45	40	Doors open, steam on
562	175	4	56.06	50.60	72.5	5	55	137	1	19:51	40	Doors open, steam on
563	175	4	53.42	47.95	74.0	43	67	11	4.5	19:57	30	Doors open, steam on
564	175	4	56.57	51.08	73.8	43	67	11	4.5	20:05	30	Doors open, steam off
565	176	4	53.63	48.12	73.6	43	67	11	4.5	20:15	30	Doors open, steam on
566	175	4	56.55	51.06	73.8	43	67	11	18	20:22	30	Doors open, steam off
567	175	4	53.19	47.71	73.0	5	70	168	0.75	20:29	40	Doors open, steam on
568	175	4	55.53	50.08	72.7	5	70	168	0.75	20:37	40	Doors open, steam off
569	175	4	55.81	50.32	72.8	5	70	168	0.75	20:50	40	Doors open, steam off
570	175	4	55.92	50.43	71.8	5	70	168	4	20:57	40	Doors open, steam on
571	175	4	52.87	47.43	72.0	22	77	21	2	21:04	30	Doors open, steam on
572	175	4	53.39	49.94	71.9	22	77	21	2	21:09	30	Doors open, steam off
573	175	4	56.93	51.46	72.2	22	77	21	2	21:16	30	Doors open, steam off
574	175	4	53.94	48.45	72.6	22	77	21	4	21:23	30	Doors open, steam off
575	175	4	55.48	50.01	70.1	5	70	168	4	21:30	40	Doors open, steam on

Date: 10/11/2001 Thursday
 Concentration: 0.0003 grams/cc

P_o = 14.1 psi

Geometry: Twin-Otter with 22.5 min. ice-shape

Airfoil AOA: -2, -1.5, -1, -0.5, 0, 0.5, 1, 1.5, 2, 2.5, 3, 3.5, 4

IRT AOA: 3.5, 3, 2.5, 2, 1.5, 1, 0.5, 0, -0.5, -1.0, -1.5, -2, -2.5

Run I.D.	TAS (mph)	AOA (deg.)	TOTAL TEMP. (°F)	STATIC TEMP. (°F)	R.H. (%)	P _{air} (psi)	P _{water} (psi)	MVD (µm)	Spray Time (sec)	Clock Time (EST)	IRT Air (psi)	Remark
576		-2										Surface Pressures, AOA Sweep, RDG=9333
		-1.5										RDG = 9334
		-1										RDG = 9335
		-0.5										RDG = 9336
		0										RDG = 9337
		0.5										RDG = 9338
		1										RDG = 9339
		1.5										RDG = 9340
		2										RDG = 9341
		2.5										RDG = 9342
		3										RDG = 9343
		3.5										RDG = 9344
		4										RDG = 9345
		0										RDG = 9346
577	175	0	61.73	56.28	71.9	6	37	79	2	17:19	40	Doors open, steam on
578	175	0	62.33	56.90	70.4	6	37	79	2	17:30	40	Doors open, steam off
579	176	0	63.86	58.35	74.0	6	37	79	2	17:43	40	Doors open, steam off
580	175	0	60.47	55.01	71.9	6	37	79	4	17:57	40	Doors open, steam on
581	174	0	61.19	55.76	72.3	43	67	11	4.5	18:14	30	Doors open, steam off
582	174	0	64.15	58.60	73.6	43	67	11	4.5	18:28	30	Doors shut, steam off
583	175	0	62.88	57.42	72.2	43	67	11	4.5	18:42	30	Doors open, steam off
584	175	0	62.93	57.49	72.3	43	67	11	18	18:54	30	Doors open, steam on
585	175	0	63.21	57.71	72.1	5	70	168	0.75	19:07	40	Doors open, steam on
586	175	0	59.90	54.40	72.3	5	70	168	0.75	19:21	40	Doors open, steam on
587	175	0	64.12	58.61	72.1	5	70	168	0.75	19:35	40	Doors shut, steam off
588	175	0	61.60	56.14	72.6	5	70	168	4	20:21	40	Doors open, steam on
589	175	0	64.12	58.59	72.7	22	77	21	2	20:35	30	Doors close, steam off
590	175	0	60.06	54.61	73.0	22	77	21	2	20:46	30	Doors open, steam off
591	176	0	63.61	58.11	72.3	22	77	21	2	21:01	30	Doors shut, steam off
592	175	0	59.64	54.18	72.5	22	77	21	4	21:13	30	Doors open, steam on
593	175	0	63.05	57.56	72.7	5	70	168	0.75	21:30	40	Doors shut, steam off
594	75	0	58.86	57.89	72.3	5	70	168	0.75	21:44	40	Doors open, steam on

During the AOA sweep, pressure ports 29 to 34, which were located near the L.E., were covered by the ice shape.

Date: 10/12/2001 Friday
 Concentration: 0.0003 grams/cc
 P_∞ = 14.3 psi
 Geometry: Twin-Otter with 45 min. ice-shape

Airfoil AOA: -2, -1.5, -1, -0.5, 0, 0.5, 1, 1.5, 2, 2.5, 3, 3.5, 4
 IRT AOA: 3.5, 3, 2.5, 2, 1.5, 1, 0.5, 0, -0.5, -1.0, -1.5, -2, -2.5

Run I.D.	TAS (mph)	AOA (deg.)	TOTAL TEMP. (°F)	STATIC TEMP. (°F)	R.H. (%)	P _{air} (psi)	P _{water} (psi)	MVD (µm)	Spray Time (sec)	Clock Time (EST)	IRT Air (psi)	Remark
595		-2										Surface Pressures, AOA Sweep, RDG=9347
		-1.5										RDG = 9348
		-1										RDG = 9349
		-0.5										RDG = 9350
		0										RDG = 9351
		0.5										RDG = 9352
		1										RDG = 9353
		1.5										RDG = 9354
		2										RDG = 9355
		2.5										RDG = 9356
		3										RDG = 9357
		3.5										RDG = 9358
		4										RDG = 9359 DO NOT USE
		4										RDG = 9360
		0										RDG = 9361
596	175	0	63.46	58.00	72.5	6	37	79	2	17:55	40	Doors shut, steam off
597	174	0	64.07	58.67	71.9	6	37	79	2	18:09	40	Doors shut, steam off
598	176	0	66.06	60.56	71.3	6	37	79	2	18:22	40	Doors shut, steam off
599	176	0	62.20	56.70	72.1	6	37	79	4	18:35	40	Doors open, steam off
600	175	0	62.23	57.77	74.8	43	67	11	4.5	18:48	30	Doors open, steam off
601	176	0	66.73	61.20	71.1	43	67	11	4.5	19:06	30	Doors shut, steam off
602	175	0	62.65	57.19	74.1	43	67	11	4.5	19:19	30	Doors open, steam off
603	176	0	65.83	60.28	73.7	43	67	11	18	19:34	30	Doors shut, steam off
604	176	0	62.28	56.76	71.7	5	70	168	0.75	19:56	40	Doors open, steam off
605	175	0	65.90	60.38	73.6	5	70	168	0.75	20:14	40	Doors shut, steam off
606	175	0	61.17	55.70	72.9	5	70	168	0.75	20:26	40	Doors open, steam on
607	175	0	62.59	57.15	74.5	5	70	168	4	20:39	40	Doors open, steam on
608	175	0	63.75	58.25	73.5	22	77	21	2	20:54	30	Doors shut, steam off
609	174	0	65.17	59.74	73.3	22	77	21	2	21:06	30	Doors shut, steam off
610	175	0	65.94	60.45	71.5	22	77	21	2	21:18	30	Doors shut, steam off
611	175	0	62.76	57.29	72.8	22	77	21	4	21:32	30	Doors open, steam on
612	125	0	63.25	60.46	74.0	5	70	168	0.75	21:45	40	Doors open, steam on
613	75	0	63.24	62.20	73.3	5	70	168	0.75	21:56	40	Doors shut, steam off

Date: 10/13/2001 Saturday
 Concentration: 0.0003 grams/cc
 $P_{\text{air}} = 14.3$ psi

Geometry: Collector Mechanism

Run I.D.	TAS (mph)	AOA (deg.)	TOTAL TEMP. (°F)	STATIC TEMP. (°F)	R.H. (%)	P_{air} (psi)	P_{water} (psi)	MVD (µm)	Spray Time (sec)	Clock Time (EST)	IRT Air (psi)	Remark
614	175	0	69.85	64.40	73.8	5	55	137	1	09:34	40	Doors open, steam on
615	175	0	69.11	63.62	73.9	5	55	137	1	09:40	40	Doors open, steam on
616	175	0	69.97	64.52	74.9	5	55	137	1	09:47	40	1 Door open, steam off
617	175	0	68.22	62.77	74.0	5	55	137	1	09:53	40	Doors open, steam off
618	175	0	68.97	63.49	76.1	5	55	137	1	10:01	40	Doors shut, steam on, with splashing tips
619	175	0	70.29	64.81	74.9	5	70	168	0.75	10:11	40	Doors shut, steam off
620	175	0	70.34	64.88	74.1	5	70	168	0.75	10:17	40	Doors open, steam off
621	175	0	71.05	65.61	74.6	5	70	168	0.75	10:23	40	Doors open, steam off
622	174	0	71.11	65.67	73.8	5	70	168	0.75	10:30	40	Doors open, steam on
623	175	0	71.01	65.55	73.3	6	37	79	2	10:37	40	1 Door open, steam off
624	175	0	71.10	65.66	74.1	6	37	79	2	10:43	40	Doors open, steam on
625	175	0	71.56	66.12	74.3	6	37	79	2	10:49	40	Doors shut, steam off
626	175	0	71.88	66.42	73.4	6	37	79	2	10:56	40	Doors open, steam on
627	175	0	70.44	64.98	73.4	22	77	21	2	11:04	30	Doors open, steam on
628	174	0	68.70	63.29	74.2	22	77	21	2	11:16	30	Doors open, steam on
629	175	0	67.95	62.49	74.1	22	77	21	2	11:22	30	Doors open, steam on
630	174	0	68.31	62.88	75.1	22	77	21	2	11:27	30	Doors open, steam on
631	177	0	68.61	63.03	72.6	43	67	11	4.5	11:33	30	1 Door open, steam on
632	176	0	68.34	62.80	74.3	43	67	11	4.5	11:39	30	Doors open, steam on
633	176	0	68.73	63.18	73.7	43	67	11	4.5	11:46	30	Doors open, steam on
634	125	0	66.82	64.03	74.0	5	70	168	0.75	11:55	40	Doors open, steam on
635	125	0	67.56	64.73	74.8	5	70	168	0.75	12:03	40	Doors shut, steam on
636	75	0	67.69	66.70	72.7	5	70	168	0.75	12:11	40	Doors shut, steam on
637	75	0	67.75	66.75	73.0	5	70	168	0.75	12:20	40	Doors shut, steam off
638	176	0	65.49	59.97	74.6	5	55	137	1	12:41	40	Doors open, steam on
639	177	0	69.01	63.43	77.7	5	55	137	1	14:04	40	Doors shut, steam on
640	177	0	69.21	63.60	72.8	5	55	137	1	14:25	40	Doors open, steam on
641	176	0	62.71	57.20	74.4	5	55	137	1	14:51	40	Doors shut, steam on
642	175	0	62.72	57.25	74.7	5	70	168	0.75	14:59	40	Doors open, steam on
643	176	0	63.86	58.35	73.9	5	70	168	0.75	15:05	40	Doors shut, steam on
644	174	0	61.01	55.60	74.8	5	70	168	0.75	15:13	40	Doors open, steam on
645	175	0	63.50	58.04	73.7	6	37	79	2	15:20	40	Doors shut, steam on
646	175	0	64.86	59.40	74.4	6	37	79	2	15:27	40	1 Door open, steam on

For Runs 614-637, the long (9 in.) collector blade was vertical.

For Runs 638-646, the long (9 in.) collector blade was horizontal.

Date: 10/15/2001 Monday
 Concentration: 0.0003 grams/cc
 P_o = 14.3 psi

Geometry: King probe (647 to 665), Icing Blade (666 to 679)

Run I.D.	TAS (mph)	AOA (deg.)	TOTAL TEMP. (°F)	STATIC TEMP. (°F)	R.H. (%)	P _{air} (psi)	P _{water} (psi)	MVD (µm)	Spray Time (sec)	Clock Time (EST)	IRT Air (psi)	Remark
647	175	NA	46.29	40.81	73.1	43	67	11	30	18:06	30	Doors closed, steam on
648	175	NA	45.78	40.35	75.5	43	67	11	30	18:10	0	Doors closed, steam off
649	175	NA	45.72	40.25	79.7	43	67	11	30	18:13	30	Doors closed, steam off
650	175	NA	46.08	40.59	74.5	22	77	21	30	18:20	30	Doors closed, steam off
651	176	NA	46.05	40.54	74.9	22	77	21	30	18:25	0	Doors closed, steam on
652	174	NA	45.68	40.24	80.2	22	77	21	30	18:30	0	Doors closed, steam on
653	175	NA	45.92	40.43	78.7	6	37	94	30	18:37	0	Doors closed, steam on
654	175	NA	45.12	39.61	70.4	6	37	94	30	18:39	40	Doors closed, steam on
655	175	NA	45.66	40.12	75.2	6	37	94	30	18:41	40	Doors closed, steam on
656	175	NA	45.78	40.30	79.3	5	55	137	30	18:48	40	Doors closed, steam on
657	175	NA	45.89	40.38	67.7	5	55	137	30	18:49	40	Doors closed, steam on
658	175	NA	45.39	39.92	73.9	5	55	137	30	18:52	0	Doors closed, steam on
659	175	NA	45.74	40.25	67.1	5	70	168	30	18:55	0	Doors closed, steam on
660	176	NA	45.36	39.85	79.9	5	70	168	30	18:58	40	Doors closed, steam on
661	175	NA	45.89	40.39	75.1	5	70	168	30	18:59	40	Doors closed, steam on
662	151	NA	44.75	40.70	71.0	5	70	168	30	19:03	40	Doors closed, steam on
663	125	NA	44.87	42.08	62.2	5	70	168	30	19:10	40	Doors closed, steam on
664	125	NA	43.88	41.08	66.2	5	55	137	30	19:14	40	Doors closed, steam on
665	150	NA	44.92	40.91	63.4	5	55	137	30	19:18	40	Doors closed, steam on
666	176	NA	45.00	39.51	75.5	6	37	79	2	20:14	40	Doors closed, steam on
667	175	NA	45.47	40.00	68.1	6	37	79	2	20:19	40	Doors closed, steam on
668	176	NA	46.26	40.75	70.4	5	55	137	1	20:25	40	Doors closed, steam on
669	176	NA	43.53	38.02	74.2	5	55	137	1	20:35	40	Doors closed, steam on
670	175	NA	45.47	40.00	72.8	43	67	11	4.5	20:42	30	Doors closed, steam on
671	175	NA	46.51	41.05	70.9	43	67	11	4.5	20:47	30	Doors closed, steam on
672	175	NA	48.20	42.74	68.8	5	70	168	0.75	21:01	40	Doors closed, steam on
673	175	NA	45.17	39.73	73.2	5	70	168	0.75	21:08	40	Doors open, steam on
674	177	NA	46.94	41.38	70.2	22	77	21	2	21:21	30	Doors closed, steam on
675	175	NA	45.36	39.92	72.3	22	77	21	2	21:29	30	Doors closed, steam on
676	176	NA	47.22	41.71	68.6	5	55	137	0.5	21:42	40	Doors closed, steam on
677	176	NA	46.43	40.92	72.9	5	55	137	0.75	22:23	40	Doors closed, steam on
678	175	NA	44.60	39.12	71.5	5	55	137	1	22:27	40	Doors closed, steam on
679	175	NA	45.50	40.03	70.4	5	55	137	0.5	22:35	40	Doors closed, steam on

Date: 10/16/2001 Tuesday
 Concentration: 0.0003 grams/cc
 P₀ = 14.3 psi

Geometry: Collector Mechanism (680-694), OAP-C Probe (695-706), OAP-Y Probe (707-714)

Run I.D.	TAS (mph)	AOA (deg.)	TOTAL TEMP. (°F)	STATIC TEMP. (°F)	R.H. (%)	P _{air} (psi)	P _{water} (psi)	MVD (µm)	Spray Time (sec)	Clock Time (EST)	IRT Air (psi)	Remark
680	176	0	48.75	43.24	74.0	6	37	79	2	16:17	40	Doors closed, steam on
681	175	0	49.34	43.87	61.5	6	37	79	2	16:32	40	Doors closed, steam on
682	175	0	46.11	40.65	65.5	6	37	79	2	16:45	40	Doors closed, steam on
683	176	0	49.16	43.66	67.3	22	77	21	2	17:10	30	Doors closed, steam off, splashed before spray
684	175	0	47.33	41.87	72.3	22	77	21	2	17:15	30	Doors closed, steam on
685	174	0	49.63	44.20	74.1	22	77	21	2	17:24	30	Doors closed, steam off
686	175	0	46.98	41.52	73.5	43	67	11	4.5	17:31	30	Doors closed, steam on
687	175	0	47.97	42.52	73.2	43	67	11	4.5	17:44	30	Doors closed, steam on
688	175	0	48.66	43.22	72.1	43	67	11	4.5	17:55	30	Doors closed, steam on
689	175	0	49.32	43.87	74.0	6	37	79	2	18:01	40	Doors closed, steam off
690	175	0	46.21	40.72	74.5	6	37	79	2	18:07	40	Doors closed, steam on
691	176	0	46.43	40.93	73.4	5	55	137	0.75	18:14	40	Doors closed, steam off
692	175	0	47.25	41.78	74.5	5	55	137	1	18:19	40	Doors closed, steam off
693	176	0	48.82	43.30	72.3	5	70	168	0.75	18:28	40	Doors closed, steam off
694	176	0	45.22	39.74	73.3	5	70	168	0.75	18:33	40	Doors closed, steam on
695	175	NA	48.67	43.18	68.7	6	37	79	150	19:53	40	Doors closed, steam on
696	175	NA	47.94	42.48	79.4	6	37	79	150	19:56	40	Doors closed, steam off
697	175	NA	48.49	43.00	68.0	5	55	137	150	19:59	40	Doors closed, steam on
698	175	NA	45.77	40.31	72.7	5	55	137	150	20:02	40	Doors closed, steam on
699	175	NA	48.33	42.86	69.7	5	70	168	150	20:08	40	Doors closed, steam off
700	175	NA	49.32	43.86	72.1	5	70	168	150	20:11	40	Doors closed, steam on
701	175	NA	46.68	41.21	72.2	22	77	21	150	20:15	30	Doors closed, steam on
702	175	NA	47.31	41.83	78.4	22	77	21	150	20:17	30	Doors closed, steam off
703	175	NA	48.33	42.86	69.7	8	40	40	150	20:21	40	Doors closed, steam on
704	176	NA	48.10	42.60	64.8	8	40	40	150	20:24	40	Doors closed, steam on
705	175	NA	48.22	42.76	73.5	5	33	80	150	20:27	40	Doors closed, steam on
706	175	NA	47.47	41.97	63.4	5	40	100	150	20:30	40	Doors closed, steam on
707	176	NA	48.61	43.10	65.8	5	70	168	150	22:17	40	Doors closed, steam on
708	175	NA	48.24	42.79	77.2	5	55	137	150	22:20	40	Doors closed, steam on
709	175	NA	48.64	43.16	66.9	6	37	79	150	22:24	40	Doors closed, steam on
710	175	NA	47.66	42.21	75.7	5	40	100	150	22:27	40	Doors closed, steam on
711	175	NA	48.94	43.49	72.0	5	55	137	150	22:30	40	Doors closed, steam on
712	175	NA	48.22	42.73	74.3	5	70	168	150	22:36	40	Doors closed, steam on
713	175	NA	48.59	43.19	67.0	5	70	168	150	22:39	0	Doors closed, steam on
714	175	NA	46.85	41.47	76.7	5	55	137	150	22:42	0	Doors closed, steam on

Appendix E—Surface Tension Measurements of Water and Blue Dye Solution

The surface tension of distilled water and blue dye samples were measured by Augustine Scientific, an Ohio-based company that specializes in surface and interface science. A dye solution sample made using distilled water (concentration 0.3 g per liter, i.e., same as that used for the impingement tests) and a sample of distilled water were tested. Measurements were made by the Wilhelmy plate method using a Kruss K11 Tensiometer, at a temperature of $22 \pm 1^\circ\text{C}$.

In the Wilhelmy plate method a platinum plate, having dimensions of 40 mm (width) by 0.2 mm (thickness) by 10 mm (height), is attached to a force measuring device (the K11 Tensiometer) and is brought down into contact with the liquid being tested (just touching the liquid free surface, along its 40 mm by 0.2 mm edge). The bottom edge of the plate is then submerged below the surface of the liquid to a depth of 2.0 mm to wet the plate. The plate is then pulled back to within 10 μm of the surface of the liquid, and the force of the liquid pulling down on the plate (the liquid's Wilhelmy force) is measured after 30 sec to allow the plate to come to a complete stop. This force is divided by the wetted length of the plate (i.e., the plate perimeter of 80.4 mm) to calculate the surface tension of the liquid being tested.

The following results were obtained in triplicate experiments:

Test no.	Surface Tension of Distilled Water (mN/m)	Surface Tension of Dye Solution (mN/m)
1	72.83	72.64
2	72.80	72.65
3	72.80	72.69
Average	72.81	72.66
Std. Dev.	0.01	0.03

The data show that the dye has no effect on the water surface tension. Thus the use of dye solution has no effect on the surface tension of the impinging droplets.

Appendix F—Trajectory Computations for 22.5- and 45-min Glaze Ice Shapes

The trajectory computations presented in the main body of the report (figs. 65 and 66) were performed with a droplet size equal to the MVD of the distribution. Although these trajectory data are useful in demonstrating the effect of MVD on trajectory characteristics they do not provide sufficient information to explain the LEWICE impingement trends presented in figures 92 and 93. To explore the reasons for the observed “peaks” and “valleys” observed in the LEWICE impingement data particularly between the ice horns, additional trajectory computations were performed with the LEWICE code for the experimental configurations listed below:

- 22.5-min ice shape: MVD =21 μm , AOA=0°
- 22.5-min ice shape: MVD =168 μm , AOA=0°
- 45-min ice shape: MVD =21 μm , AOA=0°
- 45-min ice shape: MVD =168 μm , AOA=0°

In these computations the discrete ten point droplet distributions for the 21 and 168 μm presented in table 8 were used and trajectories were computed for each droplet size in the distribution. Thus for an MVD of 21 μm , trajectories were computed using LEWICE 1.7 (with the gravity term G set to zero in NAMELIST &TRAJ1; this was done because the wing was installed vertically in the IRT) for droplet sizes of 4.04, 9.67, 14.24, 20.94, 28.15, 45.23, 70.07, 88.86, 103.41, and 163.97 μm . For each droplet size the LWC value was set according to the data presented in table 8. A total of 40 trajectory computations were performed, 10 for each of the four cases listed above. The results are presented in figures F1 to F8 and demonstrate the contribution of each droplet size in the distribution to the impingement characteristics of the two ice shapes. In addition to the trajectory data, impingement data for each droplet size in the distribution are also presented in the figures along with the composite impingement data obtained using all the droplets in the distribution.

For the 45-min ice shape with the 168 μm MVD the results of figure F7 demonstrate that the droplet sizes 15.09, 52.54, 102.25, 172.09, 264.38 and 395.58 μm contribute 95 percent to the impingement efficiency. In addition, droplets with diameters equal or greater than 102 μm have nearly straight trajectories due to the large inertia of these droplets as shown in figures F8c to F8j. The “peaks” and “valleys” in the impingement efficiency curve corresponding to points A, B, C, D, and E in figure F7 are related to the local surface slopes of the ice shape at these stations. The surface slopes at stations A, C, and D are more normal to the incoming particles than those at stations B and C and thus the impingement efficiency at these three locations is higher. Note that LEWICE does not simulate droplet splashing and droplet re-impingement and furthermore it does not simulate the flow recirculation region between the two ice horns. Thus the experimental impingement efficiency distribution will in general vary from that predicted by LEWICE.

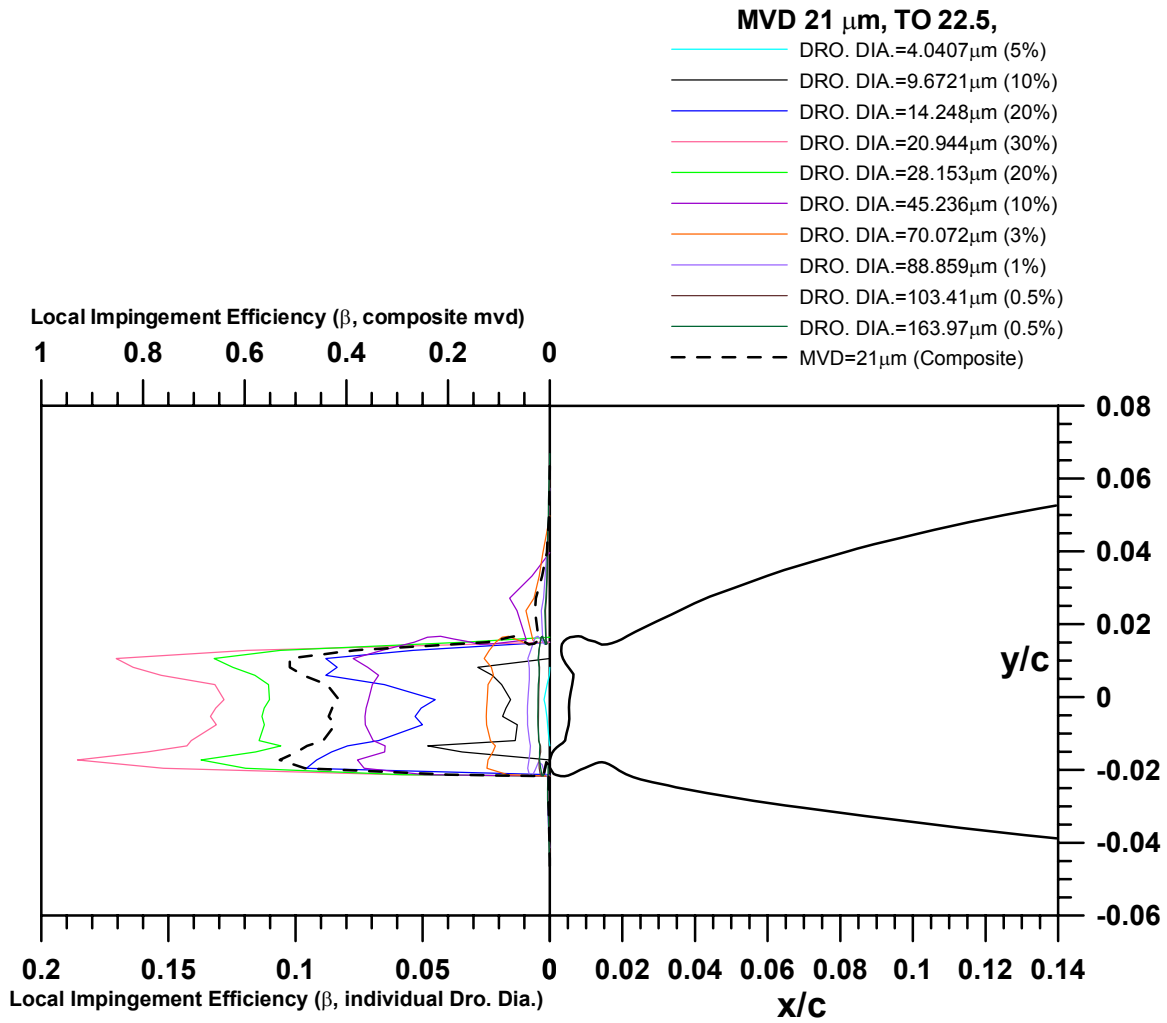
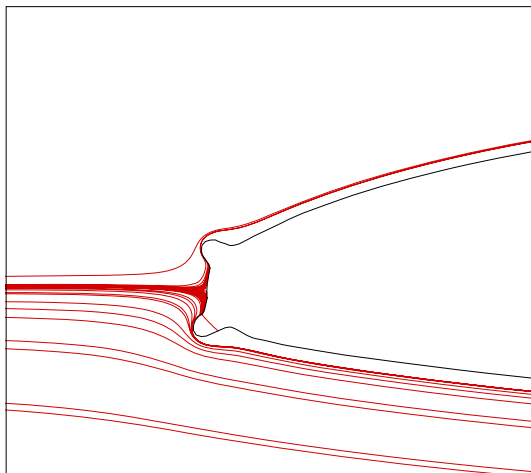
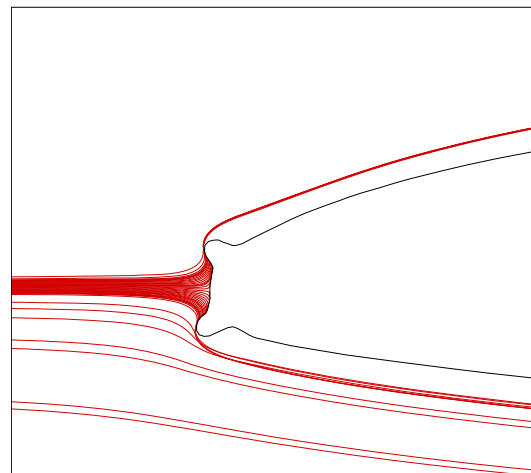


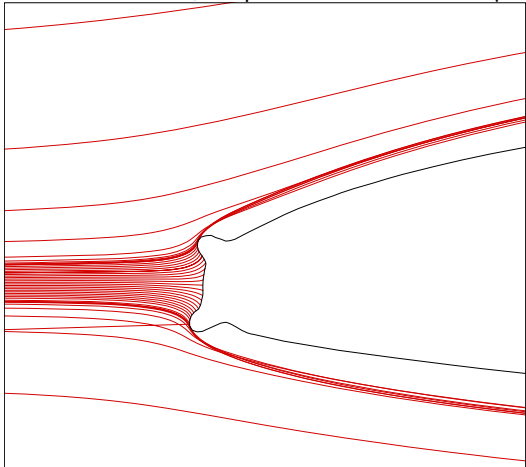
Figure F1.—Contribution to impingement efficiency by droplet diameter; Twin Otter with 22.5-min ice, 21 μm MVD.



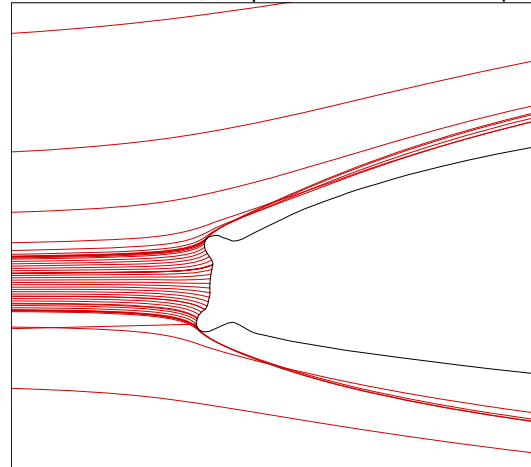
a. Twin Otter 22.5, Droplet Diameter = 4.0407 μm



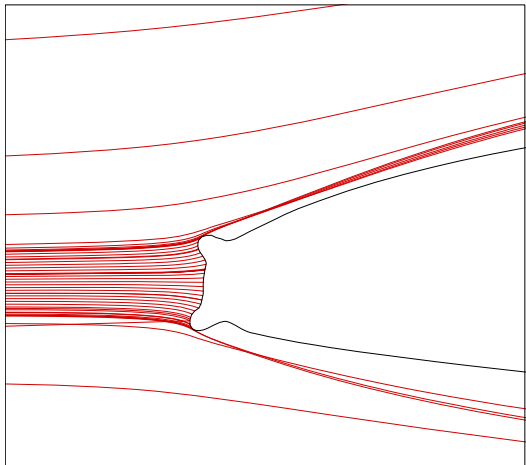
b. Twin Otter 22.5, Droplet Diameter = 9.6721 μm



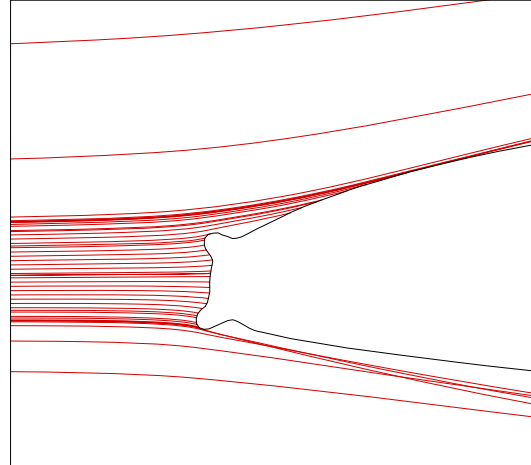
c. Twin Otter 22.5, Droplet Diameter = 14.248 μm



d. Twin Otter 22.5, Droplet Diameter = 20.944 μm

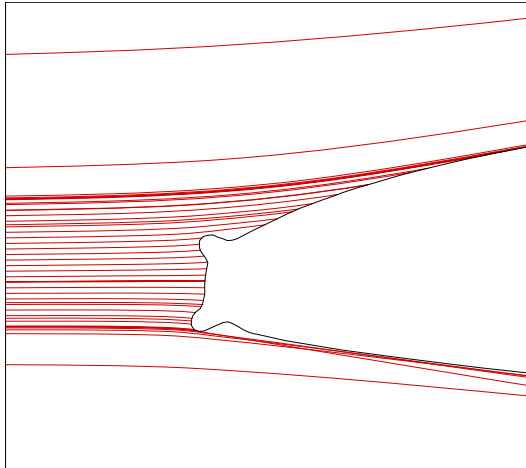


e. Twin Otter 22.5, Droplet Diameter = 28.153 μm

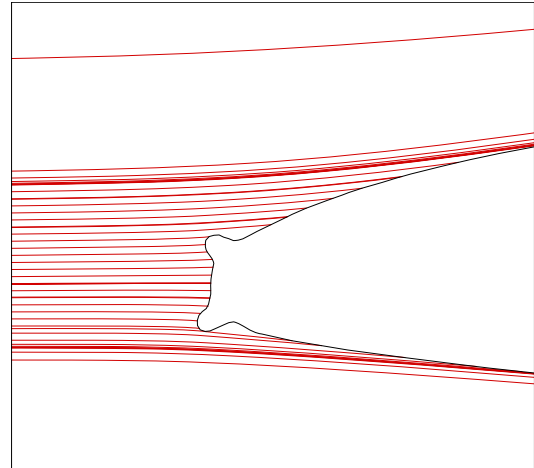


f. Twin Otter 22.5, Droplet Diameter = 45.236 μm

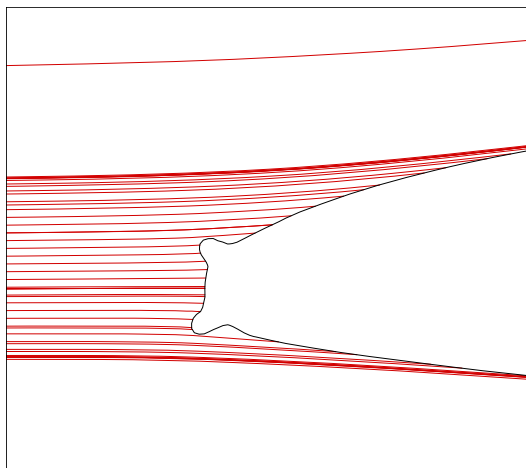
Figure F2.—Particles trajectories; Twin Otter Tail with 22.5-min ice shape.



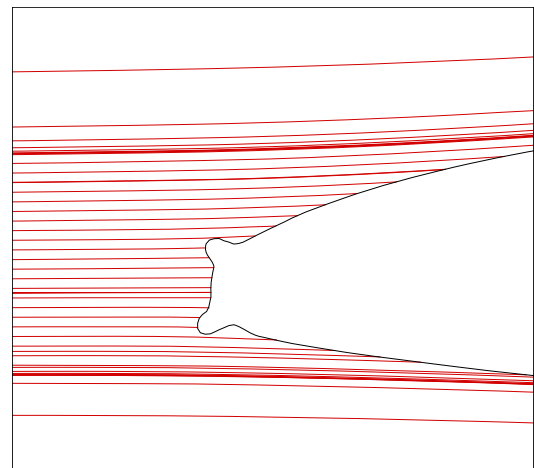
g. Twin Otter 22.5, Droplet Diameter = 70.072 μm



h. Twin Otter 22.5, Droplet Diameter = 88.859 μm



i. Twin Otter 22.5, Droplet Diameter = 103.41 μm



j. Twin Otter 22.5, Droplet Diameter = 163.97 μm

Figure F2.—Particles trajectories; Twin Otter Tail with 22.5-min ice shape.

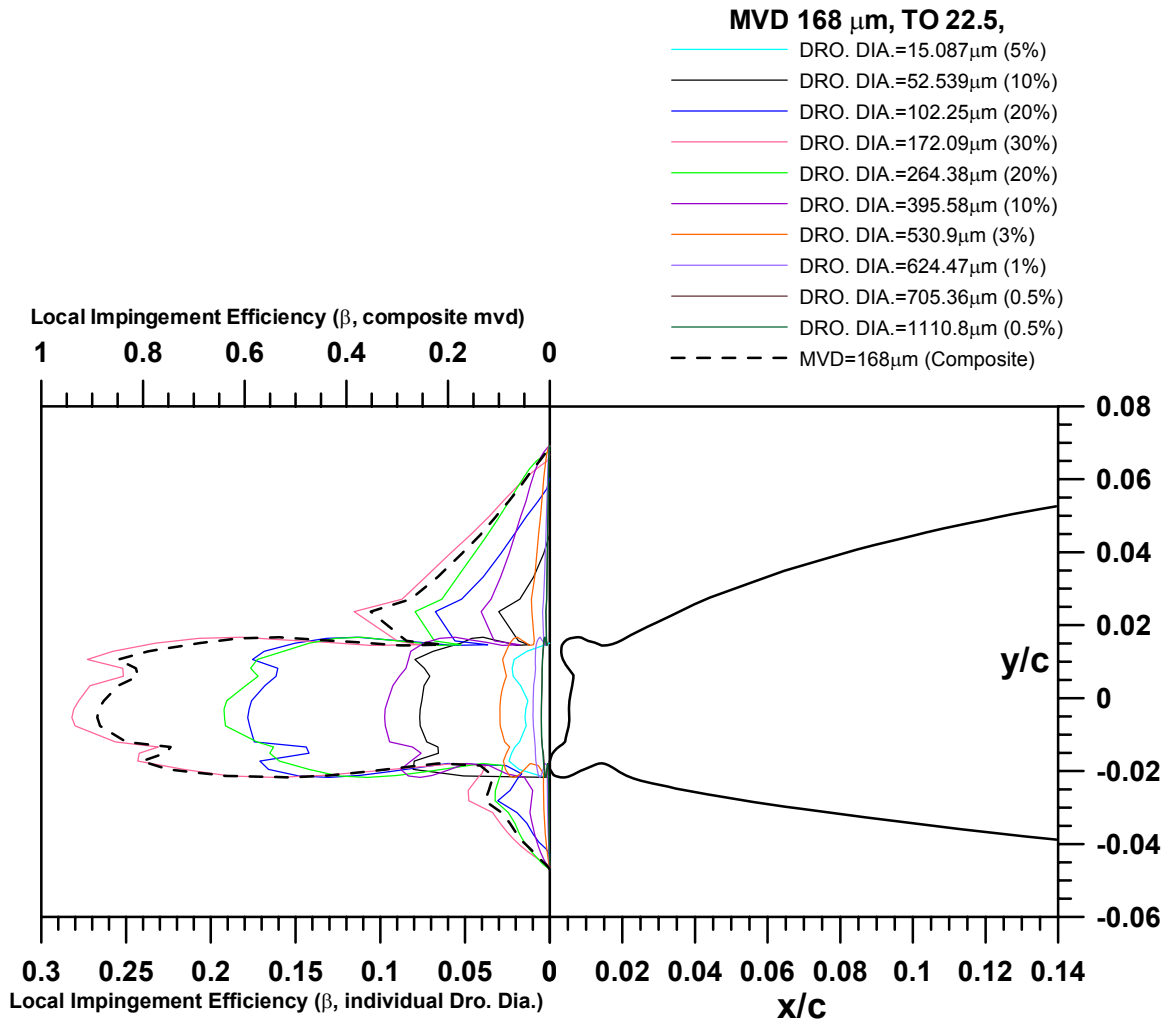
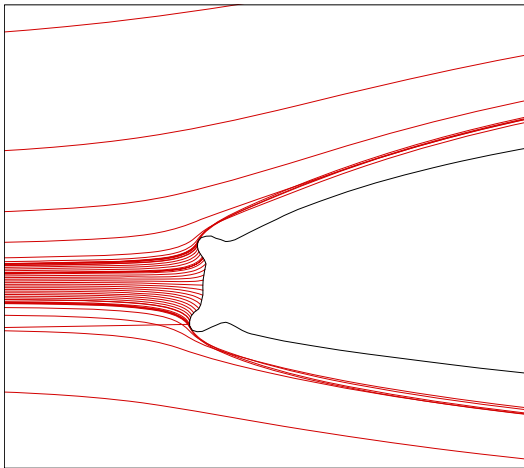
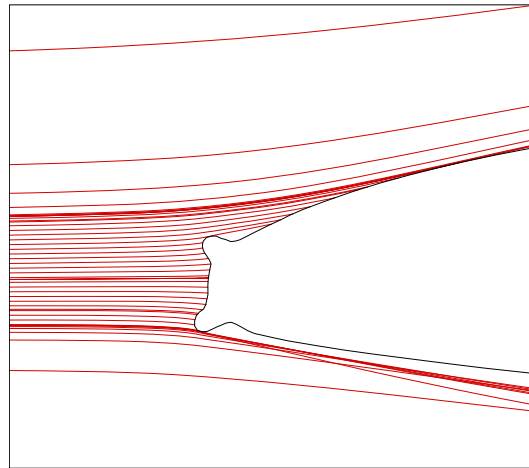


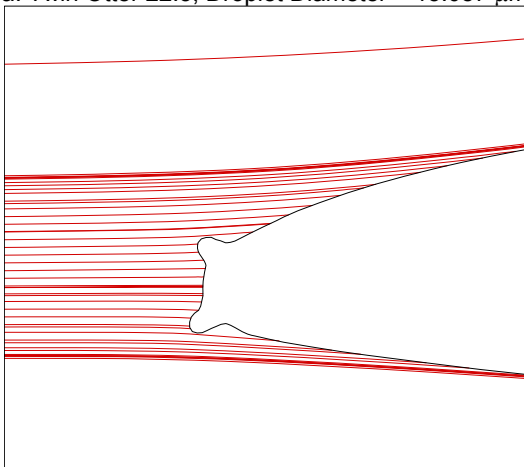
Figure F3.—Contribution to impingement efficiency by droplet diameter;
Twin Otter with 22.5-min ice, 168 μm MVD.



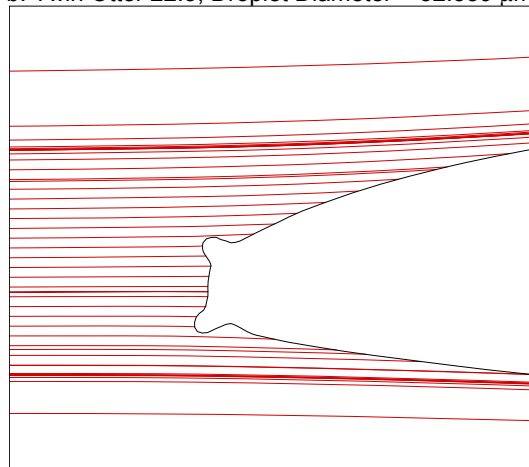
a. Twin Otter 22.5, Droplet Diameter = 15.087 μm



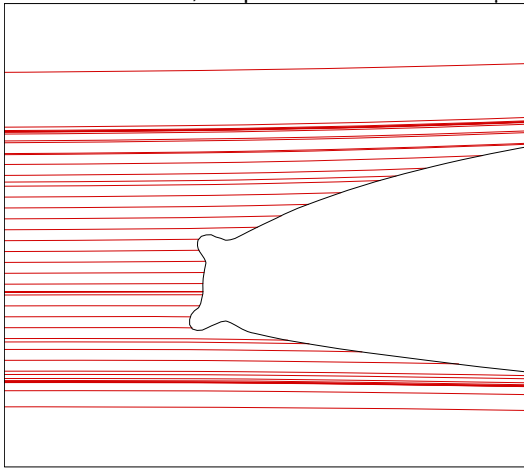
b. Twin Otter 22.5, Droplet Diameter = 52.539 μm



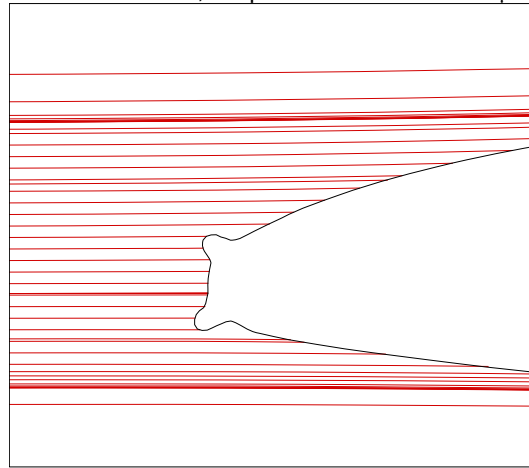
c. Twin Otter 22.5, Droplet Diameter = 102.25 μm



d. Twin Otter 22.5, Droplet Diameter = 172.09 μm

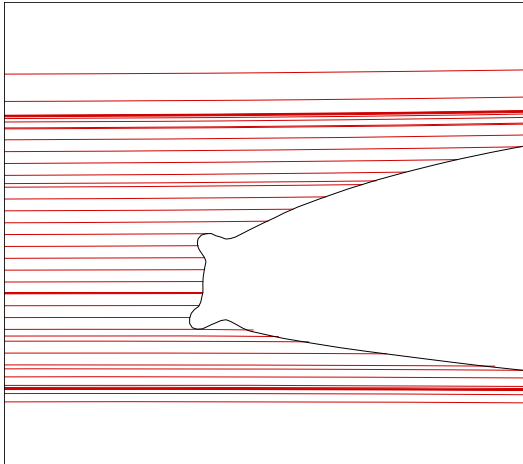


e. Twin Otter 22.5, Droplet Diameter = 264.38 μm

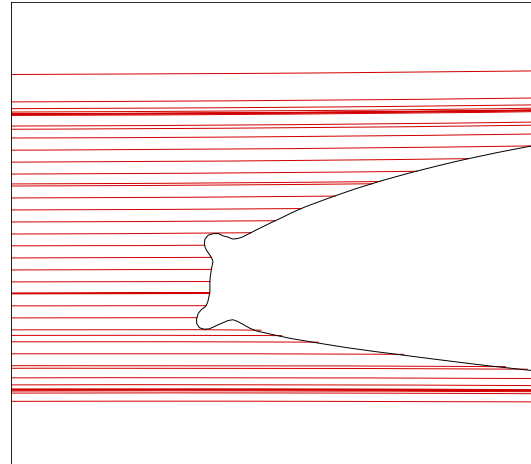


f. Twin Otter 22.5, Droplet Diameter = 395.58 μm

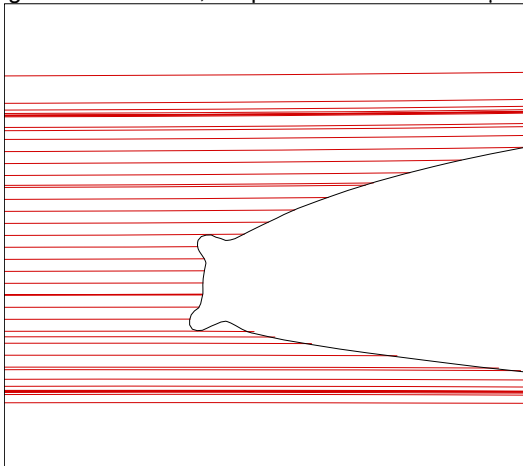
Figure F4.—Particles trajectories; Twin Otter Tail with 22.5-min ice shape.



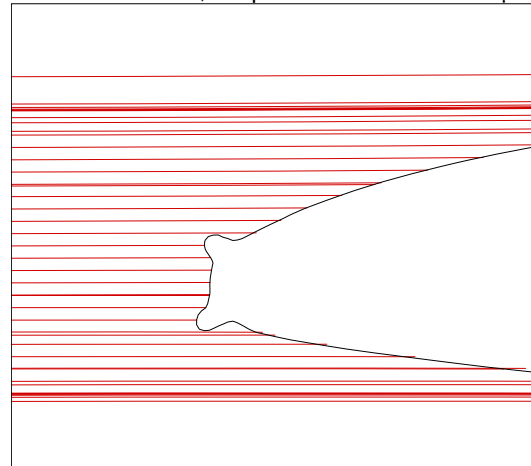
g. Twin Otter 22.5, Droplet Diameter = 530.9 μm



h. Twin Otter 22.5, Droplet Diameter = 624.47 μm



i. Twin Otter 22.5, Droplet Diameter = 705.36 μm



j. Twin Otter 22.5, Droplet Diameter = 1110.8 μm

Figure F4.—Particles trajectories; Twin Otter Tail with 22.5-min ice shape.

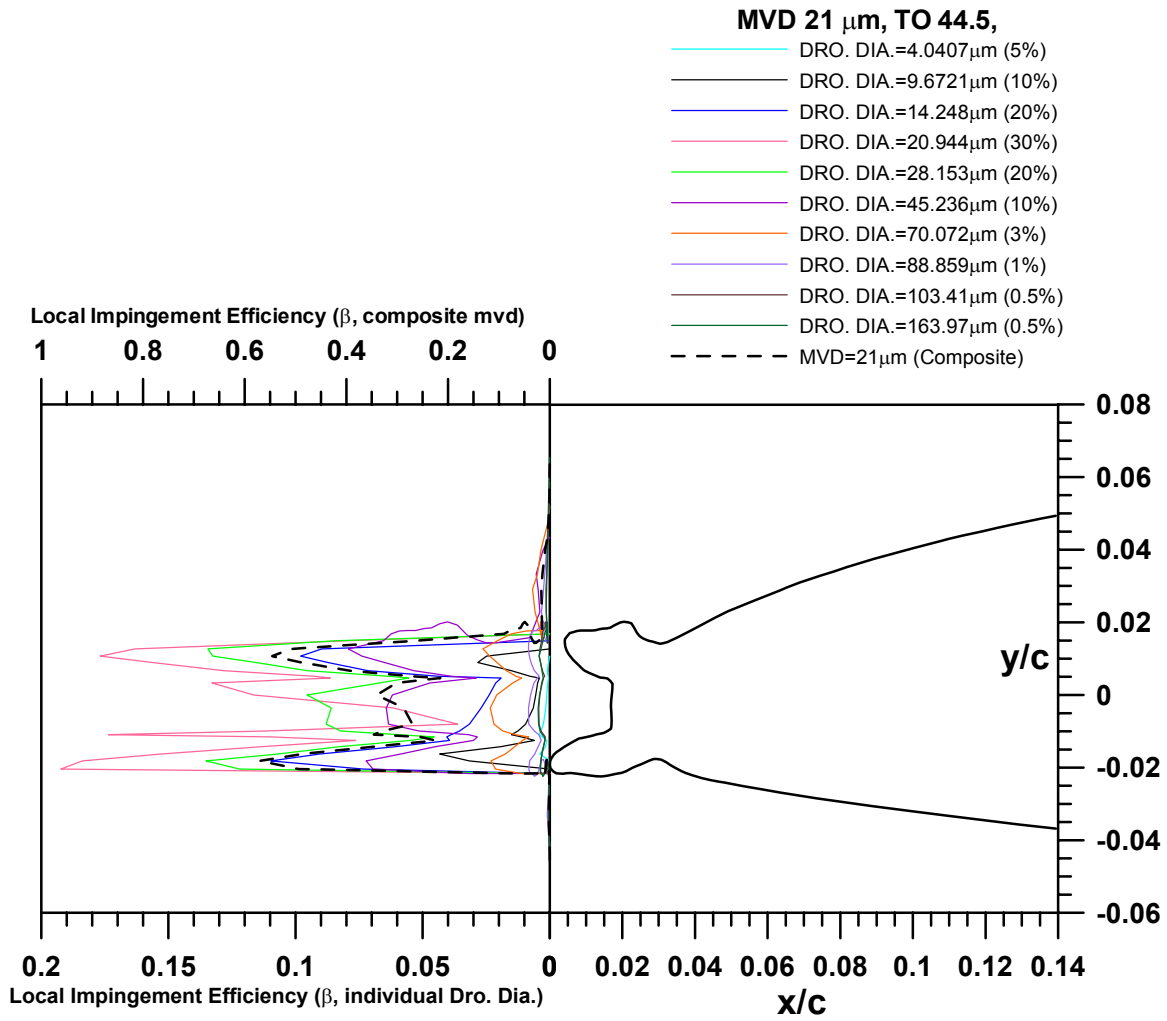
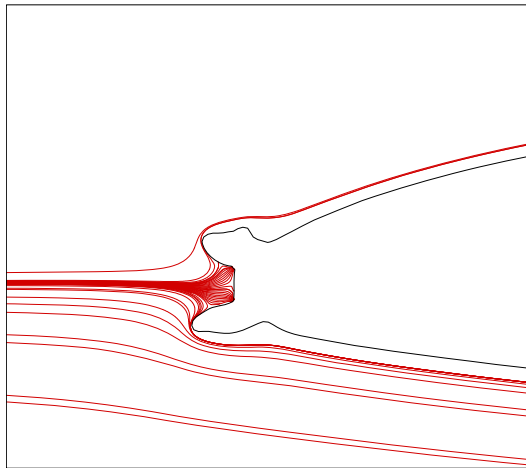
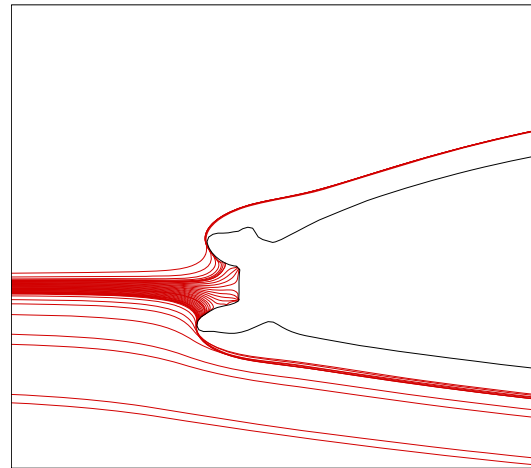


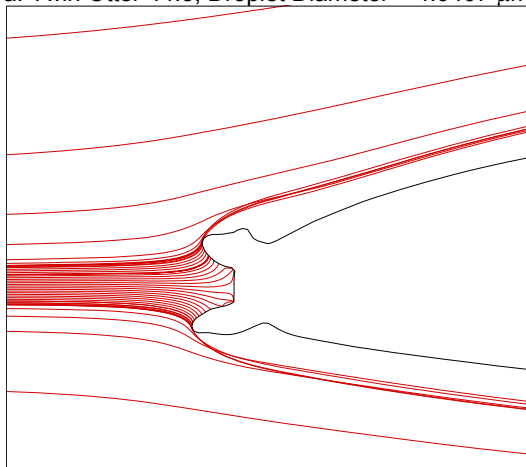
Figure F5.—Contribution to impingement efficiency by droplet diameter;
Twin Otter with 44.5-min ice, 21 μm MVD.



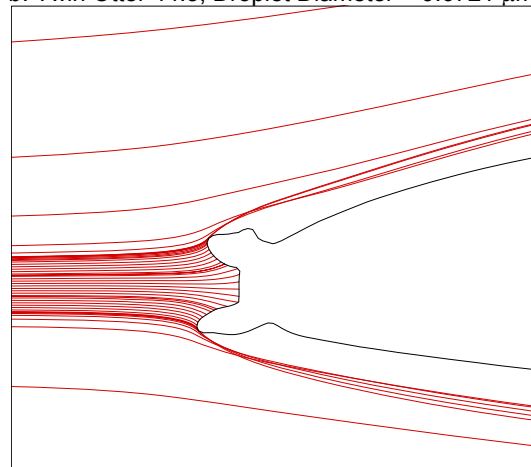
a. Twin Otter 44.5, Droplet Diameter = 4.0407 μm



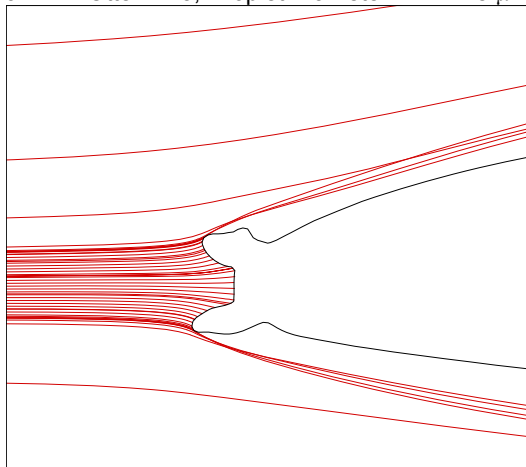
b. Twin Otter 44.5, Droplet Diameter = 9.6721 μm



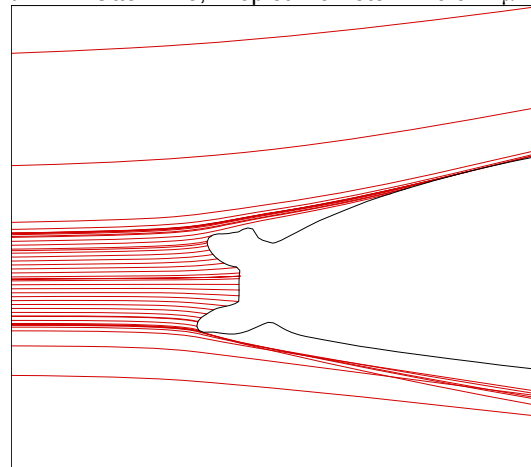
c. Twin Otter 44.5, Droplet Diameter = 14.248 μm



d. Twin Otter 44.5, Droplet Diameter = 20.944 μm

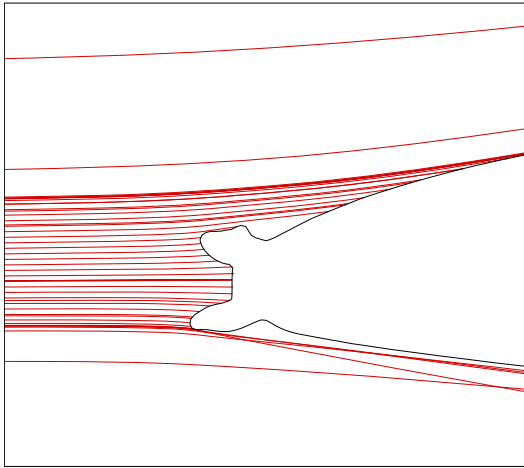


e. Twin Otter 44.5, Droplet Diameter = 28.153 μm

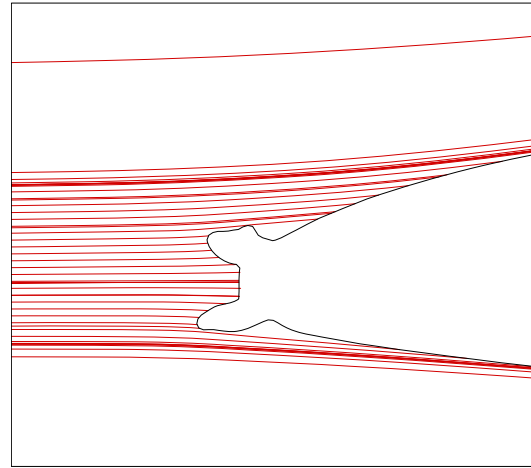


f. Twin Otter 44.5, Droplet Diameter = 45.236 μm

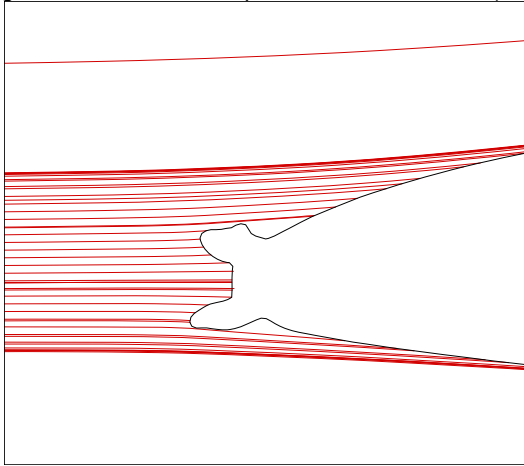
Figure F6.—Particles trajectories; Twin Otter Tail with 44.5-min ice shape.



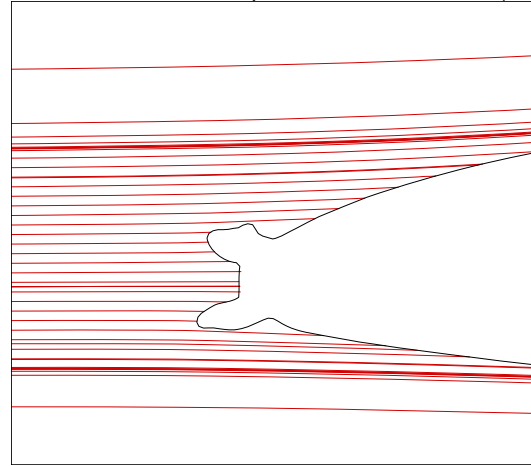
g. Twin Otter 44.5, Droplet Diameter = 70.072 μm



h. Twin Otter 44.5, Droplet Diameter = 88.859 μm



i. Twin Otter 44.5, Droplet Diameter = 103.41 μm



j. Twin Otter 44.5, Droplet Diameter = 163.97 μm

Figure F6.—Particles trajectories; Twin Otter Tail with 44.5-min ice shape.

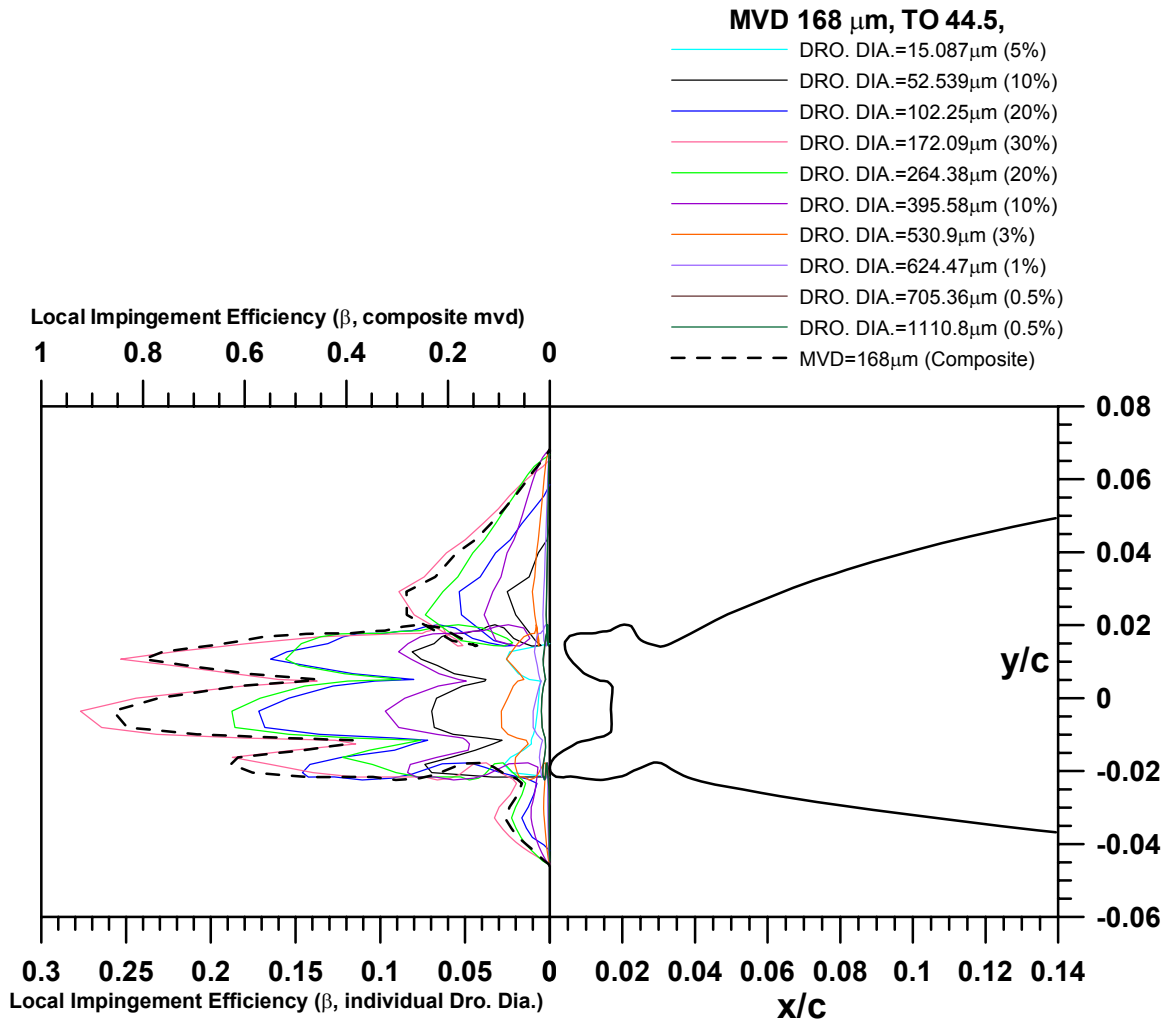
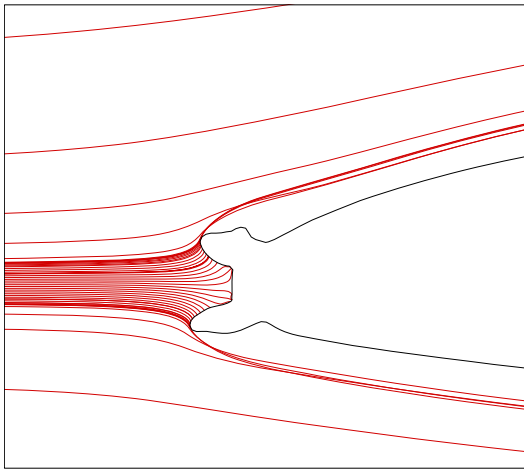
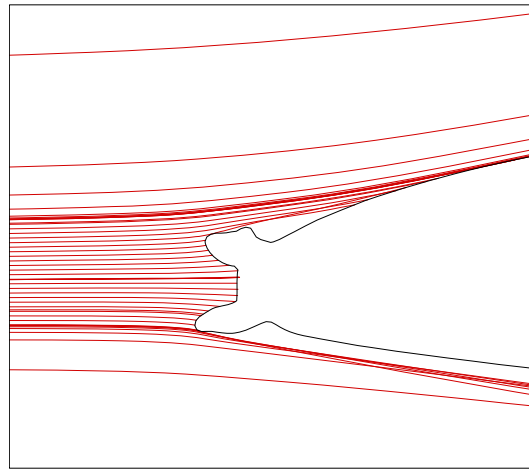


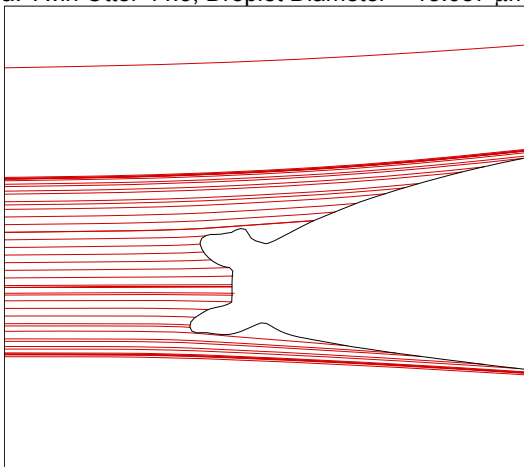
Figure F7.—Contribution to impingement efficiency by droplet diameter;
Twin Otter with 44.5-min ice, 168 μm MVD.



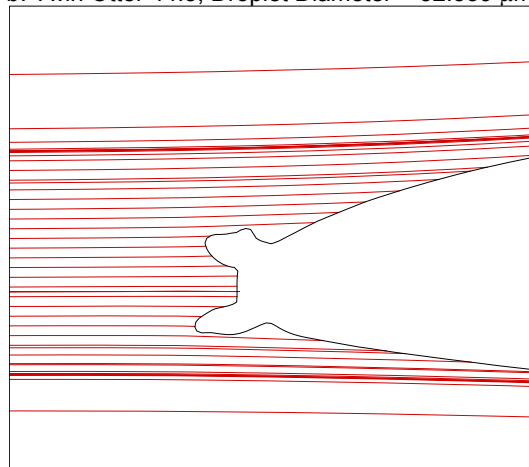
a. Twin Otter 44.5, Droplet Diameter = 15.087 μm



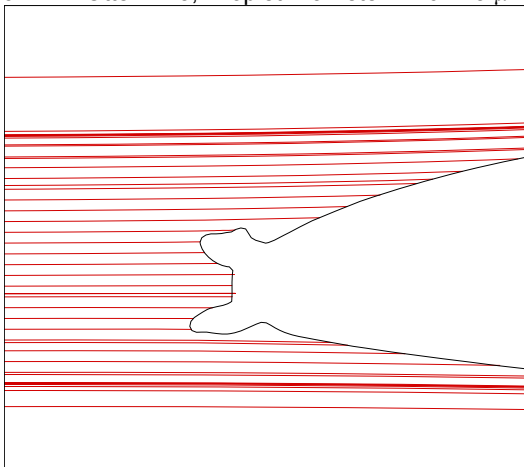
b. Twin Otter 44.5, Droplet Diameter = 52.539 μm



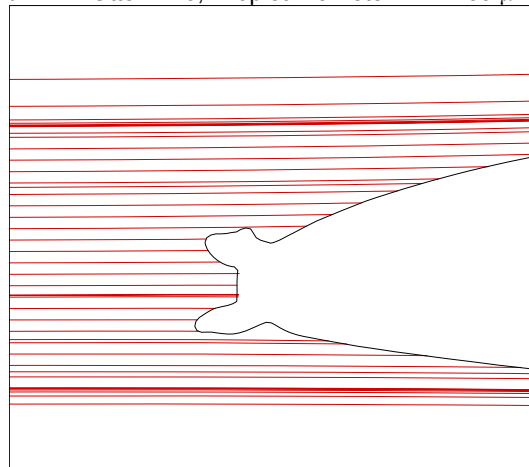
c. Twin Otter 44.5, Droplet Diameter = 102.25 μm



d. Twin Otter 44.5, Droplet Diameter = 172.09 μm

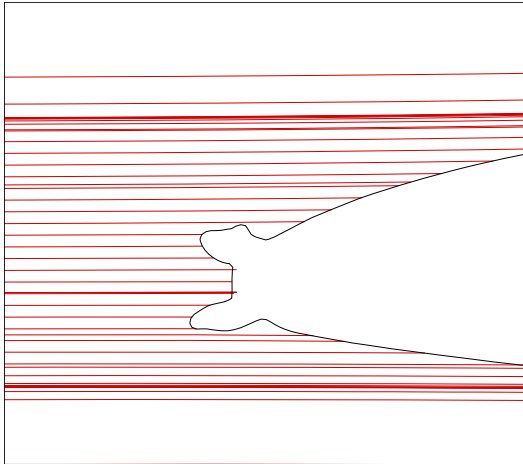


e. Twin Otter 44.5, Droplet Diameter = 264.38 μm

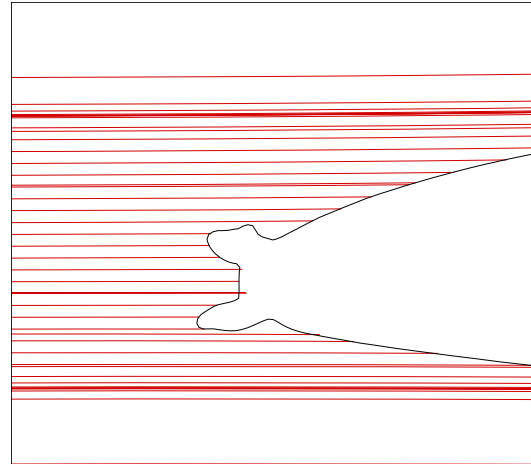


f. Twin Otter 44.5, Droplet Diameter = 395.58 μm

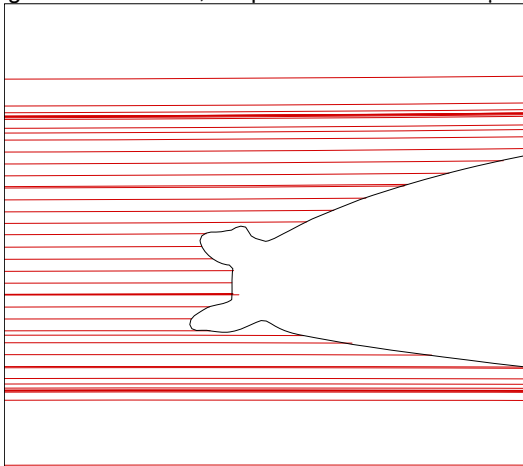
Figure F8.—Particles trajectories; Twin Otter Tail with 44.5-min ice shape.



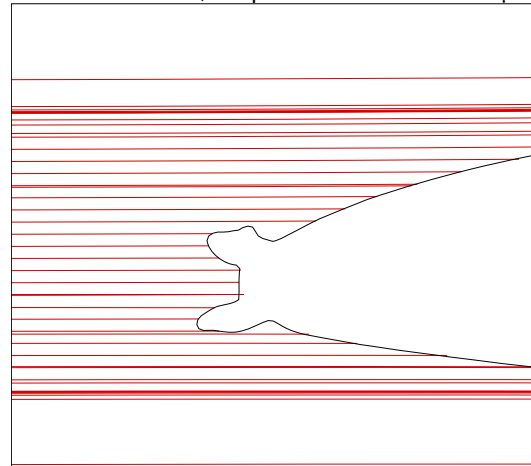
g. Twin Otter 44.5, Droplet Diameter = 530.9 μm



h. Twin Otter 44.5, Droplet Diameter = 624.47 μm



i. Twin Otter 44.5, Droplet Diameter = 705.36 μm



j. Twin Otter 44.5, Droplet Diameter = 1110.8 μm

Figure F8.—Particles trajectories; Twin Otter Tail with 44.5-min ice shape.

Appendix G—Comparison of Experimental and LEWICE Maximum and Total Impingement Efficiencies

TABLE G1.—COMPARISON OF EXPERIMENTAL AND LEWICE RESULTS

Model	Test Conditions		Experimental Results				LEWICE Results			
			β_{\max}	$A_{\bar{\beta}}$ (mm)	A_f (mm)	\bar{E}	β_{\max}	$A_{\bar{\beta}}$ (mm)	\bar{E}	Δ (%) = (LEWICE- EXP)/ LEWICE (%)
	α	MVD								
MS(1)-0317	0	11	0.35	10.496	155.493	0.0675	0.28	9.332	0.0600	-12.5
		21	0.49	28.907	155.493	0.1859	0.51	29.048	0.1868	0.5
		79	0.67	52.371	155.493	0.3368	0.80	80.597	0.5183	35.0
		137	0.75	68.403	155.493	0.4399	0.89	105.927	0.6812	35.4
		168	0.87	81.618	155.493	0.5249	0.91	114.044	0.7334	28.4
NACA 65 ₂ -415	0	11	0.46	9.674	137.323	0.0704	0.41	8.642	0.0629	-11.9
		21	0.61	23.697	137.323	0.1726	0.61	23.851	0.1737	0.6
		79	0.75	45.623	137.323	0.3322	0.85	70.884	0.5162	35.6
		137	0.9	66.666	137.323	0.4855	0.91	94.435	0.6877	29.4
		168	0.91	59.888	137.323	0.4361	0.93	101.859	0.7418	41.2
	4	11	0.39	9.76	141.329	0.0691	0.39	9.252	0.0655	-5.5
		21	0.59	28.159	141.329	0.1992	0.59	27.178	0.1923	-3.6
		79	0.72	50.861	141.329	0.3599	0.81	77.894	0.5512	34.7
		137	0.89	66.018	141.329	0.4671	0.89	100.939	0.7142	34.6
		168	0.9	67.301	141.329	0.4762	0.91	107.561	0.7611	37.4
GLC-305	1.5	11	0.48	11.704	79.321	0.1476	0.47	8.836	0.1114	-32.4
		21	0.59	16.776	79.321	0.2115	0.66	18.899	0.2383	11.2
		79	0.75	30.609	79.321	0.3859	0.87	47.036	0.5930	34.9
		137	0.89	40.059	79.321	0.505	0.93	59.926	0.7555	33.2
		168	0.89	43.444	79.321	0.5477	0.94	63.732	0.8035	31.8
Twin Otter	0	11	0.33	9.469	173.796	0.0545	0.29	9.280	0.0534	-2.0
		21	0.52	26.689	173.796	0.1536	0.51	27.216	0.1566	1.9
		79	0.73	49.374	173.796	0.2841	0.80	80.467	0.4630	38.6
		137	0.81	60.554	173.796	0.3484	0.88	110.095	0.6335	45.0
		168	0.82	63.134	173.796	0.3633	0.91	120.078	0.6909	47.4
	4	11	0.28	9.996	189.139	0.0529	0.28	8.929	0.0472	-11.9
		21	0.46	27.963	189.139	0.1478	0.50	30.269	0.1600	7.6
		79	0.62	53.762	189.139	0.2842	0.78	94.443	0.4993	43.1
		137	0.78	85.883	189.139	0.4541	0.87	125.089	0.6614	31.3
		168	0.81	88.264	189.139	0.4667	0.89	134.399	0.7106	34.3
Twin Otter and 22.5-min ice-shape	0	11	0.24	8.59	171.446	0.0501	0.29	11.605	0.0677	26.0
		21	0.53	31.516	171.446	0.1838	0.55	31.304	0.1826	-0.7
		79	0.63	44.031	171.446	0.2568	0.78	92.606	0.5401	52.5
		168	0.95	86.561	171.446	0.5049	0.89	135.720	0.7916	36.2
Twin Otter and 45-min ice-shape	0	11	0.31	12.367	173.766	0.0712	0.28	10.148	0.0584	-21.9
		21	0.55	33.837	173.766	0.1947	0.54	30.145	0.1735	-12.2
		79	0.78	52.849	173.766	0.3041	0.79	99.609	0.5732	46.9
		168	0.95	95.268	173.766	0.5483	0.88	144.909	0.8339	34.3

Appendix H—Colorimetric Analysis on Selected Cases

In order to verify the accuracy of the data reduction systems used to extract the raw impingement data from the dye-laden blotter strips, colorimetric analysis was performed on selected test cases using the procedure described in section 6.3.3. The cases selected for colorimetric analysis were as follows:

Run no. 415—NACA 65₂-415 Airfoil, AOA = 4°, MVD = 21 μm, Spray time = 4 sec

Run no. 574—Twin Otter Tail Section, AOA = 4°, MVD = 21 μm, Spray time = 4 sec

The 4-sec spray time was selected to preserve the strips of the actual cases. Figures H1 and H2 compare LEWICE analysis data with experimental data obtained with the laser data reduction system and from colorimetric analysis using a spectrophotometer. To compute the impingement efficiency for the test cases 415 and 574 (listed above) it was necessary to analyze a collector strip for the 21 μm MVD case using colorimetric analysis. The collector selected was as follows:

Run no. 439—Collector, Location at AOA = 4°, MVD = 21 μm, Spray time = 4 sec

The results shown in figures H1 and H2 demonstrate good correlation between the experimental data obtained using the laser reflectometer and colorimetric analysis.

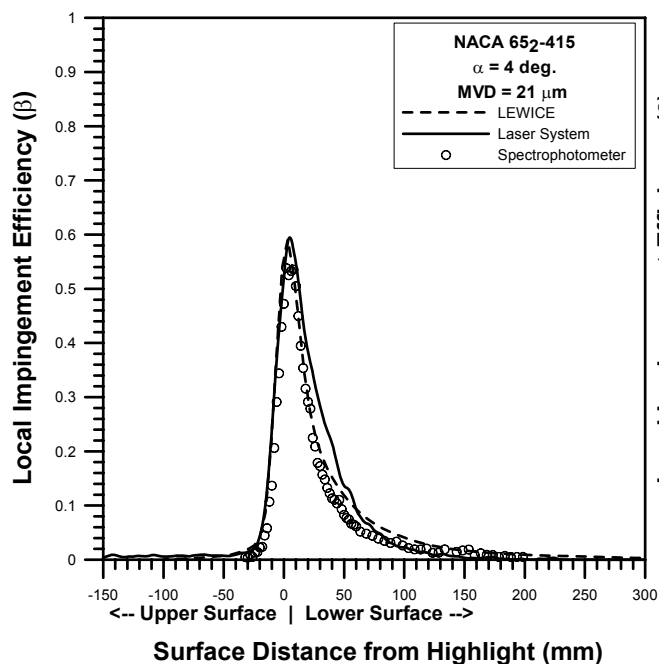


Figure H1.—Data comparison for NACA 65₂-415

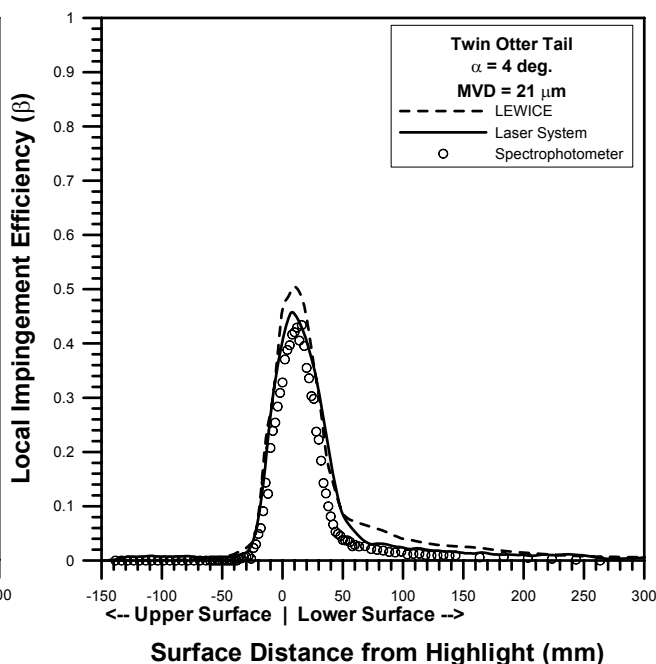


Figure H2.—Data comparison for Twin Otter Tail

REPORT DOCUMENTATION PAGE

*Form Approved
OMB No. 0704-0188*

The public reporting burden for this collection of information is estimated to average 1 hour per response, including the time for reviewing instructions, searching existing data sources, gathering and maintaining the data needed, and completing and reviewing the collection of information. Send comments regarding this burden estimate or any other aspect of this collection of information, including suggestions for reducing this burden, to Department of Defense, Washington Headquarters Services, Directorate for Information Operations and Reports (0704-0188), 1215 Jefferson Davis Highway, Suite 1204, Arlington, VA 22202-4302. Respondents should be aware that notwithstanding any other provision of law, no person shall be subject to any penalty for failing to comply with a collection of information if it does not display a currently valid OMB control number.

PLEASE DO NOT RETURN YOUR FORM TO THE ABOVE ADDRESS.

1. REPORT DATE (DD-MM-YYYY) 01-10-2007		2. REPORT TYPE Technical Memorandum		3. DATES COVERED (From - To)	
4. TITLE AND SUBTITLE Large and Small Droplet Impingement Data on Airfoils and Two Simulated Ice Shapes				5a. CONTRACT NUMBER	
				5b. GRANT NUMBER	
				5c. PROGRAM ELEMENT NUMBER	
6. AUTHOR(S) Papadakis, Michael; Wong, See-Cheuk; Rachman, Arief; Hung, Kuohsing, E.; Vu, Giao, T.; Bidwell, Colin, S.				5d. PROJECT NUMBER	
				5e. TASK NUMBER	
				5f. WORK UNIT NUMBER WBS-22-077-41-08	
7. PERFORMING ORGANIZATION NAME(S) AND ADDRESS(ES) National Aeronautics and Space Administration John H. Glenn Research Center at Lewis Field Cleveland, Ohio 44135-3191				8. PERFORMING ORGANIZATION REPORT NUMBER E-15275	
9. SPONSORING/MONITORING AGENCY NAME(S) AND ADDRESS(ES) National Aeronautics and Space Administration Washington, DC 20546-0001				10. SPONSORING/MONITORS ACRONYM(S) NASA	
				11. SPONSORING/MONITORING REPORT NUMBER NASA/TM-2007-213959	
12. DISTRIBUTION/AVAILABILITY STATEMENT Unclassified-Unlimited Subject Categories: 02, 03, and 34 Available electronically at http://gltrs.grc.nasa.gov This publication is available from the NASA Center for AeroSpace Information, 301-621-0390					
13. SUPPLEMENTARY NOTES					
14. ABSTRACT Water droplet impingement data were obtained at the NASA Glenn Icing Research Tunnel (IRT) for four wings and one wing with two simulated ice shapes. The wings tested include three 36-in. chord wings (MS(1)-317, GLC-305, and a NACA 652-415) and a 57-in. chord Twin Otter horizontal tail section. The simulated ice shapes were 22.5- and 45-min glaze ice shapes for the Twin Otter horizontal tail section generated using the LEWICE 2.2 ice accretion program. The impingement experiments were performed with spray clouds having median volumetric diameters of 11, 21, 79, 137, and 168 mm. Comparisons to the experimental data were generated which showed good agreement for the clean wings and ice shapes at lower drop sizes. For larger drop sizes LEWICE 2.2 over predicted the collection efficiencies due to droplet splashing effects which were not modeled in the program. Also for the more complex glaze ice shapes interpolation errors resulted in the over prediction of collection efficiencies in cove and shadow regions of ice shapes.					
15. SUBJECT TERMS Trajectory analysis; Validation; Aircraft icing; Ice formation; Impingement; Deicing; Airfoils; Wings; Swept wings					
16. SECURITY CLASSIFICATION OF:			17. LIMITATION OF ABSTRACT	18. NUMBER OF PAGES	19a. NAME OF RESPONSIBLE PERSON
a. REPORT	b. ABSTRACT	c. THIS PAGE			STI Help Desk (email:help@sti.nasa.gov)
U	U	U	UU	253	19b. TELEPHONE NUMBER (include area code) 301-621-0390

